Svanhild Toppe Tolaas

A Numerical and Theoretical Study of a Multi-torus Floating Solar Island Concept

Master's thesis

◘ NTNU
Norwegian University of
Science and Technology

Svanhild Toppe Tolaas

A Numerical and Theoretical Study of a Multi-torus Floating Solar Island Concept

Master's thesis in Marine Technology
Supervisor: Trygve Kristiansen
June 2020

Norwegian University of Science and Technology
Faculty of Engineering
Department of Marine Technology

Summary

Theoretical and numerical studies are carried out for a multi-torus concept with elastic bands, which is designed to be the floating foundation of a solar island. Available theory on truss and floater-modelling have been adjusted, further developed and combined in order to develop a numerical model for multi-torus structures. The result is what we call a solar island model, which can be summarized as an elastic truss model accounting for floater motion. An implicit-explicit Euler time-scheme is used. The model can in theory be applied to for all kinds of combinations of number of tori, elastic band connections, number of trusses per elastic band and mooring-configurations for a multi-torus.

The numerical model is implemented in MATLAB, and verification studies are carried out for a single torus, with and without mooring-lines. Vertical modes, surge and radial modes are first studied separately. Tme-step studies are performed. Resulting vertical mode RAOs show good accordance with zero-frequency theory. For radial modes, it is found that modes divisible by four should be excluded, while the rest of the modes are in accordance with theoretical RAOs. The results in the surge-study are also satisfying. A combined motion case with heave, surge and radial mode 2 activated is also tested for three wave frequencies and shows promising results.

Theory for hydrodynamic interaction is implemented in MATLAB, and verification studies on cross-coupled added mass terms are in good accordance with previously results in WAMIT.

Numerical resulting RAOs from a 2-torus and 5-torus model with one truss per elastic band are compared with theory. Deviations from theory will indicate structural interactions via the trusses between the tori. A minor effect is seen for vertical modes, more for radial modes, while the largest effect is seen for surge motion. For the 5-torus case, the RAO shape in surge is drastically changed with new, common peaks at $kR \simeq 4.9$ for all tori. This is believed to be due to a numerical problem, or an unwanted effect of how the elastic bands are modelled. It is found that there seems to be an instability in tension-development. Though this tendency may be linked to the strange observations in surge, it is not believed to have destroyed the rest of the presented RAOs.

An important goal is to study whether irregularities in previously obtained experimental RAOs for a 5-torus model are due to structural interactions via the elastic bands between tori. Such irregularities are not at all seen in the numerical results. However, recent inspections of the rubber bands used in the experimental model show that they do not following Hooke's law, which is assumed for the trusses in the numerical model. This of course weakens the potential of the numerical model to represent the experimental model.

The experimental irregularities cannot be explained directly from the results from the implementation of hydrodynamic interaction theory either. Nevertheless, deviations from theory due to what should be structural interactions are seen in the numerical results, and large impact is also seen for vertical modes in the hydrodynamic interaction study. These are interesting results in themselves, and indicate that both structural and hydrodynamic interaction between tori may affect the behaviour of a multi-torus.

Sammendrag

Teoretiske og numeriske studier er gjennomført for en flytende konstruksjon bestående av sirkulære flytere koblet sammen med elastiske bånd, en såkalt multiflyter. Stukturen er designet for å være et flytende fundament for en soløy. Eksisterende teori vedrørende fagverk-modellering såvel som flyter-modellering er blitt justert, videreutviklet og kombinert for å utvikle en numerisk modell for multiflytere. Resultatet er det vi har valgt å kalle en soløymodell, som enkelt forklart er en elastisk fagverksmodell som inkluderer flyterbevegelse. Et implisitt-eksplisitt Euler tidsskjema er brukt. Modellen kan i teorien bli anvendt for alle slags kombinasjoner av antall flytere, elastiske bånd mellom hver flyter og fagverkselement per elastiske bånd, såvel som ulike fortøyningsoppsett.

Den numeriske modellen implementeres i MATLAB, og verifikasjonsstudier gjennomføres for en enkel flyter, med og uten fortøyning. Vertikale moder, jaging og radielle moder studeres først separat, og sensitivitet til tiddsteg underøkes. For vertikale moder er det god overensstemmelse med null-frekvens teori. For radielle moder blir det funnet at moder som er delelig på fire må ekskluderes, mens resten av dem er i overenstemmelse med teori. Resultatene i jaging er også tilfredsstillende. En versjon hvor både hiv, jaging og radiell mode 2 er aktivert blir også testet, og gir tilfredsstillende resultat i de tre bølgefrekvensene som testes.

Teori for hydrodynamisk interaksjon blir implementert i MATLAB, og resultatene fra et verifikasjonsstudie på kryss-ledd for tilleggsmasse viser god overenstemmelse med tidligere reultat som er estimert i WAMIT.

Resulterende numeriske RAOer for 2-flyter og 5-flyter modeller med ett fagverkselement per elastiske bånd blir sammenlignet med teori. Avvik fra teoretiske RAO vil være en indikasjon på strukturelle interaksjoner mellom flytere, via fagverkselementene. Noe effekt er observert for vertikale moder, enda mer for radielle, men det er i jaging at den mest drastiske effekten er observert. For 5-flytermodellen endres selve formen på RAOen, og det oppstår en felles topp for alle flytere i $kR \simeq 4.9$. Dette tror man må komme av et numerisk problem, eller en uønsket effekt av hvordan man har modellert fagverkselementene. En ustabilitet er funnet i enkelte tidsserier for strekk i fagverkselementene. Dette kan muligens være koblet til de uventede reultatene for jaging, men man tror ikke det har ødelagt resten av de presenterte RAOene.

Et viktig mål er å studere om irregulariteter i eksperimentelle RAOer fra to tidligere tester med en 5-flyter modell kan skyldes strukturelle interaksjoner mellom flyterne. Slike irregulariteter er ikke funnet igjen i de numeriske resultatene. Det må nevnes at det ved nylige inspeksjoner av de elastiske båndene i den eksperimentelle modellen ble funnet at disse ikke følger Hookes lov, som er antatt i den numeriske modellen. Dette svekker selve grunnlaget for å bruke den numeriske modellen til å representere den eksperimentelle.

De eksperimentelle irregularitetene kan heller ikke direkte forklares ut fra resultatene fra implementering av den hydrodynamiske interaksjonsteorien i MATLAB. Det må likevel belyses at det er funnet avvik fra teoretiske RAOer på grunn av det som må være strukturelle interaksjoner i de numeriske resultatene, og også store avvik fra teori i RAOer fra hydrodynamisk interaksjonsteori. Dette er interessante resultater i seg selv, og indikerer at både strukturelle og hydrodynamiske interaksjoner potensielt kan påvirke bevegelsen til en multiflyter.

Preface

This Master's thesis is the final project of my Master of Science degree in Marine Hydrodynamics at the Department of Marine Technology, Norwegian University of Science and Technology (NTNU) in Trondheim, Norway. The work is carried out during the spring of 2020, and the workload corresponds to 30 ECTS. The Master's thesis is a continuation of the preliminary project thesis carried out during the autumn of 2019.

Professor Trygve Kristiansen suggested the topic and the development of a numerical multi-torus model for a solar island structure. Professor em. Bruce Patterson and Professor em. Frode Mo provided the main idea of a floating solar island concept, where energy is extracted for the production of solar fuel on an FPSO.

Co-student Øyvind Onestad Olsen has written a Master's thesis on the exact same topic, and we have worked closely during the entire process, under guidance by our supervisor Professor Trygve Kristiansen.

The reader should have basic knowledge within the fields of hydrodynamics and structural dynamics.

Svanhild Toppe Tolaas
17.06.2020
Trondheim, Norway

Acknowledgements

Contents

Nomenclature

Abbreviations

ft Floater truss

RAO   Response Amplitude Operator

ZFT   Zero-frequency theory

Greek Letters

β Angle used for angular position on floater [rad]. (See Figure 2.5)

λ Wave length [m]

ω Circular wave frequency [rad/s]

ϕ Velocity potential, in general

ϕ^F Far-field velocity potential

ϕ^N Near-field velocity potential

ξ Damping ratio [%]

ζ Wave profile [m]

ζ_a Wave amplitude [m]

Roman Symbols

$2p$ Spacing between tori [m]

$\boldsymbol{i}$ $[1, 0, 0]$

$\boldsymbol{j}$ $[0, 1, 0]$

$\boldsymbol{k}$ $[0, 0, 1]$

$\boldsymbol{r}$ $[\cos(\beta), \sin(\beta), 0]$

$\boldsymbol{s}_{ft}$ Unit vector of floater truss, defined from node i to j

$\boldsymbol{s}_k$ Unit vector of truss k, defined from node i to j

η_1 Surge motion [m]

η_2 Sway motion [m]

ρ Density of seawater, $\rho = 1025$ [kg/m^3]

$a_n(t)$ Mode amplitude for vertical mode n [m]

A_{11} Added mass in x-direction [kg]

a_{33}^n Two-dimensional added mass for vertical floater mode n [kg/m]

a_{rr} Added mass per unit length of the floater for radial motion [kg/m]

$A_{t,j,n}$ Vertical added mass on torus t due to mode n motion of torus j $[kg/m]$

$a_{t,j,n}$ Two-dimensional vertical added mass on torus t due to mode n motion of torus j $[kg/m]$

b Cross-sectional water plane area of torus per unit length $[m]$

$b_n(t)$ Mode amplitude for radial mode n $[m]$

c Cross-sectional radius of floater $[m]$

C_{11} Mooring stiffness term $[N/m]$

EI Torus bending stiffness $[N/m]$

$F_1^{addedmass}$ Added mass force in x-direction $[N]$

F_1^{exc} Wave excitation force in x-direction $[N]$

F_1^{truss} Truss force force in x-direction $[N]$

$f_r^{addedmass}$ Radial added mass force per unit length of the floater $[N/m]$

$f_r^{exc,gen}$ Generalized radial wave excitation force per unit length of the floater $[N/m]$

f_r^{exc} Radial wave excitation force per unit length of the floater $[N/m]$

f_r^{truss} Radial truss force per unit length of the floater $[N/m]$

g Gravitational Constant, $g = 9.81$ $[m/s^2]$

J_n Bessel function of the first kind.]

k Wave number, $k = 2\pi/\lambda$ $[rad/m]$

k_m Mooring-line stiffness $[N/m]$

m Torus mass per unit length $[kg/m]$

R Center-line curve radius of torus $[m]$

T Wave period, $T = 2\pi/\omega$ $[s]$

T_k Tension in truss k $[N]$

$v(\beta,t)$ Radial motion of floater $[m]$

$w(\beta,t)$ Vertical motion of floater $[m]$

Chapter 1

Introduction

The energy demand of the world is increasing. IEA (2017) presents an assessment by the U.S. Energy Information Administration of the outlook for international energy markets through 2050, and predict that the world energy consumption rises nearly 50% between 2018 and 2050. Among renewable energy sources, electricity generation from wind and solar resources are believed to have the largest increase towards 2050, reaching 6.7 trillion and 8.3 trillion kilowatt hours (kWh), respectively. Important reasons are the cost-competitiveness of these technologies, as well the support from government policies in many countries. By 2050, wind and solar are in fact predicted to account for over 70% of the total renewables generation in the world.

At the same time as the need of energy increases, a drastic reduction in CO_2 emissions from fossil fuel burning is required to limit the extent of global warming. However, carbon-based liquid fuels will in the foreseeable future continue to be important energy storage media.

1.1 Floating Solar Island Concept

With these problems in mind, scientists from Switzerland and Norway have joined forces and propose a combination of largely existing technologies to use solar energy to recycle atmospheric CO_2 into a liquid fuel Patterson et al. (2019). The idea is that photo-voltaic cells, laid on clusters of marine floating islands, will convert sunlight into electrical energy which powers the production of H_2 and extraction of CO_2 from seawater. This process will then have zero net CO_2 emissions, since the seawater and the atmosphere are in CO_2 equilibrium. Reacting the gases one obtains the energy carrier methanol, which is then shipped to consumers.
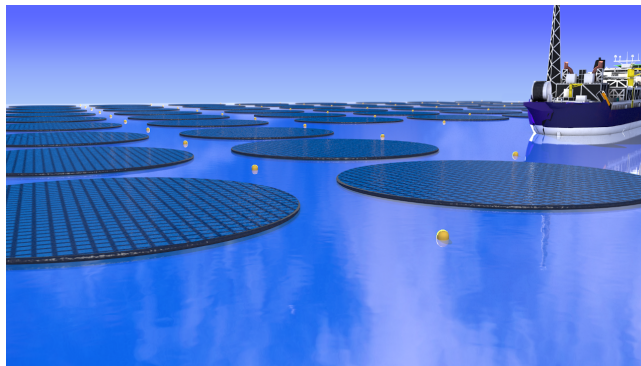
Figure 1.1: Floating Solar island Concept illustration
Illustration of solar islands in a cluster, connected to a FPSO for production of solar fuel. Courtesy of Frode Mo.

In the development of cheap and robust floating structures to carry the photov-volatic cells, scientists at NTNU have been inspired by aquaculture structures. Floating elastic tori have been used to support

fish cages, but are now presented as a plausible structural member of a solar island. Several co-centric tori would support a net-like deck carrying the PIV-cells, as illustrated in Figure 1.1. Professor Trygve Kristiansen is currently studying several aspects of the multi-torus design. This is the background for the current study, which is supervised by the Professor.

Geographical locations suitable for the proposed solar islands are illustrated in Figure 1.2. Physical conditions that must be met are average incident solar radiation $> 175\ W/m^2$, 100-year maximum wave height < 7 m, water depth < 600 m, and absence of tropical hurricanes.

Arrays of solar islands moored together would occupy much less space than typical offshore wind parks producing the same amount of energy, as illustrated in Figure 1.3. Here, the tori, marked as "floater elements", are illustrated. The fact that the photo-voltaic cells are surrounded by water increases the generated power, as the water reflects the sunlight. Lastly, it should be mentioned that the potential of the structure is not only limited to methanol production offshore, it can also be position closer to shore to supply cities with electricity through traditional cables, or work as stations for recharging electrically driven ships.
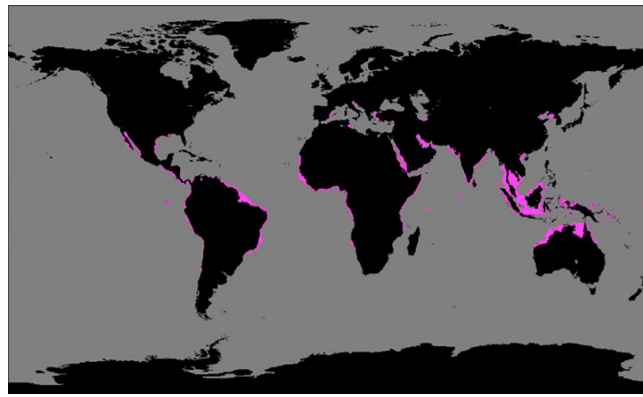
Figure 1.2: Geographical locations fit for solar islands
Geographical locations fit for solar islands are marked by magneta. Taken from Patterson et al. (2019).
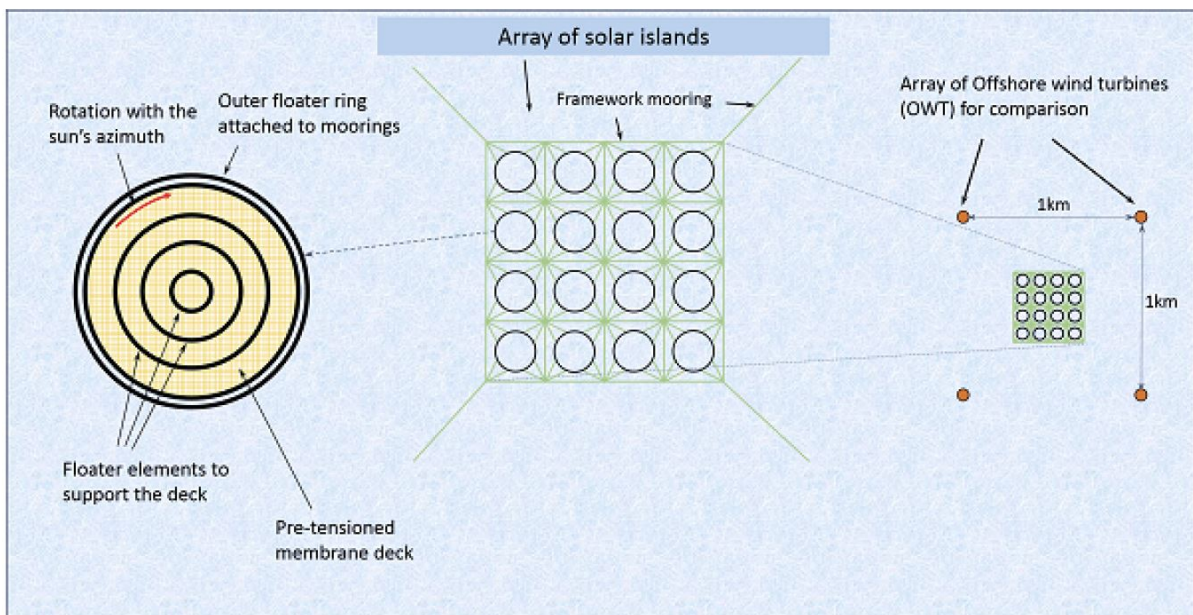
Figure 1.3: Floating solar island set-up
To the left, the proposed design of a multi-torus structure, where several co-centric tori supports a membrane deck. In the middle, an array of solar islands. To the right, the area occupied by an array of solar islands compared to the area occupied by four offshore wind turbines, producing approximately the same energy amount. Taken from Kristiansen et al. (2017)

1.2   Literature Review

There are several studies on truss models and floating tori, especially on the semi-submerged single slender torus. In this section, the main studies that lay the foundation for the current work will be presented.

The study by Faltinsen (2011) concerns either a semi-submerged elastic cocentric torus or two closely spaced ones. A slender-body theory is derived based on a rigid free-surface condition, using the limiting case that the forcing frequency $\omega \rightarrow 0$. In order to account for 3D effects, an asymptotic matching between a near-field and far-field description of the torus is used. This theory is also presented in Faltinsen (2010), where current and wave loads on floating fish farms are studied.

Faltinsen and Li (2012) derive, by matched asymptotic expansions with a near-field and far-field solution, a low-frequency slender-body theory for the vertical added mass, damping and wave excitation loads on an elastic semi-submerged torus. It is found that 3D frequency-dependent hydrodynamic interaction on the scale of the torus diameter is significant, and that hydroelasticity plays a major role.

Marichal (2003) develops an original numerical method to study the equilibrium characteristics of a cod-end towed at constant speed. It consists of applying basic mechanical equations to a line of netting twines, leading to a system of equations where the unknown tensions can be found. Implicit and explicit Euler schemes are then used to find the new positions in time.

Kristiansen (2012) has modified the truss-model by Marichal (2003) to represent a net-cage of the type used in fish farms, supported by floating collars. In the study, an expression for the acceleration of a node on the floater is derived, based on Faltinsen (2011), so that this can be included in the truss-model. Low-frequency theory is also implemented.

Faltinsen and Kristiansen (2015) investigate the mooring loads on an aquaculture net cage in current and waves by use of dedicated model tests and numerical simulations. Here, the numerical model presented by Kristiansen (2012) is used.

Patterson et al. (2019) present an elastic floating solar island concept for production of methanol fuel offshore. The solar island structure consists of several co-centric elastic tori supporting a membrane type deck carrying photo-voltaic-cells.

Winsvold (2018) performs an experimental study into the governing behaviour and response of the solar island concept proposed by Patterson et al. (2019). The experimental model consists of five co-centric, elastic tori enclosing each other, connected by elastic bands. The elastic bands enable the structure to move with the waves. Over-topping waves are identified as the main concern for the structure and solar panels, threatening the integrity of both. Irregularities are seen in the resulting RAOs when compared with theory.

Vassdokken Sigstad (2019) performs model tests with a modified version of the model used by Winsvold (2018), where the elastic bands have been replaced by new, stiffer ones, and the mooring-lines have been replaced by stiffer ones as well. Irregularities are also here seen in the resulting experimental RAOs, compared to theory. The coupled truss and floater model by Kristiansen (2012) is implemented in Python for a single, moored torus with vertical motion, but has an unresolved bug.

1.3 Objective and Scope

This Master's thesis investigates a solar island structure, consisting of multiple co-centric tori connected by elastic bands, both theoretically and numerically, and by studying experimental results. The structure will be referred to as a both a *multi-torus* and *solar island* throughout the thesis. A single torus of the structure will also be called a *single floater*, being a floater element.

A theoretical model for the multi-torus will be derived, based mainly on the single floater model by Faltinsen (2011) and the truss model by Marichal (2003). The result will be referred to as a *solar island model*, a truss model accounting for floater motion. This should be a good contribution to existing theory, which is mainly focused on single floaters. The model will be implemented in MATLAB, with the aim of comparing the resulting RAOs with the experimental ones by Vassdokken Sigstad (2019) and Winsvold (2018), in an attempt to study whether experimental irregularities are due to structural interactions via the elastic bands between the tori.

Hydrodynamic interaction theory for the multi-torus structure, recently developed by Professor Trygve Kristiansen, will also be implemented in MATLAB, with the aim of studying whether hydrodynamic interactions may contribute to the irregularities in experimental RAOs.

The work is a continuation of a preliminary study performed during the fall of 2019. The main objectives of this Master's thesis can be summarized as:

1. Develop a theoretical model for the multi-torus solar island structure, accounting for structural interactions between tori via truss-members and including both vertical and lateral modes, based on existing single floater and truss model theory.

2. Implement the numerical solar island model in MATLAB and perform verification studies for a single, moored floater case.

3. Obtain numerical RAOs for multi-torus cases and compare with single-floater theory as well as experimentally obtained RAOs.

4. Present multi-torus hydrodynamic interaction theory, implement it in MATLAB, verify with results from WAMIT, and compare resulting RAOs with single-floater theory as well as experimentally obtained RAOs.

5. Discuss potential hydrodynamic and structural interaction effects on the multi-torus.

1.4 Outline of Master's Thesis

Chapter 2 presents relevant theory, such a truss model, regular wave theory, floater modes, zero-frequency theory and single floater models for vertical and lateral motion. This is all leading up to the presentation of the developed theoretical solar island model.

Chapter 3 presents hydrodynamic interaction theory, including derivation of cross-coupled added mass terms, effects on the wave excitation force and RAOs including hydrodynamic interaction between tori.

Chapter 4 presents verification studies, both for the numerical solar island model and the hydrodynamic interaction theory, which are implemented in MATLAB.

Chapter 5 presents the set-up for previously performed model tests on multi-torus structures.

Chapter 6 presents and discusses experimental results, results obtained by the numerical solar island model as well as from hydrodynamic interaction theory.

Chapter 7 draws conclusions from the entire study and gives suggestions for further work and research topics.

Chapter 2

Solar Island Model Theory

The intention of this chapter is to present the theoretical solar island model that has been derived in this master thesis. The reader will be given some theoretical background related to the floater and truss models that have been modified and combined in order to develop the solar island model. Both mechanical vibrations, marine dynamics and hydrodynamics are highly relevant fields, and it is assumed that the reader has basic knowledge within all of them. The theoretic solar island model will be presented in full, and is in itself an important result from the work done in this thesis. The entire theoretic work has been done while closely working together with Master student Øyvind Onestad Olsen.

2.1 Truss Member

A truss is a long, slender structural member that only transmits axial force along the axis of its center-line. It can only have tension, not compression, and does not transmit moments. In several previous studies, truss members have been used to model the twines of aquaculture fish-nets, and in the present study they will be used to model the elastic bands between the tori of a multi-torus solar island. See Figure 2.1 for illustrations. Several trusses are needed in order to model one elastic in order for it to obtain a slack configuration. A lumped-mass technique will be used, as will be presented in Section 2.2.
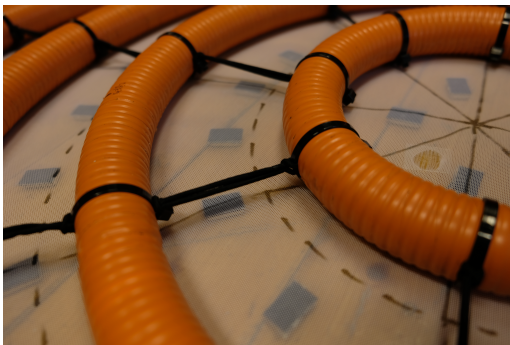
(a) Elastic bands in solar island   (b) Fish-net twines

Figure 2.1: Solar island elastics and fish-net twines
a) Elastic bands connect the floaters of the experimental solar island model. This version of the model has a membrane deck, and has been turned upside down in the photography. b) Fish-net twines.

The trusses follow Hooke's law, which describes the experimentally observed linear relation between stress and strain Dietmar. Gross et al. (2017). It's validity is restricted by the proportionality limit, which in elastic-plastic materials frequently coincides with the yield limit. Now, for an uniaxial stress state as that of a truss, Hooke's law is given by

$$T = k\Delta l \tag{2.1}$$

where $\Delta l = l - l_0$ is the difference between the original, non-tensioned length l_0 and the tensioned length l, $k = EA/l_0$ the stiffness coefficient, E Youngs modulus and A the cross-sectional area of the truss. Figure 2.2 illustrates the different parameters.
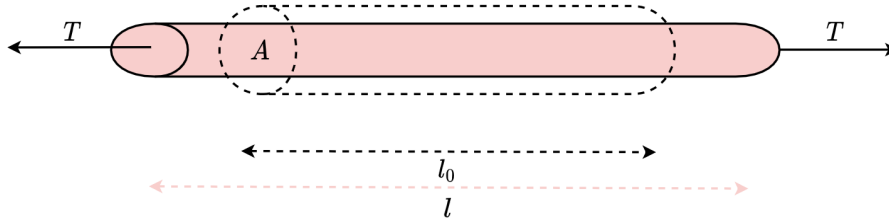
Figure 2.2: Truss with tension
T is the tension in the truss after it is stretched from its original, zero-tension length l_0 to length l. A is the original cross-sectional area of the truss.

2.2   Truss Model

In order to numerically model the mooring lines and elastic trusses between the floaters in the multi-torus solar island, a truss model developed by Marichal (2003) is used. It was derived for a numerical study of a cod end, but has since been used by Kristiansen (2012) to model the net panels in aquaculture fish farms as trusses. In this section, the derivation of the model will be presented. Hydrodynamic forces as applied to the net panels are not included, because the trusses of the solar island lie in the ocean surface and the experimental mooring setup as well. The specific derivations presented are a result of discussions with Professor Trygve Kristiansen, and are not found elsewhere in this form.

2.2.1   Truss System and Notations

A simple chain of trusses will be used to represent both elastics and mooring-lines in the solar island model. Therefore, the theory will be presented for such a simple truss system. The chain consists of of N trusses, all with nodes in both ends, meaning a total of $n = N + 1$ nodes. The mass is evenly distributed along each truss, and the total mass is lumped into its nodes. This means that an end node will include the mass halfway to its neighbouring node, while the ones in between will include the mass halfway to both its neighbouring nodes.

Figure 2.3 illustrates the truss system, with notations that will be used further in this section. As seen, both nodes and trusses are enumerated from left to right in this case. The important thing is that the enumeration is consistent, it may as well be from right to left. Further, a single truss k has end-nodes i and j. The unit vector $\boldsymbol{s}_{ij}$ from node i to node j is given by

$$\boldsymbol{s}_{ij} = \frac{\boldsymbol{x}_j - \boldsymbol{x}_i}{l_k} \tag{2.2}$$

Here $\boldsymbol{x}_i$ and $\boldsymbol{x}_j$ are the (x, y, z) coordinates for node i and j, respectively, while l_k is the length of the truss. The 3D tension in node i due to truss k is given by $\boldsymbol{s}_{ij}T_k$, where T_k is the tension in the truss. For node j it will be $\boldsymbol{s}_{ji}T_k$, so that it is equal in value but opposite direction of that in node i.

(a) Truss system
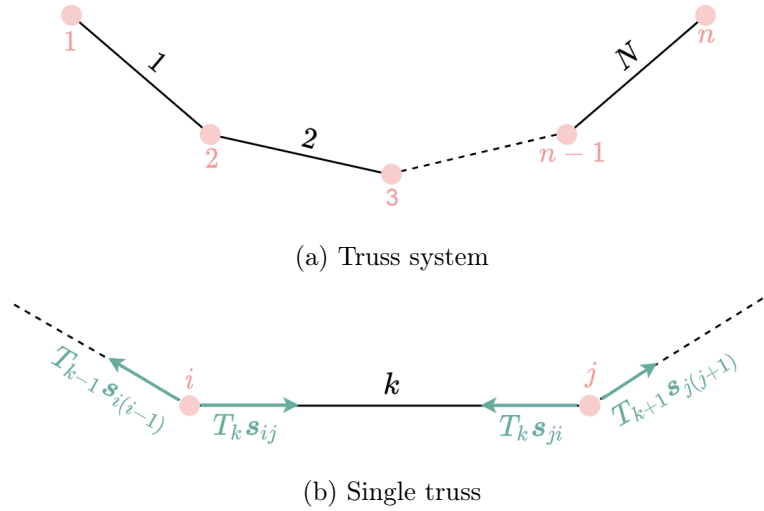
(b) Single truss

Figure 2.3: Truss notations

Truss notations. a) The truss system consists of N trusses divided by n nodes. b) A single truss number k, with nodes i and j at its left and right end, respectively. The tensions acting on both nodes are illustrated. T_k is the tension in truss k, while $\boldsymbol{s}_{ij}$ is the unit vector from node i to j. A consistent enumeration of both trusses and nodes is needed.

2.2.2 Mechanical Equations

In this subsection, the mechanical equations used will be presented. The fundamental principle of dynamics can be applied on a given node i as shown in Equation (2.3)

$$m_i\ddot{\boldsymbol{x}}_i = \sum \boldsymbol{F}_i = m_i\boldsymbol{g} + \sum_l T_{il}\hat{\boldsymbol{S}}_{il} \qquad (2.3)$$

Here m_i is the mass of the node, $\ddot{\boldsymbol{x}}_i$ its acceleration, $\boldsymbol{F}_i$ a force contribution acting on the node, $\boldsymbol{g}$ the gravitational acceleration, $\boldsymbol{s}_{il}$ the unit vector from node i to its neighboring node l and T_{il} the tension in the corresponding truss. In this standard case the gravitational force and tensions from neighbouring trusses are the only external loads acting on a the node. However, if other forces were present they should also be included. In the case where loads are distributed on the trusses, these are lumped into the nodes which form the ends of the truss such that the sum of the loads are equally distributed between them.

By Hooke's law, earlier presented in Equation (2.1), the tension of an elastic truss at time instance n can be estimated as

$$T^n = T^{n-1} + k(\Delta l)^n \qquad (2.4)$$

which by the approximation that $(\Delta l)^n = l^{n+1} - l^n$ can be written

$$l^{n+1} = l^n + \frac{T^n - T^{n-1}}{k} \qquad (2.5)$$

this can be simplified as $(\Delta T)^n = k(\Delta l)^n$, re-arranged and squared, giving

$$\frac{(l^{n+1})^2}{(l^n)^2} = 1 + 2\frac{(\Delta l)^n}{l^n} + \left(\frac{(\Delta l)^n}{l^n}\right)^2 \qquad (2.6)$$

Assuming the change in length is small between time steps, the last term is neglected, resulting in

$$(l^{n+1})^2 = (l^n)^2 + 2l^n(\Delta l)^n \tag{2.7}$$

Equation (2.7) represents the elastic length constraint. Now, Equation (2.3) and Equation (2.7) form a system of N non-linear equations. This can be solved by using an Euler time-step method originating from finite different schemes, which will be presented next.

2.2.3 Euler Schemes

With the velocity of the node being $\boldsymbol{v}_i = \dot{\boldsymbol{x}}_i$, Equation (2.3) can be written as:

$$m_i\dot{\boldsymbol{v}}_i = \sum \boldsymbol{F}_i \tag{2.8}$$

Further, the acceleration and velocity can be expressed by Equation (2.9) and Equation (2.10), respectively. Here, the notation n represents a given time instant and $n+1$ the next, which have a period of time Δt between them.

$$\dot{\boldsymbol{v}}_i \simeq \frac{\boldsymbol{v}_i^{n+1} - \boldsymbol{v}_i^n}{\Delta t} \tag{2.9}$$

$$\dot{\boldsymbol{x}}_i \simeq \frac{\boldsymbol{x}_i^{n+1} - \boldsymbol{x}_i^n}{\Delta t} \tag{2.10}$$

Now, inserting Equation (2.9) into Equation (2.8), one obtains

$$m_i(\boldsymbol{v}_i^{n+1} - \boldsymbol{v}_i^n) \simeq \Delta t\boldsymbol{F}_i^n \tag{2.11}$$

where $\boldsymbol{F}_i^n$ represents all the forces acting on node i at time instant n. Note that here velocities at time instants n and $n+1$ are used to describe the acceleration at time instant n, as an approximation. Rewriting Equation (2.10) so that terms of equal time instant are collected on each side gives Equation (2.12), which is an explicit Euler scheme.

$$\boldsymbol{v}_i^{n+1} \simeq \boldsymbol{v}_i^n + \Delta t\frac{\boldsymbol{F}_i^n}{m_i} \tag{2.12}$$

Now, with the approximation that the velocity at time instant $n+1$ is given by positions at time instances n and $n+1$, Equation (2.10) can be re-written into Equation (2.13), which is an implicit Euler scheme.

$$\boldsymbol{x}_i^{n+1} \simeq \boldsymbol{x}_i^n + \Delta t\boldsymbol{v}_i^{n+1} \tag{2.13}$$

Equations 2.12 and 2.13 now form a set of equations that can be solved as long as initial conditions are known. The latter can be further written out as:

$$\boldsymbol{x}_i^{n+1} \simeq \boldsymbol{x}_i^n + \Delta t(\boldsymbol{v}_i^n + \Delta t\frac{\boldsymbol{F}_i^n}{m_i}) \tag{2.14}$$

2.2.4   Deriving System of Equations

In this subsection, the derivation of a system of equations for finding the unknown tensions will be presented. These are needed in Equation (2.12), and must be found for each time-step in order to update the positions of the nodes.

We now study a truss k with end nodes i and j, as illustrated in Figure 2.3b. Expressing the length at time $n + 1$ by its node coordinates, the length constraint in Equation (2.7) can be written as

$$||\boldsymbol{x}_j^{n+1} - \boldsymbol{x}_i^{n+1}||^2 = (l^n)^2 + 2l^n(\Delta l)^n \tag{2.15}$$

Now, the $n + 1$ terms can be replaced by use of Equation (2.14). $\boldsymbol{a}_i^n = \frac{\boldsymbol{F}_i^n}{m_i}$ is set for simplicity, and the same for j-nodes. The resulting equation is then

$$||\boldsymbol{x}_j^n - \boldsymbol{x}_i^n + \Delta t(\boldsymbol{v}_j^n - \boldsymbol{v}_i^n) + \Delta t^2(\boldsymbol{a}_j^n - \boldsymbol{a}_i^n)||^2 = (l^n)^2 + 2l^n(\Delta l)^n \tag{2.16}$$

Next, the notations $\boldsymbol{\alpha} = \boldsymbol{x}_j^n - \boldsymbol{x}_i^n$, $\boldsymbol{\beta} = \Delta t(\boldsymbol{v}_j^n - \boldsymbol{v}_i^n)$ and $\boldsymbol{\gamma} = \Delta t^2(\boldsymbol{a}_j^n - \boldsymbol{a}_i^n)$ are set so that Equation (2.16) can be simplified as:

$$||\boldsymbol{\alpha} + \boldsymbol{\beta} + \boldsymbol{\gamma}||^2 = (l^n)^2 + 2l^n(\Delta l)^n \tag{2.17}$$

Setting $\boldsymbol{\tau} = \boldsymbol{\beta} + \boldsymbol{\gamma}$, this can further be written as:

$$||\boldsymbol{\alpha}||^2 + ||\boldsymbol{\tau}||^2 + 2\boldsymbol{\alpha} \cdot \boldsymbol{\tau} = (l^n)^2 + 2l^n(\Delta l)^n \tag{2.18}$$

As $||\boldsymbol{\alpha}||^2 = (l^n)^2$, this is again leads to:

$$||\boldsymbol{\beta}||^2 + ||\boldsymbol{\gamma}||^2 + 2\boldsymbol{\beta} \cdot \boldsymbol{\gamma} = 2l^n(\Delta l)^n - 2\boldsymbol{\alpha} \cdot \boldsymbol{\tau} \tag{2.19}$$

Writing this further out one obtains:

$$\begin{aligned}
\Delta t^2||\boldsymbol{v}_j^n - \boldsymbol{v}_i^n||^2 + \Delta t^4||\boldsymbol{a}_j^n - \boldsymbol{a}_i^n||^2 + 2\Delta t^3(\boldsymbol{v}_j^n - \boldsymbol{v}_i^n)(\boldsymbol{a}_j^n - \boldsymbol{a}_i^n) \\
+2(\boldsymbol{x}_j^n - \boldsymbol{x}_i^n)(\Delta t(\boldsymbol{v}_j^n - \boldsymbol{v}_i^n) + \Delta t^2(\boldsymbol{a}_j^n - \boldsymbol{a}_i^n)) - 2l^n(\Delta l)^n = 0
\end{aligned} \tag{2.20}$$

Now, Equation (2.20) can be simplified by neglecting the terms of $\mathcal{O}(\Delta t^4)$ and $\mathcal{O}(\Delta t^3)$, and setting $b^n = ||\boldsymbol{v}_j^n - \boldsymbol{v}_i^n||^2$ and $\boldsymbol{c}^n = \boldsymbol{v}_j^n - \boldsymbol{v}_i^n$. Further, by setting the truss unit vector $\boldsymbol{s}_k = \boldsymbol{s}_{ij}$, the equation finally becomes:

$$b^n + 2l^n\boldsymbol{s}_k \cdot (\frac{1}{\Delta t}\boldsymbol{c}^n + (\boldsymbol{a}_j^n - \boldsymbol{a}_i^n)) - \frac{1}{\Delta t^2}2l^n(\Delta l)^n \simeq 0 \tag{2.21}$$

From Equation (2.4) we have that $(\Delta l)^n = (T^n - T^{n-1})/k$. The unknown tensions at time instance n thus lie in this term as well as the acceleration terms. Re-arranging so that the unknown tensions are on the left side, the equation becomes

$$\boldsymbol{s}_k \cdot (\boldsymbol{a}_j^n - \boldsymbol{a}_i^n) - \frac{T^n}{k\Delta t^2} = -\frac{b^n}{2l^n} - \frac{1}{\Delta t}\boldsymbol{c}^n \cdot \boldsymbol{s}_k - \frac{T^{n-1}}{k\Delta t^2} \tag{2.22}$$

For the standard case of gravity and tension from neighbouring trusses being the only external loads on node i, one has that

$$a_i^n = \frac{\boldsymbol{F}_i^n}{m_i} = \frac{1}{m_i} \sum_l T_{il} \boldsymbol{s}_{il} + \boldsymbol{g} \tag{2.23}$$

and correspondingly for node j.

Equation (2.22) applies to one specific truss k, so a total of N such equations represent the chain of trusses. This forms a system of N equations that can be expressed in matrix form as illustrated in Equation (2.24). This system can be solved for the unknown tensions at each time instance, and be given as input to the Euler scheme in Equation (2.12). Given a set of initial and boundary conditions, the motion of the trusses can thus be estimated in time.

$$\begin{bmatrix} A_{11} & . & . & . & A_{1N} \\ . & . & & & \\ . & & . & & \\ . & & & . & \\ A_{N1} & & & & A_{NN} \end{bmatrix} \begin{bmatrix} T_1 \\ . \\ . \\ . \\ T_N \end{bmatrix} = \begin{bmatrix} B_1 \\ . \\ . \\ . \\ B_N \end{bmatrix} \tag{2.24}$$

2.3   Linear Wave Theory

Linear wave theory for propagating waves assumes a horizontal sea bottom and free-surface of infinite horizontal extent Faltinsen (1993). It satisfies potential theory, which assumes that the sea water is incompressible and inviscid, and the fluid motion irrotational. In linear theory the velocity potential is proportional to the wave amplitude, which is valid when the characteristic wavelength and body dimension are large relative to the wave amplitude. Its derivation uses the free-surface and sea bottom conditions together with the Laplace equation. Derivations will not be shown here, but Faltinsen (1993) gives a thorough presentation.

Some important results from linear wave theory at infinite water depth will next be presented. Regular waves with wave amplitude ζ_a and circular frequency ω propagating along the x-axis are considered. First one has the velocity potential ϕ given by

$$\phi = \frac{g\zeta_a}{\omega} \exp(kz + ikx - i\omega t) \tag{2.25}$$

where g is the acceleration of gravity, k the wave number, $i^2 = -1$, z the vertical coordinate, positive upwards with $z = 0$ being the mean water level and t a time variable. The wave period $T = 2\pi/\omega$, the wave length $\lambda = 2\pi/k$ and wave height $H = 2\zeta_a$. As seen, complex quantities are used and it is understood that the physical meaning lies in the real part of the expression.

Next, the connection between wave number and circular frequency, known as the dispersion relation, is given by

$$\omega^2 = kg \tag{2.26}$$

Figure 2.4 illustrates a linear wave and some of the parameters mentioned.
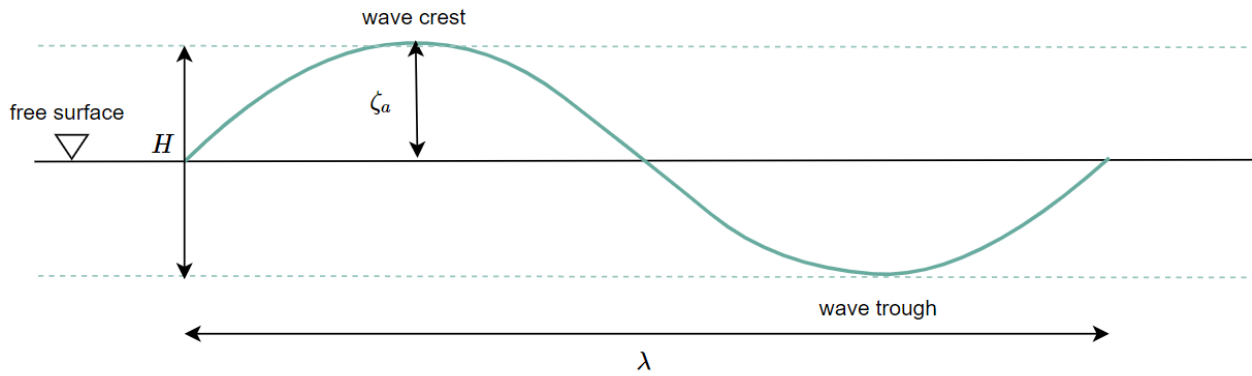
Figure 2.4: Linear wave illustration

Linear wave with wave amplitude ζ_a, wave height H and wave length λ. The free surface, wave crest and wave through are marked.

2.4 Floater Modes

The solar island consists of several co-centric floaters. When describing a single floaters motion in waves, modal superposition is very convenient. The fact that the natural modes are orthogonal makes mathematical simplifications possible, as will be seen in later sections.

Before we present the natural modes of the floater, an introduction to the floater coordinate system is necessary. It is illustrated in Figure 2.5, which shows a top view of a floater with center-line curve radius R. The angular coordinate β is connected to the Cartesian coordinate system by $x, y = R\cos(\beta), R\sin(\beta)$.
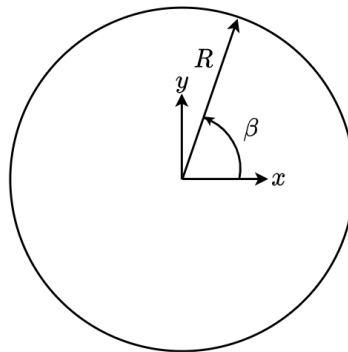
Figure 2.5: Floater Coordinate System

Top view of a floater with radius R. The z-axis is out of the paper-plane. The angular coordinate β is connected to the Cartesian coordinate system by $x, y = R\cos(\beta), R\sin(\beta)$.

2.4.1 Vertical Floater Modes

The vertical motion $w(\beta, t)$ of the floater is given as the Fourier series in Equation (2.27), where $a_n(t)$ and $\cos(n\beta)$ are modal amplitude and shape for mode n, respectively Li (2017). This representation works for waves propagating in the positive x-direction, which gives symmetric response about the x-axis.

$$w(\beta, t) = \sum_{n=0}^{\infty} a_n(t) \cos(n\beta) \tag{2.27}$$

Figure 2.6 shows the four first vertical floater modes. Mode $n = 0$ corresponds to heave, $n = 1$ to pitch, $n = 2$ to the first flexible mode, $n = 3$ to the second flexible, and so on.
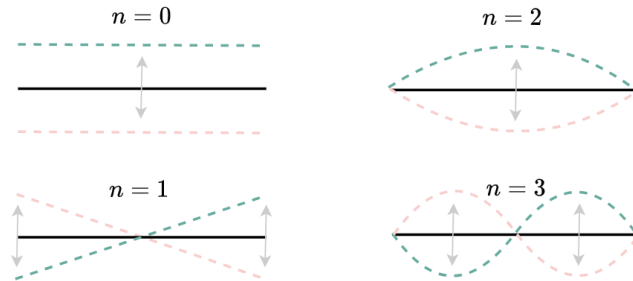
Figure 2.6: Vertical floater modes
Mode $n = 0$ corresponds to heave, $n = 1$ to pitch, $n = 2$ to the first flexible mode and $n = 3$ to the second flexible.

2.4.2 Lateral Floater Modes

The radial displacement $v(\beta, t)$ of the floater is expressed by Equation (2.28), where $b_n(t)$ and $\cos(n\beta)$ are modal amplitude and shape for mode n, respectively Faltinsen (2010). Mode 0 has here been excluded because one requires that there can be no uniform contraction or expansion of the floater. Mode 1 represents rigid-body surge, and is treated separately, while the rest of the modes are purely elastic. Figure 2.7 illustrates the first two natural lateral modes.

$$v(\beta, t) = \sum_{n=2}^{\infty} b_n(t) \cos(n\beta) \tag{2.28}$$
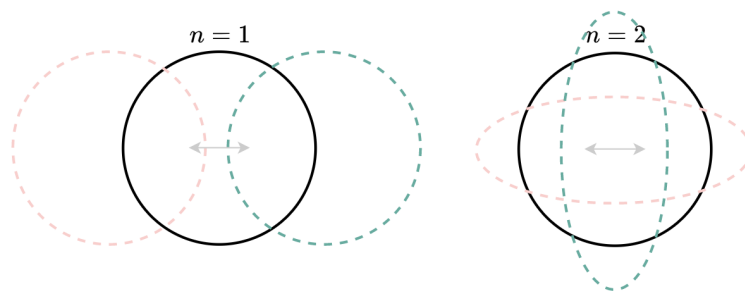
Figure 2.7: Lateral floater modes
Top view of the floater. Mode 1 corresponds to surge, while mode 2 is the first flexible mode.

2.5 Zero-Frequency Theory for a Semi-submerged Torus

Zero-frequency theory (ZFT) was developed by Faltinsen (2011) for an elastic semi-submerged torus, with the aim of describing the wave effects on it, thus being able to estimate its motion in waves. The general assumptions and principles of the theory will be briefly introduced in this section.

2.5.1 General Assumptions

The theory is based on the following assumptions:

- The torus is semi-submerged.

- The surrounding water has infinite depth and horizontal extent.

- Potential flow theory of incompressible water is valid.

- The wavelength λ is long compared to the torus cross-section $2c$, i.e. $\lambda \gg 2c$. This indicates that long-wave theory is valid and that wave radiation and scattering from the floater is negligible.

- The torus cross-section is small relative to the circular center-line curve radius R of the torus, i.e $c \ll R$. Thus, slender-body theory is appropriate.

- Hydrodynamic loads on the torus are linear.

- Current loads are negligible.

The limiting case that the forcing frequency $\omega \to 0$ is studied. In this limit, pressure disturbances are progressed infinitely fast and in phase everywhere in the water. The free surface is not disturbed, which means that a rigid free-surface condition can be used. Because linear free-surface theory is partly assumed, a sea state can be described as a superposition of regular waves.

2.5.2 Asymptotic Matching of Far-field and Near-field Solutions

Matched asymptotic expansion is used in the derivations, and it involves defining a far-field and near-field solution for the torus that are matched. The far-field and near-field descriptions are illustrated in Figure 2.8a and Figure 2.8b, respectively.

(a) Far-field view.   (b) Near-field view.
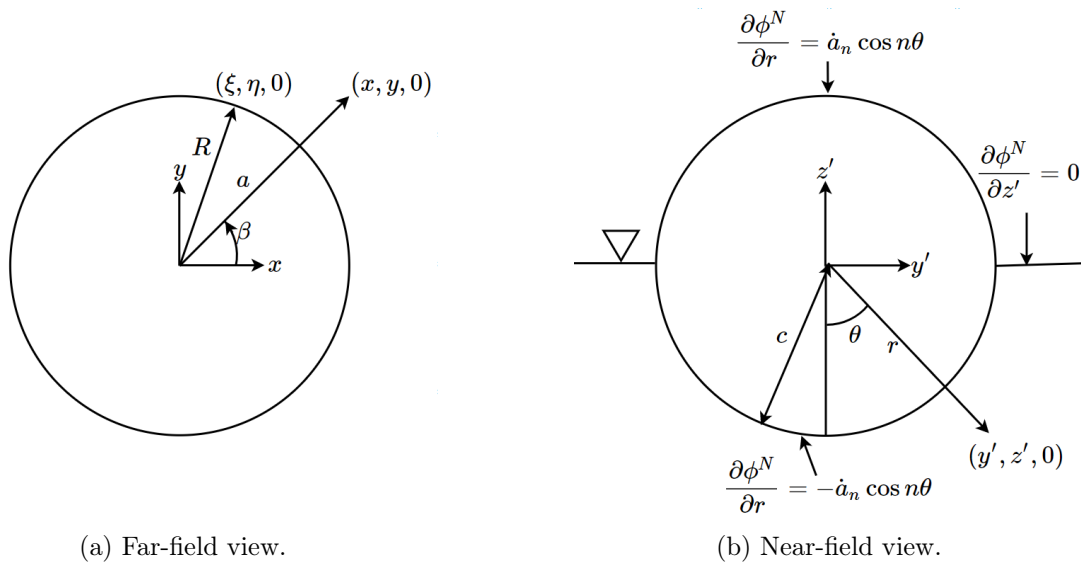
Figure 2.8: Near and far-field views of torus
To the left: far-field view of a torus. To the right: cross-section of the torus, with coordinate system and boundary conditions for the near-field solution of the velocity potential associated with forced vertical oscillations of Fourier component n. Slightly modified from Faltinsen (2011).

For the far-field view, both a Cartesian coordinate system (x, y, z) and a cylindrical coordinate system (a, β, z) are defined, with the mean free surface at $z = 0$ and z positive upwards from the sea surface. The waves propagate in the positive x-direction. Further, the center-line of the torus is given by coordinates $(\xi, \eta, 0)$. The far-field description does not include cross-sectional details of the torus, and the flow appears as a line distribution of sources with constant density along the center line. In

accordance with the floater modes presented in Section 2.4, the vertical vibration velocity of the floater can be expressed as $\sum_{n=0}^{\infty} \dot{a}_n(t) \cos(n\beta)$.

The cross-sectional details are seen in the near-field view. Both a local Cartesian coordinate system (O, y', z') and polar coordinate system (O, r', θ) are defined. Now, the submerged semi-circle is forced vertically with velocity $\dot{a}_n \cos(n\theta)$, corresponding to vertical mode n. At the same time, the image semi-circle about the free surface is moving with opposite sign to the submerged one. The consequence of this is that the rigid free-surface condition is satisfied. The complete near field solution of the velocity potential, ϕ^N is found by asymptotic matching with the far-field velocity potential, and is presented in Equation (2.29). A constant in the near-field solution is determined by the matching, and makes the solution unique.

$$\phi^N = \dot{a}_n \cos(n\theta) \left\{ \frac{2c}{\pi} \left[\ln(\frac{8R}{r}) - K_n \right] - \sum_{m=1}^{\infty} c^{2m+1} \frac{3\cos(m\pi) + \cos(3m\pi)}{\pi 2m(4m^2-1)} \frac{\cos(2m\theta)}{\pi 2m(4m^2-1)} \right\} \quad (2.29)$$

The constant K_n is given by

$$K_n = \frac{1}{2\sqrt{2}} \int_0^{2\pi} \frac{1-\cos(nx)}{\sqrt{1-\cos(x)}} dx \quad (2.30)$$

2.5.3   ZFT Vertical Added Mass

Having found the near-field velocity potential for a given mode n, the added mass is easily obtained through the vertical linear hydrodynamic force associated with each mode. The two-dimensional vertical added mass for mode n is given by

$$a_{33}^n = 2\rho c^2 \left\{ \frac{2}{\pi} \left[\ln\left(\frac{8R}{c}\right) - K_n \right] + \underbrace{\sum_{n=1}^{\infty} \frac{(3\cos(n\pi) + \cos(3n\pi))\cos(n\pi)}{2\pi n(4n^2-1)^2}}_{0.07238725793} \right\} \quad (2.31)$$

where ρ is the fluid density. The three-dimensional added mass is given by

$$A_{33}^n = 2\pi R a_{33}^n \quad (2.32)$$

2.6   Vertical Floater Model from Curved Beam Equation

In the extension of his ZFT study of the semi-submerged elastic floater, Faltinsen (2010) applies a curved beam equation as a basis to estimate its motions, both vertical and lateral. A modified version including a bending stiffness term accounting for the curvature effect of the floater is later presented by Li (2017). Further, Kristiansen (2012) demonstrates how both forces from the fish net and mooring lines can be included as external truss forces on a fish-cage floater. That is, both mooring-lines and the upper row of fish-net twines are modelled as truss members.

In this section, a single floater model for vertical motions, adapted to best represent a solar island floater, will be presented. We will use the modified curved beam equation by Li (2017) and the same principles of including truss forces as Kristiansen (2012). For our solar island structure, the trusses connected to the floater will be elastic bands and horizontal mooring-lines, so that several forces important for submerged members can be neglected. A lateral solar floater model is presented later in Section 2.7, following the same principles.

Figure Figure 2.9 illustrates a solar island floater with evenly spaced points of truss connections. Several trusses may be attached to the same connection point.
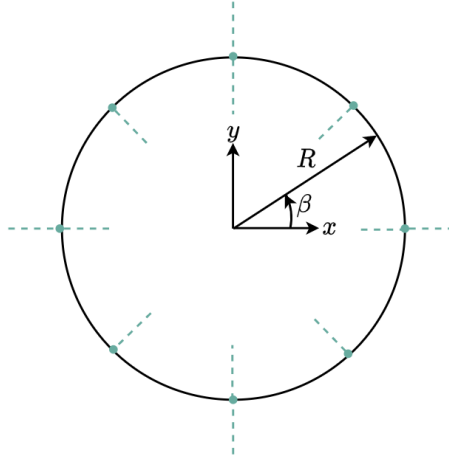
Figure 2.9: Solar island floater
Top view of a floater with radius R and evenly spaced truss-connection points (marked in green). Each truss connection point may have several trusses attached to it. The z-axis is out of the paper-plane. The angular coordinate β is connected to the Cartesian coordinate system by $x, y = R\cos(\beta), R\sin(\beta)$.

2.6.1 Vertical Curved Beam Equation

Li (2017) presents a generalized Euler-Bernoulli beam equation for prediction of the vertical motion w of a semi-submerged elastic torus, accounting for both curvature and axial stiffness. The latter is important when studying fish farm floaters due to drag on the submerged net-panels, but is neglected for the solar-island torus. The equation then becomes

$$m\frac{\partial^2 w}{\partial t^2} + \rho g b w + EI\frac{\partial^4 w}{\partial s^4} + \frac{EI}{R^2}\frac{\partial^2 w}{\partial s^2} = f_3(s,t) \tag{2.33}$$

where m is the floater mass per unit length, EI the bending stiffness, ρ the fluid density, g the gravitational acceleration, $b = 2c$ the cross-sectional water plane area per unit length, R the center-line curve radius and $\frac{\partial}{\partial s}$ means differentiation along the center line of the torus. The latter is related to the angular position β by $\frac{\partial}{\partial s} = R^{-1}\frac{\partial}{\partial \beta}$.

The equation is based on Newton's second law. The first term from the left accounts for the acceleration of the floater, the second for buoyancy and the third for bending stiffness. The fourth is an extra bending stiffness term due to the curvature effect of the torus, which is needed together with the previous in order to describe a rigid torus when $EI \to \infty$. The right hand term is the the sum of the vertical added mass, wave excitation and truss forces per unit length, $f_3 = f_3^{addedmass} + f_3^{exc} + f_3^{truss}$. Potential truss forces will be from elastic bands towards other tori and mooring lines.

2.6.2 Vertical Modal Equation of Motion

As presented earlier in Equation (2.27), the vertical torus motion $w(\beta, t)$ may be decomposed into natural modes: $w(\beta, t) = \sum_{n=0}^{\infty} a_n(t)\cos(n\beta)$. By inserting this into Equation (2.33), multiplying the new expression by $\cos m\beta$ and integrating from $\beta = 0$ to 2π, one can take advantage of orthogonality of cosines so that the expression simplifies. The result is the equation of motion for mode n amplitude $a_n(t)$,

$$(m + a_{33}^n)\ddot{a}_n + \left(\rho g b + \frac{EI}{R^4}(n^4 - n^2)\right)a_n = f_{3n}^{ex,gen} + \frac{1}{\alpha_n \pi}\int_0^{2\pi} f_3^{truss}\cos(n\beta)d\beta \tag{2.34}$$

where $\alpha_n = 2$ for $n = 0$ and 1 for $n \geq 1$, $f_{3n}^{ex,gen}$ is the generalized wave excitation force and a_{33}^n is the two-dimensional added mass for mode n. The latter is given in Equation (2.31).

2.6.3 Vertical Wave Excitation Load

The vertical wave excitation load per unit length is divided into a Froude-Kriloff part and a diffraction part, given by Equations 2.35 and 2.36, respectively Faltinsen (2010). This is based on the velocity potential from deep-water regular waves propagating along the x-axis, presented in Equation (2.25).

$$f_3^{FK} = i\rho g \zeta_a \left[J_o(kR) + \sum_{n=1}^{\infty} 2i^n J_n(kR) \cos(n\beta) \right] b \exp(-i\omega t) \tag{2.35}$$

$$f_3^D = -i\omega^2 \zeta_a \left[J_o(kR)a_{33}^0 + \sum_{n=1}^{\infty} 2i^n J_n(kR)a_{33}^n \cos(n\beta) \right] \exp(-i\omega t) \tag{2.36}$$

Here $J_n(kR)$ are Bessel functions of the first kind, k the wave number, ω the wave frequency and $i^2 = -1$. With this, it can be shown that the vertical wave excitation force becomes,

$$f_3^{exc} = \zeta_a \exp(-i\omega t) \sum_{n=0}^{\infty} (3 - \alpha_n) i^n J_n(kR) \cos(n\beta)(\rho g b - \omega^2 a_{33}^n) \tag{2.37}$$

and further the generalized vertical wave excitation force

$$f_{3n}^{exc,gen} = i^{n+1}(\rho g b - \omega^2 a_{33}^n)\zeta_a(3 - \alpha_n)J_n(kR)\exp(-i\omega t) \tag{2.38}$$

2.6.4 Generalized Vertical Truss Force

The last term in Equation (2.34), the generalized truss force, depends on the specific configuration of trusses that are attached to the floater, denoted *floater trusses* from now on. For a configuration where truss-connection points are evenly distributed along the solar island floater, we may approximate the integral as

$$\int_0^{2\pi} f_3^{truss} \cos(n\beta) d\beta \approx \sum_{ft=1}^{N_{ft}} f_{3,ft}^{truss} \cos(n\beta_{ft}) \Delta\beta$$

$$= \frac{1}{\Delta s} \sum_{ft=1}^{N_{ft}} \gamma_{ft} T_{ft} (\boldsymbol{s}_{ft} \cdot \boldsymbol{k}) \cos(n\beta_{ft}) \Delta\beta \tag{2.39}$$

$$= \frac{1}{R} \sum_{ft=1}^{N_{ft}} \gamma_{ft} T_{ft} (\boldsymbol{s}_{ft} \cdot \boldsymbol{k}) \cos(n\beta_{ft})$$

where ft denotes a certain floater truss, N_{ft} the total number of floater trusses, $\Delta\beta$ the angular distance between the truss connection points, and $f_{3,ft}^{truss}$ the vertical truss force per unit length of the floater from truss ft along the stretch Δs which it covers. Following the notations used in Section 2.2, T_{ft} and $\boldsymbol{s}_{ft}$ are the tension and unit vector of truss ft, respectively. As the unit vector is defined from node i to node j of a truss, the constant γ_{ft} must be included to assure correct direction for the tension. It takes the value $\gamma_{ft} = 1$ if the truss has node i on the floater, and $\gamma_{ft} = -1$ if it has node j on the floater. The tension is multiplied by $\boldsymbol{k} = [0, 0, 1]$ to get the vertical component of it. See Figure 2.10 for an illustration of the approximation.

$$T_{ft}\,\boldsymbol{s}_{ft}\gamma_{ft}$$

$$\Delta s$$
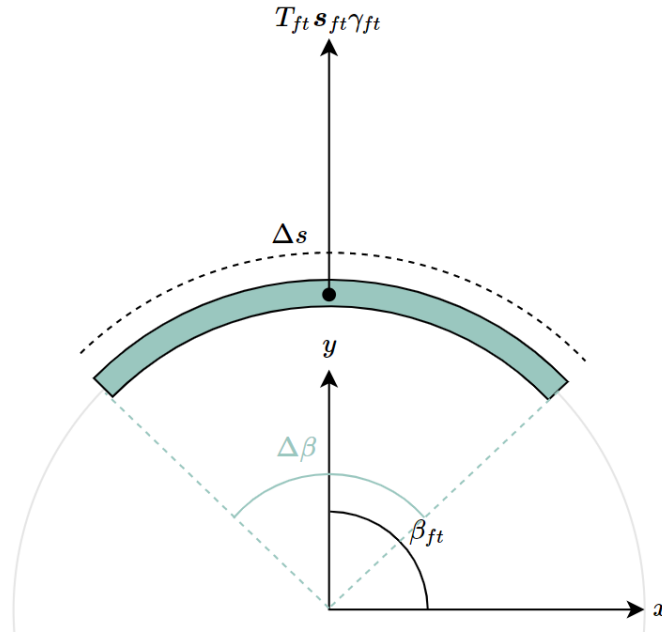
$$y$$

$$\Delta\beta$$

$$\beta_{ft}$$

$$x$$

Figure 2.10: Truss force per unit length

A top view illustration of a floater truss ft in a configuration where truss connection points are evenly spaced with angular distance $\Delta\beta$. T_{ft} and $\boldsymbol{s}_{ft}$ are the tension and unit vector of the truss, respectively. $\gamma_{ft} = 1$ if the truss has node i on the floater, and $\gamma_{ft} = -1$ if it has node j on the floater. This is to assure correct direction of the tension. Δs is the stretch along the floater covered by the specific truss.

Do note that this type of approximation works especially well for the case of a aquaculture floater due to the dense configuration of top trusses, that is, N_{ft} being large and thus $\Delta\beta$ being small.

2.7 Lateral Floater Model

In this section, a model for lateral floater motions will be presented. The same general steps used in the derivation of the vertical floater model in Section 2.6 are applied, but an important difference is that strip theory can be used to estimate the added mass terms. Also, the wave excitation force will differ. The elastic radial motions are derived based on a radial version of the curved beam equation, while surge is handled separately by a rigid body model. The solar island floater with evenly spaced truss connection points is illustrated in Figure 2.9.

2.7.1 Radial Curved Beam Equation

The beam equation for radial floater motion v is given by

$$\frac{m\partial^2 v}{\partial t^2} + EI\left(\frac{\partial^4 v}{\partial s^4} + \frac{1}{R}\frac{\partial^2 v}{s^2}\right) = f_r^{addedmass} + f_r^{exc} + f_r^{truss} \tag{2.40}$$

where m is the floater mass per unit length, EI the bending stiffness, R the center-line curve radius and $\frac{\partial}{\partial s}$ means differentiation along the center line of the torus. The latter is related to the angular position β by $\frac{\partial}{\partial s} = R^{-1}\frac{\partial}{\partial\beta}$. Further, $f_r^{addedmass}, f_r^{exc}$ and f_r^{truss} are the radial added mass, wave excitation and truss forces per unit length on the floater. Potential truss forces will be from elastic bands towards other tori and mooring lines.

The curved beam model requires that the forces act laterally in the cross-sectional plane, and the structural inertia force due to rigid body surge can therefore not be properly accounted for. This is why surge motion will be modelled separately by a rigid body model, while the elastic radial modes of the floater will be modelled based on the radial curved beam equation.

2.7.2 Radial Modal Equation of Motion

As presented earlier in Equation (2.28), the radial displacement of the floater may be expressed by its natural modes, $v(\beta, t) = \sum_{n=2}^{\infty} b_n(t) \cos(n\beta)$. This is inserted into Equation (2.40). By multiplying the new expression with $\cos(m\beta)$ and integrating from 0 to 2π, orthogonality of the modes will simplify the expression. The result is the equation of motion for mode $n > 2$ amplitude $b_n(t)$,

$$(m + a_{rr})\ddot{b}_n + \frac{EI}{R^4}(n^4 - n^2)b_n = \frac{1}{\pi} f_{rn}^{exc,gen} + \frac{1}{\pi} \int_0^{2\pi} f_r^{truss} \cos(n\beta)d\beta \qquad (2.41)$$

where $f_{rn}^{exc,gen}$ is the generalized radial wave excitation force per unit length of the floater. a_{rr} is the added mass for radial motion, given by

$$a_{rr} = \rho \frac{\pi}{2} c^2 \qquad (2.42)$$

where c is the cross-sectional radius of the torus.

2.7.3 Radial Wave Excitation Load

The incident wave potential for deep-water regular waves propagating along the x-axis, presented earlier in Equation (2.25), is considered. From this, the radial wave excitation force per unit length of the floater can be expressed as

$$f_r^{exc} = 2a_{rr}\omega^2 \zeta_a \exp(-i\omega t) \left[J_0(kR) + \sum_{n=1}^{\infty} 2i^n J_n(kR) \cos(n\beta) \right] \cos(\beta) \qquad (2.43)$$

where $J_n(kR)$ are Bessel functions of the first kind, k is the wave number, ω the wave frequency, ζ_a the wave amplitude and $i^2 = -1$ Faltinsen (2010). The generalized wave excitation force can from this be expressed as

$$f_{rn}^{exc,gen} = 2a_{rr}\pi\omega^2 \zeta_a \exp(-i\omega t)i^{n-1} \left[J_{n-1}(kR) - J_{n+1}(kR) \right] \qquad (2.44)$$

2.7.4 Generalized Radial Truss Force

The last term in Equation (2.41), the generalized radial truss force, is found by the same method as for the vertical case presented in Section 2.6.4. The important difference is that we now want the radial truss force contributions instead of the vertical ones. This is taken care of by use of the radial vector $\boldsymbol{r} = [\cos(\beta), \sin(\beta), 0]$.

$$\int_0^{2\pi} f_r^{truss} \cos(n\beta)d\beta \approx \sum_{ft=1}^{N_{ft}} f_{r,ft}^{truss} \cos(n\beta_{ft})\Delta\beta$$

$$= \frac{1}{\Delta s} \sum_{ft=1}^{N_{ft}} \gamma_{ft} T_{ft}(\boldsymbol{s}_{ft} \cdot \boldsymbol{r}) \cos(n\beta_{ft})\Delta\beta \qquad (2.45)$$

$$= \frac{1}{R} \sum_{ft=1}^{N_{ft}} \gamma_{ft} T_{ft}(\boldsymbol{s}_{ft} \cdot \boldsymbol{r}) \cos(n\beta_{ft})$$

See Section 2.6.4 for explanations of the different parameters, and Figure 2.10 for an illustration of the approximation. Figure 2.11 shows how multiplying a floater truss unit vector $\boldsymbol{s}_{ft}$ with $\boldsymbol{r}$ will give the its radial component.
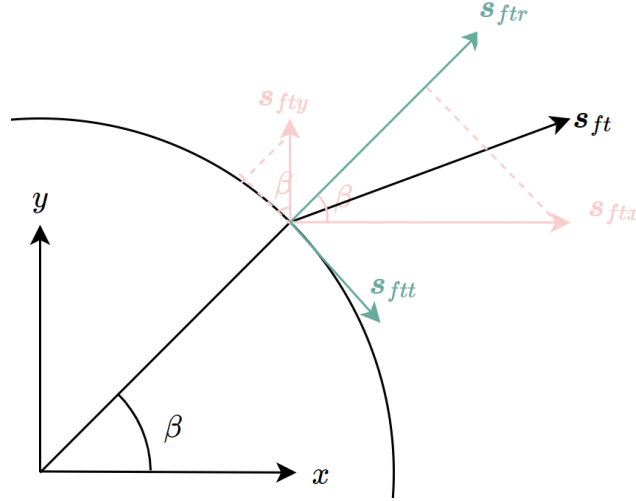
Figure 2.11: Radial component of truss unit vector

Top view of a floater truss with a node located with angle β on the floater. $\boldsymbol{s}_{ft}$ is its unit vector, while $\boldsymbol{s}_{ftx}$ and $\boldsymbol{s}_{fty}$ are its components in x and y-direction, respectively. $\boldsymbol{s}_{ftt}$ and $\boldsymbol{s}_{ftr}$ are its components in tangential and radial direction, respectively. It is seen that $\boldsymbol{s}_{ftr} = \boldsymbol{s}_{ftx}\cos(\beta) + \boldsymbol{s}_{fty}\sin(\beta)$.

2.7.5   Surge Motion from Rigid Body Model

The surge motion of the floater η_1 is expressed by a rigid body model. We look to the presentation by Kristiansen (2012), and modify the truss forces to fit our solar island floater. The equation of motion is found from Newton's second law and is given by

$$M\ddot{\eta}_1 = F_1^{exc} + F_1^{addedmass} + F_1^{truss} \tag{2.46}$$

where M is the total mass of the floater and F_1^{exc}, $F_1^{addedmass}$ and F_1^{truss} are the wave excitation, added mass and truss forces respectively along the x-direction. The wave excitation force is once again found from the incident velocity potential from regular deep-water waves propagating in the positive x-direction,

$$F_1^{exc} = 2A_{11}\zeta_a\omega^2\left(J_0(kR) - J_2(kR)\right)\exp(-i\omega t) \tag{2.47}$$

where A_{11} is the three-dimensional added mass in x-direction. In surge, the radial motion along the floater is $\eta_1\cos(\beta)$, and from this it can be shown that

$$A_{11} = \pi R a_{rr} \tag{2.48}$$

Further, the added mass force is given by

$$F_1^{addedmass} = -A_{11}\ddot{\eta}_1 \tag{2.49}$$

The truss force is found by summation of the x-component of tension from all the floater trusses, as shown in Equation (2.50). Here, $\boldsymbol{i} = [1, 0, 0]$

$$F_1^{truss} = \sum_{ft=1}^{N_{ft}} \gamma_{ft} T_{ft} \boldsymbol{s}_{ft} \cdot \boldsymbol{i} \tag{2.50}$$

2.8   Solar Island Model - A Truss Model Including Floater Motion

In this section the final derivations leading to the theoretical solar island model will be presented. The procedure is inspired by Kristiansen (2012), who includes the motion of a single elastic fish cage floater by Faltinsen (2011) into the truss-model by Marichal (2003).

In our case, the main steps are using the vertical and lateral floater models to find the acceleration of truss connection points on the floater, and then including it as a truss node acceleration in the truss model. With this, the truss equation system includes floater motion and can be solved to find the total motion of the system. The result is what we name a solar island model, which can be used to represent the full multi-torus solar island. Structural interactions are accounted for through the elastic bands between the tori. Mooring-lines may also be included.

We will first focus on a single floater node q, lying at a truss connection point. The position of the node will be $(x_q, y_q) = R(\cos \beta_q, \sin \beta_q)$. We will present the node acceleration from vertical and lateral motions separately, and then finally how these are all included in the truss equation system.

Lastly, we have a look at the full solar island truss system. The different truss types that it consists of will be presented, and how each of them are included in the truss equation system.

2.8.1   Node Acceleration from Vertical Floater Motion

The vertical node acceleration w_q is the sum of all vertical modes, i.e.

$$\ddot{w}_q = \sum_{n=0}^{\infty} \ddot{a}_n \cos(n\beta_q) \tag{2.51}$$

The mode acceleration $\ddot{a}_n$ is found by simply re-arranging Equation (2.34), giving

$$\ddot{a}_n = \frac{1}{(m + a_{33}^n)} \left[f_{3n}^{ex,gen} + \frac{1}{\alpha_n \pi} \int_0^{2\pi} f_3^{truss} \cos(n\beta) d\beta - \left(\rho g b + \frac{EI}{R^4}(n^4 - n^2) \right) a_n \right] \tag{2.52}$$

Inserting this into Equation (2.51) one obtains

$$\ddot{w}_q = \sum_{n=0}^{\infty} \left\{ \frac{\cos n\beta_q}{m + a_{33}^n} \left[f_{3n}^{ex,gen} + \frac{1}{\alpha \pi} \int_0^{2\pi} f_3^{truss} \cos n\theta d\theta - \left(\rho g b + \frac{EI}{R^4}(n^4 - n^2) \right) a_n \right] \right\} \tag{2.53}$$

Here, θ is used for the truss integral just for a cleaner expression. By expressing the truss integral as the sum in Equation (2.39), this can rather be written as

$$\ddot{w}_q = \underbrace{\sum_{n=0}^{\infty} \left\{ \frac{\cos n\beta_q}{\alpha_n \pi R(m + a_{33}^n)} \sum_{ft=1}^{N_{ft}} T_{ft} \gamma_{ft} (\boldsymbol{s}_{ft} \cdot \boldsymbol{k}) \cos n\theta_{ft} \right\}}_{\ddot{w}_q^T} \\ + \underbrace{\sum_{n=0}^{\infty} \left\{ \frac{\cos n\beta_q}{m + a_{33}^n} \left[f_{3n}^{ex,gen} - \left(\rho g b + \frac{EI}{R^4}(n^4 - n^2) \right) a_n \right] \right\}}_{\ddot{w}_q^{rest}} \tag{2.54}$$

The tension related part of the vertical acceleration is denoted $\ddot{w}_q^T$, while the the rest is denoted $\ddot{w}_q^{rest}$. This can next be made three-dimensional by multiplying with $\boldsymbol{k} = [0, 0, 1]$.

2.8.2 Node Acceleration from Surge Floater Motion

The acceleration in surge $\ddot{\eta}_1$ is found directly by re-arranging Equation (2.46) and is given by

$$\ddot{\eta}_1 = \underbrace{\frac{1}{M + A_{11}} 2A_{11}\zeta_a\omega^2 \left(J_0(kR) - J_2(kR)\right)\exp(-i\omega t)}_{\ddot{\eta}_1^{rest}} + \underbrace{\frac{1}{M + A_{11}} \sum_{ft=1}^{N_{ft}} \gamma_{ft}T_{ft}\boldsymbol{s}_{ft}\boldsymbol{i}}_{\ddot{\eta}_1^T} \qquad (2.55)$$

where the tension related part is denoted $\ddot{\eta}_1^T$ and the rest is denoted $\ddot{\eta}_1^{rest}$. This will then be the surge acceleration for all floater nodes q. It is made three-dimensional by multiplying it with $\boldsymbol{i} = [1, 0, 0]$.

The potential acceleration in sway $\ddot{\eta}_2$ due to surge motion is expressed by Equation (2.56) and is denoted $\ddot{\eta}_2^T$ as it is a tension-related term. It is made three-dimensional by multiplying with $\boldsymbol{j} = [0, 1, 0]$.

$$\ddot{\eta}_2 = \underbrace{\frac{1}{M + A_{11}} \sum_{ft=1}^{N_{ft}} \gamma_{ft}T_{ft}\boldsymbol{s}_{ft}\boldsymbol{j}}_{\ddot{\eta}_2^T} \qquad (2.56)$$

2.8.3 Node Acceleration from Radial Floater Motion

The radial node acceleration $\ddot{v}_q$ is expressed by its natural modes, and given by

$$\ddot{v}_q = \sum_{n=2}^{\infty} \ddot{b}_n \cos(n\beta) \qquad (2.57)$$

The mode acceleration $\ddot{b}_n$ is found by simply re-arranging Equation (2.41), giving

$$\ddot{b}_n = \frac{1}{m + a_{rr}} \left(\frac{1}{\pi} f_{rn}^{exc,gen} + \frac{1}{\pi} \int_0^{2\pi} f_r^{truss} \cos(n\beta)d\beta - \frac{EI}{R^4}\left(n^4 - n^2\right)b_n\right) \qquad (2.58)$$

Inserting this into Equation (2.57) and expressing the truss integral by Equation (2.45), we next obtain

$$\ddot{v}_q = \underbrace{\sum_{n=2}^{\infty} \frac{\cos n\beta}{m + a_{rr}} \frac{1}{\pi R} \sum_{ft=1}^{N_{ft}} \gamma_{ft}T_{ft}(\boldsymbol{s}_{ft} \cdot \boldsymbol{r})\cos(n\beta_{ft})}_{\ddot{v}_q^T} + \underbrace{\sum_{n=2}^{\infty} \frac{\cos n\beta}{m + a_{rr}}\left(\frac{1}{\pi} f_{rn}^{exc,gen} - \frac{EI}{R^4}\left(n^4 - n^2\right)b_n\right)}_{\ddot{v}_q^{rest}}$$

$$(2.59)$$

Here, the tension related part of the radial acceleration is denoted $\ddot{v}_q^T$, while the rest is denoted $\ddot{v}_q^{rest}$. The radial acceleration can be made three-dimensional by multiplying it with the radial vector $\boldsymbol{r} = [\cos\beta, \sin(\beta), 0]$. Do note that it has components in both x and y direction.

2.8.4 Adding Floater Motion to Truss Equations

We revisit Equation (2.22), which applies to each truss and forms the truss system of equations in the truss model. The node accelerations $\boldsymbol{a}_i^n$ and $\boldsymbol{a}_j^n$ for truss nodes i and j respectively should here be substituted by floater-node accelerations if they in fact lie on a floater.

For a floater node q, the acceleration is given by

$$\boldsymbol{a}_q = [a_{q1}, a_{q2}, a_{q3}] \qquad (2.60)$$

where a_{q1}, a_{q2}, a_{q3} are the acceleration components in x, y and z directions, respectively. From Equation (2.54), Equation (2.55), Equation (2.56) and Equation (2.59) it is seen that these are in fact given by

$$a_{q1} = \ddot{\eta}_1 + \ddot{v}_q \cos(\beta), \quad a_{q2} = \ddot{\eta}_2 + \ddot{v}_q \sin(\beta), \quad a_{q3} = \ddot{w}_q \tag{2.61}$$

so that the acceleration vector is given by

$$\boldsymbol{a}_q = \ddot{\eta}_1 \boldsymbol{i} + \ddot{\eta}_2 \boldsymbol{j} + \ddot{v}_q \boldsymbol{r} + \ddot{w}_q \boldsymbol{k} \tag{2.62}$$

This is the floater node acceleration that should be inserted into Equation (2.22). Doing so, we collect the tension related parts on the left and the rest on the right. The results are as shown in Equation (2.63) and Equation (2.64) for the case of the floater node being an i and j node, respectively.

$$\boldsymbol{s}_k \cdot \left[\boldsymbol{a}_j^n - (\ddot{\eta}_1^T \boldsymbol{i} + \ddot{\eta}_2^T \boldsymbol{j} + \ddot{v}_q^T \boldsymbol{r} + \ddot{w}_q^T \boldsymbol{k}) \right] - \frac{T^n}{k\Delta t^2} = -\frac{b^n}{2l_k} - \boldsymbol{s}_k \left[\frac{1}{\Delta t} \boldsymbol{c}^n - (\ddot{\eta}_1^{rest} \boldsymbol{i} + \ddot{v}_q^{rest} \boldsymbol{r} + \ddot{w}_q^{rest} \boldsymbol{k}) \right] - \frac{T^{n-1}}{k\Delta t^2} \tag{2.63}$$

$$\boldsymbol{s}_k \cdot \left[(\ddot{\eta}_1^T \boldsymbol{i} + \ddot{\eta}_2^T \boldsymbol{j} + \ddot{v}_q^T \boldsymbol{r} + \ddot{w}_q^T \boldsymbol{k}) - \boldsymbol{a}_i^n \right] - \frac{T^n}{k\Delta t^2} = -\frac{b^n}{2l_k} - \boldsymbol{s}_k \left[\frac{1}{\Delta t} \boldsymbol{c}^n + (\ddot{\eta}_1^{rest} \boldsymbol{i} + \ddot{v}_q^{rest} \boldsymbol{r} + \ddot{w}_q^{rest} \boldsymbol{k}) \right] - \frac{T^{n-1}}{k\Delta t^2} \tag{2.64}$$

With this, we have a system of equations for the solar island model which can be solved for the unknown truss tensions at each time step. Inserting this in the Euler scheme, we obtain the entire systems motion in regular waves.

2.8.5   Solar Island Truss System

The time is now ripe for an overview of the entire solar island truss system. Figure 2.12 shows a case consisting of three floaters with eight elastic bands connecting each one to the next, these again consisting of three individual trusses. Four mooring-lines connected to the outer torus are also included. Do note that this case is just one of many possible configurations. The tori may have different structural properties, such as cross-sectional and center-line curve diameter, mass per unit length and stiffness.

As seen in the figure, there are really three types of trusses and nodes that the system is built up by. The node types are *floater nodes*, which lie on a floater, *connecting nodes* which do not and are free, and lastly *mooring nodes* which are fixed. The truss types are *floater trusses* which have at least one floater node, *connecting trusses* between connecting nodes, and lastly mooring trusses between floater nodes and mooring nodes.
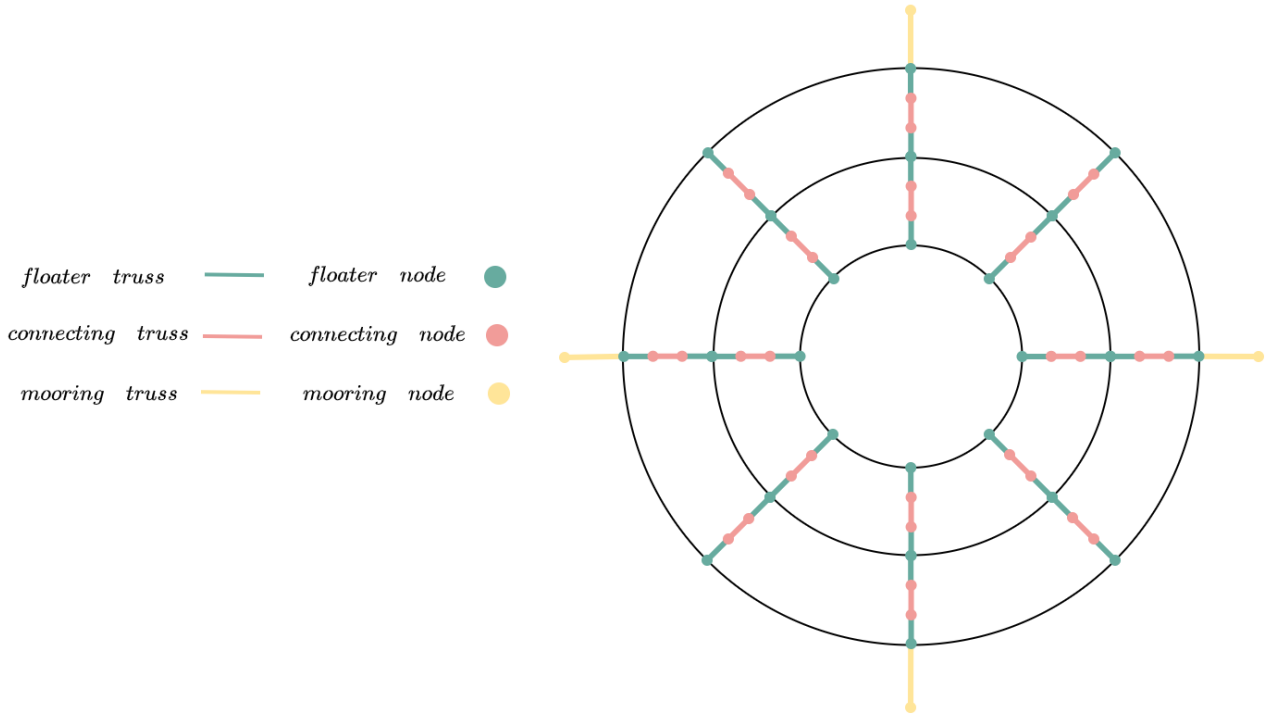
Figure 2.12: Solar Island Truss System

A solar island represented by a truss system consisting of *floater trusses* and *floater nodes*, *connecting trusses* and *connecting nodes*, and *mooring trusses* and *mooring nodes*.

Now, for each truss in the system, its end node types will decide what modifications are needed in Equation (2.22) in order to include its node accelerations. When this is known, one can easily add the truss into the matrix system to be solved in Equation (2.24). For a connecting node, its acceleration is simply given by the sum of tensions and gravitational force acting on it, as presented in Equation (2.23). For a floater node, it is based on the motion of the floater it is attached to and given by Equation (2.62). Lastly, for a mooring node it is always zero. To summarize, the possible accelerations for the nodes of a truss k in the solar island system are given by

$$\boldsymbol{a}_q = \ddot{\eta}_1 \boldsymbol{i} + \ddot{v}_q \boldsymbol{r} + \ddot{w}_q \boldsymbol{k} \tag{2.65}$$

$$\boldsymbol{a}_{ci} = T_k \boldsymbol{s}_k - T_{k-1} \boldsymbol{s}_{k-1} + \boldsymbol{g} \tag{2.66}$$

$$\boldsymbol{a}_{cj} = T_{k+1} \boldsymbol{s}_{k+1} - T_k \boldsymbol{s}_k + \boldsymbol{g} \tag{2.67}$$

$$\boldsymbol{a}_m = [0, 0, 0] \tag{2.68}$$

Here, $\boldsymbol{a}_{ci}$ is connecting node i acceleration, $\boldsymbol{a}_{cj}$ is connecting node j acceleration, and $\boldsymbol{a}_m$ is mooring node acceleration. For the connecting nodes, $k-1$ denotes the neighbouring truss connected to node i of truss k, while $k+1$ denotes the neighbouring truss connected to node j of truss k.

The specific set-up of the A-matrix and B-vector of the truss matrix system in Equation (2.24) depends on the specific solar island truss system and chosen indexing of the different nodes and trusses.

2.9   Response Amplitude Operators

In this section, the theoretical response amplitude operators (RAOs) for the different vertical and lateral modes of a single floater will be presented. These are all based on the modal equation of motions presented in Section 2.6 and Section 2.7.

2.9.1 Vertical Mode RAOs

The general expression for the RAO of a vertical mode n is given by

$$RAO_n = \left| \frac{a_{n,a}}{\zeta_a} \right| \tag{2.69}$$

where $a_{n,a}$ is the amplitude of the specific mode amplitude motion $a_n(t)$. It is assumed that the mode amplitude has a harmonic motion, so that

$$a_n(t) = a_{n,a} \exp(-i\omega t) \tag{2.70}$$

where ω is the circular wave frequency of the incident wave. This means that the mode acceleration $\ddot{a}_n(t)$ becomes

$$\ddot{a}_n(t) = -\omega^2 a_{n,a} \exp(-i\omega t) \tag{2.71}$$

The mode amplitude and acceleration in Equation (2.70) and Equation (2.71) are next inserted into the vertical modal equation of motion in Equation (2.34), neglecting truss forces. The exponential terms can then be cancelled, and the equation re-arranged to give the RAO of the mode. The result is

$$\left| \frac{a_{n,a}}{\zeta_a} \right| = \left| \frac{(3 - \alpha_n)(\rho g b - \omega^2 a_{33}^n)i^{n+1}J_n(kR)}{-\omega^2(m + a_{33}^n) + \rho g b + \frac{EI}{R^4}(n^4 - n^2)} \right| \tag{2.72}$$

Here ρ is the fluid density, g the gravitational acceleration, b floater cross-section, $a_{33}^{(n)}$ the 2D added mass of mode n, $J_n(kR)$ Bessel functions of the first kind, k the wave number, m the mass per unit length, E Young's modulus, and I the area moment of inertia. $\alpha_n = 2$ for $n = 0$ and 1 for $n > 0$.

2.9.2 Surge RAO

For surge motion, the RAO is given by

$$RAO = \left| \frac{\eta_{1,a}}{\zeta_a} \right| \tag{2.73}$$

where $\eta_{1,a}$ is the amplitude of the surge motion. As in the previous section, it is assumed a harmonic motion in surge, so that the surge motion $\eta_1(t)$ and acceleration $\ddot{\eta}_1(t)$ are given by

$$\eta_1(t) = \eta_{1,a} \exp(-i\omega t), \quad \ddot{\eta}_1(t) = -\omega^2 \eta_{1,a} \exp(-i\omega t) \tag{2.74}$$

Inserting this into the surge equation of motion in Equation (2.46), neglecting truss forces, the exponential terms can be cancelled and the equation re-arranged to give

$$\left| \frac{\eta_{1,a}}{\zeta_a} \right| = \left| \frac{2A_{11}(J_0(kR) - J_2(kR))}{-(M + A_{11})} \right| \tag{2.75}$$

where A_{11} is the added mass in x-direction. For the case of a moored single floater, the effect of the mooring lines can be included in the RAO by use of a stiffness term presented by Faltinsen (1993). This is given by

$$C_{11} = \sum_{mt=1}^{N_{mt}} k_{mt} \cos^2 \beta_{mt} \tag{2.76}$$

where the summation is over all mooring trusses mt, N_{mt} is the total number of mooring trusses attached to the floater, k_{mt} is truss stiffness, and β_{mt} is the truss angle, defined earlier in Figure 2.5. Including the mooring-lines in the RAO, the result becomes

$$\left| \frac{\eta_{1,a}}{\zeta_a} \right| = \left| \frac{2A_{11}\omega^2 \left(J_0(kR) - J_2(kR) \right)}{C_{11} - \omega^2(M + A_{11})} \right| \tag{2.77}$$

2.9.3 Radial Mode RAOs

The general expression for the RAO of a radial mode n is given by

$$RAO_n = \left| \frac{b_{n,a}}{\zeta_a} \right| \tag{2.78}$$

where $b_{n,a}$ is the amplitude of the specific mode amplitude motion $b_n(t)$. Once again it is assumed that the mode amplitude has a harmonic motion, so that $b_n(t)$ and $\ddot{b}_n(t)$ are given by

$$b_n(t) = b_{n,a} \exp(-i\omega t), \quad \ddot{b}_n(t) = -\omega^2 b_{n,a} \exp(-i\omega t) \tag{2.79}$$

The mode amplitude and acceleration are next inserted into the radial modal equation of motion in Equation (2.41), neglecting truss forces. Cancelling the exponential terms, the equation is re-arranged to give the RAO of the mode. The result is

$$\left| \frac{b_{n,a}}{\zeta_a} \right| = \left| \frac{2a_{rr}\omega^2 i^{n-1}[J_{n-1}(kR) - J_{n+1}(kR)]}{-\omega^2(m + a_{rr}) + \frac{EI}{R^4}(n^4 - n^2)} \right| \tag{2.80}$$

where a_{rr} is the radial added mass per unit length.

2.10 Natural Frequencies

The natural frequencies of a floater in different modes are found by the same methods as for the RAOs, that is, by assuming harmonic motion. Now, there are however no external forces. Equation (2.81) gives the natural frequency in vertical modes, Equation (2.82) in surge, and Equation (2.83) in radial modes.

$$\omega_{n,vertical} = \sqrt{\frac{\rho g b + (n^4 - n^2)\frac{EI}{R^4}}{m + a_{33}^n}} \tag{2.81}$$

$$\omega_{n,surge} = \sqrt{\frac{C_{11}}{M + A_{11}}} \tag{2.82}$$

$$\omega_{n,radial} = \sqrt{\frac{(n^4 - n^2)\frac{EI}{R^4}}{m + a_{rr}}} \tag{2.83}$$

2.11 Rayleigh Damping

A Rayleigh type damping may be necessary in the numerical runs of the solar island model in order to avoid unphysically large floater motions when waves coincide with the natural frequencies. This means that there will be added a damping force in the modal equation of motions for each torus in each mode. The damping term is defined as a fraction ξ of the critical damping in this mode. This is then multiplied with the specific mode velocity to get the damping force.

For vertical modes n, the damping force to be included on the right hand side in Equation (2.34) is thus given by

$$f_{vertical}^{rayleigh} = -2\xi(m + a_{33}^n)\omega_{n,vertical}\dot{a}_n \tag{2.84}$$

For surge motion, the damping force to be included on the right hand side in Equation (2.46) is given by

$$f_{surge}^{rayleigh} = -2\xi(M + A_{11})\omega_{n,surge}\dot{\eta}_1 \tag{2.85}$$

For radial modes n, the damping force to be included on the right hand side in Equation (2.41) is given by

$$f_{radial}^{rayleigh} = -2\xi(m + a_{rr}^n)\omega_{n,radial}\dot{b}_n \tag{2.86}$$

Chapter 3

Hydrodynamic Interaction Theory

In this chapter, a method to include hydrodynamic interaction forces between the solar island tori in the form of vertical added mass cross-terms will be presented. This theory was derived by Kristiansen (2020) during the last few weeks of May 2020 and has therefore not yet been published. He derives approximate formulas for cross-coupling added mass coefficients, and incorporates them in the floater equations of motion. The derivation of the added mass cross-terms will be presented first, then adjustments made in the wave excitation force, and lastly how to obtain RAOs with these terms included.

3.1 Multi-torus Geometry

Figure 3.1 illustrates the multi-torus solar island structure, now with focus on the tori. It consists of a number of T tori, equally spaced with distance $2p$ between their center-lines, connected by elastic bands and with mooring-lines at the outer torus. The outer torus is given the index 1, while the inner then becomes torus number T. Further, the global radius of a torus is $2R_t$. As before, structural properties such as mass per unit length, m_t, cross-sectional diameter $2c_t$ and bending stiffness EI_t may vary from torus to torus.
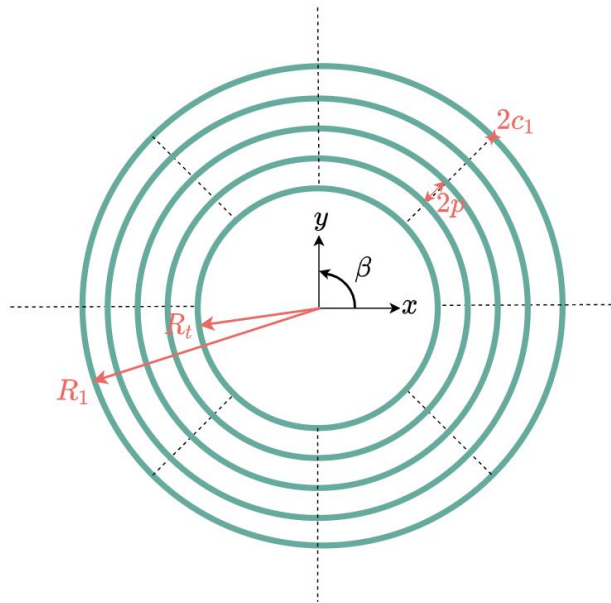

Figure 3.1: Multi-torus geometry

3.2   Hydrodynamic Interaction in Floater Equations

The modified curved beam equation, presented earlier in Equation (2.34), is still used to model the vertical motion w of a torus. The aim now, however, is to include hydrodynamic interaction forces on the specific torus due to the presence of the other tori in the system. Including a hydrodynamic force term, the equation becomes

$$m_t \frac{\partial^2 w}{\partial t^2} + \rho g b_t w + EI_t \frac{\partial^4 w}{\partial s^4} + \frac{EI_t}{R^2} \frac{\partial^2 w}{\partial s^2} = f_t^{addedmass} + f_t^{exc} + f_t^{truss} + f_t^{hydr,int} \qquad (3.1)$$

where $f_t^{addedmass}$, f_t^{exc}, f_t^{truss} and $f_t^{hydr,int}$ are vertical added mass, wave excitation, truss and hydrodynamic interaction forces per unit length on torus t, respectively. The previously used vertical index 3 has here been removed.

Following the procedure in Section 2.6, the vertical motion is decomposed into its natural modes and inserted into Equation (3.1). Multiplying the new expression by $\cos m\beta$ and integrating from $\beta = 0$ to 2π, one can take advantage of orthogonality so that the expression simplifies. The result is the equation of motion for mode n amplitude $a_{t,n}$ of torus t,

$$(m_t + a_{t,t,n})\ddot{a}_{t,n} + \left(\rho g b + \frac{EI}{R^4}(n^4 - n^2) \right) a_{t,n} = f_{t,n}^{exc,gen} + \frac{1}{\alpha_n \pi} \int_0^{2\pi} f_t^{truss} \cos(n\beta)d\beta + f_{t,n}^{hydr,int,gen} \quad (3.2)$$

where $a_{t,t,n}$ is the added mass per unit length on torus t due to its mode n motion. The generalized hydrodynamic interaction force, $f_{t,n}^{hydr,int,gen}$, will be expressed by cross-coupling (off-diagonal) added mass terms.

Now, picture a torus t in the structure moving. This will induce a pressure disturbance throughout the water, and thus induce a pressure load on all the other tori. Since we consider the zero-frequency limit, the induced load will be in phase with the motion of the moving torus. We remember from Section 2.5 that pressure disturbances are progressed infinitely fast and in phase everywhere in the water when this limit is considered. The free surface is not disturbed. Further, because of orthogonality of the modes, a motion of a torus in a given mode will only induce a load in the *same mode* on the other tori. Looking at the case in Figure 3.1, this means that forced heave motion of torus 1 will induce added mass forces in heave only on tori 2-5. No loads are induced in the other modes. This is very fortunate, as the number of necessary cross-coupling added mass terms in the equation of motion reduces.

From the discussion above, the hydrodynamic interaction force can be expressed as the sum of added mass forces on torus t from the other tori. Equation (3.2) is accordingly re-written, resulting in

$$m_t \ddot{a}_{t,n} + \left(\rho g b + \frac{EI}{R^4}(n^4 - n^2) \right) a_{t,n} = f_{t,n}^{exc,gen} + \frac{1}{\alpha_n \pi} \int_0^{2\pi} f_t^{truss} \cos(n\beta)d\beta - \sum_{j=1}^{T} a_{t,j,n} \ddot{a}_{j,n} \qquad (3.3)$$

Here, $a_{t,j,n}$ is the added mass per unit length on torus t from mode n motion of torus j, and $\ddot{a}_{j,n}$ is the mode n acceleration of torus j. As seen, the generalized added mass and hydrodynamic interaction forces have been combined into a summation expression over all tori in the structure, from the outer torus $j = 1$ to the inner $j = T$. In this sum, $a_{t,t,n}\ddot{a}_{t,n}$ is the added mass force per unit length on the torus t due to its own mode n motion, while for $j \neq t$ the force is a cross-coupling added mass force.

3.3   Zero-frequency limit radiation problem

We consider the zero-frequency radiation problem in Figure 3.2, where torus j is heaving a distance $2p$ from its neighbouring torus t. The cross-sectional diameter is $2c$ for both tori.
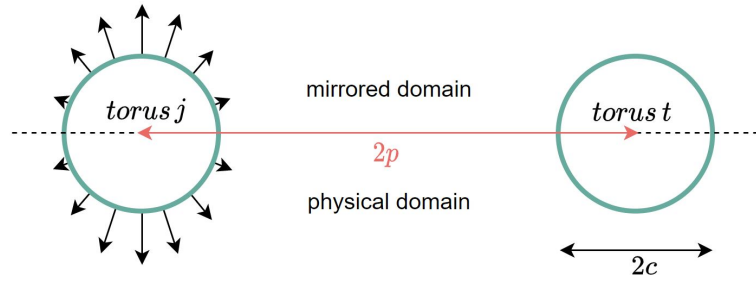
Figure 3.2: Zero-frequency radiation problem
The zero-frequency radiation problem of two neighbouring tori j and t, where torus j is heaving. The physical domain is mirrored to the upper half-plane. The cross-sectional diameter of the tori is $2c$, and the distance center-to-center between the tori is $2p$. The dashed line is the still free-surface at $z = 0$. Slightly modified from Kristiansen (2020).

We assume that the presence of the other (fixed) tori does not significantly affect the diagonal added mass term $A_{j,j,n}$ as long as the spacing is above some value, say $p/c > 2$. The thought behind this assumption is that the other tori represent small dipol-like obstacles, so that they will only disturb the pressure distribution from the moving torus locally near themselves, and not close to the moving torus. With this, the the ZFT added mass for a single torus presented in Equation (2.32) is still used for the diagonal added mass terms.

Now over to the cross-coupled added mass terms. The moving torus j induces a source-like flow, it gives a net mass flux in the combined physical/mirrored domain and thus induces pressure far from itself. We therefore expect that it induces loads on the other tori. The mirrored problem is not given by a single potential source, but its far-field behaviour is however given by a source. The reason is that the non-constant normal velocity results in disturbances only very local to the torus, which are decaying rapidly, while the (logarithmic) source term is not. The source-like far-field behavior is illustrated in Figure 4. As seen, some distance away the flow is well represented by a source at the torus center, while this is not the case near the torus.
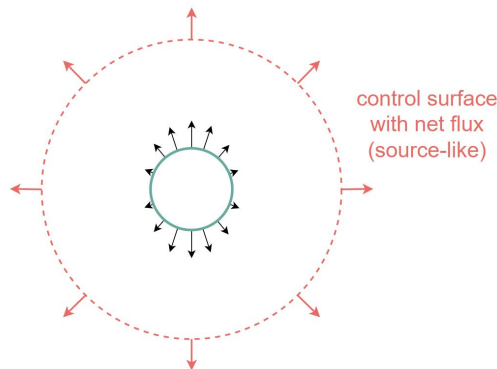

Figure 3.3: Source-like far-field behaviour
Mirrored problem of a semi-submerged torus j heaving. As seen, the far-field behaviour is source like. Slightly modified from Kristiansen (2020).

Now, since we can assume that the induced flow is only slightly affected by the presence of the other tori, we use the far field solution of the moving torus j as incident flow on the fixed torus t. Further, we assume that the induced ambient pressure is uniform over torus t. This is integrated to get the Froude-Kriloff load. There is no vertical diffraction problem since the flow is nearly horizontal near the surface.

3.4   Cross-Term Added Mass from Far-Field Solution

To represent the induced pressure, either the outer expansion of the near field solution or the far-field solution of the moving torus may be used. Kristiansen (2020) presents both methods, but only the latter will be presented here.

The far-field velocity potential due to forced vertical mode n motion of torus j is given by

$$\phi_j^F(x,y,z,t) = \frac{Q}{4\pi} \int_0^{2\pi} \frac{\cos n\beta_0}{|\boldsymbol{x} - \boldsymbol{x}_0|} R_j d\beta_0 \tag{3.4}$$

where $\boldsymbol{x}_0 = [x_0, y_0, z_0]$ are the source points, located on the circular center axis of the torus. We take $z = z_0$, so that the vertical coordinate is at the free-surface, and transform into cylindrical coordinates by the relations $x = r\cos\beta, y = r\sin\beta$. With this we get

$$\phi_j^F(r,\beta,0,t) = \frac{QR_j}{4\pi} \int_0^{2\pi} \frac{\cos n\beta_0}{\left(r^2 + r_0^2 - 2rr_0\cos(\beta - \beta_0)\right)^{0.5}} d\beta_0 \tag{3.5}$$

Now, evaluating this at $r = R_t$ and $R_0 = R_j$ the resulting expression is

$$\phi_j^F(R_t,\beta,0,t) = \frac{QR_j}{4\pi} \int_0^{2\pi} \frac{\cos n\beta_0}{\left(R_t^2 + R_j^2 - 2R_tR_j\cos(\beta - \beta_0)\right)^{0.5}} d\beta_0 \tag{3.6}$$

Further, Q is determined by satisfying the body-boundary condition in the inner problem and is presented by Faltinsen (2011) to be

$$Q = 4c\dot{a}_{j,n} \tag{3.7}$$

By the Bernoulli equation, the induced pressure by the torus j motion is given by

$$p_j = -\rho \frac{\partial \phi_j^F(R_k,\beta,0,t)}{\partial t} \tag{3.8}$$

and the total load per unit length on torus t is then found by integrating the pressure over its cross-sectional wetted area, resulting in

$$f_{t,j,n}(\beta,t) = -\ddot{a}_{j,n} \frac{2}{\pi}\rho c^2 R_j \int_0^{2\pi} \frac{\cos n\beta_0}{\left(R_t^2 + R_j^2 - 2R_tR_j\cos(\beta - \beta_0)\right)^{0.5}} d\beta_0 \tag{3.9}$$

where one has used that $\int_{-\pi/2}^{\pi/2} \cos\theta'' d\theta'' = 2$.

Looking back at Equation (3.1), the vertical hydrodynamic interaction force per unit length for torus t may now be expressed as a sum of modal loads per unit length,

$$f_t^{hydr,int} = \sum_{n=0}^{\infty} \sum_{j=1}^{T} f_{t,j,n} \tag{3.10}$$

Now, the generalized hydrodynamic interaction force, $f_{t,n}^{hydr,int,gen}$, is found by multiplying this force with $\cos(m\beta)$ and integrating from 0 to 2π, resulting in

$$f_{t,n}^{hydr,int,gen} = \frac{1}{\alpha_n \pi} \int_0^{2\pi} \sum_{j=1}^{T} f_{t,j,n} \cos n\beta \, d\beta \tag{3.11}$$

where $\alpha_0 = 2$ and $\alpha_n = 1$ for $n \geq 1$. The summation term over modes has been cut due to the fact that only the term where $m = n$ will stand left because of orthogonality of cosine integrals. By comparing with the generalized hydrodynamic interaction force term in Equation (3.3), it is seen that the cross-term added mass (for $j \neq t$) is given by

$$a_{t,j,n} = \frac{2}{\alpha_n \pi^2} \rho c^2 R_j \int_0^{2\pi} \int_0^{2\pi} \frac{\cos n\beta_0 \cos n\beta}{(R_t^2 + R_j^2 - 2R_t R_j \cos(\beta - \beta_0))^{0.5}} d\beta_0 d\beta \tag{3.12}$$

3.5 Including Hydrodynamic Interaction in Wave Excitation Force

The wave excitation force will also have to be adjusted for hydrodynamic interaction between tori. The Froude-Kriloff part is of course as for a single torus, and the part of the diffraction force due to the diffraction by torus t itself is also as for a single torus. However, the diffraction force involves a boundary layer problem with body velocity equal to minus the incident wave velocity, and there is therefore a hydrodynamic interaction load due to the other tori, similar as in the radiation problem.

By satisfying the boundary condition on the center-axis of each torus and use of the far-field approach, the generalized wave excitation force per unit length accounting for hydrodynamic interaction can be expressed as

$$f_{t,n}^{exc,gen} = \zeta_a \left(2\rho g c J_n(kR_t) - \omega^2 \sum_{j=1}^{T} a_{k,j,n} q_n J_n(kR_j) \right) i^{n+1} e^{-i\omega t} \tag{3.13}$$

This can then be used in the modal equation of motion, Equation (3.3).

3.6 RAOs accounting for Hydrodynamic Interactions

The modal equation of motion in Equation (3.3) can be used to obtain the floater-node accelerations to be used in the numerical solar island presented in chapter 2. However, neglecting the trusses between the tori, a much simpler solution method in the frequency domain can be applied to obtain vertical mode RAOs. This will then not account for structural interactions between the tori, only hydrodynamic ones. The method will be presented briefly in this section, using a 2-torus case as an example, as this is sufficient to describe the procedure. The cross-sectional radius and mass per unit length are set to be identical for the tori. The modal equations of motions are in this case

$$
\begin{aligned}
(m + a_{1,1,n})\ddot{a}_{1,n} + a_{1,2,n}\ddot{a}_{2,n} + \frac{EI_1}{R_1^4}(n^4 - n^2)a_{1,n} + \rho g 2 c a_{1,n} = f_{1,n}^{exc,gen} \\
(m + a_{2,2,n})\ddot{a}_{2,n} + a_{2,1,n}\ddot{a}_{1,n} + \frac{EI_2}{R_2^4}(n^4 - n^2)a_{2,n} + \rho g 2 c a_{2,n} = f_{2,n}^{exc,gen}
\end{aligned}
\tag{3.14}
$$

We further assume steady state conditions, i.e that $a_{t,n} = \tilde{a}_{t,n} e^{-i\omega t}$. With this, the set of equations can be stated in matrix form as

$$
\begin{bmatrix}
-\omega^2(m + a_{1,1,n}) + \frac{EI_1}{R_1^4}(n^4 - n^2) + 2\rho g c & -\omega^2 a_{1,2,n} \\
-\omega^2(m + a_{2,2,n}) + \frac{EI_2}{R_2^4}(n^4 - n^2) + 2\rho g c & -\omega^2 a_{2,1,n}
\end{bmatrix}
\begin{bmatrix}
\tilde{a}_{1,n} \\
\tilde{a}_{2,n}
\end{bmatrix}
=
\begin{bmatrix}
\tilde{f}_{1,n}^{exc,gen} \\
\tilde{f}_{2,n}^{exc,gen}
\end{bmatrix}
\tag{3.15}
$$

where ˜ refers to motion or force amplitude. RAO-values for different ω can then be obtained by $|\tilde{a}_{t,n}/\zeta_a|$.

3.7 Three-Dimensional Cross-Coupled Added Mass

In this section, the derivation of three-dimensional cross-coupled added mass will be presented.

The vertical load in mode m on torus t can be found by multiplying the vertical load per unit length in Equation (3.9) by the mode shape $\cos m\beta$ of torus t and integrating this over torus t. The result is then that the vertical load in mode m of torus t due to a mode n motion of torus j is given by

$$F_{t,j,m,n}(\beta,t) = -\ddot{a}_{j,n}\frac{2}{\pi}\rho c^2 R_j R_t \int_0^{2\pi} \int_0^{2\pi} \frac{\cos n\beta_0}{\left(R_t^2 + R_j^2 - 2R_t R_j \cos(\beta-\beta_0)\right)^{0.5}} d\beta_0 \cos m\beta d\beta \quad (3.16)$$

so that the cross-coupled added mass is accordingly given by

$$A_{t,j,m,n}(\beta,t) = \frac{2}{\pi}\rho c^2 R_j R_t \int_0^{2\pi} \int_0^{2\pi} \frac{\cos n\beta_0}{\left(R_t^2 + R_j^2 - 2R_t R_j \cos(\beta-\beta_0)\right)^{0.5}} d\beta_0 \cos m\beta d\beta \quad (3.17)$$

As discussed earlier, $A_{t,j,m,n} = 0$ for $m \neq n$, so the expression can rather be written

$$A_{t,j,n}(\beta,t) = \frac{2}{\pi}\rho c^2 R_j R_t \int_0^{2\pi} \int_0^{2\pi} \frac{\cos n\beta_0 \cos n\beta}{\left(R_t^2 + R_j^2 - 2R_t R_j \cos(\beta-\beta_0)\right)^{0.5}} d\beta_0 d\beta \quad (3.18)$$

Chapter 4

Verification Studies

In this chapter, verification studies for both the numerical solar island model and the hydrodynamic interaction theory will be presented. For the numerical solar island, vertical modes, surge and radial modes will first be studied separately for a single floater, with and without mooring-lines. Lastly, a combined motion case where both heave, surge and the first flexible lateral mode are activated will be studied. In the hydrodynamic interaction verification studies, cross-coupled added mass terms for a 5-torus case will be studied, and compared to previous results from WAMIT.

In the preliminary project thesis, verification studies on simple inelastic and elastic truss cases were performed, and showed good results. The elastic verification cases are added in Appendix B. A flowchart of the numerical solar island model is illustrated in Figure H.1.

4.1   Introduction to Single Floater Verification Studies

A simple, single floater geometry will be the basis for the verification studies on the numerical solar island model. This is illustrated in Figure 4.1. $fnode$ denotes floater-node, and as seen there are four of them. For the tests including mooring-lines, these will be modelled by one truss each, with indexing as seen in the figure. The floater-nodes are defined to be j nodes, so that the $\boldsymbol{s}_{ft}$-vectors of the trusses are pointing towards the floater.
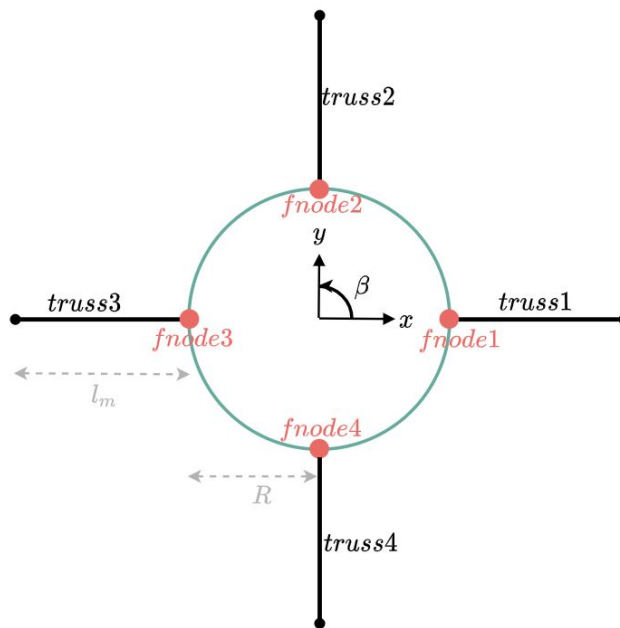

Figure 4.1: Solar island configuration for verification studies
.

Torus properties are constant throughout the studies, and set to be equal to the full scale values for the experimental multi-torus model by Vassdokken Sigstad (2019). In the hope of using a pre-tension value more fitting for a single moored floater, it is set equal to the full scale value used by Li (2017) in his model tests on a single moored torus. The values are listed in Table 4.1. Further, descriptions for varying parameter values that will be presented later for each study are listed in Table 4.2. The ramping is included by simply multiplying the wave excitation force by $t/(end - time)$ for all time-instances t up until the defined $end - ramp$. Very long ramping-times are generally used throughout the verification studies, which is done to absolutely assure stable runs. Of course this is quite extreme, and makes the runs take much longer time than what is probably necessary. Quite large kR-ranges are also tested for the RAOs, as it is interesting to see how the model works for a wide set of wave frequencies, even though many of these will represent nonphysical waves.

Table 4.1: Constant parameter values in single floater verification studies

Description	Parameter	Value
Density of seawater	$\rho \ [kg/m^3]$	1025
Bending stiffness	$EI \ [Nm^2]$	$2.65 \cdot 10^8$
Cross-sectional diameter of torus	$b_w \ [m]$	1.6
Radius of torus	$R \ [m]$	25
Pre-tension in mooring-trusses	$Tpm \ [N]$	78125

Table 4.2: Varying parameter values in single floater verification studies

Description	Parameter
Mooring-truss stiffness	$k_m \ [N/m]$
Mooring-truss length	$l_m \ [m]$
Wave amplitude	$\zeta_a \ [m]$
Wave period	$T_w \ [s]$
Time-step	$dt \ [s]$
End of time-series	$end - time \ [s]$
End of ramping of wave excitation force	$end - ramp \ [s]$
Start of stable region of time-series	$stable - time \ [s]$
Damping ratio, for Rayleigh damping	$\xi \ [\%]$

When reading through the verification studies on the numerical solar island model, some of the choices made along the way may seem strange, such as varying ramping for the runs as well as not checking the exact same time-steps in the time-step studies for the different modes. The reader should however keep in mind that these verification studies are from a process stretching over several months. Vertical motion, surge and radial modes for a single moored floater were implemented separately before they were combined, and verification studies were carried out on each of them. Therefore, different aspects were studied for each of them. The final verification of the numerical solar island model is far from complete, but the studies so far show promising results, which is why one went on to expand to several tori rather than keep working on verification studies.

4.2   Vertical Motion of Single Floater

In this section, the verification study of a single floater with vertical motion will be presented.

4.2.1   Including Ramping and Rayleigh Damping

The effect of including ramping of the wave excitation force as well as Rayleigh damping to avoid excitation of the natural modes of the floater are studied. A realistic wave condition is tested. The

parameter-values used in the runs are listed in Table 4.3, and mooring-lines are included. The mooring-truss stiffness is set equal to that in the experimental model by Vassdokken Sigstad (2019).

Table 4.3: Parameter values - ramping and Rayleigh damping study

vertical modes	ζ_a [m]	T_ω [s]	k_m [N/m]	l_m [m]	dt [s]	end-time [s]	ξ [%]	end-ramp [s]
$0:3$	0.1	10	$35.9 \cdot 10^3$	1000	0.001	$40 \cdot T_w$	3	$10 \cdot T_w$

Figure 4.2 shows the resulting tension time-series from different combinations of including ramping and/or Rayleigh damping. Comparing Figure 4.2a and Figure 4.2b it is seen that including ramping stabilizes the solution, natural frequencies are suppressed. Still we see some influence in tension, especially for truss 1. From Figure 4.2a and Figure 4.2c it is seen that including Rayleigh damping stabilizes the solution after some time, but at the very start the natural frequencies are excited, which is still not preferable. In Figure 4.2d, both ramping and Rayleigh damping are included, and the tension development is entirely stabilized. This is clearly the best option.
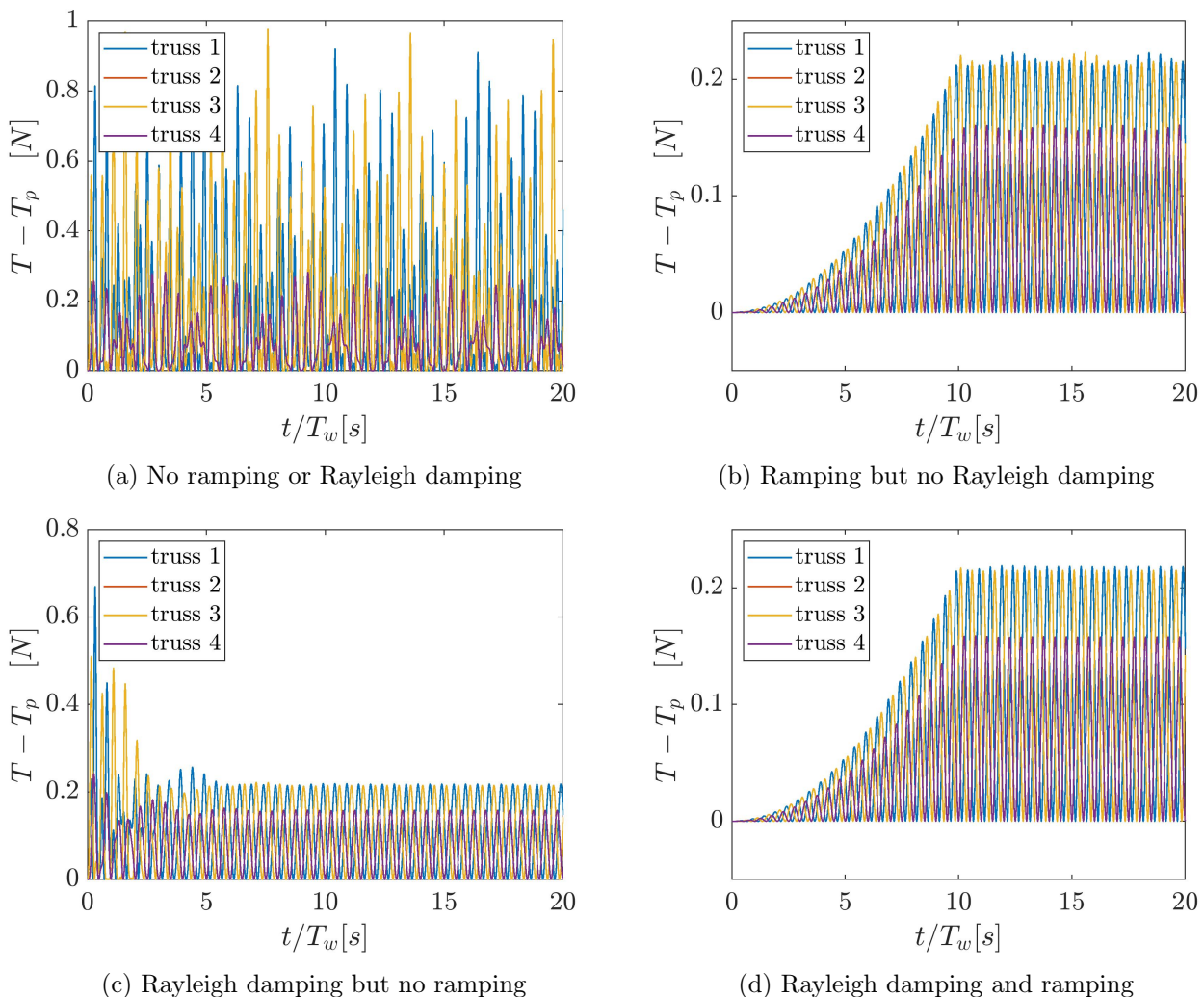

(a) No ramping or Rayleigh damping

(b) Ramping but no Rayleigh damping

(c) Rayleigh damping but no ramping

(d) Rayleigh damping and ramping

Figure 4.2: Including ramping and Rayleigh damping
Tension time-series are presented for the case of a floater with vertical modes $0-3$ activated, for all 4 of its mooring-trusses. The difference in tension T from the initial pre-tension T_p is plotted. The effects of ramping of the wave excitation force and Rayleigh damping of natural modes are shown from the different time-series.

Regarding the resulting tension-values, these are all reasonable. Truss 1 and 3 lie along the x-axis and are thus most affected by the wave so that they get largest fluctuations in tension. Truss 2 and 4 lie

along the y-axis and thus get less. Also, none of the truss-tensions go below pre-tension, as it should be when there is only vertical motion activated for the floater.

We also find satisfying effect of including ramping and Rayleigh damping in FFT transform of the signal, as seen in Figure 4.3. In this case, the FFT of the z-position of node 1 is taken. $|P_1|$ is the single-sided amplitude spectrum of $Z_1(t)$ for node 1. Including ramping and Rayleigh damping, the natural frequencies of the modes are no longer excited, and the only peak is at the wave frequency, as it should be.

(a) No ramping or Rayleigh damping   (b) Rayleigh damping and ramping
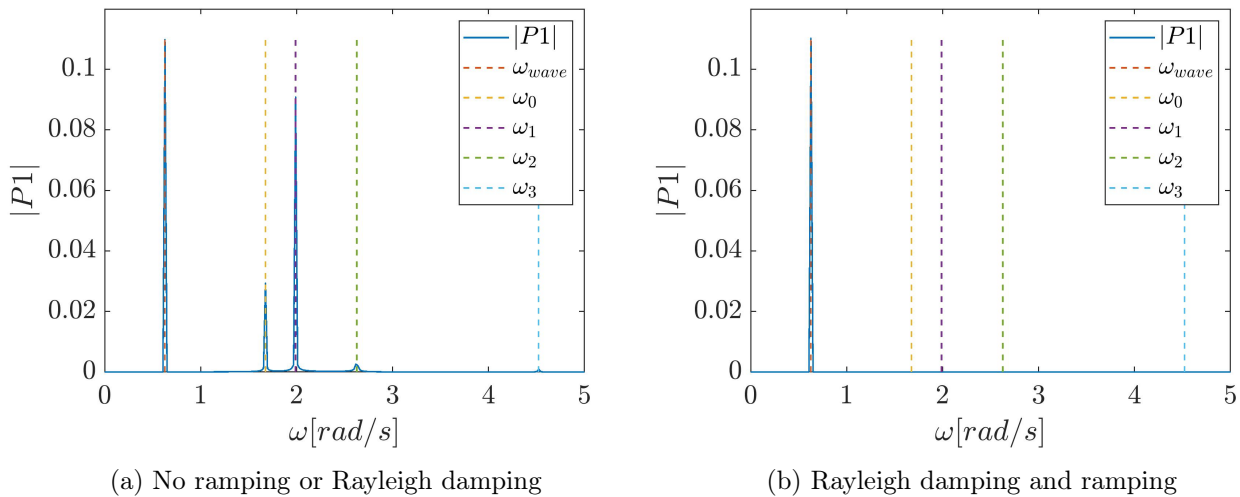
Figure 4.3: Effect on FFT from ramping and Rayleigh damping
Single-sided amplitude spectra $|P1|$ of the z-position time-series $z_1(t)$ of node 1 are presented, for the case of including ramping and Rayleigh damping and not. Natural frequencies for the single floater in the activated vertical modes, $\omega_0 - \omega_3$ are marked by stippled lines, as well as the incident circular wave frequency ω_{wave}.

Time-series for modal amplitudes, as well as z-position for the 4 floater-nodes are added in Appendix C.1. For the rest of the runs in the verification studies on a single floater, ramping and Rayleigh damping is always included in order to assure stable runs.

4.2.2 Time-Step Study of Heave RAO

A time-step study of the single floater model RAO in heave is performed. The mooring-lines are removed, so that the resulting RAO should follow the ZFT RAO in Equation (2.72). A set of 80 kR values in the range 0.01 to 11 are run, the amount of points being denser near the value corresponding to the natural frequency in heave, kR_n. RAO values from each kR run are found by dividing the single-sided spectrum peak of the heave modal amplitude time-series by the incoming wave amplitude ζ_a. The Fourier transform is taken for a stable range of the time-series, from *stable-time* to *end-time*. To find such a stable region, a wave condition at kR_n is run to assure that it is stable even when the incoming circular wave frequency coincides with the natural frequency in heave. A time-series illustrating this is added in Appendix C.2.

Table 4.4 presents the parameter values used in the runs. The wave period T_ω is of course set by the specific kR number for a run. Do also notice that a constant wave amplitude ζ_a is used, so that the tested waves do not have the same steepness. The largest will be $H/\lambda = \zeta_a kR/(\pi R) \simeq 0.014$ for $kR = 11$.

Table 4.4: Parameter values - time step study for heave RAO

vertical modes	ζ_a [m]	dt [s]	ξ [%]	end-ramp [s]	stable-time [s]	end-time [s]
0	0.1	$0.0005 - 0.2$	1	$100 \cdot T_w$	$150 \cdot T_w$	$200 \cdot T_w$

We see from Figure 4.4 that the resulting RAOs are all seemingly identical to ZFT, except from close to kR_n. Here, they are damped due to the fact that Rayleigh damping is included. The damping effect seems somewhat large considering the damping ratio is set to 1% only. We see that there is increased damping for increased time-step. There seems to be a convergence for $dt = 0.005$ s, and for this time-step the peak matches kR_n perfectly. This time-step will therefore be used in the rest of the vertical mode studies.

(a) Full kR range
(b) Zoomed in around kR_n
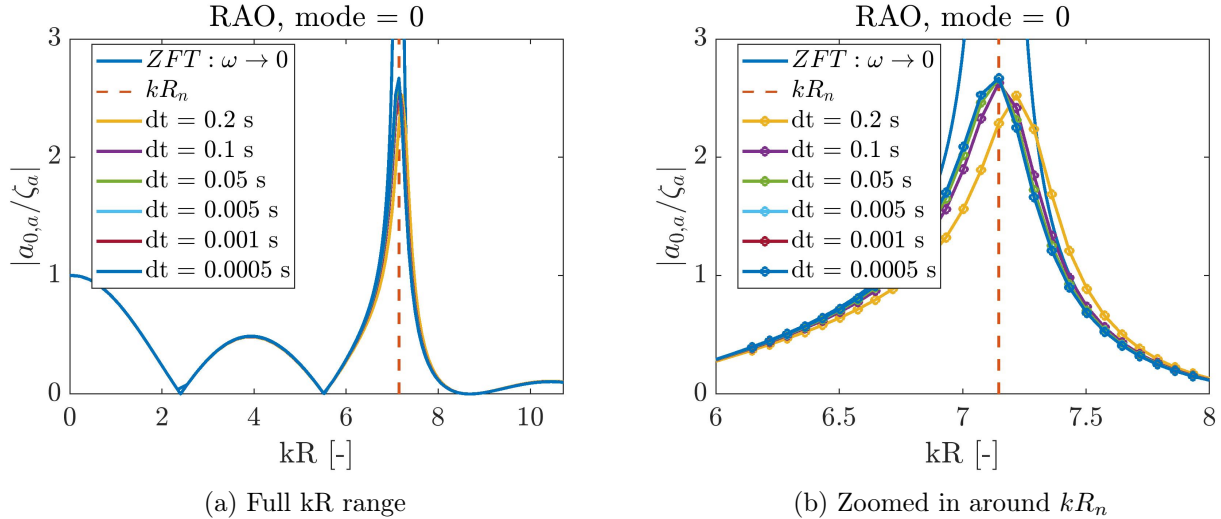
Figure 4.4: Time-step study of heave RAO
Numerical RAO's in heave for a single floater using different time-steps ranging from $dt = 0.2$ to 0.0005 s are shown. These are plotted against the corresponding theoretical ZFT RAO, and the theoretical kR value at natural frequency in heave, kR_n, is marked by a stippled line. Figure a) shows the full kR-range tested, while figure b) is a zoomed in version showing the details around kR_n. Rayleigh damping $\xi = 1\%$ is used in the numerical runs.

4.2.3 Vertical Mode RAOs

In this subsection, resulting RAOs for vertical modes of a single floater without mooring-lines will be presented, and compared to ZFT. Damping ratios of both 1,2 and 3% are tested. Parameter values listed in Table 4.5 are used in the runs. Each run has only one mode activated, so that the vertical modes are studied separately.

Table 4.5: Parameter values - vertical mode RAOs

ζ_a [m]	dt [s]	ξ [%]	end-ramp [s]	stable-time [s]	end-time [s]
0.1	0.005	1, 2, 3	$200 \cdot T_w$	$300 \cdot T_w$	$350 \cdot T_w$

RAOs for heave. pitch and the 1st flexible mode are shown in Figure 4.5. Detailed plots of the area near the kR corresponding to the natural frequency in the specific mode n, kR_n are also included. As seen, the numerical RAOs are seemingly identical to the ZFT RAOs, except for the area near kR_n, where they are damped. Increased damping lowers the peaks, as it should. Increased damping also shifts the peaks to the left in heave, which is in accordance with simple harmonic oscillator theory, the damped natural frequency being lower than the un-damped. One may notice that the numerical results do not match perfectly with the kR_n values for mode 2 and 3, even for Rayleigh damping of 1%. This difference is however quite low and all in all the results are seen as satisfactory.

(a) Heave RAO

(b) Heave RAO -zoomed in around kR_n

(c) Pith RAO

(d) Pitch RAO - zoomed in around kR_n

(e) 1st flexible RAO

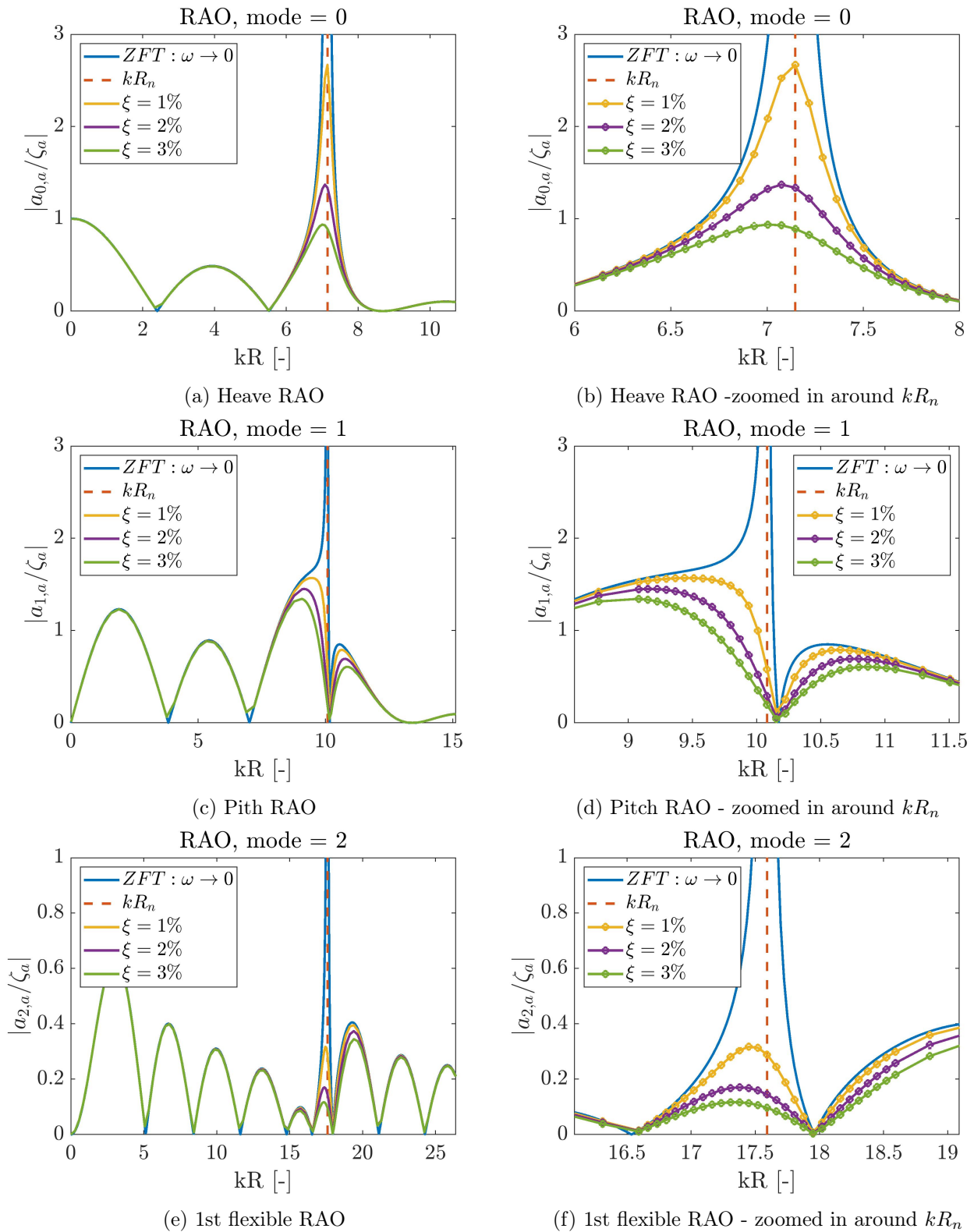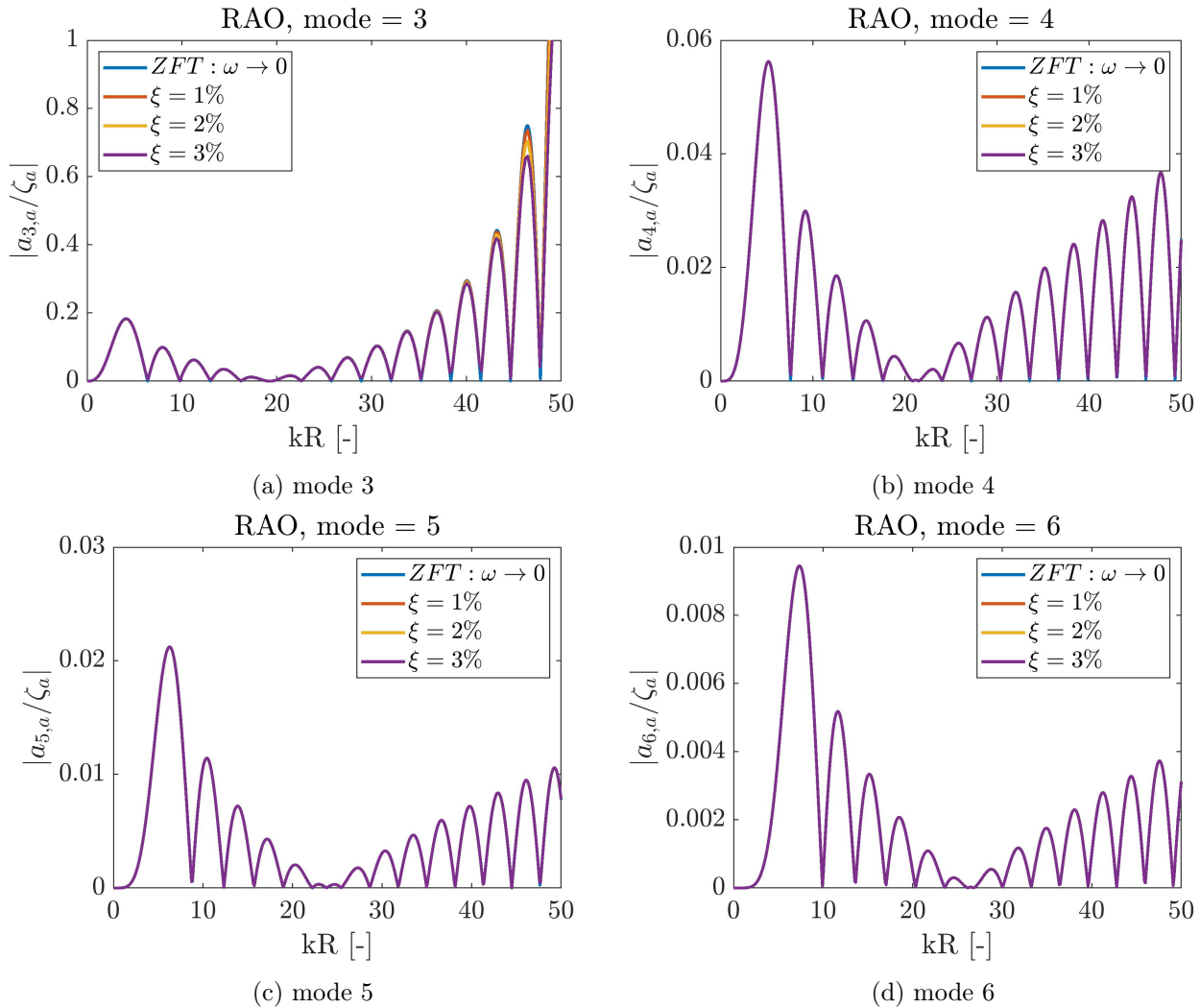(f) 1st flexible RAO - zoomed in around kR_n

Figure 4.5: RAOs for the 3 first vertical modes
Numerical RAO for a single floater without trusses, plotted against the corresponding theoretical ZFT RAO, for both heave, pitch and first flexible vertical mode. The theoretical kR value at natural frequency in mode n, kR_n, is marked by a stippled line. Both the full kR-range tested and zoomed in version showing the details around kR_n are included for all modes. Rayleigh damping of $\xi = 1, 2$ and 3% are used in the numerical runs.

Figure 4.6 shows the resulting RAOs for the modes $3 - 6$, from runs of 500 kR-values in the range $0.01 - 50$. The natural frequencies in these modes correspond to such large kR-values that they are not included in this range and are not of interest. For mode 3 we see some influence to the right in the

plot, as this is close to kR_n for this mode. For the rest of the modes, there is full accordance between the numerical results and ZFT. Similar plots for modes $7 - 20$ are added in Appendix C.3, and also show good accordance with ZFT.

(a) mode 3

(b) mode 4

(c) mode 5

(d) mode 6

Figure 4.6: RAO's for vertical modes 3 to 6
Numerical RAO's for a single floater without trusses, plotted against the corresponding theoretical ZFT RAO, for vertical modes $3 - 6$. Rayleigh damping of $\xi = 1, 2$ and 3% are used in the numerical runs.

All in all, the results from the vertical motion study of the single floater are satisfactory. Though RAOs with mooring-lines are not run, we have seen from the time-series in Section 4.2.2 that there is reasonable tension behaviour.

4.3 Surge Motion of Single Floater

In this section, the verification study of the single floater with surge motion will be presented.

4.3.1 Trusses vs Theoretical Mooring Stiffness Term

In this subsection, we compare results using trusses to model the mooring-lines of the floater versus using the mooring-line stiffness expression in Equation (2.76) to include an additional stiffness force $-C_{11}\eta_1$ in the equation of motion for surge, Equation (2.46). The latter option means that one can just update the nodal acceleration directly from the modal equation of motion, as there is no need to solve for unknown tension. However, we will still calculate the distance from the floater-nodes to the

mooring-nodes, so that we get the length of the "virtual" truss that is expressed through the stiffness term. The parameter values used in the runs are listed in Table 4.6.

Table 4.6: Parameter values - trusses vs C11-term Test

ζ_a [m]	k_m [N/m]	l_m [m]	dt [s]	ξ [%]	end-ramp [s]	end-time [s]
1	$35.9 \cdot 10^3$	100	0.005	3	$50 \cdot T_w$	$100 \cdot T_w$

Figure 4.7 shows the resulting x-position of floater nodes by use of the numerical solar island model, and by the mooring-stiffness term alternative. As seen, the methods give almost identical results. This indicates that the trusses behave as they should in surge motion, they give the wanted influence on the motion of the floater-nodes. We also notice that all floater-nodes have the same motion, as it should be in surge motion as the whole floater moves as a rigid body.

(a) Floater node 1 x-position

(b) Floater node 2 x-position

(c) Floater node 3 x-position

(d) Floater node 4 x-position
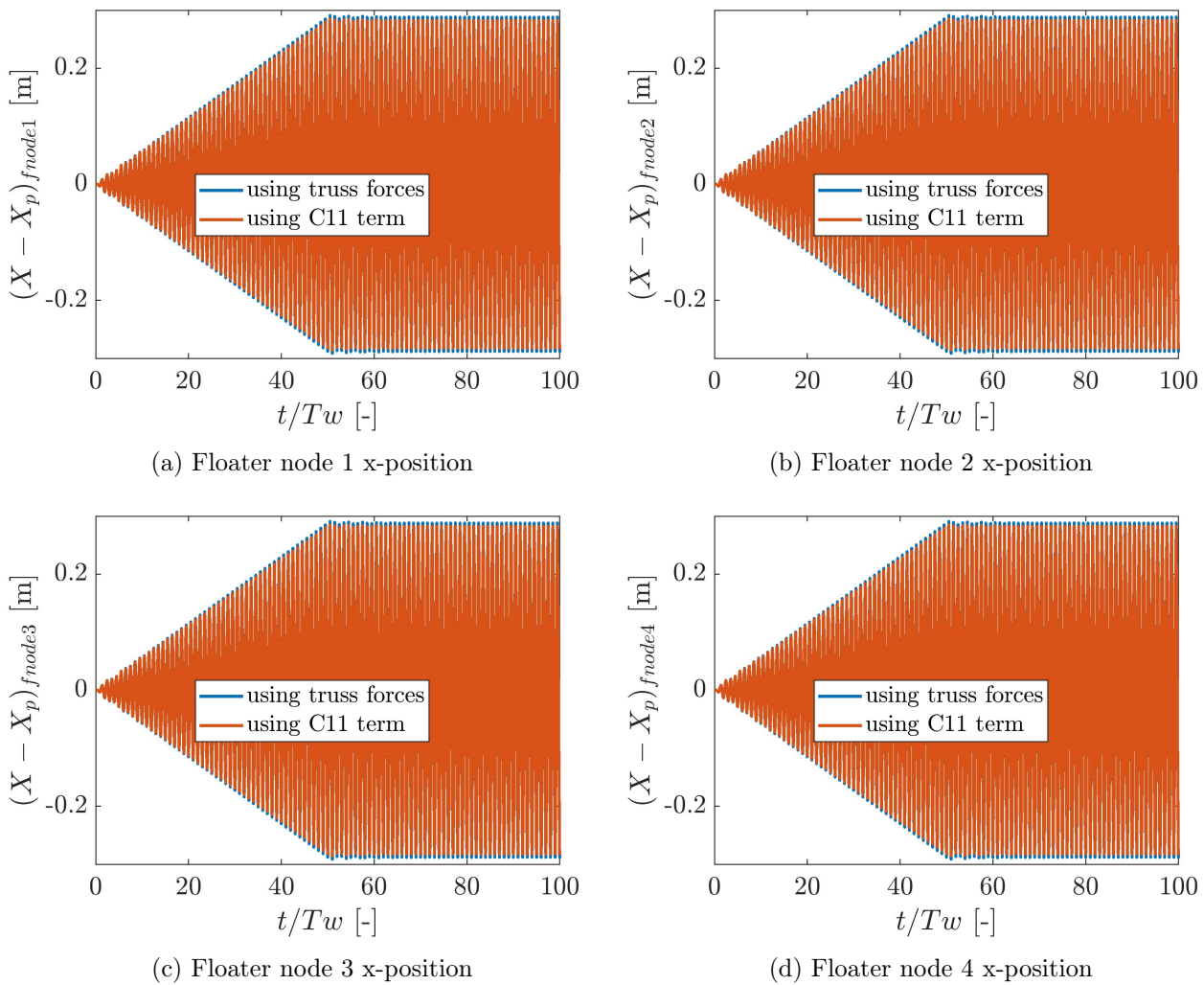
Figure 4.7: Truss Forces vs Stiffness Term
Time-series for x-position of floater-nodes. $X - X_p$ is the difference in x-position X from the position X_p in the initial, pre-tensioned set-up. Each plot includes the resulting time-series from using truss forces (solar island model), and replacing the truss-forces with an additional stiffness force in the equation of motion in surge, $-C_{11}\eta_1$.

4.3.2 Time-step Study of Surge RAO

A time-step study of the surge RAO of the single, moored floater is conducted. A range of time-steps are studied, from $dt = 0.1$ to 0.001 s. The kR-range is concentrated around the natural frequency for

the floater in this mode, $kR_n \simeq 0.75$. The parameter values used in the runs are are listed in Table 4.7.

Table 4.7: Parameter values - time step study of surge RAO

ζ_a [m]	k_m [N/m]	l_m [m]	dt [s]	ξ [%]	end-ramp [s]	stable-time [s]	end-time [s]
0.1	$35.9 \cdot 10^3$	100	$0.001 - 0.1$	1	$150 \cdot T_w$	$200 \cdot T_w$	$250 \cdot T_w$

Figure 4.8 shows the resulting RAOs for the different time-steps used, plotted against the theoretical RAO. The latter is calculated form Equation (2.77). As seen, the RAOs are seemingly identical, exept for in the area near kR_n, where the numerical RAO is damped. We observe that the peak is somewhat shifted to the right compared to the ZFT peak. This is quite a small difference, and we must also keep in mind that the influence of the pre-tension is not included in the theoretical RAO. Further, as for the heave RAO, increased time-step increases the damping of the peak. The results from time-steps $dt = 0.005$ and $dt = 0.001$ are very close, and lower time-steps are not tested due to the long run-time. A time-step of $dt = 0.005$ gave convergence for the heave RAO case, and from the surge RAO also seems to be sufficient enough, just giving a somewhat smaller peak tan $dt = 0.001$ s. It will therefore be used in the rest of the surge motion verification studies for the single, moored floater.

(a) Full kR range

(b) Zoomed in around kR_n
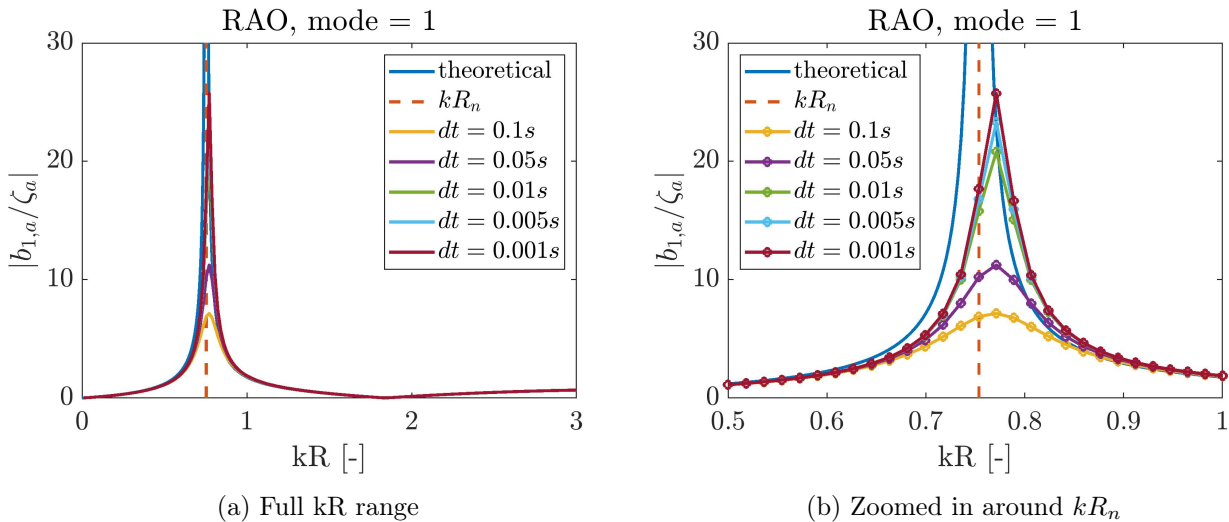
Figure 4.8: Time-step study of surge RAO
Numerical RAOs in surge for the single, moored floater using different time-steps ranging from $dt = 0.1$ to 0.001 s are shown. These are plotted against the theoretical RAO, and the theoretical kR-value at natural frequency in surge, kR_n, is marked by a stippled line. Figure a) shows the full kR-range, while figure b) is a zoomed in version around kR_n. Rayleigh damping $\xi = 1\%$ is used in the numerical runs.

4.3.3 RAOs in Surge

RAOs in surge for the single, moored floater are run for three different values of Rayleigh damping, $\xi = 1, 2$ and 3%. The parameter-values used are listed in Table 4.8. The mooring-stiffness has been lowered to get a more realistic natural period in surge of 30 s.

Table 4.8: Parameter values - time step study of surge RAO

ζ_a [m]	k_m [N/m]	l_m [m]	dt [s]	ξ [%]	end-ramp [s]	stable-time [s]	end-time [s]
0.1	$35.9 \cdot 10^3$	100	0.005	$1 - 3$	$150 \cdot T_w$	$200 \cdot T_w$	$250 \cdot T_w$

Figure 4.9 shows the resulting RAOs, plotted against the theoretical RAO in surge. First of all, the peak value is decreasing with increased Rayleigh damping, as it should be. Secondly, we observe that

the peak is somewhat shifted to the right, for all the three different damping values. This does not represent a large mismatch in natural frequency, and we also keep in mind that the theoretical RAO does not take into account the pre-tension of the mooring-lines. All in all, the implementation of surge motion for a single moored floater is thought to be successful.

It should be mentioned that the natural frequency in surge is quite high with the applied mooring-stiffness value for this single floater case, and is more appropriate for the multi-torus case. The effect on the theoretical RAO when lowering the mooring-line stiffness is shown in Figure D.1b. When the mooring-line stiffness decreases, the natural frequency decreases and the peak shifts to the left.

(a) Full kR range

(b) Zoomed in around kR_n
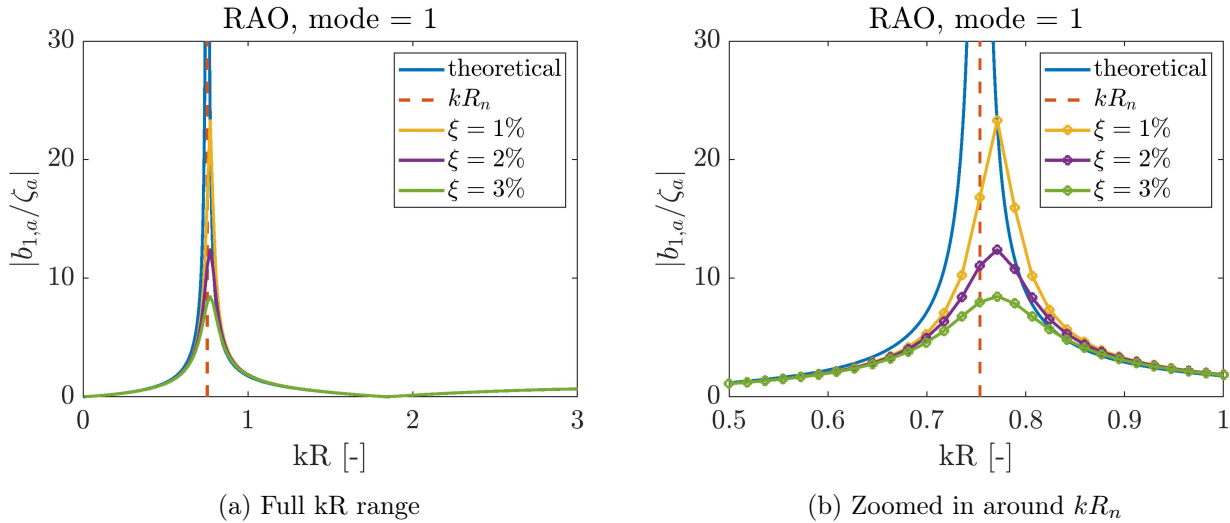
Figure 4.9: Damped RAOs in surge
Numerical RAOs in surge for a single, moored floater using different values for Rayleigh damping ξ, plotted against theory, The theoretical kR value at natural frequency in surge, kR_n, is marked by a stippled line. Figure a) shows the full kR-range, while figure b) is a zoomed in version around kR_n.
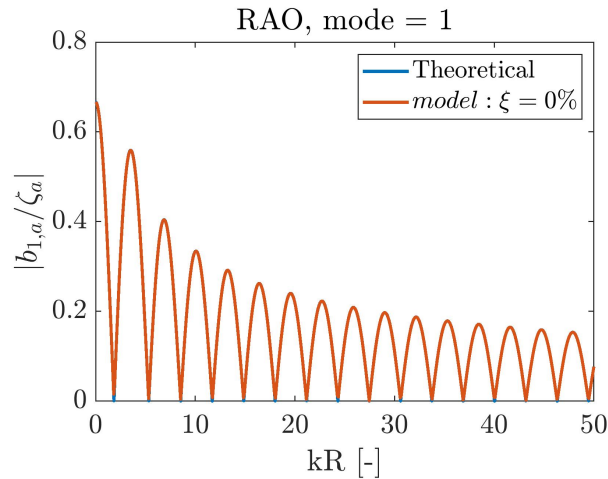
Figure 4.10: RAO in surge without mooring-lines
Numerical RAO in surge for a single floater without mooring-lines is plotted against the corresponding theoretical RAO. No Rayeligh damping is used.

A RAO is also run for the case of no mooring-lines. The truss-forces are then turned off, and the node accelerations found directly from the floater equations. Since there is no natural frequency in surge for this case, the Rayleigh damping is set to 0. The result is shown in Figure 4.10, and the theoretical RAO is also plotted. The latter is then calculated form Equation (2.77), but the mooring-stiffness term C_{11} is set to zero. The numerical result is seen to be identical to the theoretical, indicating that the floater equations (without truss-forces) are implemented correctly.

4.4 Radial Motion of Single Floater

The verification study for the single floater with radial motion is presented in this section.

4.4.1 Time-step Study of First Flexible Lateral Mode RAO

A time-step study is performed for the first flexible lateral mode, radial mode 2, for the single floater with no mooring-lines. The parameter-values used are listed in Table 4.9.

Table 4.9: Parameter values - time step study of 1st flexible lateral mode RAO

ζ_a [m]	dt [s]	ξ [%]	end-ramp [s]	stable-time [s]	end-time [s]
0.1	$0.1 - 0.001$	1	$150 \cdot T_w$	$200 \cdot T_w$	$300 \cdot T_w$

The resulting RAOs for the different time-steps are plotted together and against the theoretical RAO for this mode. The latter is calculated by Equation (2.78). The result is seen in Figure 4.11. We observe that to the left of kR_n, increased time-step gives slightly increased damping, while to the right it gives slightly increased damping. Furthermore, there seems to be a convergence at $dt = 0.01$ s, so a time-step of $dt = 0.005$ s, which was found to be fitting for vertical modes and surge, is thought to be a good choice for the radial modes as well, and will be used for the rest of the radial mode runs.

(a) Full kR range   (b) Zoomed in around kR_n
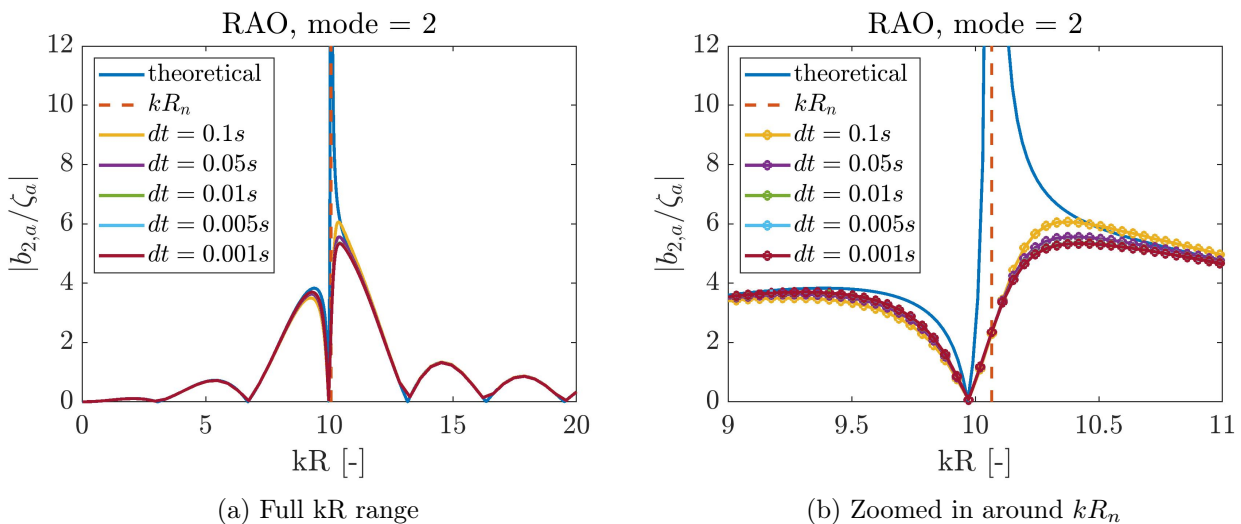
Figure 4.11: Time-step study of 1st flexible lateral mode RAO
Numerical RAOs in 1st flexible lateral mode, radial mode 2, for a single floater using different time-steps ranging from $dt = 0.1$ to 0.001 s are shown. These are plotted against the corresponding theoretical RAO, and the theoretical kR value at natural frequency, kR_n, is marked by a stippled line. Figure a) shows the full kR-range, while figure b) is a zoomed in version around kR_n. Rayleigh damping $\xi = 1\%$ is used in the numerical runs.

All radial modes above 2 have natural frequency corresponding to kR_n larger than 50, which is not a range of interest. It should however bee noted should one want to study the resulting RAOs also in this area, the time-step must be significantly reduced in order to obtain a proper amount of points during a wave period. As an example, a time-step of $dt = 0.0005$ s improves the RAO for mode 20 significantly compared to using $dt = 0.005$s. This is illustrated in Figure D.2.

4.4.2 Radial Mode RAOs

RAOs for radial modes in the range $2 - 20$ are next studied. Damped RAOs using damping ratios of 1 and 3% are obtained from runs in MATLAB for the single floater without mooring-lines, and also RAOs for the case that the floater is moored, using damping ratio 1%. A kR-range of $0.01 - 50$ is run,

consisting of 500 points for the moored case, and somewhat more for the floater-only case. Each mode is studied separately, so there is only one mode activated in each run. The parameter-values used are listed in Table 4.10.

Table 4.10: Parameter values - Radial RAOs

ζ_a [m]	k_m [N/m]	l_m [m]	dt [s]	ξ [%]	end-ramp [s]	stable-time [s]	end-time [s]
0.1	5325	100	0.005	1, 3	$150 \cdot T_w$	$200 \cdot T_w$	$300 \cdot T_w$

Figures 4.12a and 4.12b show the resulting RAO for radial mode 2 of the single floater without mooring-lines, plotted against the theoretical RAO. Increased Rayleigh damping is seen to give increased damping, and there is generally good accordance with the theoretical RAO. Figures 4.12c and 4.12d show the resulting RAO for the case with mooring-lines, plotted against the corresponding theoretical RAO as well as the resulting RAO for the case without mooring-lines at the same damping level. We observe that some distance away from kR_n, the RAO is unaffected by the mooring-lines, there is a good match. Near the peak, however, we see a spike, a larger value for the case with mooring-lines. The moored RAO values are even larger than the theoretical RAO for some kR-values. We keep in mind that the theoretical RAO does not include stiffness or pre-tension effects from the mooring-lines. The truss-forces in radial direction are quite large compared to in vertical direction, so such a deviance from the theoretical RAO is not unreasonable.

RAO plots for radial modes $3 - 10$, for the single floater without mooring-lines, are added in Appendix D.3. The natural kR value for these modes all lie above $kR = 50$, and for the studied range the RAOs are practically identical to the theoretical RAO.

(a) without mooring-lines, full kR range

(b) without mooring-lines, zoomed in around kR_n

(c) With vs. without mooring-lines, full kR range

(d) With vs. without mooring-lines, zoomed in around kR_n
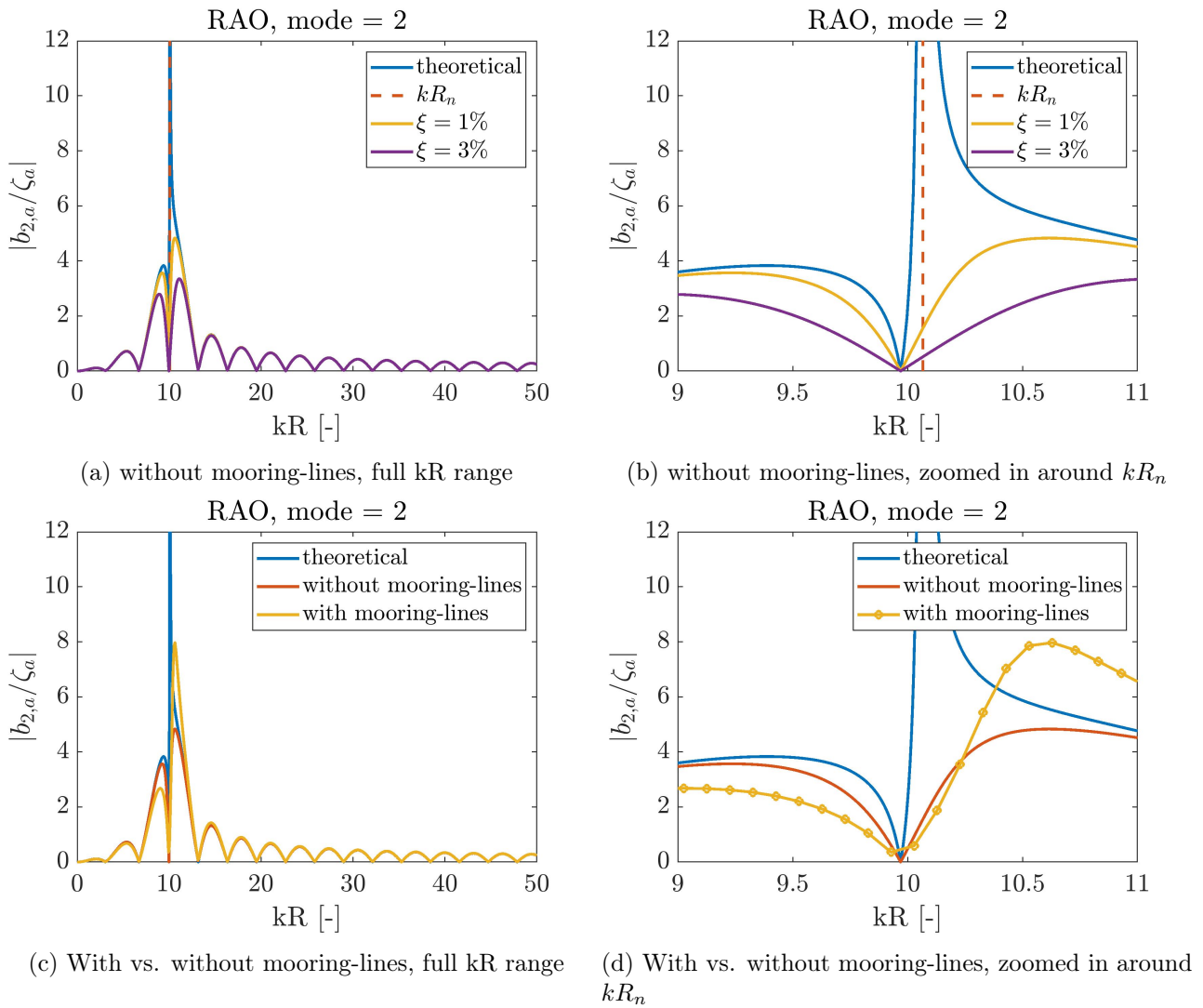
Figure 4.12: RAOs for the first flexible lateral mode

Figure a) shows the resulting RAOs for the 1st flexible lateral mode, radial mode 2, for the single floater without mooring-lines, for Rayleigh damping values of 1 and 3%, plotted against the theoretical RAO. Figure b) is the same plot, just zoomed in around kR_n. Figure c) shows the resulting RAO for a single floater with mooring-lines with Rayleigh damping of 1% applied. The corresponding RAO for the case without mooring-lines is also plotted, as well as the theoretical RAO. Figure d) is the same plot as c), just zoomed in around kR_n.

Figure 4.13 shows the resulting RAOs with and without mooring-lines for radial modes $3-8$, plotted against the corresponding theoretical RAO. Except for modes 4 and 8, both the moored and un-moored case fit the theoretical RAO extremely well. For mode 4 and 8, the RAO without mooring-lines fits the theoretical RAO, while the one with mooring-lines included lies at a much higher, constant value. The results for modes $9-20$ are added in Appendix D.4. Here, the same strange result is seen for modes 12, 16 and 20. This will be studied more in detail in the next subsection.

(a) Mode 3

(b) Mode 4

(c) Mode 5

(d) Mode 6

(e) Mode 7

(f) Mode 8
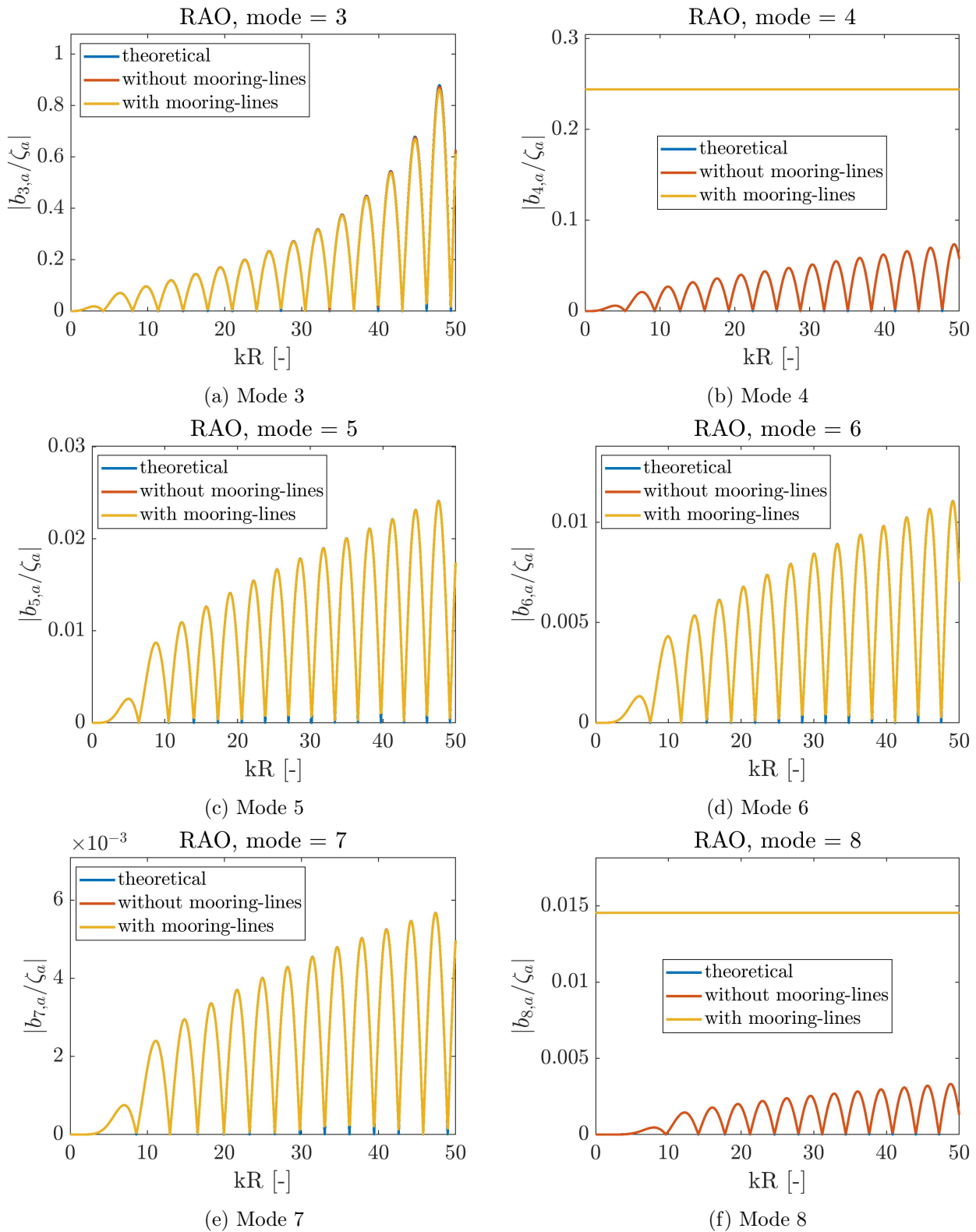
Figure 4.13: Radial mode 3-8 RAOs - with vs without mooring-lines
Resulting numerical RAOs for the single floater, run both with and without mooring-lines. A Rayleigh damping value of 1% is used. The corresponding theoretical RAO is also plotted.

4.4.3   Problem With Modes Divisible by Four

From the resulting RAOs, there is clearly a problem with radial modes $4, 8, 12, 16$ and 20 for the single floater with mooring-lines. These are all modes divisible by four. The problem is further studied by looking at the radial modal amplitude and generalized radial truss force time-series for a specific wave-condition, with parameter-values listed in Table 4.11 used for the run.

Table 4.11: Parameter values - radial mode time-series

ζ_a $[m]$	T_w $[m]$	k_m $[N/m]$	l_m $[m]$	dt $[s]$	ξ $[\%]$	end-ramp $[s]$	end-time $[s]$
0.1	$\sqrt{g}$	5325	100	0.005	1	$150 \cdot T_w$	$300 \cdot T_w$

Figure 4.14a shows the resulting radial mode amplitude time-series. We immediately observe that mode 4 has an impulse-like behaviour from the very start, and oscillates at a level of about 0.025 m. This is certainly not the wanted or expected behaviour. Most of the modes oscillate about zero, and slowly build up during the ramping of the wave-excitation force, which is the expected behaviour. In Figure 4.14b one has zoomed in on the two first wave-periods in the time-series, and also focused on what happens closer to the time-axis. As seen, modes $8, 12, 16$ and 20 all have the same impulse-like behaviour as mode 20, oscillating at positive, non-zero levels.

Now, what is the reason for the strange behaviour of the radial modes divisible by four? The answer is related to the generalized radial truss force expression in Equation (2.45) as well as the specific mooring-truss configuration used, illustrated in Figure 4.1. In the truss-integral, the term $\cos(n\beta_{ft}) = 1$ for all truss positions $\beta_{ft} = 0, \pi/2, \pi$ and $3\pi/2$ for modes n divisible by four. In addition, the start configuration of the trusses makes it so that the truss-force contribution at start, $\gamma_{ft} T_{ft}(\boldsymbol{s}_{ft} \cdot \boldsymbol{r}) = T_{ft}$ for all the trusses ft. By this, we get maximum generalized radial truss force from the very start. This is indeed seen in the time-series of the generalized radial truss forces, added in Appendix D.5. It is identical for all the modes divisible by four, oscillating at a level near 4000 N from the very start. The rest of the modes oscillate around zero. This explains the impulse-like behaviour in mode-amplitude for the modes divisible by four, and why they oscillate at positive non-zero levels throughout the time-series.

It is interesting to see the effect of lowering the pre-tension in the mooring-trusses. The same case is therefore run with a pre-tension of $T_{pm} = 781.25$ N, which is 100 times lower than the initial run. The resulting plots are added in Appendix D.5. Though the resulting mode-amplitude time-series appears much better, with no impulse behaviour seen with the mere eye, the same problem is in fact seen when studying a zoomed-in version of the plot. Radial modes divisible by four are still oscillating at positive non-zero levels, just with smaller amplitudes and closer to the time-axis. It is therefore decided to stick with radial modes 2 and 3 only in future runs, to avoid potential problems arising when when including mode 4.
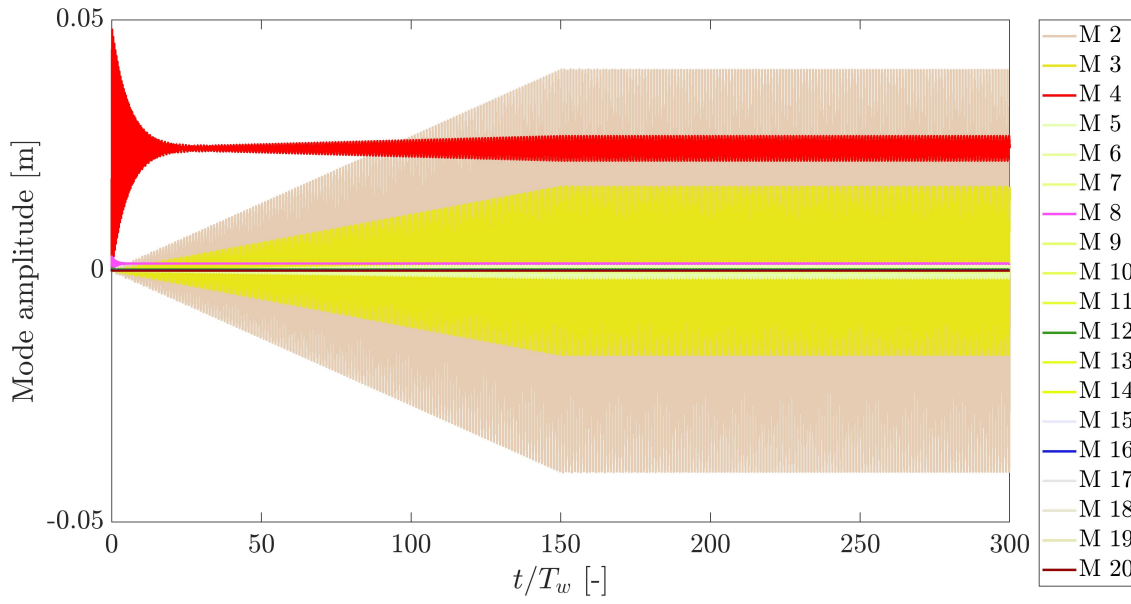
(a)
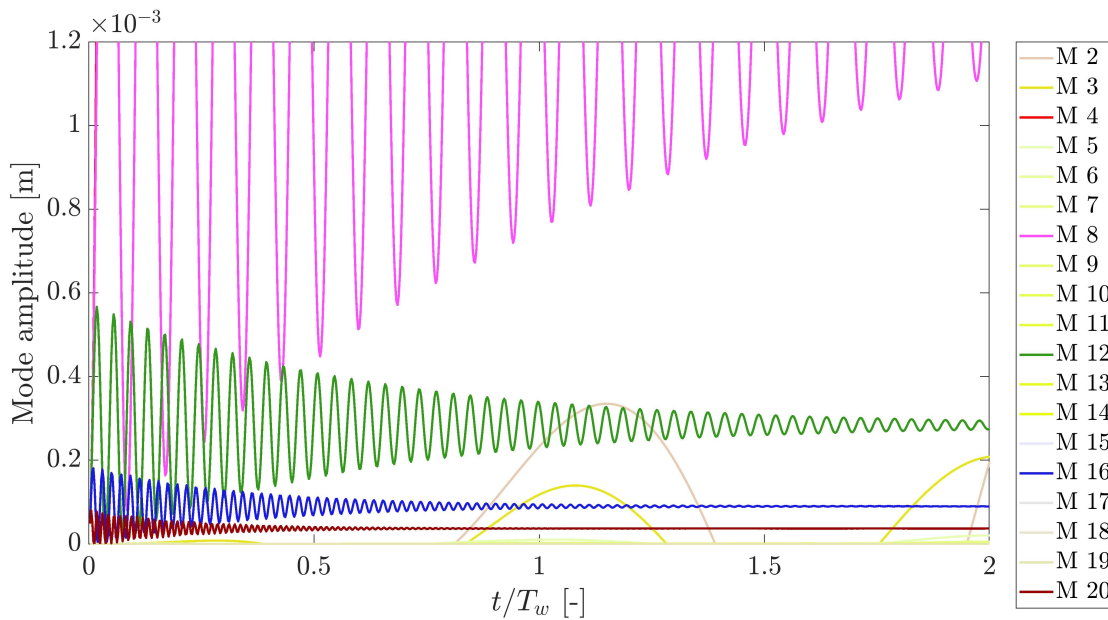
(b)

Figure 4.14: Mode Amplitude Problem
Mode amplitude time-series are plotted for radial modes $M = 2 - 20$. Figure a) shows the full time-series, while b) is zoomed in version of the same plot, the mode amplitude axis shortened to $0 - 1.2 \cdot 10^{-3}$ m and the time-axis to $0 - 2$. A pre-tension of $Tpm = 78125$ N is used.

4.5 Combined Motion of Single Floater

Having studied vertical and lateral modes separately, the next step is to test a single, moored floater with combined modes. The case of surge, heave and radial mode 2 activated is therefore studied. Three different cases of wave frequencies are tested in order to see if the resulting time-series seem reasonable. These are $T_w \approx 1.675, 1.988$ and 0.698 s. The first is the natural frequency in heave, the second to the natural frequency in radial mode 2, while the third corresponds to a more realistic wave condition with wave period of 9 s. The parameter values used in all three runs are listed in Table 4.12. Though a wave condition corresponding to the natural frequency in surge is not tested, it should be mentioned that it is 0.209 rad/s.

Table 4.12: Parameter values - combined mode cases

ζ_a [m]	k_m [N/m]	l_m [m]	dt [s]	ξ [%]	end-ramp [s]	end-time [s]
0.1	5325	100	0.005	3	$100 \cdot T_w$	$200 \cdot T_w$

4.5.1   Case 1 - Natural Frequency in Heave

The natural frequency in heave is found from Equation (2.81) and is 1.675 rad/s. The resulting node motion time-series for the four floater-nodes using this as the incoming wave frequency are presented in Figure 4.15. Heave clearly dominates, as expected at this wave frequency. The amplitude of the z-motion is close to the incoming wave amplitude, $\zeta_a = 0.1$ m. Further, nodes 1 and 3 do not have any motion in y-direction, as it should be for the activated modes. The motion in x-direction for these nodes are from a combination of surge and the first flexible lateral mode. The difference in x-motion amplitude is thought to come from the interaction between surge and the first flexible radial mode. Lastly, nodes 2 and 4 have identical motion, where radial mode 2 for these nodes only gives motion in y-direction.

Time-series for truss-tension, as well as mode amplitudes are added in Appendix E, and also give satisfying results. The tension is in accordance with node-motions, and the mode-amplitudes are stable. All in all, this case is thought to give reasonable results.
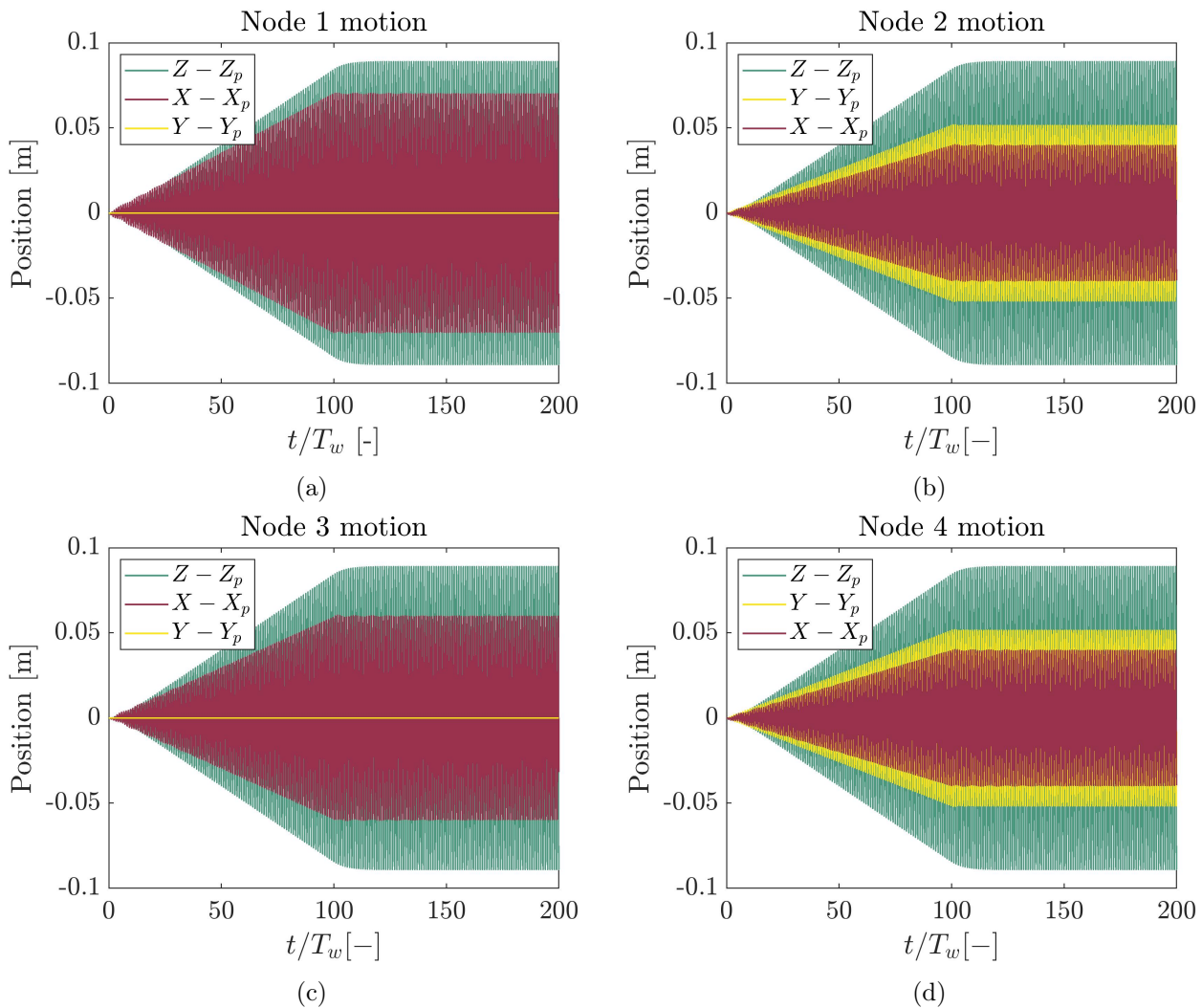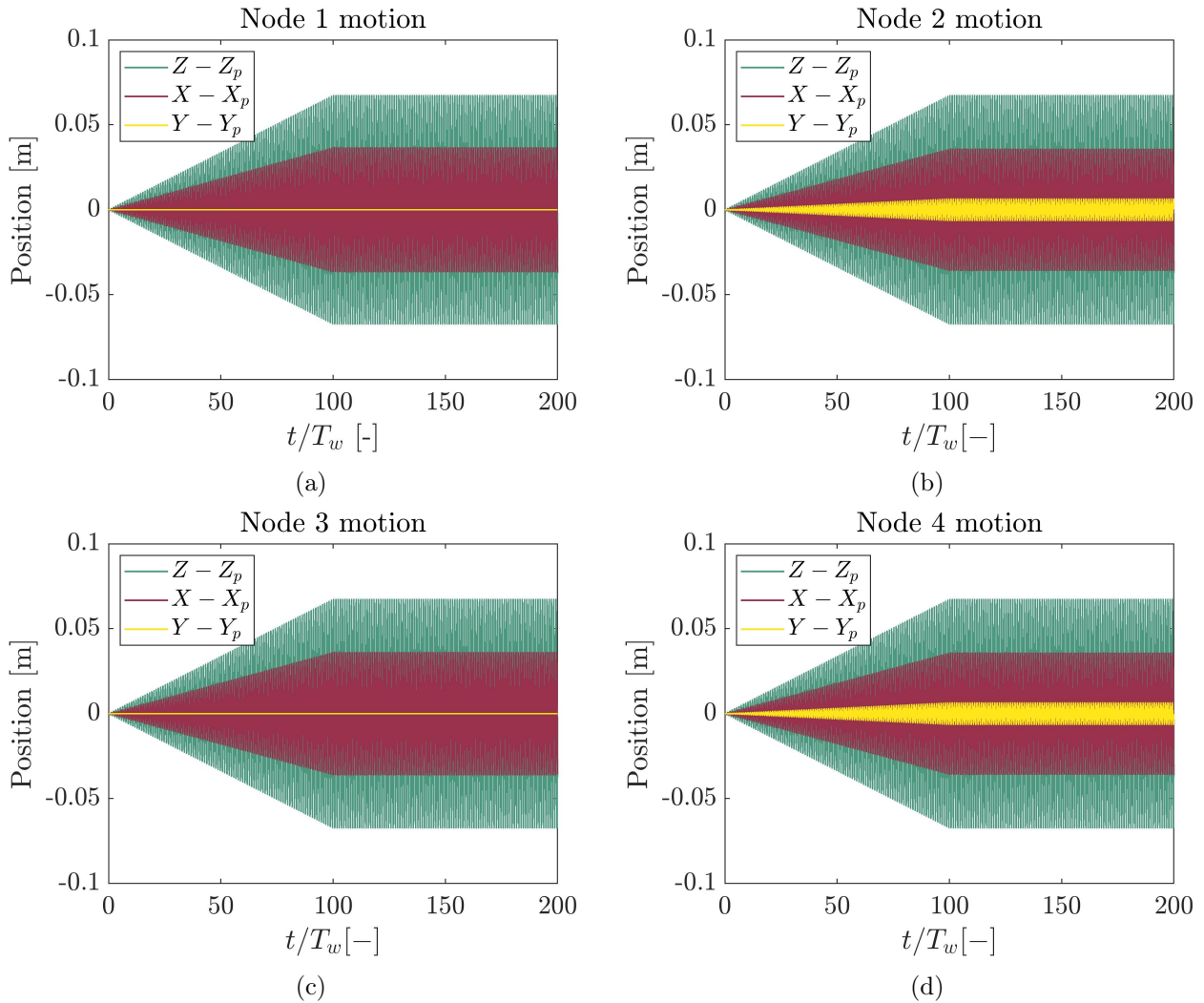

Figure 4.15: Node motion for combined mode case 1
Node motion time-series for the four floater-nodes of a single, moored floater. X, Y and Z are the x,y and z-position of a node, while X_p, Y_p and Z_p are the corresponding initial positions for the pre-tensioned floater.

4.5.2 Case 2 - Natural Frequency in Radial Mode 2

The natural frequency in radial mode 2 is found from Equation (2.83) and is 1.988 rad/s. The resulting node-motion time-series using this as the incoming wave frequency are shown in Figure 4.16. The motion is now largest in x and y-direction, which means that radial mode 2 is dominating, as one would expect for this wave condition. Other than this, the general expected behaviour discussed for case 1 are still seen; the z-displacement is identical for all nodes since heave is the only vertical mode included, nodes 2 and 4 have identical motion and there is no motion in y-direction for nodes 1 and 3. The x-displacement amplitude is still larger for node 1 than node 3, likely because of the interaction between surge and radial mode 2.

Time-series for truss-tension as well as mode-amplitudes are added in Appendix E. The tension in the trusses follow the node-motions, and the mode amplitudes are all stable. With this, the results from the tested case seem reasonable all over.
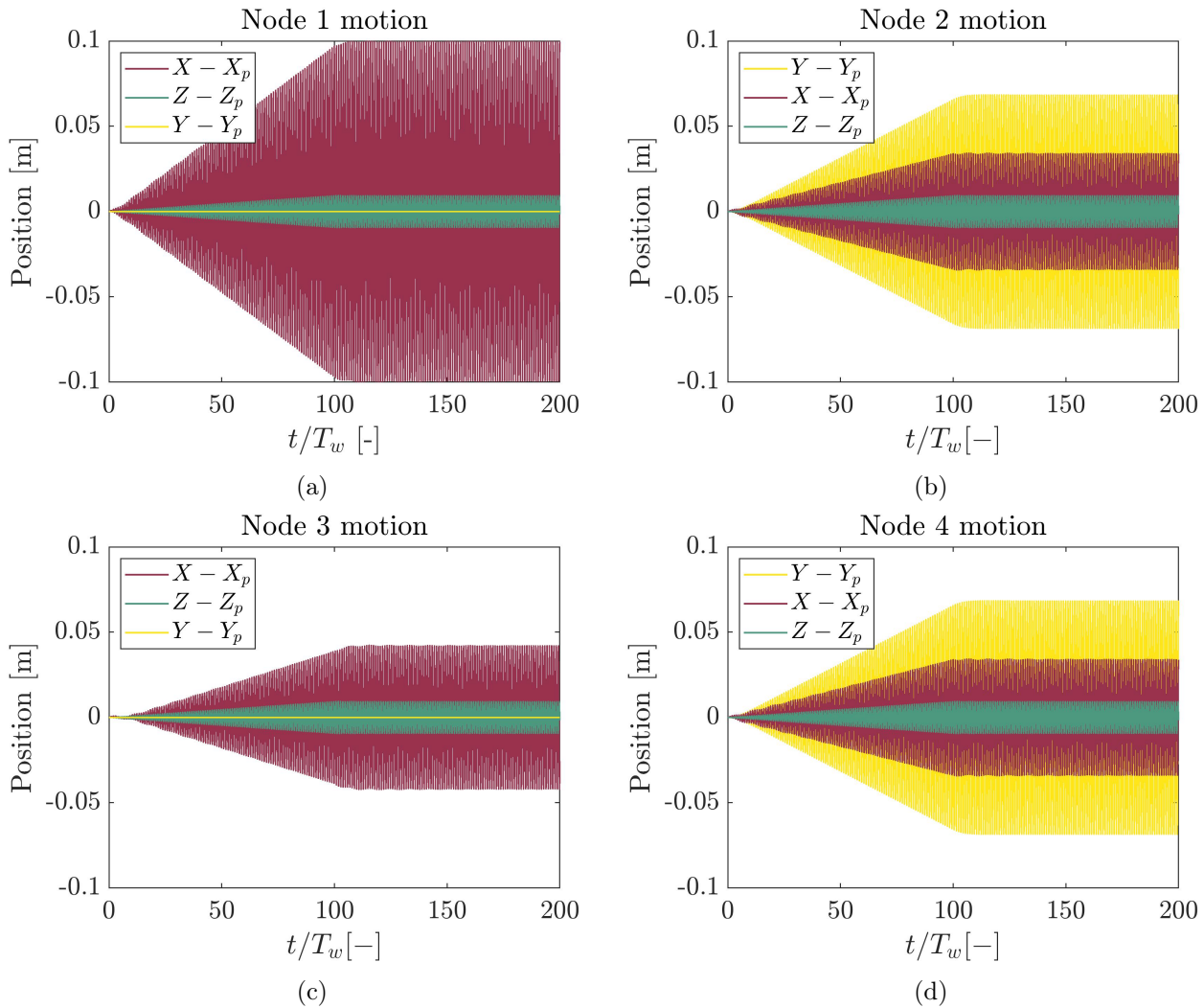
Figure 4.16: Node motion for combined mode case 2
Node motion time-series for the four floater-nodes of a single, moored floater. X, Y and Z are the x,y and z-position of a node, while X_p, Y_p and Z_p are the corresponding initial positions for the pre-tensioned floater.

4.5.3 Case 3 - Relevant Wave Frequency

Figure 4.17 shows the resulting node-motion time-series for the case of an incoming wave frequency of 0.698 s, which corresponds to a wave period of 9 s. This represents a realistic and relevant wave frequency, away from the natural frequencies of the floater in the activated modes. We observe quite identical motion for all nodes in both x and z-direction, and also y-motion for nodes 2 and 4 due to

radial mode 2. The difference in x-motion amplitude is no longer apparent between floater-nodes 1 and 3, which must simply mean that surge and radial mode 2 no longer interact in such a way that this happens. Put differently, that the floater is perfectly circular at both ends of maximum surge displacement.

Additional plots for truss-tension and mode amplitudes are added in Appendix E. These also show satisfactory behaviour of the floater. All in all, the results from this case are thought to be reasonable.

Figure 4.17: Node motion for combined mode case 3

Node motion time-series for the four floater-nodes of a single, moored floater. X, Y and Z are the x,y and z-position of a node, while X_p, Y_p and Z_p are the corresponding initial positions for the pre-tensioned floater.

4.6   Verification Study of Hydrodynamic Interaction Theory

In this section, verification studies on the hydrodynamic interaction theory in chapter 4 will be presented. First, the three-dimensional cross-coupled added mass in heave for a 2-torus case will be compared with previous results from WAMIT. Lastly, different mode combinations are tested for the same case in order to study whether off-diagonal terms become zero, as discussed in the derivation of the theory.

4.6.1   Comparing Cross-coupled Added Mass with WAMIT

The expression for the three-dimensional cross-coupled added mass in Equation (3.18) is implemented in MATLAB, so that the resulting values can be studied. The expression includes an inner integral of the type

$$\int \frac{1}{(a - b\cos\alpha)^{0.5}}\,d\alpha$$

where $a > b > 0$. This will involve elliptic integrals, and as it is not known how to solve this analytically, it is rather integrated numerically in MATLAB. A lowest order, basic numerical integration scheme is used.

Emilie Debernard performed a study on zero-frequency limit added mass coefficients on multi-torus models in WAMIT during the summer of 2019. We will compare our results with the ones she obtained for a 2-torus model in heave, with the outer torus radius being $R_1 = 25$ m, the inner being $R_2 = 20$ m and the cross-sectional radius of both tori being $c = 0.8$ m. Figure 4.18 shows her resulting added mass coefficients plotted for different distances $2p$ between the center-lines of the tori. The added masses are non-dimensionalized by the body mass of each torus, $M_t = \rho\pi^2 R_t c^2$. We digitize the two lines of interest, which are the added mass on the inner torus due to the outer torus and the added mass of the outer torus due to the inner torus. With our notations, these correspond to the cross-coupled added mass terms $A_{2,1,0}/M_2$ and $A_{1,2,0}/M_1$.
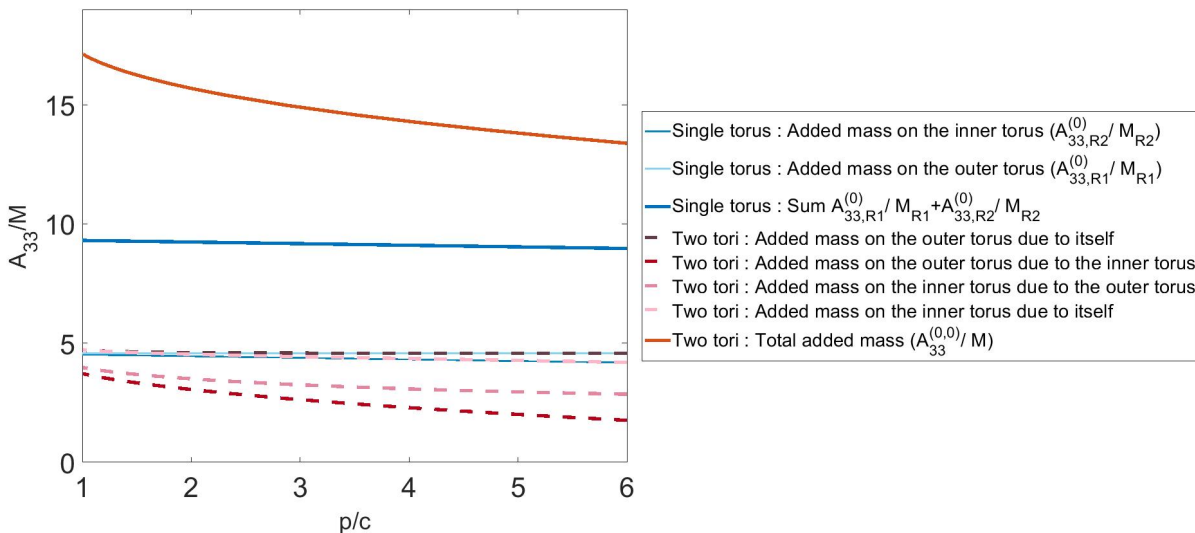
Figure 4.18: WAMIT computations for 2-torus model
Zero-frequency limit added mass coefficients due to forced heave of each torus in a 2-torus model. The radius of the outer torus is $R_1 = 25$ m, while the radius of the inner is $R_2 = R_1 - \frac{2p}{c}$ m. The cross-sectional radius is $c = 0.8$ m for both. The coefficients are non-dimensionalized by the body mass of each torus, $M_t = \rho\pi^2 R_t c^2$.
Courtesy of Emilie Debernard.

The exact same case is tested for the far-field theory expression, and plotted against the digitized data.

The result is seen in Figure 4.19. There is good accordance with WAMIT for the entire variation of spacing between tori.
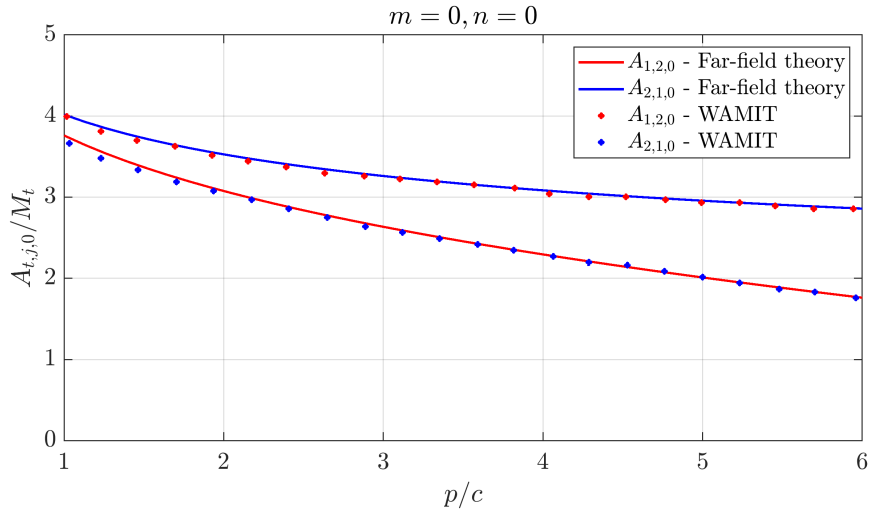
Figure 4.19: Non-dimensional cross-term heave added mass

Non-dimensional cross-term added mass in heave for a 2-torus case using far-field approach, plotted against WAMIT results. The radius of the outer torus is $R_1 = 25$ m, while the radius of the inner is $R_2 = R_1 - \frac{2p}{c}$ m. The cross-sectional radius is $c = 0.8$ m for both.

4.6.2 Studying Off-diagonal Added Mass Cross-terms

In the derivation of the hydrodynamic interaction theory, it is discussed that cross-term added mass is zero for $n \neq m$, that is, off-diagonal terms are zero. In order to verify this, all possible 16 combinations of the four lowest modes $n = 0, 1, 2, 3$ are tested for the same 2-torus geometry.

Figure 4.20 shows the results for all of the 16 tested combinations. As seen, only the diagonal terms are non-zero. This indicates clearly that off-diagonal added mass cross-terms can be set to zero.
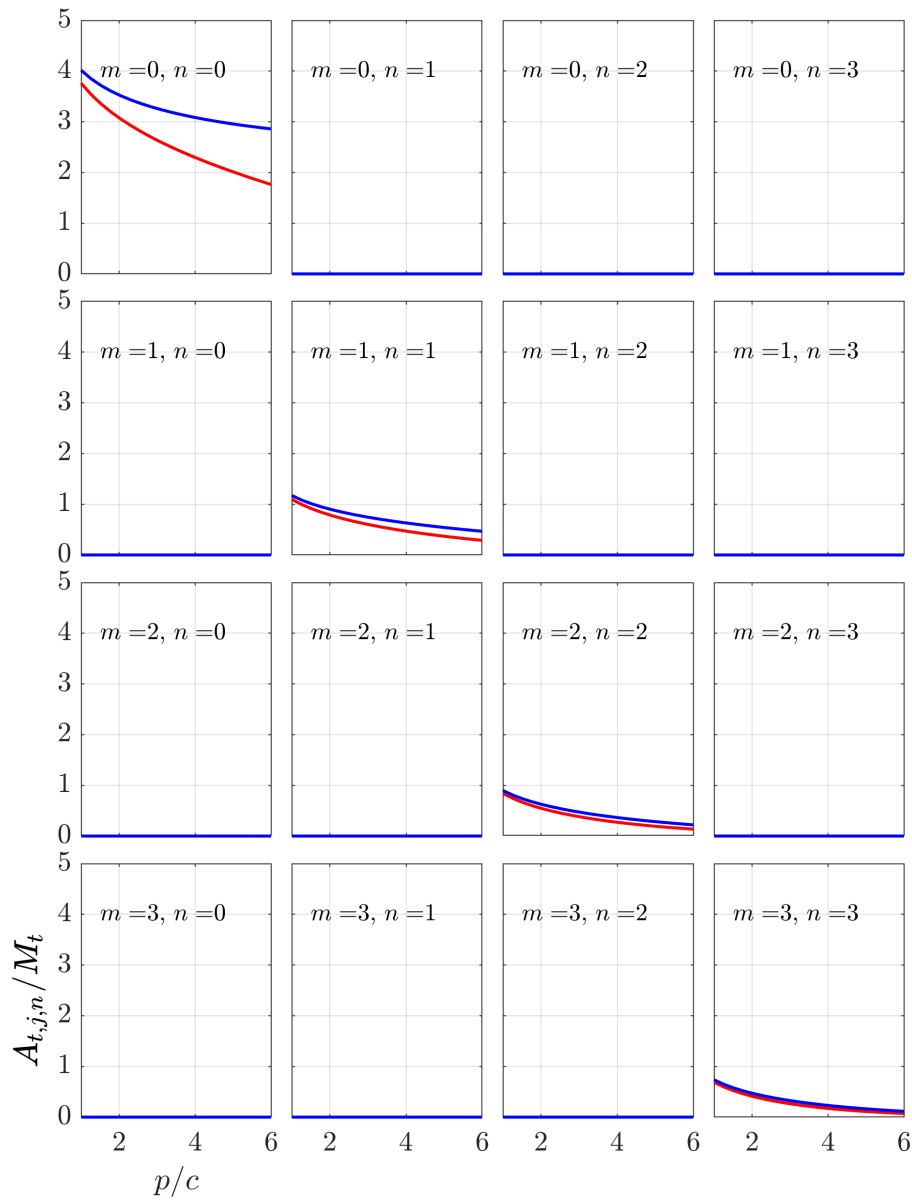
Figure 4.20: Non-dimensional cross-term added mass for different mode combinations

The red line corresponds to $A_{1,2,m,n}/M_1$, that is, non-dimensional added mass on torus 1 in mode m due to mode n motion of torus 2. The blue line corresponds to $A_{2,1,m,n}/M_2$, that is, non-dimensional added mass on torus 2 in mode m due to mode n motion of torus 1. The radius of the outer torus is $R_1 = 25$ m, while the radius of the inner is $R_2 = R_1 - \frac{2p}{c}$ m. The cross-sectional radius is $c = 0.8$ m for both.

Chapter 5

Previous Model Tests

In this section, previously conducted model tests on the studied solar island model concept will be presented. The resulting experimental RAOs from these tests are of special interest when studying our own numerical results. The first model tests were conducted by Winsvold (2018), who performed an experimental study into the governing behaviour and response of a solar island structure consisting of five elastic tori enclosing each other, connected through elastic bands. Later on, Vassdokken Sigstad (2019) performed experiments on a slightly different version of the model used by Winsvold (2018), and eventually added a membrane to simulate the deck carrying photo-voltaic cells.

Both of the experimental studies cover multiple aspects of the behaviour of the solar island structure, such as response in irregular wave conditions and over-topping. However, when presenting these model tests our focus will lie on the parts that are essential when comparing experimental and numerical results later on. In other words, an overview of the experimental set-up as well as model properties. For a more detailed presentation of the experimental studies, one should therefore look to the original master theses by Winsvold (2018) and Vassdokken Sigstad (2019).

5.1 Model Tests by Winsvold

5.1.1 The model

Figure 5.1 shows a photo of the multi-torus model used in the experimental studies by Winsvold (2018), with instrumentation and mooring-lines. Corrugated tubes are used for the tori, and water-repellent tape is wrapped around them in order to increase their bending stiffness and also make them smoother. The elastic bands connecting the tori have a rubber core with polyester silk enclosing them. Each torus has eight evenly spaced plastic strips enclosing them, where the elastic bands are connected. With this, there are a total of 32 elastic bands in the model.

The model is built in the scale 1:50, and Froude scaling is used when scaling all parameters. The model properties are presented in Table 5.1, for both model and full scale. Here, the spacing $2p$ is taken from the center-line of one torus to the next, and constant between all tori. The outer torus is indexed as number 1, so that the inner torus becomes number 5.

Figure 5.1: Multi-torus model by Winsvold

Multi-torus model with instrumentation and mooring-lines. Grey, round reflexive markers as well as rectangular accelerometers are seen. Taken from Winsvold (2018).

Table 5.1: Main parameters for multi-torus model by Winsvold

Description	Parameter	Model scale	Full scale
Cross-sectional diameter of single torus	$2c$	$32\ mm$	$1.6\ m$
Torus mass per unit length	m_t	$0.257\ kg/m$	$642.5\ kg/m$
Torus bending stiffness	EI	$0.8467\ Nm^2$	$2.65 \times 10^8\ Nm^2$
Mooring-line spring stiffness	k_m	$25.9\ N/m$	$64.8\ kN/m$
Elastic band spring stiffness	k_e	$45\ N/m$	$112.5\ kN/m$
Cross-sectional diameter of elastic bands	d_e	$4\ mm$	$0.2\ m$
Diameter of outer torus	D_1	$1.02\ m$	$50\ m$
Spacing between tori	$2p$	$\approx 0.1\ m$	$5\ m$

5.1.2   Test Set-Up and Procedure

The model is tested in the Small Towing Tank at the Norwegian University of Science and Technology, in Trondheim, Norway during February and March of 2018. The test set-up is illustrated in Figure 5.2, and both force-rings, accelerometers and wave probes are marked. The model has four horizontal mooring-lines symmetrically distributed on the outer torus at $\beta = 45, 135, 225$ and $315\,\mathrm{deg}$. They are subjected to a pre-tension of $T_p = 5$ N, which corresponds to 640.624 kN in full scale.

As seen , there are 8 evenly spread accelerometers on the outer torus, and these are for some runs moved to other tori in order to measure their accelerations as well. Two motion-caption cameras measure the 3D motions of the multi-torus, and a total of 24 reflexive markers are used, 8 on torus 1 and 2, 4 on the third and 2 on the fourth and inner torus. These are seen in Figure 5.1.
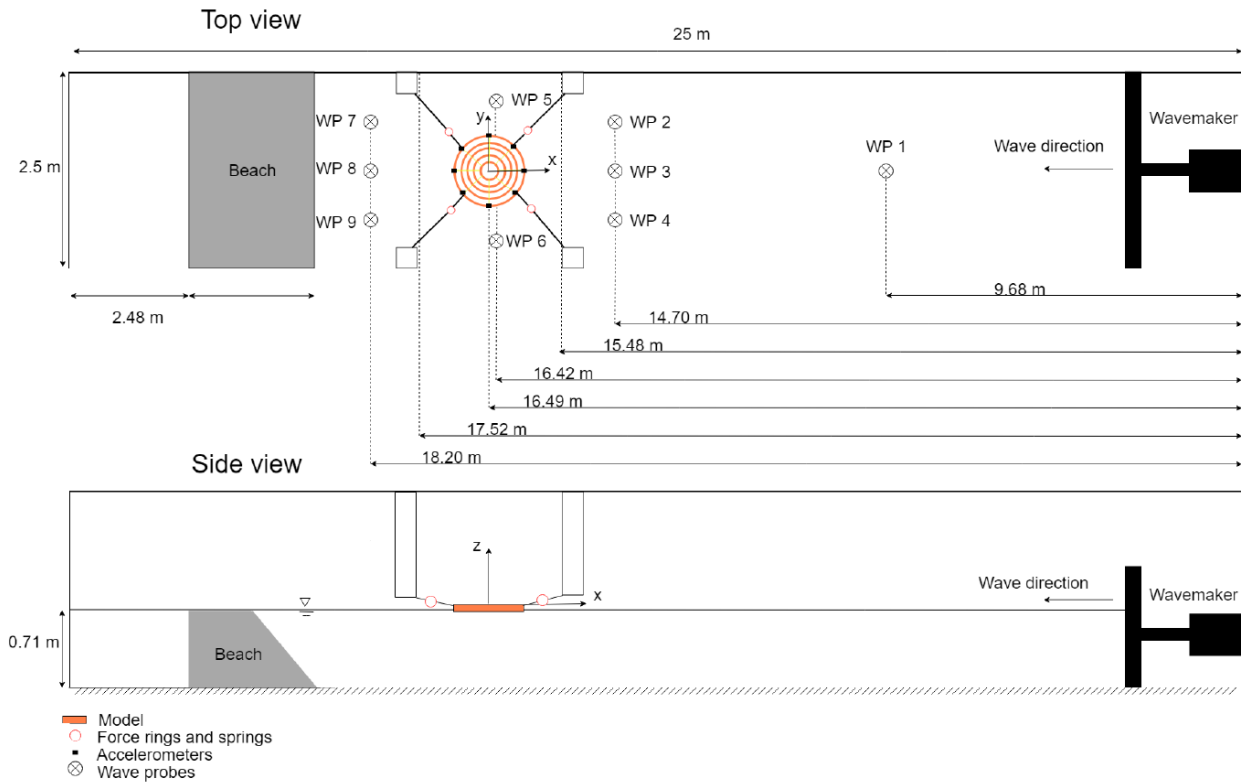
Figure 5.2: Illustration of model test set-up by Winsvold
Test location is Lilletanken. The upper figure shows the top-view, while the lower shows the side-view. Taken from Winsvold (2018).

The multi-torus model is tested in both regular and irregular waves. Forces acting on the mooring-lines, wave-elevation, accelerations of the structure in response to the waves and the all-over movement of it are measured and pre-processed. The regular waves tested have full scale wave periods ranging from $2-14$ s, and wave steepness values $H/\lambda = 1/60, 1/40, 1/30$ and $1/20$ are tested. This corresponds to full scale kR values in the range of approximately $0-20$, where the radius is of the outer torus. The full test matrix is shown in Figure F.1.

5.2 Model Tests by V. Sigstad

5.2.1 The Model

Vassdokken Sigstad (2019) tested a multi-torus model both with and without a weighted membrane. As the numerical model does not represent such a membrane, only the plain version of the experimental model will be presented. The model is a modified version of that of Winsvold (2018), where the elastic bands have been replaced by new, stiffer ones, and the mooring-lines having been replaced by stiffer ones as well.

The multi-torus is shown in Figure 5.3, and the model properties listed in Table 5.2 both in model and full scale. Do note that the truss and mooring-properties are the only ones different than what Winsvold (2018) presented. Froude scaling is still used.
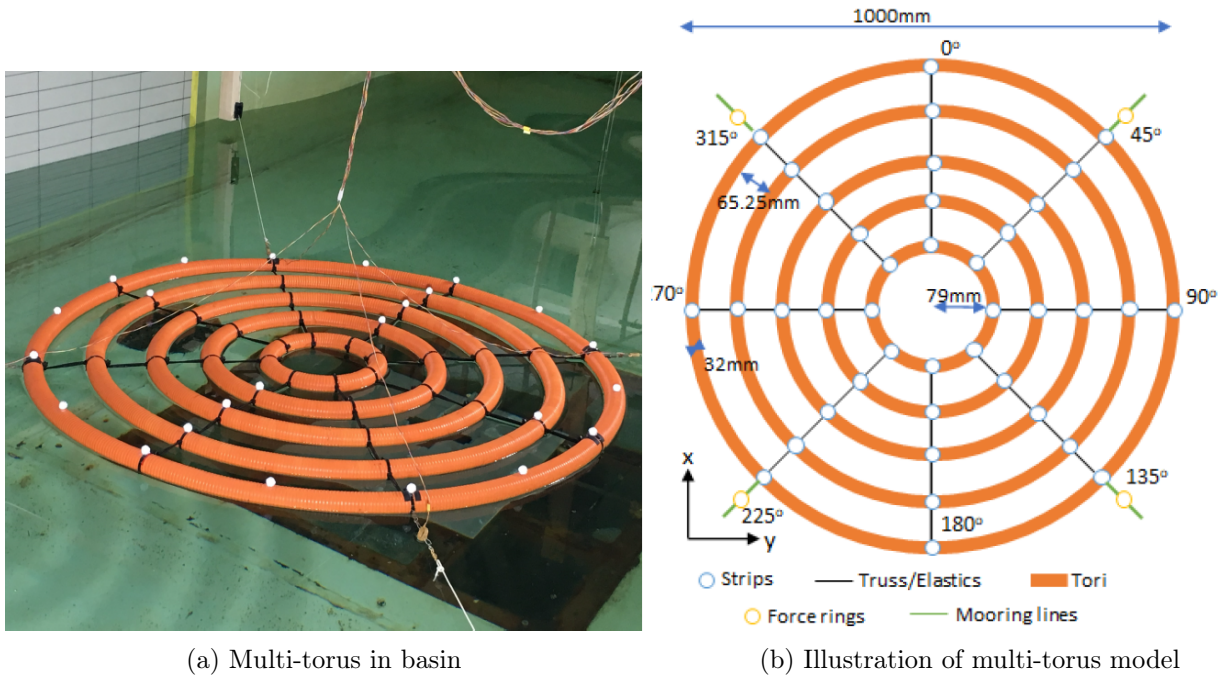
(a) Multi-torus in basin

(b) Illustration of multi-torus model

Figure 5.3: Figure a) shows the multi-torus installed in the basin, with motion capture globes attached. Figure b) is an illustration of the multi-torus model with its different components. Both are taken from Vassdokken Sigstad (2019).

Table 5.2: Main parameters for multi-torus model by V. Sigstad

Description	Parameter	Model scale	Full scale
Cross-sectional diameter of single torus	$2c$	32 mm	1.6m
Torus mass per unit length	m_t	0.257 kg/m	642.5 kg/m
Torus bending stiffness	EI	0.8467 Nm^2	2.65×10^8 Nm^2
Mooring-line spring stiffness	k_m	14.0 N/m	35.9 kN/m
Elastic band stiffness	k_e	57.9 N/m	148.4 kN/m
Cross-sectional diameter of elastic band	d_e	3 mm	0.15 m
Diameter of outer torus	D_1	1.02 m	50 m
Spacing between tori	$2p$	≈ 0.1 m	5 m

5.2.2   Test Set-Up and Procedure

The model is tested in the same wave tank as that used by Winsvold (2018), namely the Small Towing Tank at the Norwegian University if Science and Technology, in Trondheim, Norway. The tests are conducted during February of 2019. The test set-up is illustrated in Figure 5.4, and is quite similar to the previous one. The 3D motions of the model are measured by 24 Qualisys markers, distributed as shown in Figure 5.3a.

Each mooring-line consists of a thin nylon rope, a spring and a chain. The spring models the flexibility that a mooring rope in full scale would have. The mooring line is thread through a hoise positioned 5 cm over the water level at the tank wall, and adjusted so that the pre-tension in model scale is 2.6 N. This corresponds to a full-scale value of 333.125 kN, and is approximately half of that in the model tests by Winsvold (2018). Since the force rings are attached close to the model and the deflection of the ropes are small compared to the force applied, it is assumed that the eventual elasticity does not affect the mooring-line forces. An illustration of the mooring-line set-up as well as a photography of it are shown in Figure F.2.
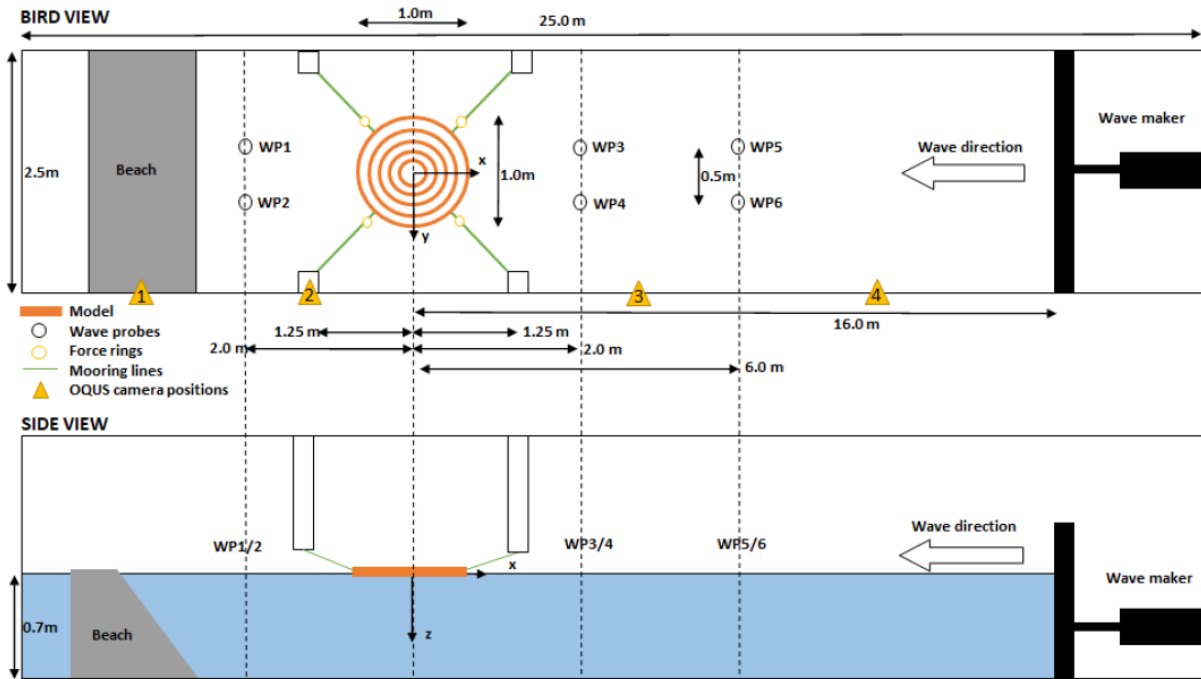
Figure 5.4: Illustration of model test set-up
Test location is Lilletanken. Both bird and side view are illustrated. No instrumentation except cameras for plain recording will be used for the current experiments. Taken from Vassdokken Sigstad (2019).

The regular waves run during the model tests are in the kR range of about 0.7 to 6.3, with R being the radius of the outer torus. Wave steepness values of both $1/60, 1/50, 1/40$ and $1/30$ are tested. The full test matrix is added in Appendix F.1.2.

Chapter 6

Results and Discussion

6.1 Previous Experimental Results

In this section, relevant experimental results from the previous model tests presented in chapter 5 will be discussed. First the ones by Winsvold (2018) and subsequently the ones by Vassdokken Sigstad (2019). The focus will lie on the RAOs for the outer torus, as the motion is best captured for this torus in both the experimental studies.

6.1.1 Experiments by Winsvold

Figure 6.1 shows the resulting RAOs for the three outer tori, for the first three vertical modes of each of them. Do note that here the notation b is used for the vertical modes, and not a as used throughout chapter 2. The top figure shows the resulting experimental RAOs in heave for the three outermost tori of the multi-torus model, plotted agains the ZFT RAOs for each of them. $R1$ denotes the outer torus, $R2$ the second-most outer and $R3$ the middle torus in the multi-torus system. The experimental data are from measurements with the motion-capture cameras. The figure in the middle is a similar plot, only for pitch motion, and the lower figure is for the first flexible vertical mode. Legends for all three plots are added in the lower figure, as well as the kR-axis. Do note that the ZFT RAOs all end at $kR = 4$, which was done to indicate that the theory is applicable only in the low-frequency limit. These results are from Kristiansen and Winsvold (2019), who discuss the results from the model tests.

Studying Figure 6.1 more in detail, we interestingly observe that there are some patterns between cancellation of certain RAOs and local peaks in others. For instance, there are local peaks in the experimental heave RAOs at $kR_1 \simeq 3.85$, marked by green circles in the plot, which corresponds to the first cancellation wave number in ZFT pitch of the outer torus, marked by a green square in the plot. Next, there are also local peaks in the experimental heave RAOs at $kR_1 \simeq 5.2$, marked by yellow circles in the plot, which corresponds to the first cancellation wave number in the ZFT first flexible mode of torus 1. Since the ZFT plot was cut at $kR_1 = 4$, the line is extended to illustrate the rest of it. The mentioned correlations indicate non-negligible interactions between the modes of each torus, and also interactions between tori. Both hydrodynamic and structural interactions are here possible candidates.

The experimental data of the outer torus show similar trends to that of ZFT, but the cancellations appear at different wave numbers. The reason for this may be structural interactions, as any hydro-dynamic interaction may only provide modifications of the motions for the wave numbers where the excitation force is non-zero, and cannot influence the cancellation points.

A plot of heave RAOs for torus 1 for the full kR range tested is added in Figure G.1.
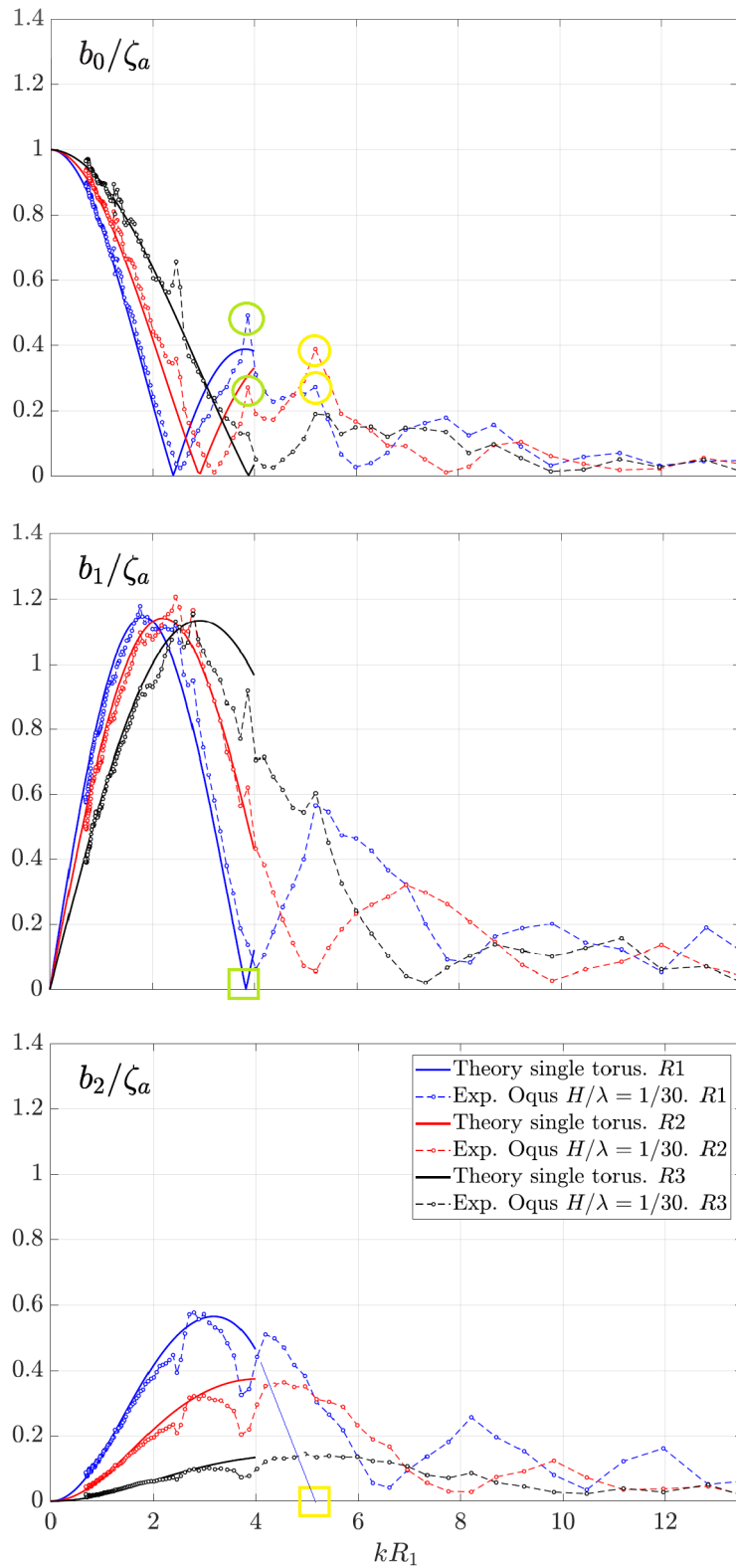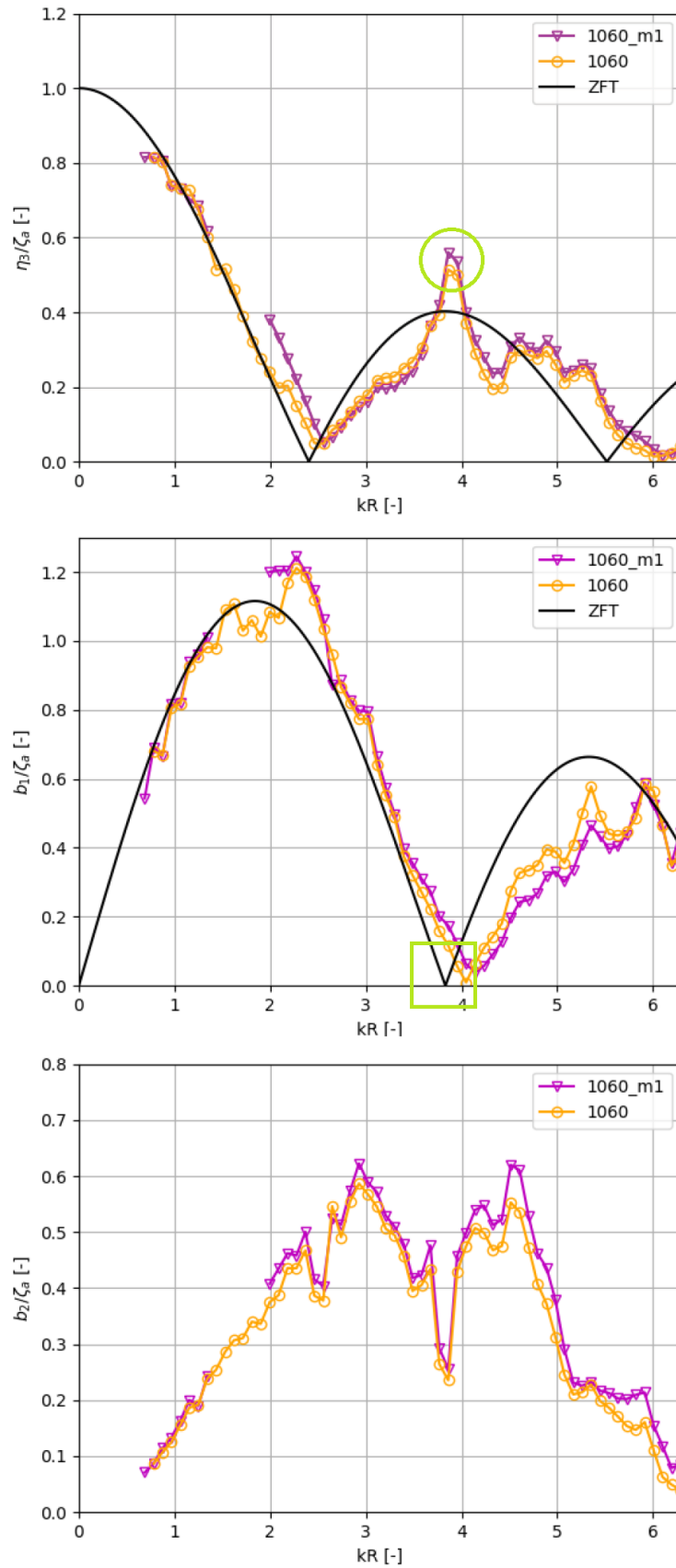
Figure 6.1: Resulting RAOs from Winsvold model tests

The top figure shows the resulting experimental RAOs in heave for the three outermost tori, plotted against the ZFT RAOs for each of them. The experimental data are from measurements with the motion-capture cameras. The figure in the middle is a similar plot for pitch motion, and the lower figure is for the first flexible vertical mode. Legends for all three plots are added in the lower figure, as well as the kR_1-axis. $R1$ denotes the outer torus, $R2$ the second-most outer and $R3$ the middle torus in the multi-torus system. Green and yellow circles mark local peaks, while the squares mark cancellation wave numbers for R_1. In the bottom plot, the ZFT RAO for R_1 has been extended for illustrative purposes. Slightly modified from Kristiansen and Winsvold (2019).

6.1.2 Experiments by V. Sigstad

Figure 6.2 shows the resulting experimental RAOs in both heave, pitch and the first flexible vertical mode for the outer torus in the multi-torus system. Plots from both the model with (1060_{m1}) and without (1060) the membrane deck are included, and are quite similar. However, only the latter is of interest when comparing with numerical results. For heave and pitch the corresponding ZFT RAO is also plotted. The experimental results are for a wave steepness $H/\lambda = 1/60$, but results for the same modes using $H/\lambda = 1/30$ are also presented by Vassdokken Sigstad (2019) and are quite similar, showing the same tendencies. A difference to mention is that peak in pitch at $kR \simeq 2.3$ is not there for the less steep wave runs, it rather follows the ZFT curve.

In the top figure, showing the heave RAO, we observe a local peak at a similar location as in Figure 6.1, $kR \simeq 3.85$. This is indicated by a green circle. Once again this corresponds to the first wave cancellation number for the pitch RAO, indicated by a green square. There is still tendencies of a second local peak in the heave RAO at $kR \simeq 5.2$, though not as apparent as in Figure 6.1. All in all the presented RAOs are quite similar to those by Winsvold (2018), showing the same tendencies. This strengthens the theory that hydrodynamic and/or structural interactions are affecting the torus motion in a non-negligible manner. We also keep in mind that as Vassdokken Sigstad (2019) used double the amount of global markers compared to Winsvold (2018), the accuracy of the higher mode responses, calculated by modal analysis, should increase.

It should lastly be noted that the changes made to the muti-torus model by Vassdokken Sigstad (2019), including a decrease in mooring-line spring stiffness and pre-tension as well as increase of truss spring stiffness, has not seemed to affect the response of the outer torus significantly in neither heave, pitch or the first flexible vertical mode.

Additional resulting RAOs for the outer torus from the model tests are added in Appendix G.2.

Figure 6.2: Resulting RAOs from V. Sigstad model tests

The top figure shows the resulting experimental RAOs in heave for the outer torus, for the model with membrane (1060_{m1}) and without (1060), plotted against the ZFT RAO. The wave steepness is $H/\lambda = 1/60$. The figure in the middle is a similar plot for pitch motion, and the lower figure is for the first flexible vertical mode. The outer torus radius is used in the non-dimensional wave number kR. Green and yellow circles mark local peaks, while the square marks cancellation wave number. Slightly modified from Vassdokken Sigstad (2019).

6.2 Numerical Solar Island Model Results

In this section, results from the numerical solar island implemented in MATLAB will be presented. The results will be discussed in terms of how well they correspond with theoretical RAOs, and also in relation to the experimental results by Winsvold (2018) and Vassdokken Sigstad (2019). The resulting RAOs from the latter study have been digitized by use of the software *GetData Graph Digitizer*, in order to compare more easily with numerical results.

6.2.1 Introduction to Multi-Torus Cases

Both a multi-torus consisting of 2 tori and another consisting of 5 are tested in MATLAB. The radius of the outer torus, the spacing between tori and torus properties are identical for both cases, and are listed in Table 6.1. The inner torus is indexed as number 1, and the indexes increase outwards. Do note that the listed properties are identical to the full-scale values of the experimental multi-torus models by both Winsvold (2018) and Vassdokken Sigstad (2019), except for the torus mass per unit length. Our value corresponds to a halfway submerged torus, while the experimental models in fact have lower drafts.

Table 6.1: Torus properties used in numerical models

Description	Parameter	Value
Cross-sectional diameter of single torus	$2c \ [m]$	1.6
Torus mass per unit length	$m_t \ [kg/m]$	1030.4
Torus bending stiffness	EI $[Nm^2]$	2.65×10^8
Radius of outer torus	$R_{outer} \ [m]$	50
Spacing between tori	$2p \ [m]$	5

Further, the elastic bands in the presented cases are modelled by one truss each only. This is chosen because one had troubles when using several trusses to model elastic bands earlier on, and thus decided to simplify the problem. One concern was that the behaviour of the trusses did not represent an uniform elastic band, and potentially destroyed the results. A strong point of rather using one truss, however, is that it will have floater-nodes in each end, so that the floaters are directly linked and potential structural interactions should become apparent. Mooring-lines are not included in the numerical models, a choice once again made to simplify the problem and focus on potential structural interactions between tori.

Table 6.2 lists the standard connecting-truss properties used for the numerical multi-torus models. Note that the stiffness-value corresponds to the elastic band spring stiffness in Table 5.2, which is for the model by Vassdokken Sigstad (2019). She did however not present the pre-tension of the elastic bands, but referred to them as *slightly pre-tensioned*. A value of $T_{pct} = 37100N$ is therefore set, corresponding to an original length to pre-tensioned length ratio of $l_0/l_p = 0.95$. The truss-mass is not listed, simply because the tested models are built up by floater-nodes only, so that node-masses are not needed in the equation system.

Table 6.2: Standard truss-properties used in numerical models

Description	Parameter	Value
Pre-tension in connecting-trusses	$T_{pct} \ [N]$	37100
Stiffness of connection-trusses	$k_{ct} \ [N/m]$	$148.4 \cdot 10^3$

Table 6.3 lists additional parameter values used in the numerical runs, for both the 2-torus and 5-torus model. A set of 50 non-dimensional wave numbers ranging from $kR_{outer} = 0.3$ to 10 are run to obtain RAOs for the different tori. However, most of the resulting plots will be cut at $kR = 6$ as this is the range of interest, especially with regards to the experimental results. FFT is used on the stable

region between $stable - time$ and $end - time$ of the mode-amplitude time-series in order to obtain RAO-values. Vertical modes $0 - 4$ are activated, as well as lateral modes $1 - 3$. Lateral mode 1 is surge, while 2 and 3 are radial, elastic modes.

Table 6.3: Additional parameter values used in numerical runs

Description	Parameter	Value
Time-step	$dt \, [s]$	0.0025
Time at end of ramping	$end - ramp \, [s]$	$10 \cdot T_w$
Start of stable region	$stable - time \, [s]$	$15 \cdot T_w$
End of time-series	$end - time \, [s]$	$30 \cdot T_w$
Damping-ratio	$\xi \, [\%]$	3
Included vertical modes	$v - modes$	0,1,2,3,4
Included lateral modes	$l - modes$	1,2,3

6.2.2 Numerical 2-Torus Model Results

Figure 6.3 shows the geometry of the numerical 2-torus model in its pre-tensioned, initial state, with both node and truss numbering. Lines are drawn between the nodes in order to illustrate the floaters, which are perfectly circular in their pre-tensioned state. The inner torus is indexed as number 1, so that the outer becomes number 2.

(a)

(b)
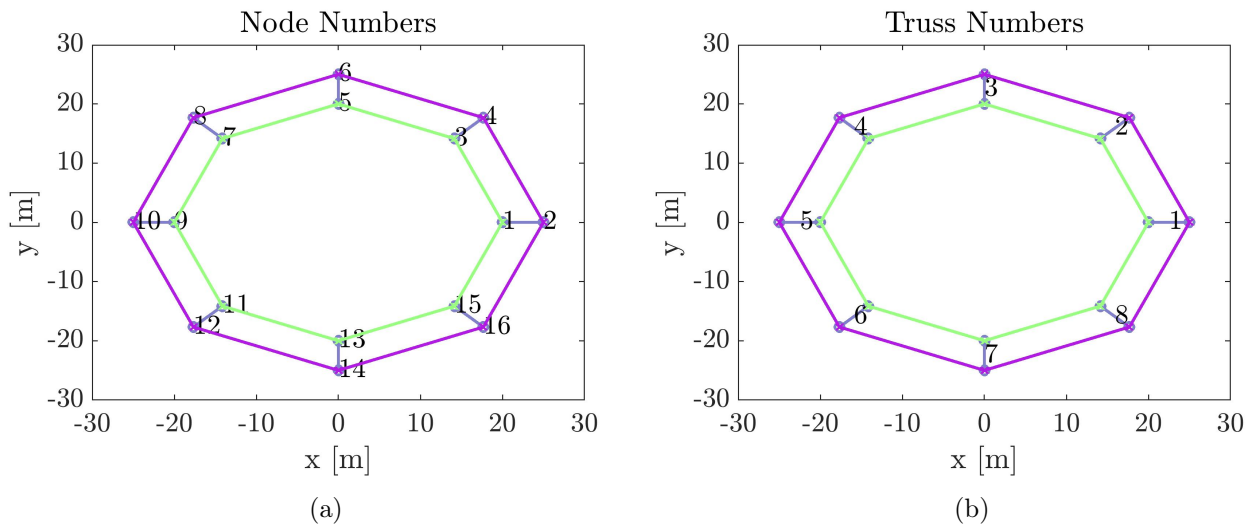
Figure 6.3: Geometry of 2-torus model

Illustration of pre-tensioned 2-torus numerical model in MATLAB. a) shows node numbering, while b) shows truss-numbering. All nodes lie at $z = 0$. Lines are drawn between the nodes to illustrate the floaters, which are perfectly circular in their pre-tensioned state. The inner torus is indexed as number one, while the outer is number 2.

The resulting RAOs for the two tori in their different modes will now be presented. They are all plotted against kR_2. A constant wave steepness of $HDL = 1/200$ is used.

Figure 6.4 shows the resulting numerical RAOs in the first four vertical modes plotted against ZFT, for each of the two tori. Here, *num* denotes numerical data, $T1$ torus 1 and $T2$ torus 2. For heave, the numerical RAOs both follow ZFT up until $kR \simeq 4.5$, where torus 1 starts to deviate, and soon after the outer torus. The second cancellation wave number for torus 2 is shifted slightly to the right for the numerical RAO compared to ZFT. These small deviations from ZFT indicate structural interactions, but local peaks as those found in the experimental results are not seen at all. In pitch we see some deviation for torus 2 only, while the higher vertical modes seem to have a perfect match for both tori. The same goes for vertical mode 4 which is presented in Appendix H.2.
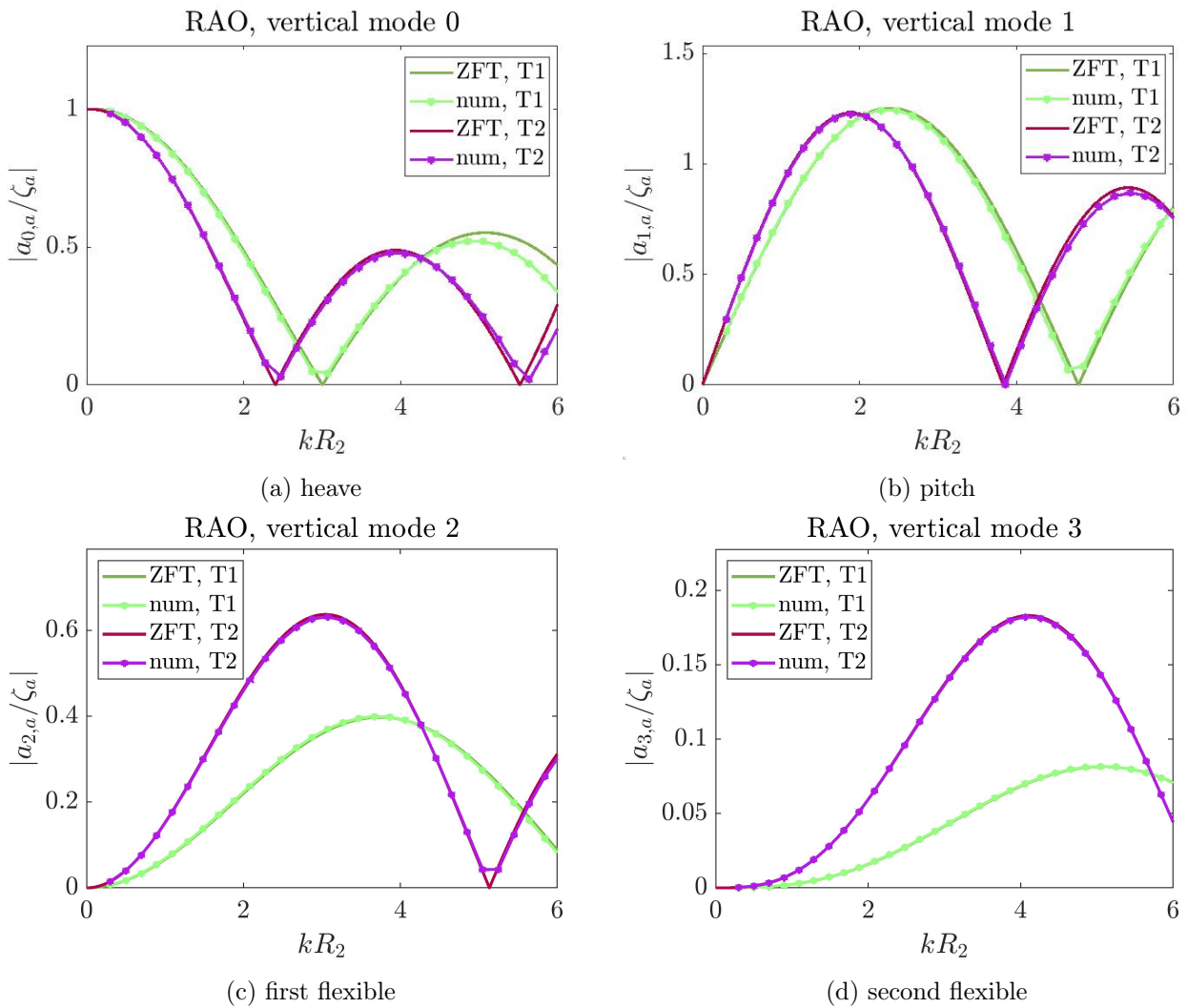
Figure 6.4: Vertical mode RAOs for 2-torus model

Resulting numerical RAOs in the first four vertical modes plotted against single floater ZFT, for each of the two tori in the 2-torus model. *num* denotes numerical results. Further, $T1$ denotes torus 1 and $T2$ torus 2, where the latter is the outer torus of the system.

Figure 6.5 shows the resulting RAOs in surge for each of the tori, plotted against their corresponding theoretical RAOs. Here we observe much larger deviations from the theoretical RAOs. For the inner torus it seems to be shifted to the left, and for the outer to the right, so that they become almost identical up to about kR 4. Again, this indicates structural interactions. They may be larger for this mode due to the fact that the truss-forces generally have a larger contribution for this mode compared to the vertical ones. Do note that the Rayleigh damping in surge is set to 0 as there are no mooring-lines, and therefore - we assume, no natural frequency.

Figure 6.6 shows the resulting RAOs for the radial modes for both tori. Also here the RAO of the inner torus is shifted to the left compared to its corresponding theoretical RAO, while the outer torus is shifted to the right. This is seen for both modes, but is most apparent for mode 2.
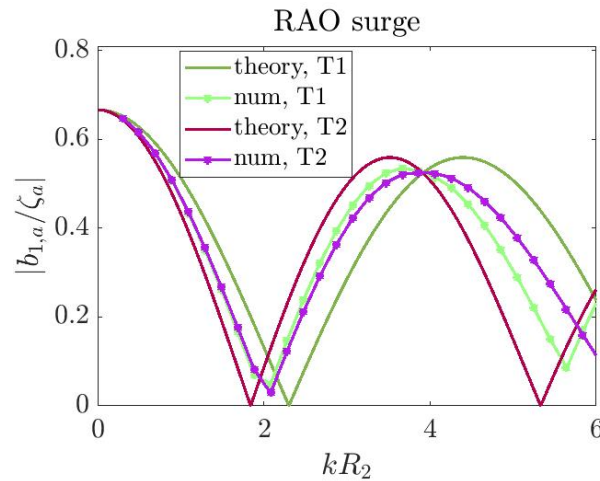
Figure 6.5: Surge RAO for 2-torus model

Resulting numerical RAOs in surge plotted against single floater theoretical ones, for each of the two tori in the 2-torus model. *num* denotes numerical results, and *theory* theoretical ones. Further, $T1$ denotes torus 1 and $T2$ torus 2, where the latter is the outer torus of the system.
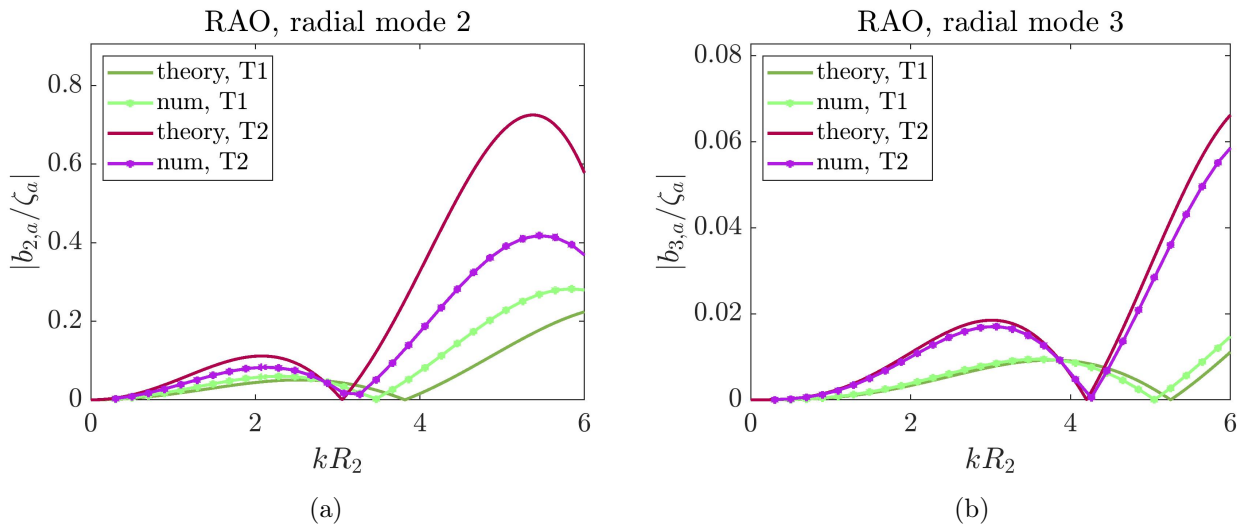
Figure 6.6: Radial mode RAOs for 2-torus model

Resulting numerical RAOs in radial mode 2 and 3 plotted against single floater theoretical ones, for each of the two tori in the 2-torus model. *num* denotes numerical results, and *theory* theoretical ones. Further, $T1$ denotes torus 1 and $T2$ torus 2, where the latter is the outer torus of the system.

A run with half the original pre-tension in the connective trusses, $Tpct = 18550N$, is run to check the effect on the RAOs. Figure 6.7 shows the resulting RAOs in heave and pitch for this new case, with the original ones still included. A small effect is seen for torus 1 in heave, as it increases slightly towards the end. In pitch, no difference is seen. No significant difference from the original runs are seen for the rest of the modes either, which are added in Appendix H.2

(a) heave   (b) pitch
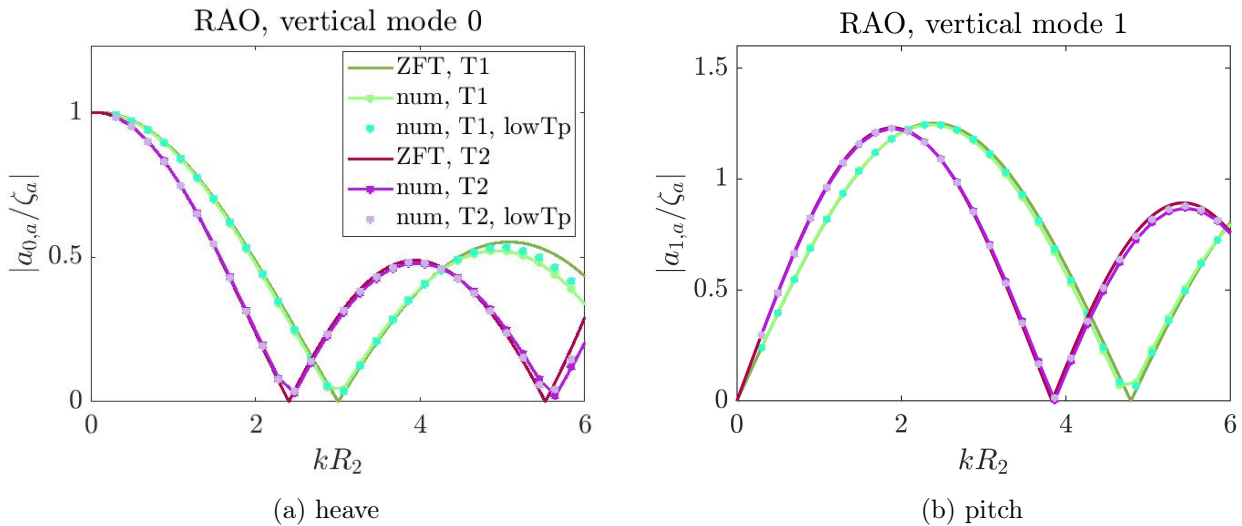
Figure 6.7: Low pre-tension - RAOs for heave and pitch
Resulting numerical RAOs in heave and pitch plotted against single floater theoretical ones, for each of the two tori in the 2-torus model. The legend in a) is for b) as well. *num* denotes numerical results, and *theory* theoretical ones. Further, $T1$ denotes torus 1 and $T2$ torus 2, where the latter is the outer torus of the system. *lowTp* is for a run with lowered pre-tension, $T_{pct} = 18550N$, which is half of the pre-tension in the initial run.

It is of interest to take a closer look on the behaviour of the trusses. Resulting time-series for $kR = 1$ and 4 for the original case with $Tp_{ct} = 37100N$ are therefore studied, and some interesting observations are made. As seen in Figure 6.8a, the level of oscillation seems to increase slightly upwards for truss 2 in the run with $kR = 1$. The same tendency can be seen for the rest of the trusses. Figure 6.8 shows the tension time-series of truss 2 for $kR = 4$, which is quite wiggly. As we know, the trusses have floater-nodes in both ends, which means that this pattern must come from the combination of the movements of the tori. We keep in mind that the presented tension plots show deviation from the initial pre-tension, and so the total tension in the trusses is very much constant.

(a) kR = 1   (b) kR = 4
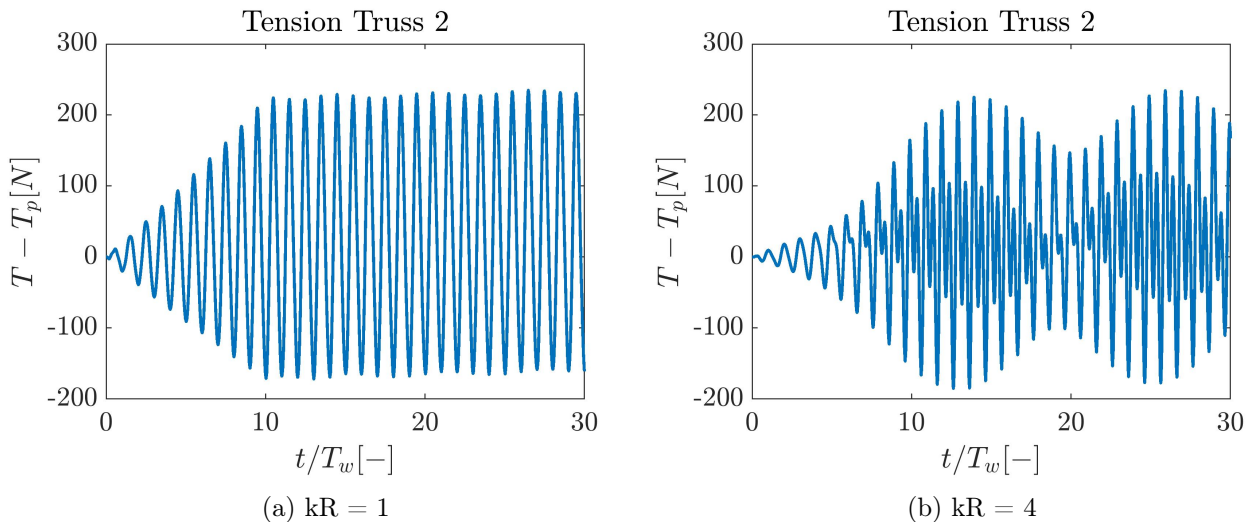
Figure 6.8: Tension time-series
Tension time-series for truss 2 for $kR = 1$ and 4. The difference in tension T from the initial pre-tension at start, T_p, is plotted.

Both mode-amplitudes and generalized forces are checked for the two kR-values, and are all stable. As an example, the generalized truss-forces on the outer torus in heave are shown in Figure 6.9a for the case of $kR = 4$. Further, the vertical mode-amplitudes for the outer torus for the same kR-value are shown in Figure 6.9b. Several of the RAO-peaks are in the area of $kR = 4$, so seeing that all

mode-amplitudes are stable for this value indicates that the presented RAOs are in fact based on stable runs.

(a) Vertical forces on torus 2 in heave

(b) Vertical mode-amplitudes for torus 2
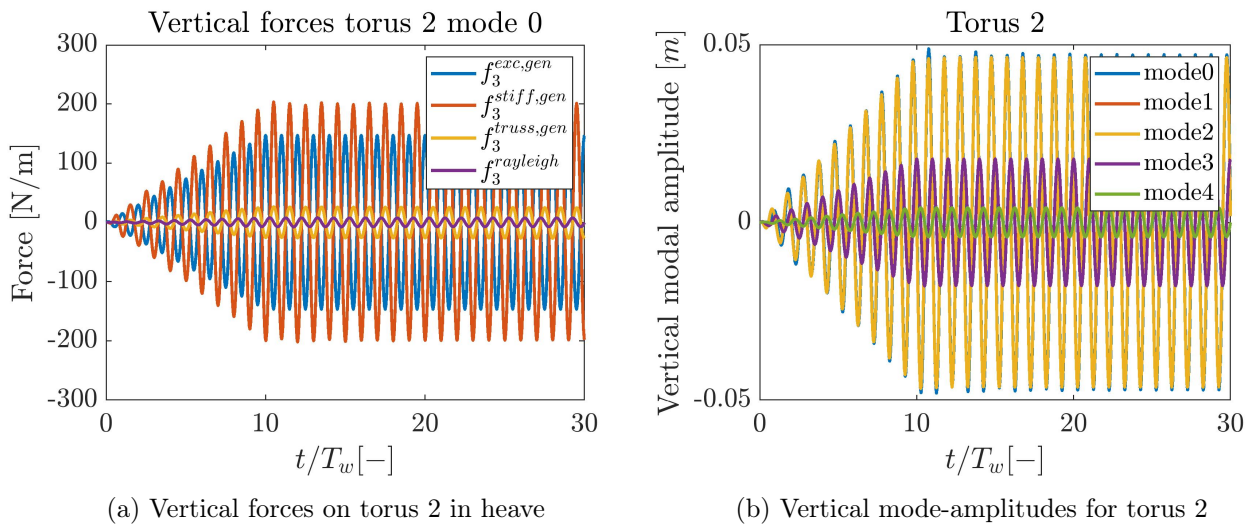
Figure 6.9: Vertical mode-amplitudes and heave-forces on torus 2
a) shows the vertical generalized forces in heave on torus 2. b) shows the vertical mode amplitudes on the same torus. These plots are both for $kR = 4$.

6.2.3   Numerical 5-Tori Model Results

Figure 6.10 shows the geometry of the numerical 5-torus model in its pre-tensioned, initial state, with both node and truss numbering. Lines are drawn between the nodes in order to illustrate the floaters, which are perfectly circular in their pre-tensioned state. The inner torus is indexed as number 1, so that the outer becomes number 5.

(a)

(b)
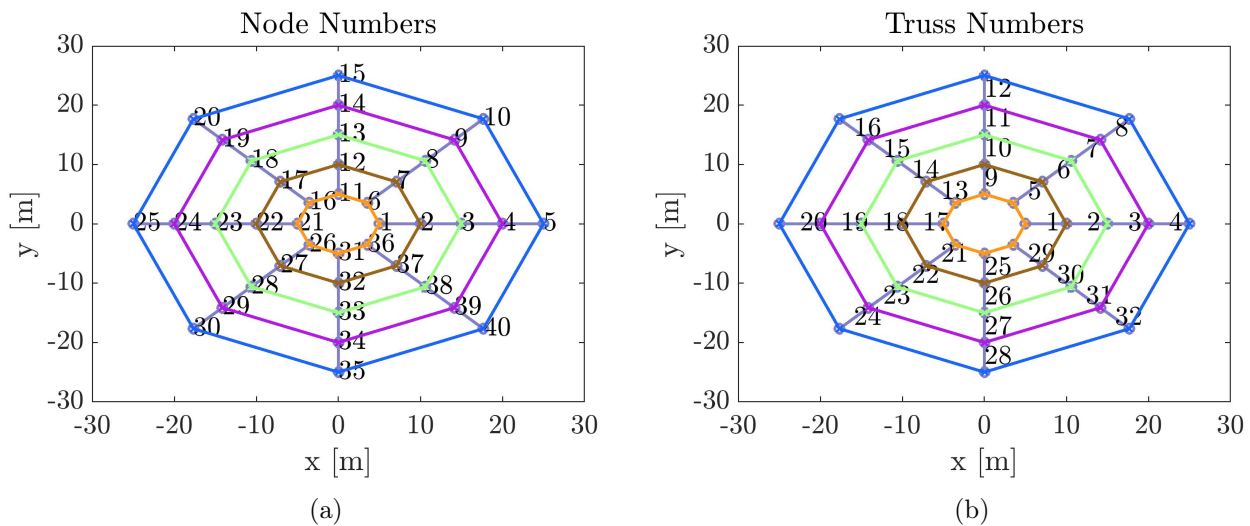
Figure 6.10: Geometry of 5-torus model
Illustration of pre-tensioned 5-torus numerical model in MATLAB. a) shows node numbering, while b) shows truss-numbering. All nodes lie at $z = 0$. Lines are drawn between the nodes to illustrate the floaters, which are perfectly circular in their pre-tensioned state. The inner torus is indexed as number one, so that the outer torus becomes number 5.

The resulting RAOs for the three outer tori in their different modes will now be presented. They are all plotted against kR_5, and a constant wave steepness of $HDL = 1/1000$ is used in the runs. The two inner tori have been excluded to make the plots more easy to read, and also because the outer tori are of most interest with regards to experimental results.

Figure 6.4 shows the resulting numerical RAOs in the first four vertical modes plotted against ZFT, for each of the three tori. Here, *num* denotes numerical data, $T3$ torus 3, $T4$ torus 4 and $T5$ torus 5. We observe from Figure 6.11a that the RAOs in heave deviate slightly from ZFT for the higher kR-values. As for the 2-torus case, the second wave cancellation number of the outer torus is shifted slightly to the right. Some deviation is seen for the pitch RAOs in Figure 6.11b as well, while the first and second flexible modes seem to have a perfect match with ZFT for all tori. The same can be said for the third flexible mode, which is added in Appendix H.3. The local peaks seen in experimental results do once again not appear in our numerical results. However, the deviations from ZFT that we do see indicate structural interaction.

(a) heave

(b) pitch

(c) first flexible

(d) second flexible
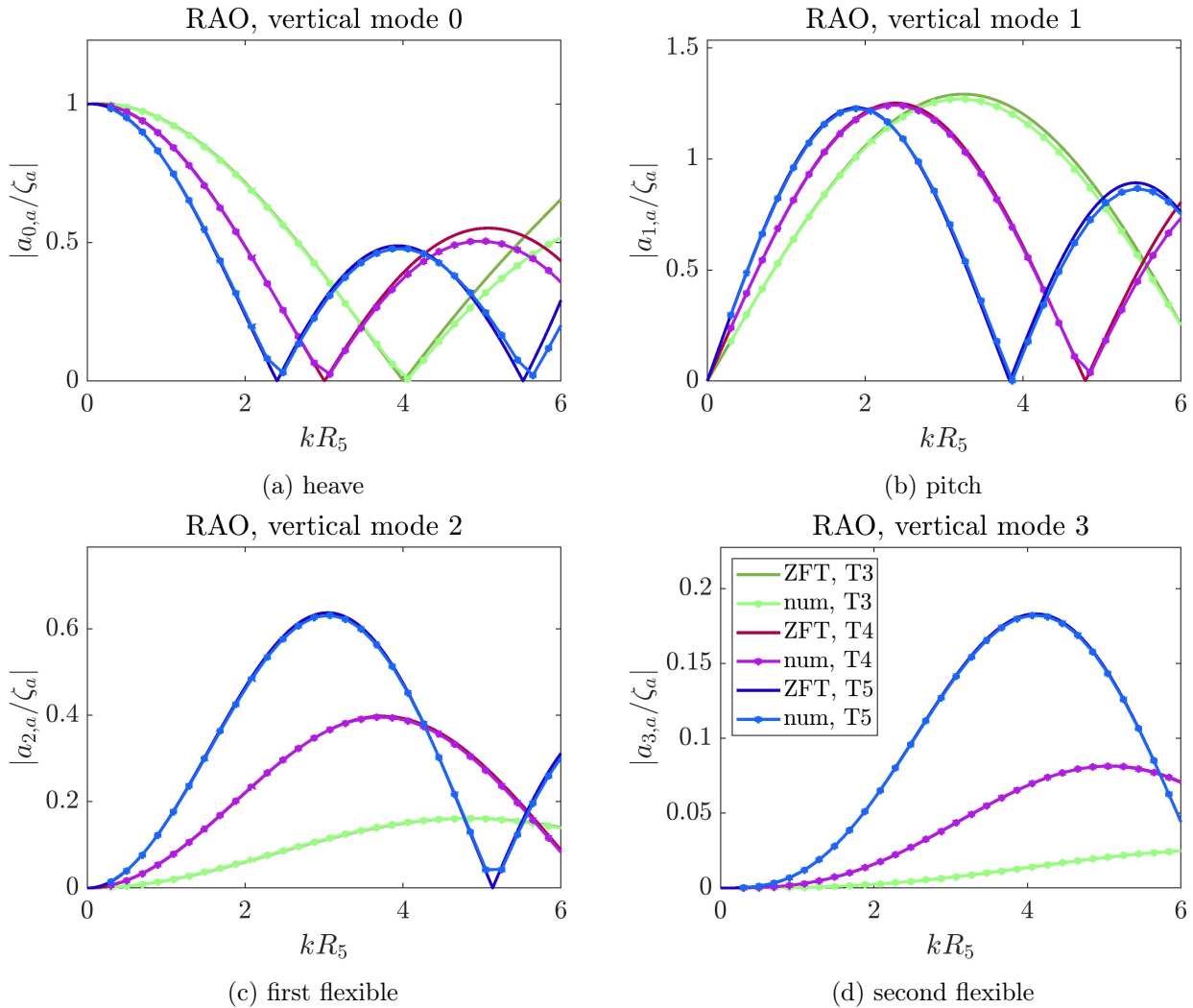
Figure 6.11: Vertical mode RAOs for 5-torus model
Resulting numerical RAOs in the first four vertical modes plotted against ZFT, for each of the three outer tori in the 5-torus model. *num* denotes numerical results. Further, $T3$ denotes torus 3, $T4$ torus 4 and $T5$ torus 5, where the latter is the outer torus of the system. The legend in d) is for all four plots.

Figure 6.12 shows the resulting RAOs in surge for each of the tori, plotted against their corresponding theoretical RAOs. As for the 2-torus case, the Rayleigh damping in surge is set to 0 as there are no mooring-lines, and therefore - we assume, no natural frequency. Surprisingly, the numerical RAOs all have a peak at $kR_5 \simeq 4.9$, which seems like one, common natural frequency. Potential reasons for this may be structural interaction amplifying the motion at this kR-value, some sort of numerical problem or perhaps an effect due to the way the trusses are modelled. It is not easy to estimate potential natural frequencies of the trusses themselves, as their mass is not included in our simplified set-up.
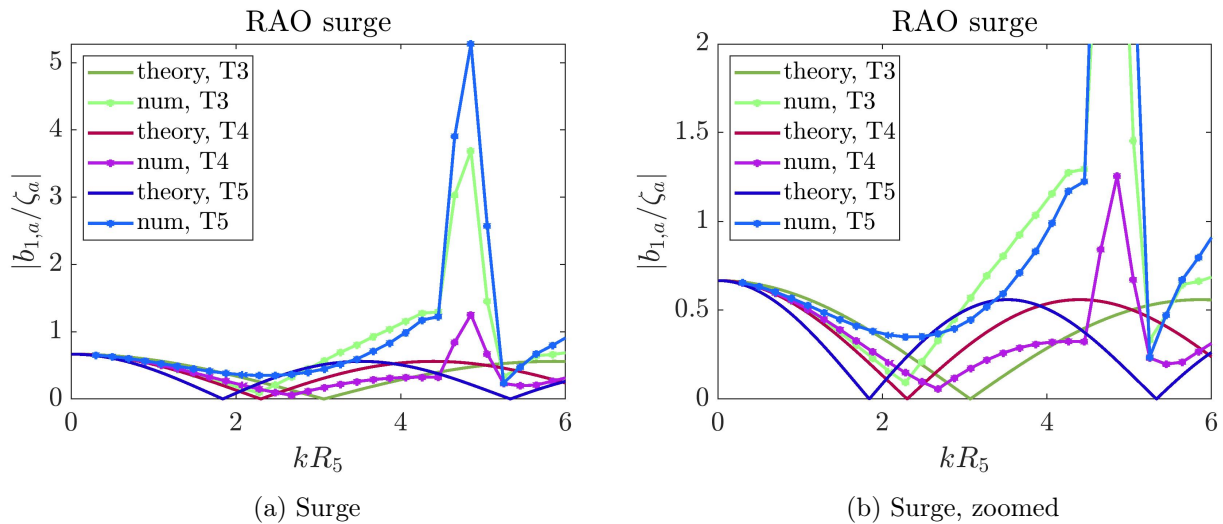
Figure 6.12: Surge RAOs for 5-torus model

Resulting numerical RAOs in surge plotted against single floater theoretical ones, for each of the three outer tori in the 5-torus model. Figure b) is just a zoomed in version of a). *num* denotes numerical results. Further, $T3$ denotes torus 3, $T4$ torus 4 and $T5$ torus 5, where the latter is the outer torus of the system.

Figure 6.13 shows the resulting RAOs for the radial modes for both tori. As for the 2-torus case, the RAO of the outer torus is shifted to the right, and the inner ones to the left. This is seen for both modes, but is most apparent for mode 2.
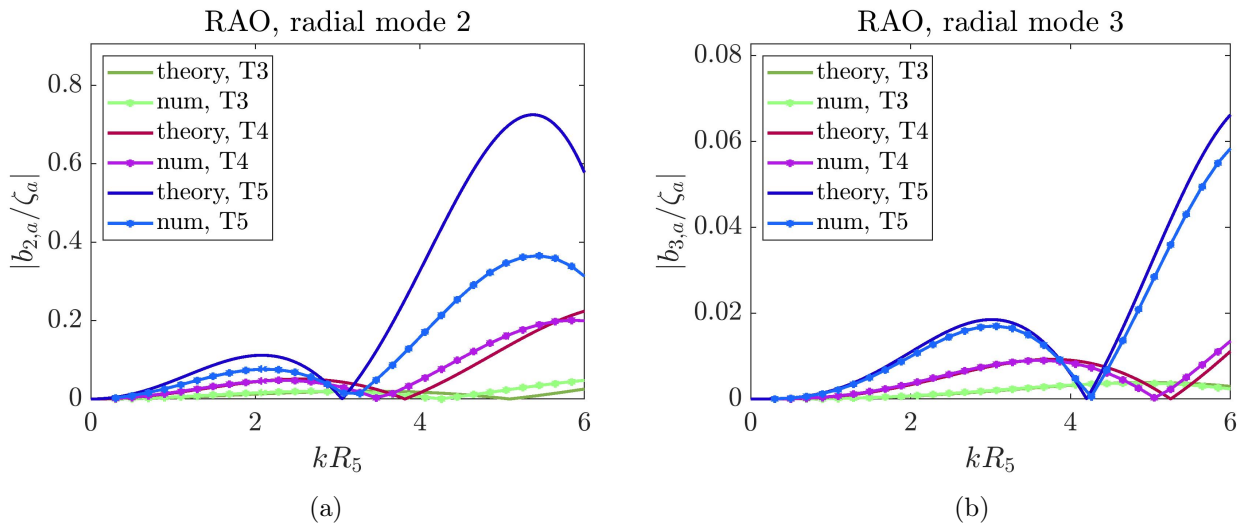
Figure 6.13: Radial mode RAOs for 5-torus model

Resulting numerical RAOs in radial modes plotted against single floater theoretical ones, for each of the three outer tori in the 5-torus model. *num* denotes numerical results. Further, $T3$ denotes torus 3, $T4$ torus 4 and $T5$ torus 5, where the latter is the outer torus of the system.

The resulting RAOs for the three outermost tori in the 5-torus model have so far been presented. Similar plots for the two most inner tori are added in Appendix H.3. Deviations from theoretical RAOs are seen also for these tori, and the same peak in surge is observed. Interestingly, the peaks are even larger for the inner tori.

It is now of interest to study the effect of lowering the pre-tension in the connecting-trusses. Therefore, as was done for the 2-torus case, a new run with half the original pre-tension, $T_{pct} = 18550$ N, is run. In addition, it is decided to also run a 5-torus case with mooring-lines. Four mooring-trusses are added to the initial geometry, as illustrated in Figure 6.14. The mooring-truss length is $l_m = 100$ m, the pre-tension $T_{pm} = 36 \cdot 10^3$ N and the stiffness $k_m = 36 \cdot 10^3$ N/m. The latter corresponds to the

mooring-line spring stiffness used by Vassdokken Sigstad (2019) in her experiments. Of course both the mooring-line length as well as the pre-tension was much smaller in the experimental set-up. As discussed in chapter 4, the mooring-line length is set to be quite large due to a debugging process where one thought that numerical problems arise when the mooring-lines become too steep. In hindsight, it is believed that the mooring-lines could in fact be shorter. As for the mooring-truss pre-tension, it is lowered compared to the experimental value because the solution has had an unstable tendency for high pre-tension in the trusses. This will be discussed more in detail later.
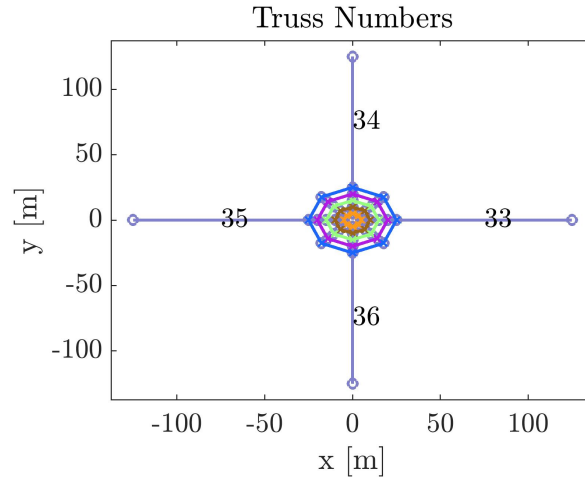
Figure 6.14: 5-Torus model geometry, with mooring-lines
Illustration of 5-torus model geometry in MATLAB, adjusted to include 4 mooring-line trusses. Only the mooring-line trusses are indexed, the rest of the truss-numbers are as given in Figure 6.10.

Figure 6.15 shows the resulting RAOs in heave for the three outermost tori, for both the lowered pre-tension version ($lowTp$) and the mooring version ($moor$), plotted against the original 5-torus case RAOs as well as ZFT. As seen, adding the mooring-lines makes no difference in the resulting RAOs. Lowering the pre-tension, however, has some effect at the higher kR_5 values, where the solution seems to deviate slightly less from ZFT. The same tendency is seen in pitch, while for the rest of the vertical modes neither the lowered pre-tension version or mooring version have any effect on the original 5-torus case results. These are all added in Appendix H.4.
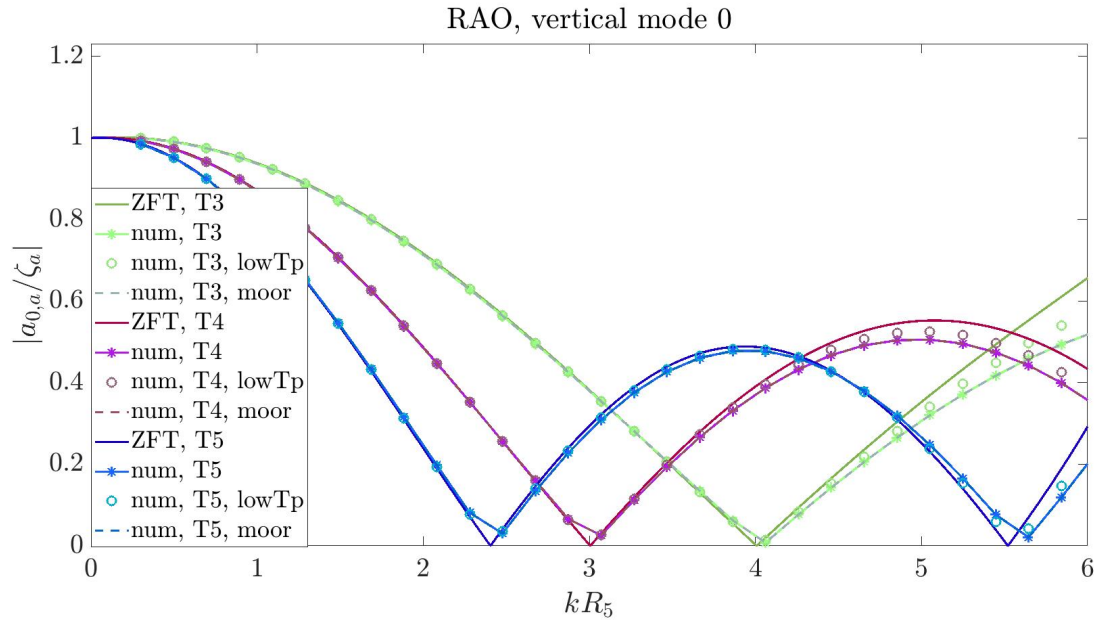
Figure 6.15: Heave RAOs: 5-torus case vs. altered versions

Resulting numerical RAOs in heave plotted against ZFT RAOs for the three outermost tori in the 5-torus model. *num* denotes numerical results. Further, $T3$ denotes torus 3, $T4$ torus 4 and $T5$ torus 5, where the latter is the outer torus of the system. *lowTp* is for a version with half the original pre-tension, $T_{pct} = 18550$ N, and *moor* is for the moored-version of the 5-torus case.

Moving on to surge, we observe much larger effects of lowering the pre-tension. As seen in Figure 6.16, the peaks around $kR_5 \simeq 4.9$ are significantly damped. This plot is for torus 4 and 5, but the same tendency is observed for the other tori.

Regarding the the moored version, one estimated the natural frequency in surge for the entire structure as $w_{n,surge} = \sqrt{2k_m/(M + A_{11})}$, where M and A_{11} are the total mass and added mass in surge of the entire structure, and $C_{11} = 2_{km}$ the stiffness term from the mooring-lines. This was used to set the Rayleigh damping term for surge motion, given by $2(M + A_{11})\xi w_{n,surge}$, where the damping ratio was set equal to the value for the rest of the modes, $\xi = 0.03$. Lastly, the theoretical expression for the surge RAO, given in Equation (2.77), had to be altered to rather describe the global surge motion. That is, using the mass, added mass and radius of the entire structure. The resulting RAOs for the moored-version of the 5-torus case are shown in Figure 6.17. As a global surge motion is assumed, the theoretical RAO is identical for all tori. We do observe that all the numerical RAOs seem to rise near the theoretical natural frequency at $kR_5 \simeq 0.25$. This specific kR-value would need to be run in order to see if there in fact is a peak at this frequency. We further observe that all tori have peaks in the area of $kR_5 = 4 - 5$, though lowered compared to the peaks seen for the original 5-torus case. This is probably due to the fact that there was no Rayleigh damping in the original case.
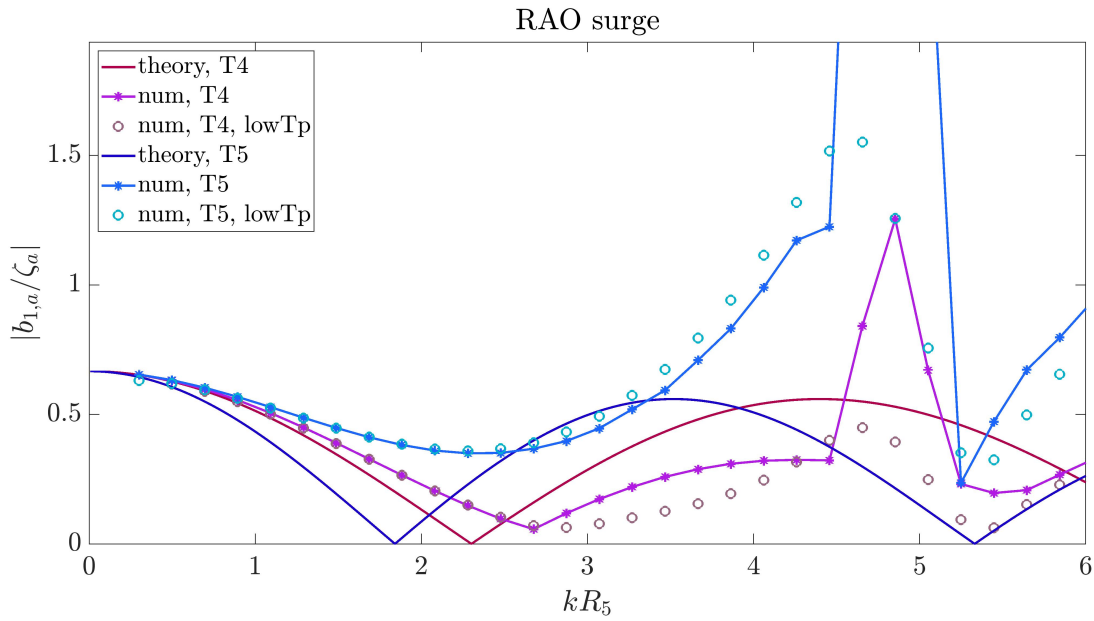
Figure 6.16: Surge RAOs: 5-torus case vs. lowered pre-tension version
Resulting numerical RAOs in surge plotted against single floater theoretical RAOs for the two outermost tori
in the 5-torus model. *num* denotes numerical results. Further, $T4$ denotes torus 4 and $T5$ torus 5, where the
latter is the outer torus of the system. *lowTp* is for a version with half the original pre-tension, $T_{pct} = 18550$
N. .
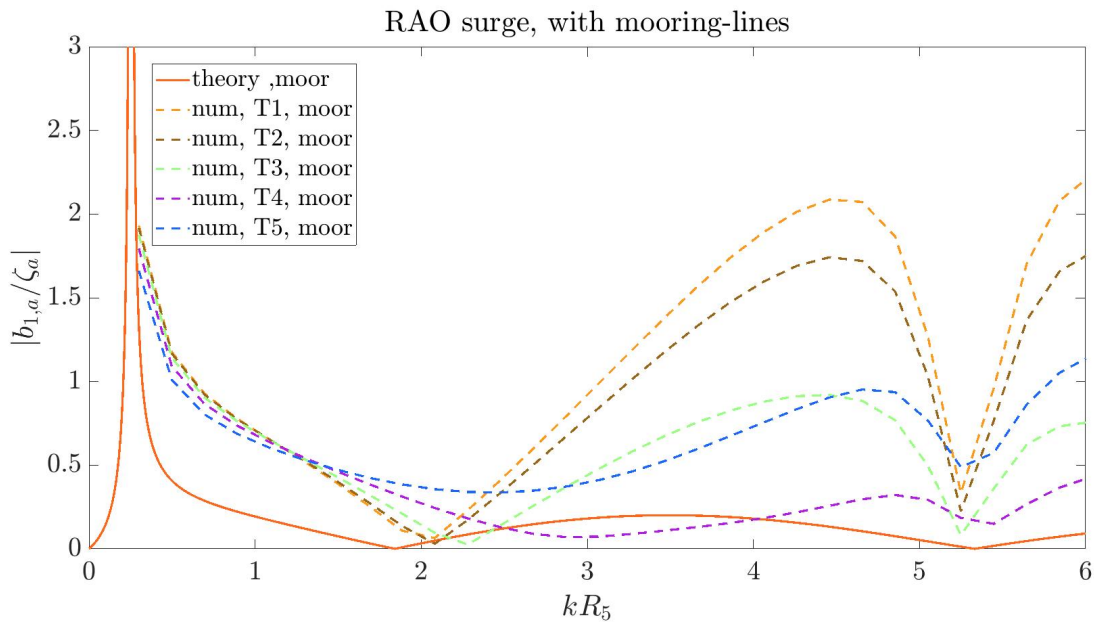
Figure 6.17: Surge RAOs: moored version of 5-torus case
Resulting numerical RAOs in surge plotted against single floater theoretical RAOs for all tori in the moored
version of the 5-torus model. *num* denotes numerical results. Further, $T1$ to $T5$ denotes torus 1 to 5, where
the latter is the outer torus of the system.

The radial mode RAOs for the altered versions of the 5-torus case are added in Appendix H.4. No
effect is seen at all from lowering the pre-tension. The mooring-case, however, deviates significantly
from the original case for the two outer tori. Radial mode 3 is particularly strange for the outer torus.

Some resulting time-series are next studied for the 5-torus case, as well as the moored-version of it,
in order to observe the behaviour of the trusses and see if the runs are in fact stable. $kR_5 = 1$ and
4 are tested, as was done for the 2-torus case. Figure 6.18a shows the resulting tension time-series

for truss 1 in the 5-torus case for $kR_5 = 4$. A wiggly behaviour is observed, and this tendency is in fact seen for all the trusses except the ones along the y-axis. For the trusses along the y-axis, the level of oscillation increases steadily throughout the time-series, as shown for truss 9 in Figure 6.18c. This is a truss on torus 1, and in fact the tendency decreases outwards, so that for truss 12, the outer truss along the y-axis, the time-series is pretty straight. See Figure 6.10 for truss-numbering. Similar tension time-series have been included for the moored version of the 5-torus case in Figure 6.18b and Figure 6.18d. There is still the same increasing oscillation level for the trusses along the y-axis, but the wiggly behaviour for the rest of the trusses is gone. This is likely due to the fact that the surge-motion is damped for this case.

(a) 5-torus case

(b) 5-torus case, moored

(c) 5-torus case

(d) 5-torus case, moored
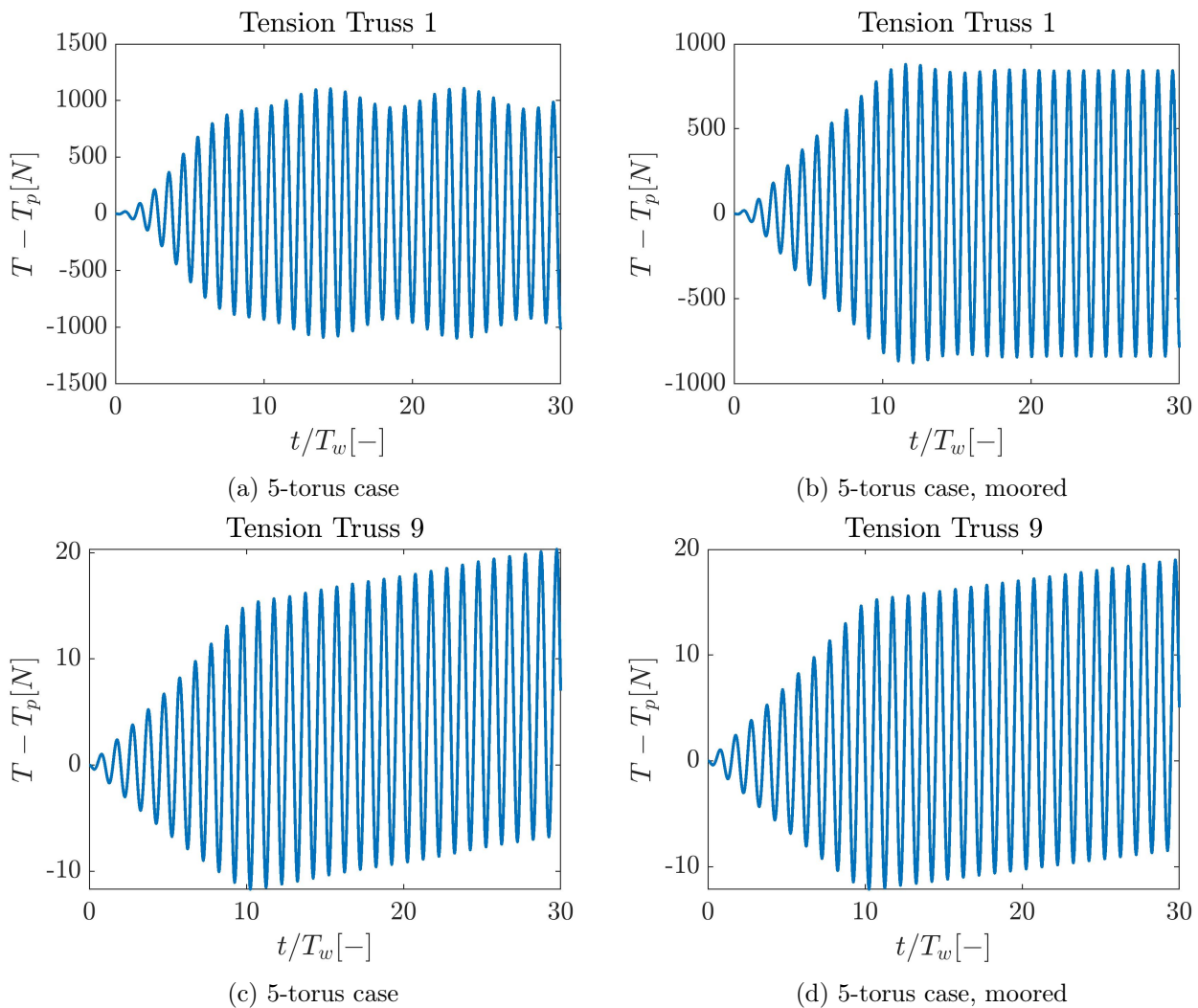
Figure 6.18: Tension time-series for $kR_5 = 4$

Tension time-series for $kR_5 = 4$. The difference in tension T from the initial pre-tension at start, T_p, is plotted. a) shows the tension in truss 1 for the 5-torus case, while b) shows the same for the moored version of this case. c) shows the tension in truss 9 for the 5-torus case, while d) shows the same for the moored version of this case. These plots are all for $kR_5 = 4$.

Figure 6.19a shows the resulting forces in surge for torus 1 in the 5-torus model, still for $kR_5 = 4$. The truss-forces are here dominant, and have the same wiggly pattern seen for the tension time-series. Thus, the mode amplitude in surge also gets the same effect, as seen in Figure 6.19c. The same tendencies are seen for corresponding plots for the rest of the tori in the system. For the moored case, however, both the surge forces and mode amplitudes are stable for all tori. The plots for torus 1 are added in Figure 6.19b and Figure 6.19d, as an example. These plots are stable due to the fact that the increased oscillation level makes almost no change to the total tension signal. The wiggly behaviour has a larger impact.
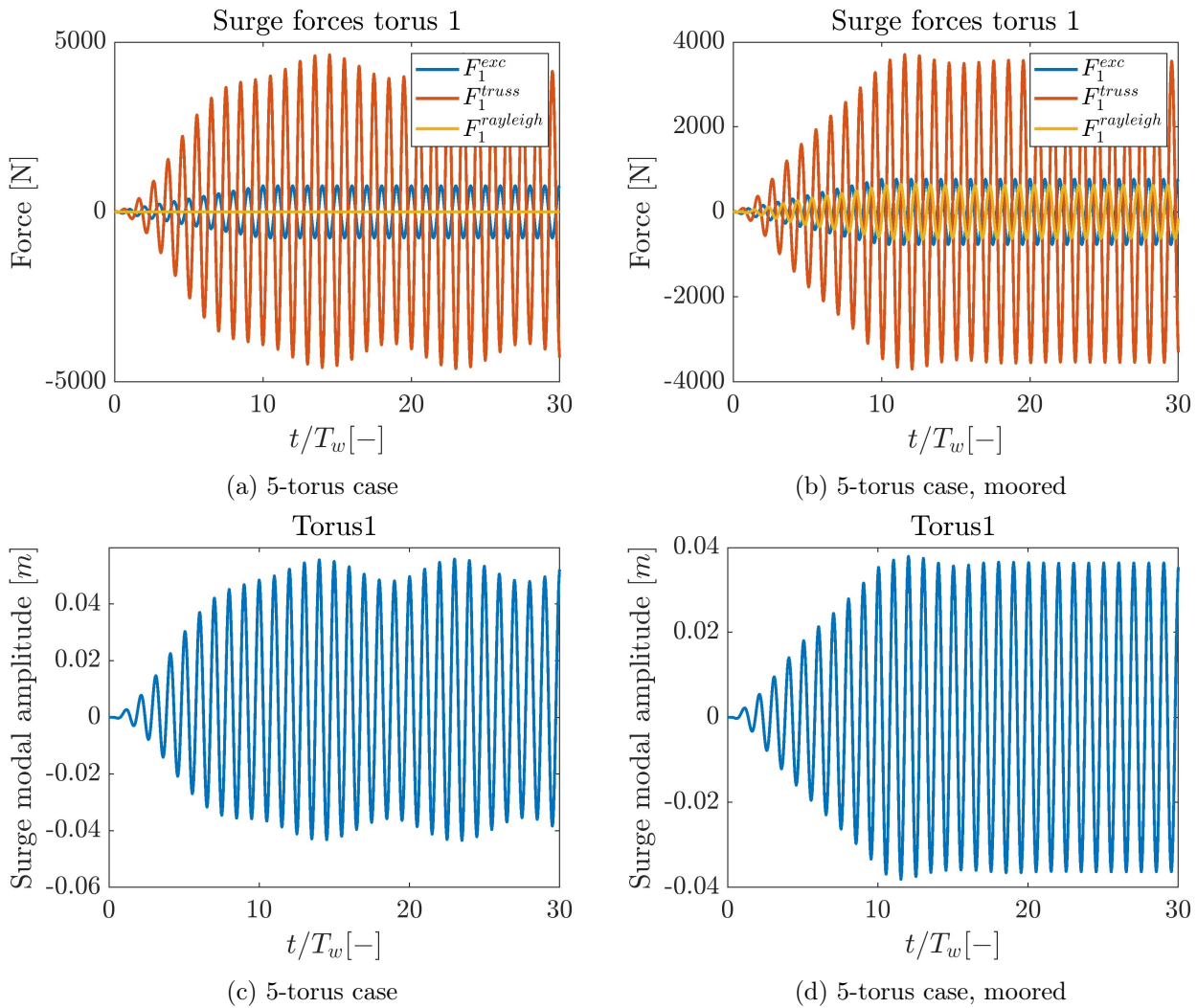
Figure 6.19: Surge mode-amplitudes forces on torus 1 for $kR_5 = 4$

a) shows the surge forces on torus 1 for the 5-torus case, while b) shows the same for the moored version of this case. c) shows the mode amplitude in surge for the 5-torus case, while d) shows the same for the moored version of this case. These plots are all for $kR_5 = 4$.

The results for $kR_5 = 1$ are somewhat more stable, but do have the same tendencies as discussed above. Some additional time-series are added in Appendix H.5, and show that there is also a minor problem regarding the generalized truss-forces for vertical forces on torus 1. The level of oscillation decreases slightly downwards, both for the original and moored 5-torus case. However, these forces are very small compared to the rest of the generalized vertical forces, so the vertical mode-amplitudes are all stable. Regarding radial modes, both mode amplitudes and forces are all stable, for both the original and moored version of the 5-torus case.

To summarize our time-series study, there is clearly some instability in the tension development. The wiggly tension behaviour is removed by introducing surge damping, but the increased oscillation-levels are of concern. Due to time limitations, this phenomenon can not be studied more in detail. It should however be mentioned that in the process of landing on the 5-torus case presented in this section, several attempted models have shown the same increased oscillation level in tension and in the end, the solutions have exploded. The problem seems to increase with increased pre-tension. Potential reasons may be a simple bug in the code, numerical instability, or something related to how the trusses are modelled. Either way, for the 5-torus case presented in this section, the resulting RAOs are not believed to have been destroyed by this bug in tension development. At least not the general behaviour. The only exception may be surge, and time-series from kR-values more in the peak-region of the surge RAOs should be studied to determine this.

6.2.4 Comparing with Experimental Results

It this subsection, the numerical results from both the 2-torus and 5-torus model will be compared with the experimental vertical mode RAOs by Vassdokken Sigstad (2019). The outer torus is studied. We keep in mind that the 2-torus model is in fact identical to the 5-torus model, just with the three inner tori having been removed. It is therefore of interest to compare with also the outer torus of the 2-torus model, as you get the same type of effect from its inner torus.

Figure 6.20 shows the comparison for vertical modes of the outer torus. The numerical results from the 2-torus and 5-torus model are in fact identical. An instant observation is that our ZFT RAO in heave is taller than the one presented by Vassdokken Sigstad (2019) in Figure 6.2, though they should be identical. At least if the mass of the torus is set to make it halfway-submerged. We know that the experimental model has a lower mass, so this may be one reason. Our ZFT pitch RAO is also somewhat taller. We find out that this is due to Vassdokken Sigstad (2019) having included a bending stiffness-term which is actually cancelled for pitch mode.

In heave, the numerical model RAOs are slightly shifted to the right of ZFT from $kR_5 \simeq 5$. In pitch, they are slightly lower than ZFT at the end. These are the only minor effects that remind of how the experimental RAO deviates from ZFT.
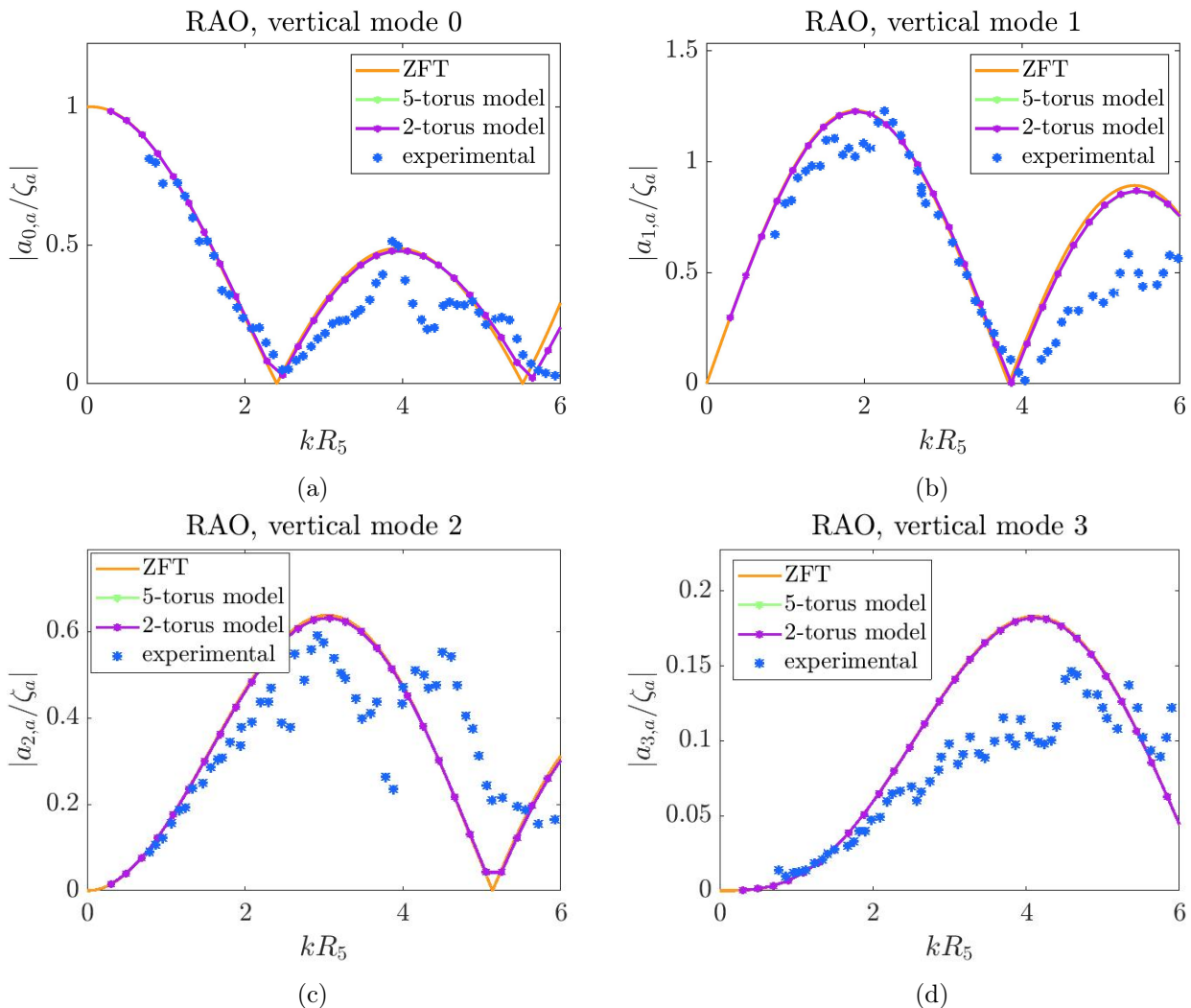
Figure 6.20: Numerical vs experimental vertical mode RAOs for outer torus

Numerical vertical mode RAOs for the outer torus, from both the 2-torus and 5-torus model, are plotted against ZFT and experimental data by Vassdokken Sigstad (2019). R_2 in the 2-torus model is identical to R_5 in the 5-torus model.

Based on the numerical results, the deviations from ZFT in the experimental vertical RAOs do not

seem to come from structural interactions. However, we must keep in mind that the numerical model does not represent the experimental model in an accurate manner. The pre-tension in the connective trusses of the experimental model is unknown, and a tentative value is set for the numerical runs. Knowing that the pre-tension then also seems to worsen the problem with tension development, this makes the entire comparison difficult. Furthermore, representing the elastic bands by one truss each is maybe not the best option. What we have modelled is in reality 5 m long mass-less elastic bands.

At a late stage in the work on this master thesis, it was also discovered that the elastic bands used in the experimental model do not seem to actually follow Hooke's law. New deflection-tests were performed, both on elastics in the solar island model, as well as similar, new elastic bands. Neither can be said to have followed Hooke's law. The problem is especially that they have to be stretched significantly before they tend to get a linear relation, while in the solar island model many of them were quite slack. Also, none of them returned to their initial state after the deflection tests were performed, they were permanently elongated and had lost their original flexibility.

6.2.5 Comments on Modelling of Elastic Bands

In the multi-torus cases presented so far, only one truss has been used to model each elastic band. However, a numerous amount of cases using more trusses to model each elastic band have previously been tested. Even though results from these cases have not been presented, as there was no time to go back and study them further after having improved the results for the simplified models, some aspects related to these type of cases should be discussed.

First of all, using several trusses to model each elastic band means that there will be connecting-node masses along it that are free to vibrate. Therefore, damping of the these nodes by the use of Rayleigh damping was applied, to avoid excitation of the natural frequency of the elastic band. In order to estimate this frequency, the fundamental frequency of transverse vibration for a pre-tensioned string fixed in both ends was used. This is added in Appendix A.1.

It was believed that a potential problem in previous runs was the fact that the natural frequency of the elastic bands were excited. However, damping the connecting nodes did not seem to improve the results. Eventually it was concluded that treating the elastic bands as uniform springs is probably not accurate. After all, for a case using 5 connecting trusses to model each elastic band in the 5-torus model, what you really get is 1 m long trusses between each connecting mass. Running such a case would often take over 2 days, so increasing the number of connecting trusses to make the elastic bands become more like uniform springs will make the runs extremely slow.

It was further observed for some runs that the trusses in the elastic bands did not seem to expand uniformly. The trusses near the floaters would behave differently than the ones in the middle. It may be that if coarsely dividing the elastic bands into trusses, they should rather be thought of as individual springs in a spring-mass array, and be damped accordingly. These thoughts would be studied further if one had time to go back to these type of cases.

6.3 Hydrodynamic Interactions

In this section, the results from the theoretical study on hydrodynamic interaction will be presented, and compared with experimental results.

The 5-torus system is studied, with torus parameter valuers as given in Table 6.4. This corresponds to the full-scale values presented for both experimental models. The mass is then smaller than that displaced by a half submerged torus, $0.5\rho\pi c^2 \simeq 1030 kg$, but is expected not to be sensitive. Further, $\rho = 1025$ kg/m is used. We ignore the effect of the elastic bands, and thus study the effect of hydrodynamic interaction only. We keep in mind that we have assumed ZFT, which is potentially not appropriate for several of the considered wave lengths.

Table 6.4: Torus properties used in hydrodynamic interaction solution

Description	Parameter	Value
Cross-sectional diameter of single torus	$2c\ [m]$	1.6
Torus mass per unit length	$m_t\ [kg/m]$	642.5
Torus bending stiffness	EI $[Nm^2]$	2.65×10^8
Radius of outer torus	$R_{outer}\ [m]$	50
Spacing between tori	$2p\ [m]$	5

Figure 6.21 shows the resulting RAO in heave for the outer torus in the 5-torus system, from both ZFT, the hydrodynamic interaction theory presented in chapter 3 and experimental results by both Vassdokken Sigstad (2019) and Winsvold (2018). We observe that the resulting RAO from hydrodynamic interaction theory appears to have new natural periods, at $kR_5 \simeq 3$ and 10. These do not match the local experimental peaks in $kR_5 \simeq 3.8$ and 5.2, but at least they show disruption from ZFT. We also keep in mind that there are possible large experimental errors from the high frequency range $kR_5 \gtrsim 8$.
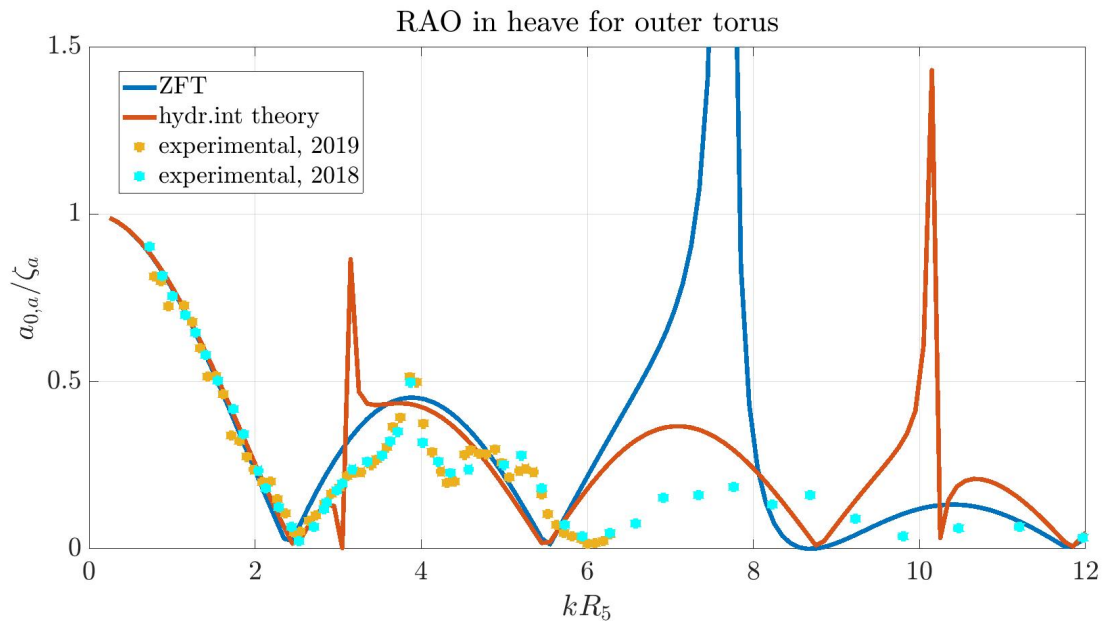
Figure 6.21: RAO in heave for outer torus in 5-torus system
RAO in heave for the outer torus in the 5-torus system, from both ZFT, hydrodynamic interaction theory and experiments by Vassdokken Sigstad (2019) as well as Winsvold (2018). The radius of the outer torus, R_5 is used in the non-dimensional wave number.

Figure 6.22 shows the resulting RAO in pitch for the outer torus in the 5-torus system, from both ZFT, hydrodynamic interaction theory and experimental results by both Vassdokken Sigstad (2019). Several of the experimental irregularities in the experimental RAO cannot be explained by the hydrodynamic interaction theory.

To summarize, the developed hydrodynamic theory does not explain the specific irregularities seen in the experimental results. However, a large impact from hydrodynamic interaction is observed compared to ZFT. So, it is believed that hydrodynamic interactions must have influenced the experimental RAOs, though this cannot be seen directly from this brief study.
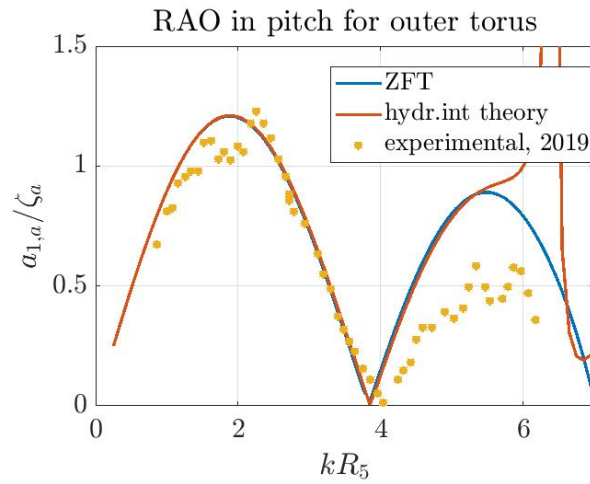
Figure 6.22: RAO in pitch for outer torus in 5-torus system
RAO in pitch for the outer torus in the 5-torus system, from both ZFT, hydrodynamic interaction theory and experiments by Vassdokken Sigstad (2019). The radius of the outer torus, R_5 is used in the non-dimensional wave number.

6.4   Final Discussion

In this chapter, potential structural interactions have been studied through the numerical solar island model, and potential hydrodynamic interactions through the newly developed theory by Kristiansen (2020). One could also study these two candidates combined, by adding cross-added mass terms into the numerical floater equations, as presented in chapter 3. This was not done simply due to time limitations.

It must also be stressed that though the presented numerical cases in Section 6.2 are quite simple in the sense that the elastic bands are modelled by only one truss each, more complex versions may easily be studied. By the developed method, all kinds of combinations of number of tori, number of elastic band connection points, trusses per elastic band and mooring-configurations are in theory possible. It is mostly due to the time spent on debugging when implementing the model in MATLAB that more trusses per elastic bands could not be presented, as was initially intended.

The presented numerical results are in fact a product of a long, spiralling process of both debugging and testing different combinations of parameter values that make the runs stable. It is a complex method, built on a large amount of equations, so that potential bugs when implementing it in MATLAB are many. We do however believe that the potential of the developed method is large, and even more so with the possibility of adding hydrodynamic interaction effects into it.

Chapter 7

Concluding Remarks and Further Work

A numerical solar island model in form of an elastic truss-model accounting for floater motion is developed, based on truss theory by Marichal (2003), the ZFT floater-model by Faltinsen (2011), modified beam equation by Li (2017) as well as methods for combining the truss and floater model by Kristiansen (2012). Elements of all the mentioned theories are adjusted to best fit the multi-torus structure of the solar island, as they are all originally based on fish-case structures. The resulting solar island model is quite complex, and can in theory be applied to model all kinds of combinations of number of tori, elastic band connections, number of trusses per elastic band and mooring-configurations of a multi-torus structure. This is a significant development, as previous studies seem to have focused on single floaters.

The numerical solar island is implemented in MATLAB, and verification studies are carried out for a single moored torus where the mooring-lines are modelled by elastic trusses. Satisfactory effect of Rayleigh damping and ramping is assured to damp out the excitation of natural frequencies of the floater. Vertical modes, surge and radial modes are studied separately, and also some cases of combined motion. Resulting RAOs for the vertical modes are in good accordance with ZFT. For the surge-study, satisfactory effect of the trusses is assured by comparing the resulting motion with the case of rather using a mooring-line stiffness term by Faltinsen (1993). The resulting RAO is is in accordance with theory. For the radial modes, it is found that all modes except the ones divisible by four get reasonable numerical RAOs. The reason for the unrealistic RAOs is that the generalized truss-forces in the problem-modes get an impulse-like behaviour from the very start of the runs. These modes should therefore be excluded, and including only modes 2 and 3 is seen as sufficient. For the combined motion cases, where heave, surge and radial mode 2 are activated, reasonable resulting motions are seen for all of the three different wave-frequencies that are tested. Though the single moored floater case could be studied more in detail, the promising results were at the time seen as a good basis for expanding to several tori.

The hydrodynamic interaction theory by Kristiansen (2020) is also implemented in MATLAB for a 2-torus case, and the cross-coupled added mass terms show good correspondence to previously obtained results in WAMIT. Off-diagonal terms are found to be zero in a study of the four lowest vertical modes.

The numerical results from the 2-torus and 5-torus cases show some, but little effect on vertical modes, more for radial modes, while the largest effect is seen for surge motion. For the 2-torus case, the surge RAOs are shifted significantly to the right, while for the 5-torus case the shapes are drastically changed with peaks at $kR_5 \simeq 4.9$ for all tori. Lowering the pre-tension in the connecting trusses lowers these peaks, as well does introducing Rayleigh damping for surge motion when adding mooring-lines to the problem. The tendency of a common natural frequency in this kR_5 area is not expected. It could be a result of structural interaction, but it is rather believed to be due to a numerical problem of some sort or perhaps an effect of how the trusses are modelled.

The instability in tension observed in some numerical runs is believed to come from a simple bug in the code, numerical instability of some sort, or again how the trusses are modelled. Though this instability

tendency may be linked to the strange observations for surge in the 5-torus case, it is not believed to have destroyed the rest of the presented RAOs.

The irregularities in the experimental RAOs by Vassdokken Sigstad (2019) and Winsvold (2018) cannot be directly explained by our numerical solar island model or the results from hydrodynamic interaction theory. The fact that the elastic bands of the experimental model were found to actually not follow Hooke's law weakens the numerical models potential of explaining the experimental irregularities. Nevertheless, deviations from single floater theory due to what should be structural interactions are seen in the numerical results, and large impact is also seen for vertical modes in the hydrodynamic interaction study. These are interesting results in themselves, and indicate that both structural and hydrodynamic interaction may affect the behaviour of a multi-torus.

7.1   Further Work

The presented studies in this master thesis can be pursued further in many areas. Some of them will be presented here.

7.1.1   Further Use of Numerical Solar Island Model

There is great potential in the developed numerical solar island model. Although the elastic bands of the experimental model were found to not follow Hooke's law, it could still be relevant in future studies. Strong points are that it accounts for motion in both vertical and lateral modes, and the possibility to include hydrodynamic interaction. Potentially, a spider-web like system of trusses could be modelled across the tori to represent a membrane type of deck.

Should however this model be used further, it is recommended that more detailed verification studies are performed, such as a time-step study also for the single-floater combined motion case as well as multi-torus cases. The sensitivity of other parameter-values should also be studied in more detail, such as ramping, pre-tension and stiffness. It would also be wise to have a closer look at the truss-force expression used in the Euler beam equations, as it is in fact a coarse approximation when the spacing between elastic bands on a floater is large.

Further, the modelling of an elastic band by several trusses must be checked. A proposition is to focus on a chain of elastic trusses fixed in each end, and see whether the resulting motion follows the fundamental frequency of an uniform string fixed in both ends.

7.1.2   Experimental Model and Tank Wall Interference Effects

Should new model tests be performed for the multi-torus structure, one could potentially replace the elastic bands by new ones that more accurately follow Hooke's law, and do not loose their flexibility as easily. Preferably, the experimental pre-tension in the bands should be estimated. This would make it easier to model the structure numerically. Though it is not believed to effect the behaviour of the structure in any significant manner, the mass of the floaters could be increased so that they float halfway submerged.

Li (2017) discusses tank-wall interference effects possibly contaminating experimental test results in his study on an elastic fish cage floater. The torus diameter was 1.5 m and the tank width 6.45 in his set-up, and it was discussed that there in fact would potentially be some minor tank wall interference. Considering the torus diameter was quite similar, 1 m, but the tank width only 2.5 m in the model tests by Vassdokken Sigstad (2019) and Winsvold (2018), such effects can possibly have influenced their experimental results. So, this is also a candidate for the irregularities in the experimental RAOs. This can be further studied in WAMIT version 7.3 that has recently been released.

7.1.3 New Simplified Model for Elastic Bands

An alternative to the solar island truss model presented in this master thesis is of course preferable. It has proven complicated to implement and requires very small time-steps to be stable.

At the very end of working on the master thesis, discussions between Professors Odd M. Faltinsen and Trygve Kristiansen resulted in a proposition for a new, simplified model for the elastic bands. They are still assumed to be strings following Hooke's law, as an initial, first step in developing the method. Vertical motions only are considered. Observing the structure from the side, the tension of the elastic bands can then actually be found directly by geometrical relations. This is illustrated in Figure 7.1, showing a truss between the outer torus 1 and inner torus 2. As seen, the vertical tension-component in the truss is given by $T_z = T_0 \tan \alpha \approx T_0 \alpha$ for small angles α, T_0 being the initial pre-tension. The angle is in its turn given by $\sin \alpha \approx \alpha = (w_2(\beta, t) - w_1(\beta, t))/l_0$, where $w1$ and w_2 are the vertical position of the end nodes of the string and l_0 the initial length.

(a) 3D view   (b) Seen from the side
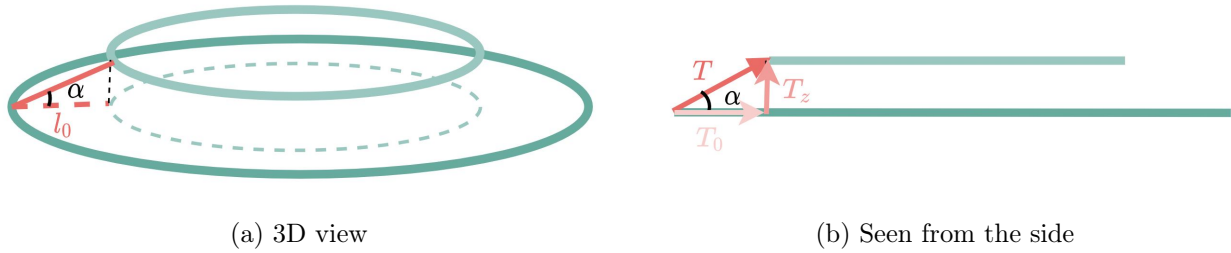
Figure 7.1: Alternative model for elastic bands

With this, the generalized truss force to be included in the generalized vertical beam equation for a torus k can rather be expressed as

$$f_{k,3}^{truss,gen} = \int_0^{2\pi} \sum_p \sum_{i=1}^{N_p} \frac{T_0}{l_0} \left(w_p(\beta, t) - w_k(\beta, t) \right) \cos(n\beta) d\beta \tag{7.1}$$

where the first sum is over neighbouring trusses p and the next over all the N_p elastic bands between torus p and the studied torus k. $N_p = 8$ in the experiments, for example.

The unknowns in the floater system of equations will now lie in expressions of this type for each torus. This has to be solved either in an implicit manner, or one could use the pragmatic solution of using values from the previous time-step for the vertical node-motions w_p and w_k.

This new model for elastic bands is more efficient and easier to implement than the one studied in this master thesis, and should be studied further as a candidate to the current model.

Bibliography

Dietmar. Gross, Wolfgang. Ehlers, Peter. Wriggers, Jörg. Schröder, and Ralf. Müller (2017). *Mechanics of Materials – Formulas and Problems: Engineering Mechanics 2* (1st ed. 2017. ed.). Berlin, Heidelberg: Springer Berlin Heidelberg : Imprint: Springer.

Faltinsen, O. (1993, September). *Sea Loads on Ships and Offshore Structures.* Cambridge University Press. Google-Books-ID: qZq4Rs2DZXoC.

Faltinsen, O. M. (2010). Current and wave loads on floating fish farms. Technical report, CeSOS. Preliminary.

Faltinsen, O. M. (2011). Hydronamic aspects of a floating fish farm with circular collar. Technical report, Centre for Ships and Offshore Structures & Department of Marine Technology, NTNU, Trondheim, Norway.

Faltinsen, O. M. and T. Kristiansen (2015). Experimental and numerical study of an aquaculture net cage with floater in waves and current. *Journal of Fluids and Structures 54*, 1–26.

Faltinsen, O. M. and P. Li (2012). Wave-induced vertical response of an elastic circular collar of a floating fish farm. In *10th International Conference on Hydrodynamics*, Volume 2, St. Petersburg, Russia, pp. –.

IEA (2017). International energy outlook 2019. Technical report, U.S. Energy Information Administration, Washington,DC 20585.

Kristiansen, T. (2012). Linearized hydroelastic theory of circular floater in "fishFarm" Fortran code. PostDoc, NTNU. PostDoc.

Kristiansen, T. (2020). Unpublished. Technical report, NTNU, Trondheim.

Kristiansen, T., C. Lugni, T. Søreide, H. S. Alsos, and J. Birknes-Berg (2017). Floating marine structures for harvesting solar energy to power synthetic carbon-neutral fuel production from recycled co2. unpublished preposal to martera. Technical report.

Kristiansen, T. and J. Winsvold (2019). Unpublished -investigation of a flexible multi-torus solar island. Technical report, NTNU, Trondheim.

Li, P. (2017). A Theoretical and Experimental Study of Wave-induced Hydroelastic Response of a Circular Floating Collar. Technical report, Norwegian University of Science and Technology, Faculty of Engineering Science and Technology, Department of Marine Technology, Trondheim.

Marichal, D. (2003). Cod- end numerical study. In *Proceedings of the 3rd International Conference on Hydroelasticity in Marine Technology*, Oxford, United Kingdom.

Marino, E., J. Kiendl, and L. De Lorenzis (2019). Explicit isogeometric collocation for the dynamics of three-dimensional beams undergoing finite motions. *Computer Methods in Applied Mechanics and Engineering 343*, 530–549.

Patterson, B. D., F. Mo, A. Borgschulte, M. Hillestad, F. Joos, T. Kristiansen, S. Sunde, and J. A. v. Bokhoven (2019, June). Renewable CO2 recycling and synthetic fuel production in a marine environment. *Proceedings of the National Academy of Sciences 116*(25), 12212–12219.

Rao, S. S. (1995). *Mechanical Vibrations*. Addison-Wesley. Google-Books-ID: 7XceAQAAIAAJ.

Strang, G. and E. Herman (2016). *Calculus Volume 3*. Houston, Texas: OpenStax.

Vassdokken Sigstad, M. (2019, June). A Numerical and Experimental Study of a Multi-torus Solar Island Concept. Master thesis, NTNU, Trondheim.

Winsvold, J. (2018). An Experimental Study on the Wave-Induced Hydroelastic Response of a Floating Solar Island.

Appendix A

Additional Theory

A.1 Fundamental Frequency of Vibration for a Fixed String

The fundamental frequency f of transverse vibration for a pre-tensioned string fixed in both ends is given by

$$f = \frac{1}{2l}\sqrt{\frac{T}{\mu}} \tag{A.1}$$

where l is the pre-tensioned length of the string, T the tension and μ the density of the truss material Rao (1995). This can be used to estimate the fundamental frequency of the elastics in the solar island model. The more trusses per elastic, the more the lumped mass system begins to resemble a uniform string, and thus the more fitting Equation (A.1) will be for a modeled elastic.

Appendix B

Simple Truss Verification Study

A verification study was performed for the truss model in the preliminary project thesis during fall of 2019. A set of simple truss cases, both elastic and inelastic were tested. The study on the elastic cases will be presented briefly here.

B.1 Set-Up

There are two verification cases for the elastic truss model, namely a spring-mass system and an elastic pendulum. These are illustrated in Figure B.1, and the boundary conditions are listed in Table B.1.

(a) Spring -mass system

(b) Elastic pendulum
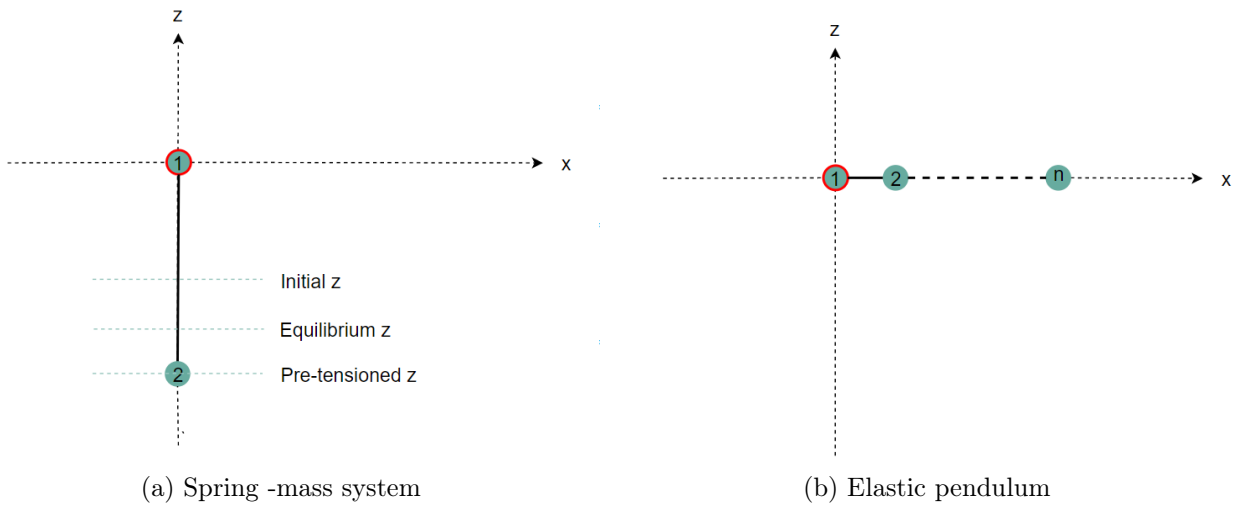
Figure B.1: Elastic verification cases
Initial geometry is illustrated. Red denotes fixed node. *Initial Z* is node 2 position without point mass, *equilibrium Z* is the position with point mass added and in equilibrium with spring tension, and *pre-tensioned Z* is the pre-tensioned position from which the point mass is released.

Table B.1: Boundary conditions - elastic cases

	Vertical pre-tensioned spring	Elastic pendulum
Node 1	Fixed	Fixed
Node n	Free	Free

Marino et al. (2019) presents an explicit numerical solution for an elastic pendulum using beam elements. The resulting displacement and deformation show good correspondence with other relevant

articles using both implicit and explicit numerical methods. Therefore, the parameter values for the elastic pendulum case are set to be equal that of the one presented in Marino et al. (2019). These are listed in Table B.2, E is Young's modulus, D the diameter of the truss, ρ the density of the truss and T_p the pre-tension of each truss. The mass of the truss is found from the cross-sectional area and density of the truss. This assures a realistic relationship between mass and stiffness.

Table B.2: Parameter values - elastic pendulum

t_{end} [s]	dt [s]	$N_{trusses}$ [-]	θ_0 [rad]	m_{truss} [kg]	l_{truss} [m]	E [$\frac{N}{m^2}$]	D [m]	ρ [$\frac{kg}{m^3}$]	T_p [N]
1	10^{-5}	30	90	$2.9 \cdot 10^{-3}$	$1/30$	$5 \cdot 10^6$	0.04	1100	0

The parameter values used for the spring-mass system case are as listed in Table B.3, where l_{0truss} is the natural, initial length of the truss, T_p the pre-tension and dl the elongation of the truss that leads to this pre-tension. Note that this case is equal to a mass-less spring with a point mass $m_{truss}/2$ kg at the end.

Table B.3: Parameter Values - Spring-Mass System

t_{end} [s]	dt [s]	$N_{trusses}$ [-]	m_{truss} [kg]	k [N/m]	l_{0truss} [m]	T_p [N]	dl [m]
10	$10^{-4}, 10^{-5}, 10^{-7}$	1	1	1000	1	9.81	$4.9 \cdot 10^{-3}$

The elongation is set to be equal to the distance between the initial and equilibrium positions. With this, the point mass should oscillate around the equilibrium position, and be bounded by the initial and pre-tension positions. So, the value is set to $dl = m_{truss}g/2k$, and thus the pre-tension is $T_p = m_{truss}g/2 + kdl$. See Appendix B.3.1 for an illustration of a general spring-mass system.

B.2   Results

Figure B.2 shows the elastic pendulum at several time instances during the first second, while Figure B.3 shows the vertical displacement of the tip during the same period. It is observed that the length of the trusses are no longer constant, as anticipated having included elasticity.

The corresponding figures for the elastic beam pendulum of Marino et al. (2019) are added in Appendix B.3.2. Comparing our results with these, it is seen that the correspondence is generally good. However, since the truss model does not include bending stiffness, which the beam model does, the truss model bends more at the tip and the angles are changing more brutally between the elements. All in all, the implementation of the elastic pendulum case is thought to be successful.
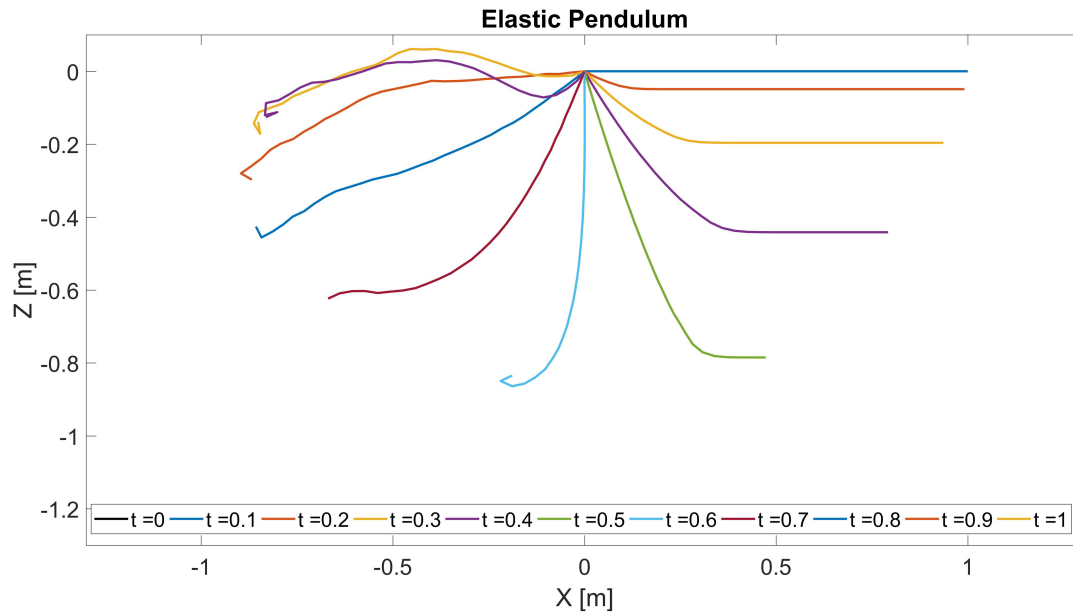
Figure B.2: Elastic pendulum during the first second
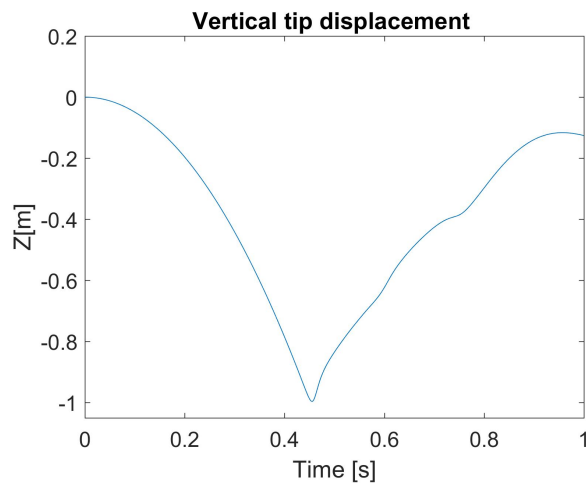
Figure B.3: Vertical tip displacement of elastic pendulum

Figure B.4 shows the time-series for the point-mass displacement for a time-step of 10^{-4} seconds. As seen, the point mass oscillates around the equilibrium position, bounded by the initial and pre-tension positions. In this manner it behaves as one intended when setting the elongation value in Table B.3. However, the oscillation is rapidly damped out, which it should not be since there is no damping in the system. This must then come from numerical damping.
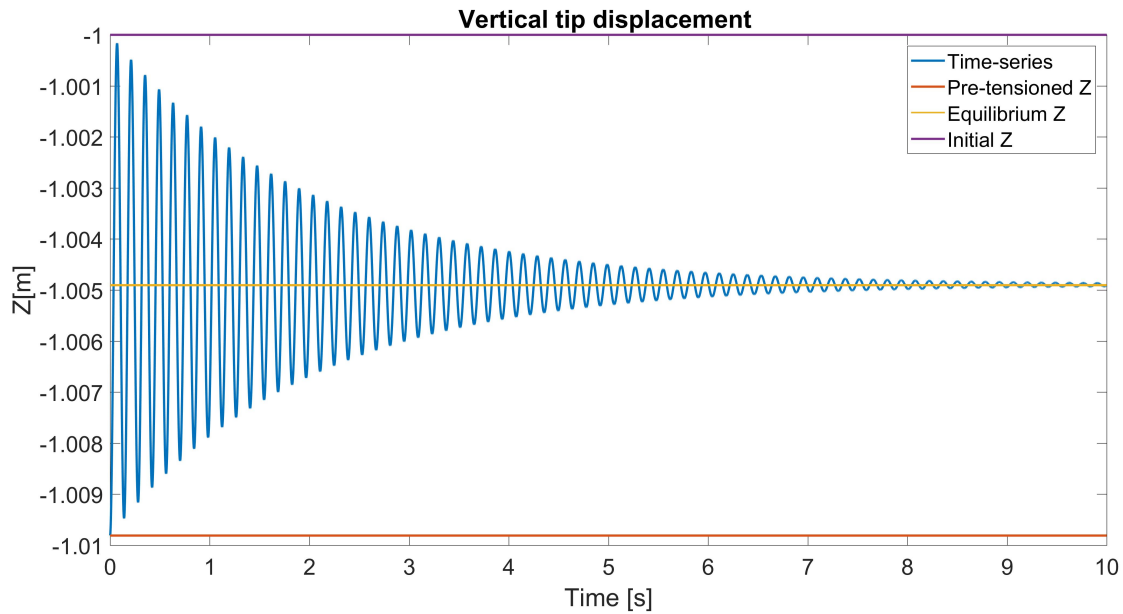
Figure B.4: Spring motion for $dt = 10^{-4}$ s

Figure B.5 and Figure B.6 show the resulting time-series for time-steps of 10^{-5} and 10^{-7}, respectively. It is observed that the damping decreases for decreased time-step, and for the smallest time-step the oscillation acts like the un-damped spring-mass system that it should. It has a harmonic oscillation with period $T_n = \sqrt{2k/m}$, and takes both compression and tension. So, the truss model describes the system in a satisfactory way as long as the time-step is small enough. A time-step of 10^{-7} seconds is of course very low, and the time-step influence should be studied more in detail.
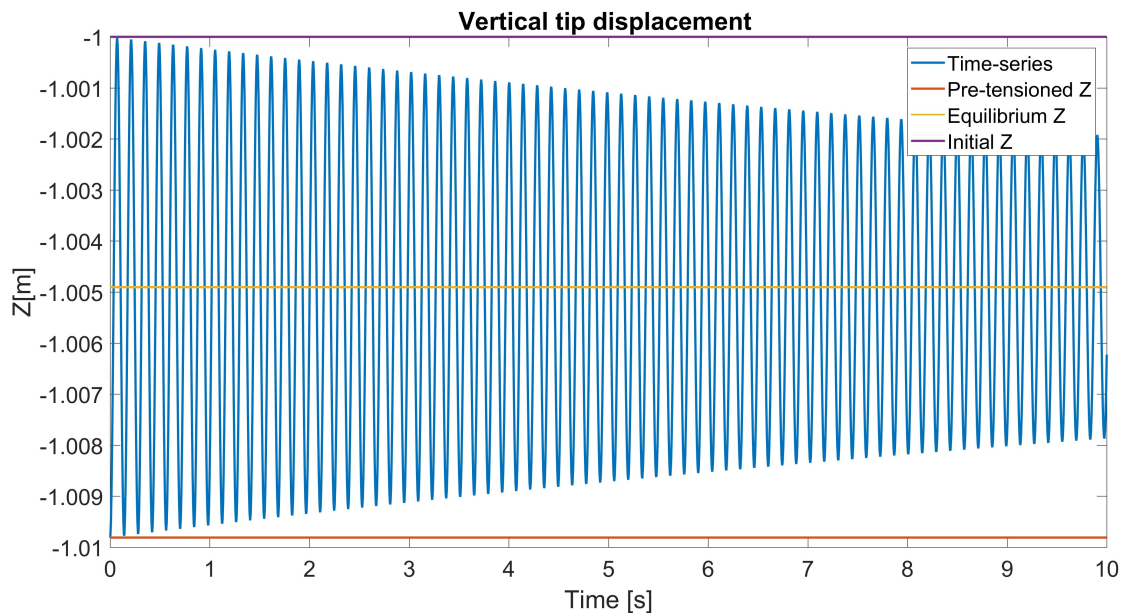
Figure B.5: Spring motion for $dt = 10^{-5}$ s
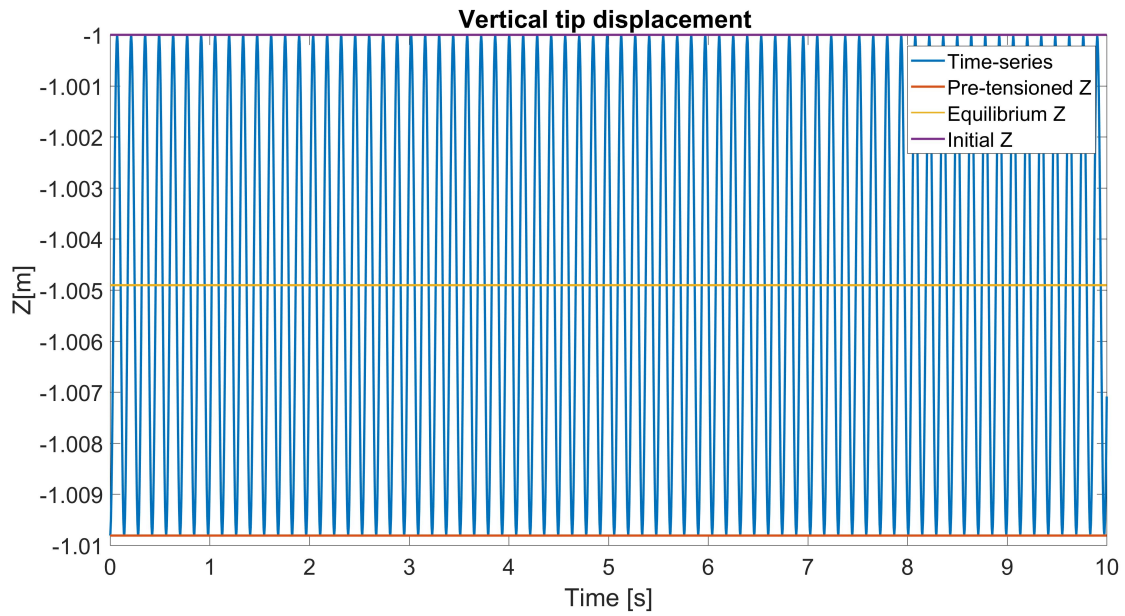
Figure B.6: Spring motion for $dt = 10^{-7}$ s

B.3   Supplement for Simple Truss Verification Cases

B.3.1   Spring-Mass System Illustration
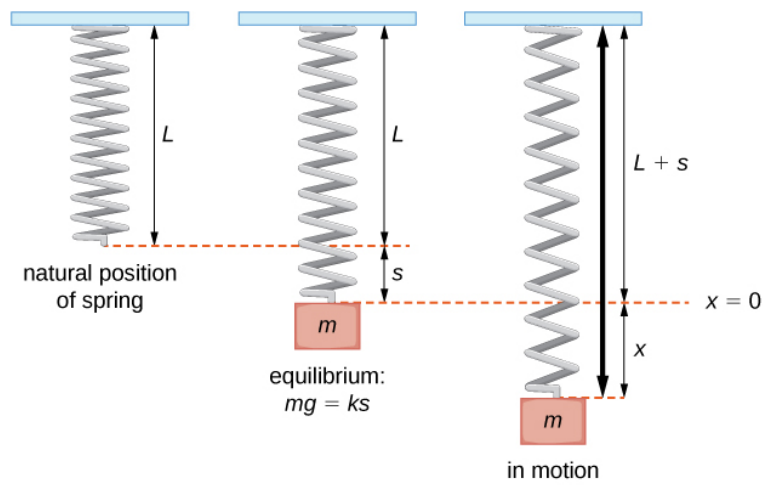
Figure B.7: General Spring-Mass System
Taken from Strang and Herman (2016)

B.3.2   Elastic Beam Pendulum
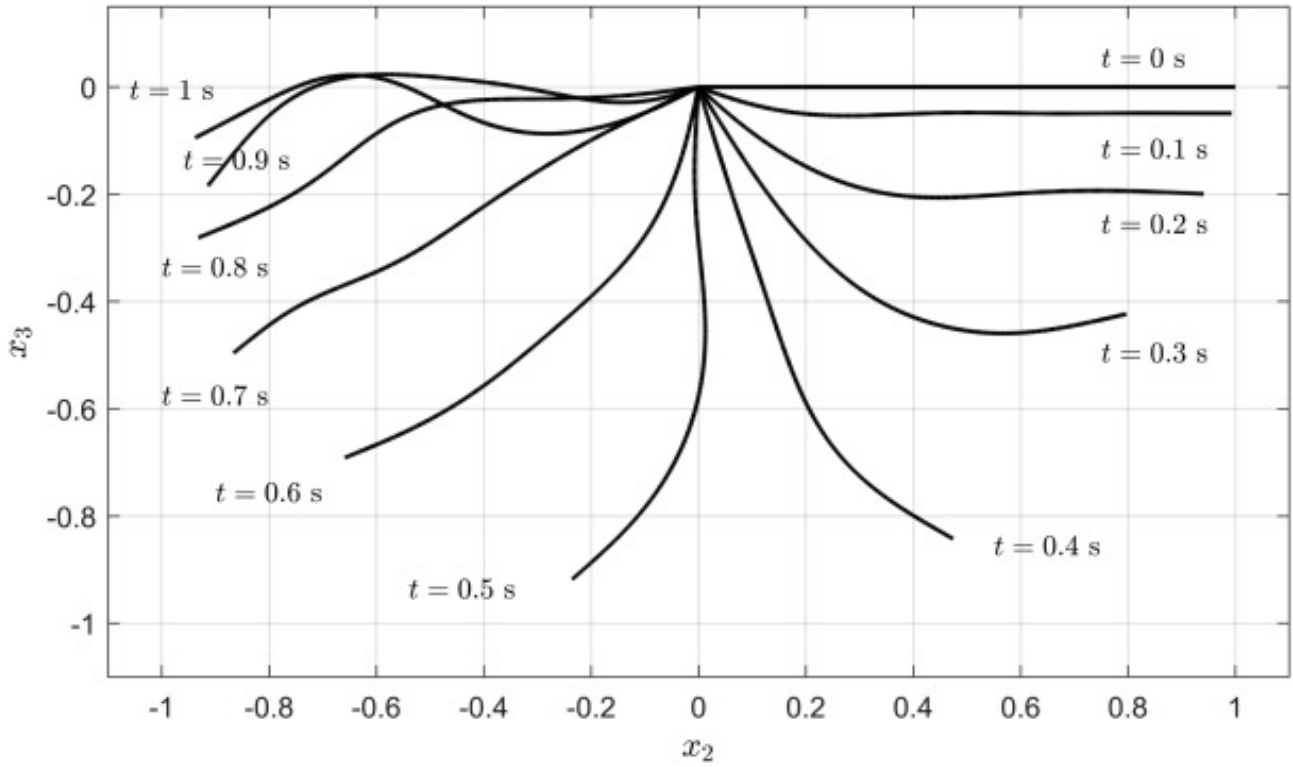
Figure B.8: Elastic Beam Pendulum During the First Second
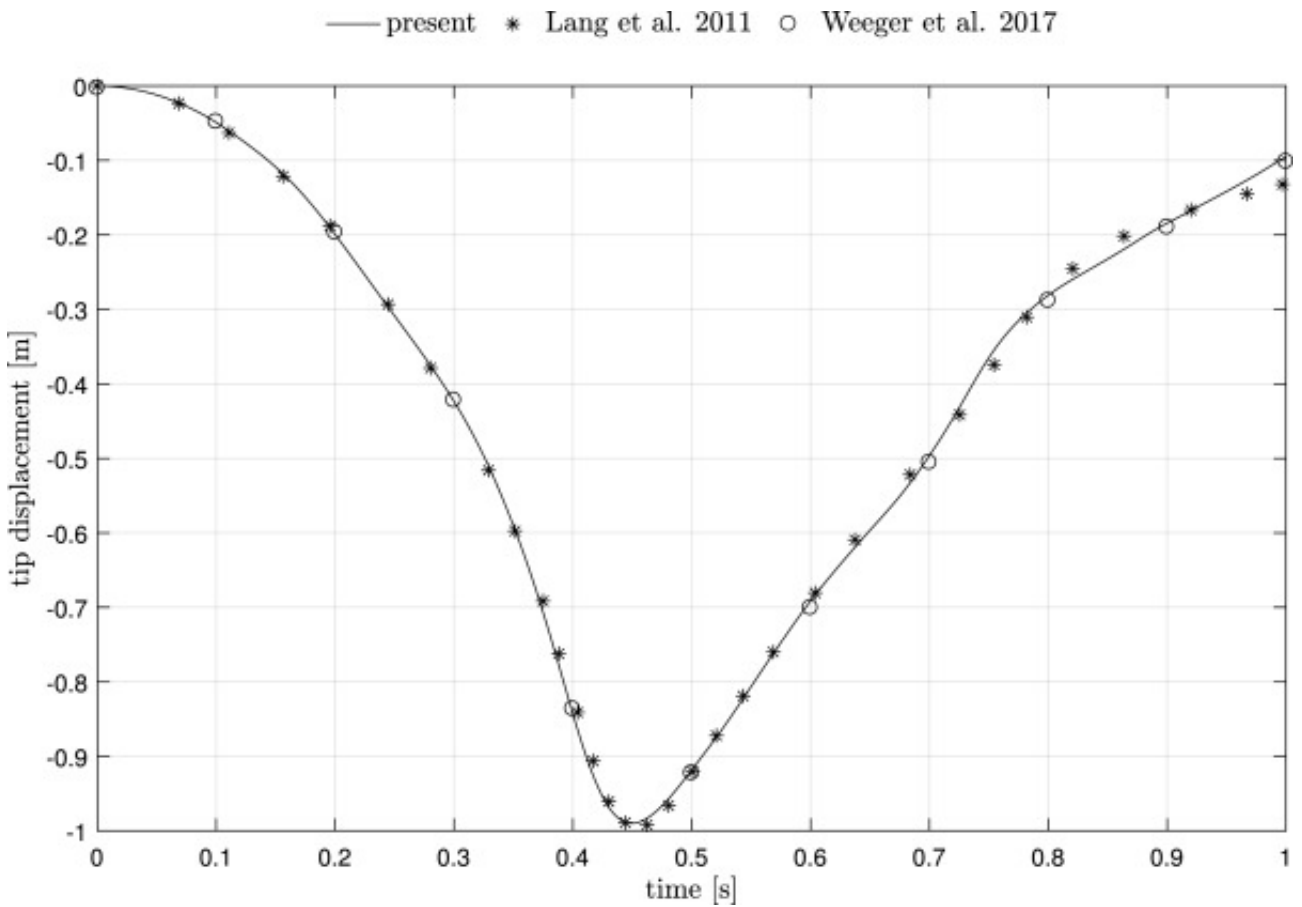
Figure B.9: Vertical Displacement at Tip for Elastic Beam Pendulum

Appendix C

Supplement for Single Floater Vertical Motion Verification

C.1 Additional Ramping and Rayleigh Damping Plots

Here are additional plots from the study of including ramping and Rayleigh damping in Section 4.2.1.

(a) No ramping or Rayleigh damping

(b) Ramping but no Rayleigh damping

(c) Rayleigh damping but no ramping

(d) Rayleigh damping and ramping
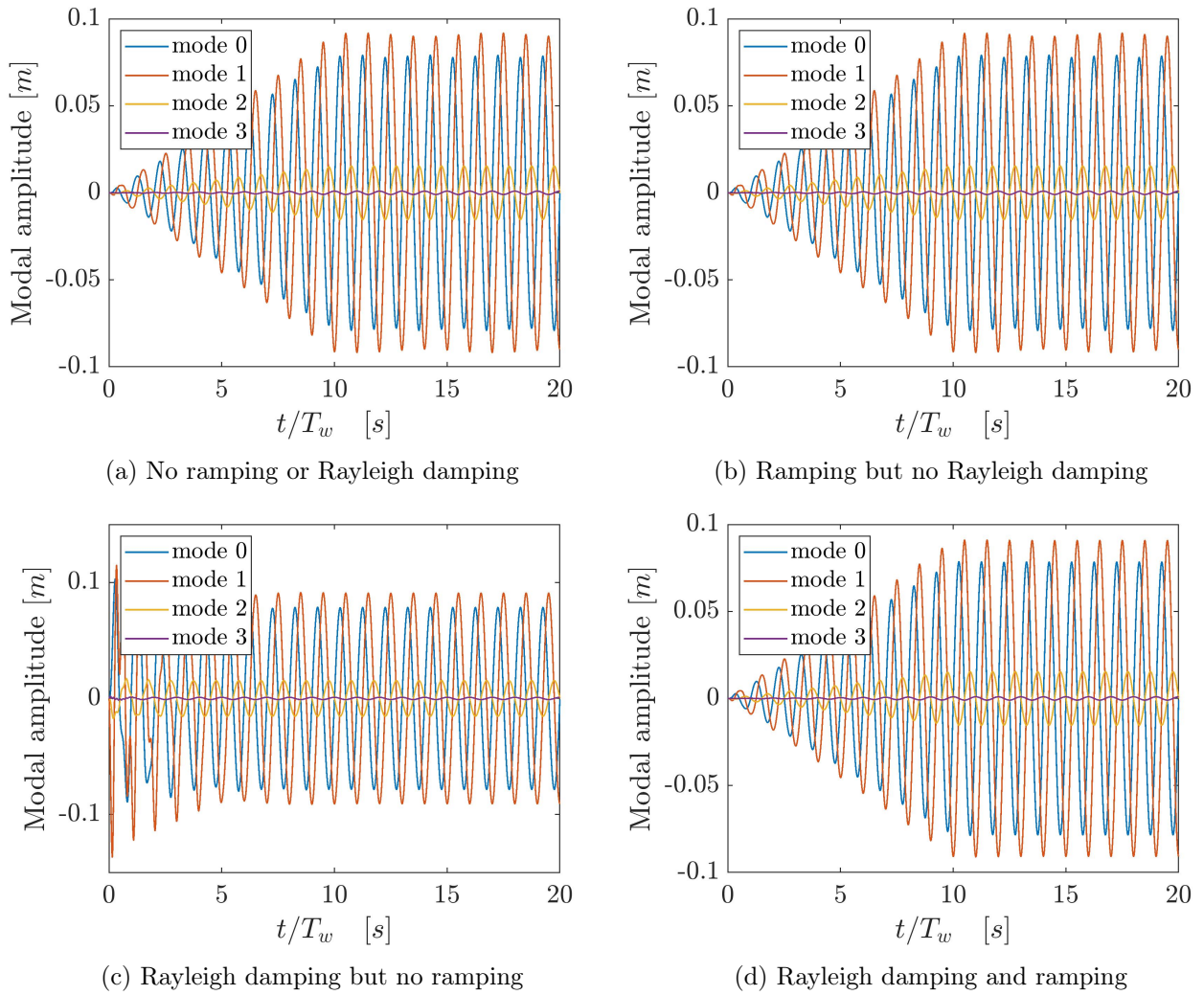
Figure C.1: Effect on modal amplitudes from ramping and Rayleigh damping
Modal amplitude time-series for all activated vertical modes $0 - 4$ are presented. The effects of ramping of the wave excitation force and Rayleigh damping of natural modes are shown from the different time-series.

(a) No ramping or Rayleigh damping

(b) Ramping but no Rayleigh damping

(c) Rayleigh damping but no ramping

(d) Rayleigh damping and ramping
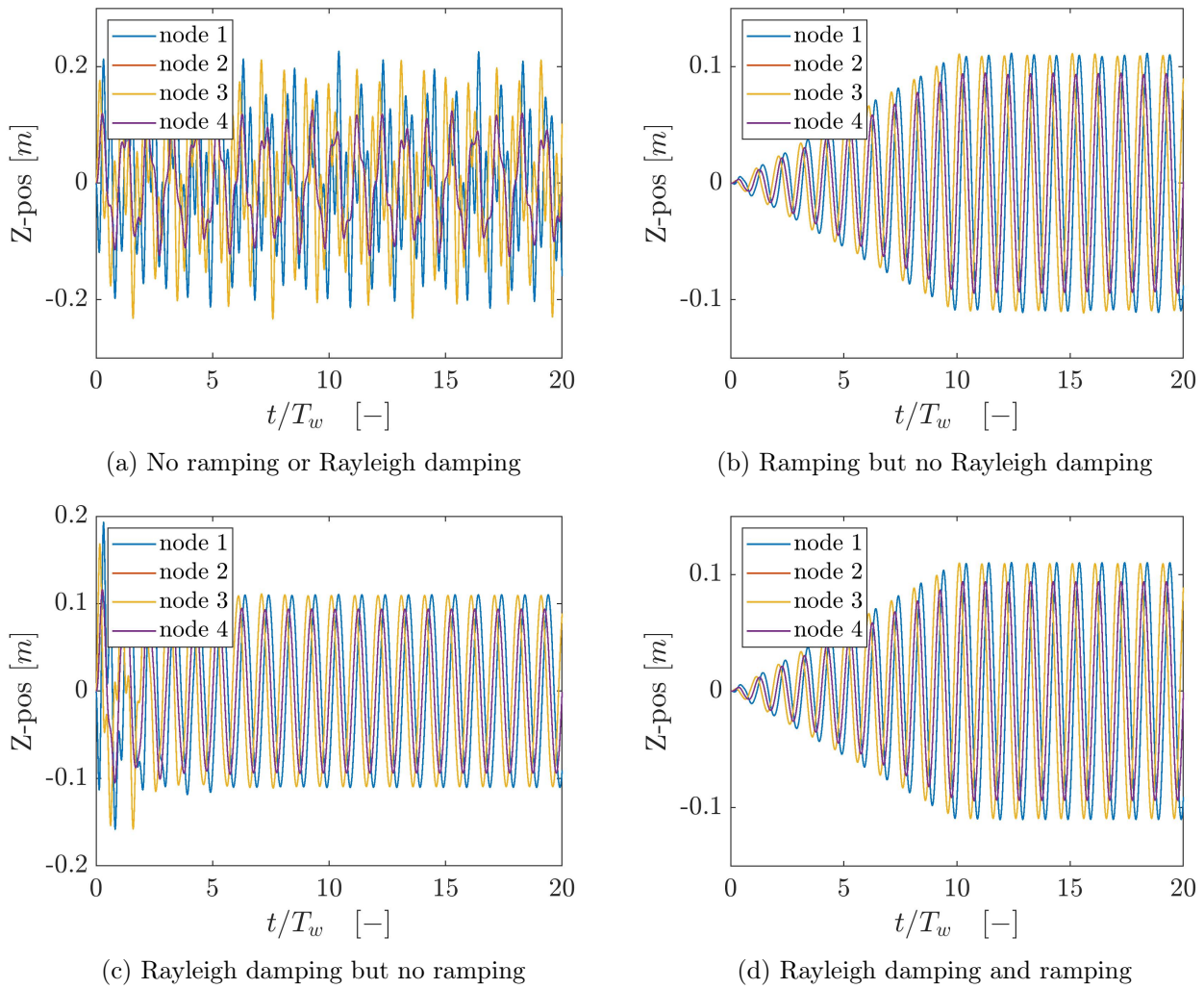
Figure C.2: Effect on Z-position from ramping and Rayleigh damping
Z-position time-series are presented, for all the for floater-nodes. The effects of ramping of the wave excitation force and Rayleigh damping of natural modes are shown from the different time-series.

C.2 Modal Amplitude for Heave at Natural Frequency in Heave

Figure C.3 is supplementary to Section 4.2.2, and illustrates the stable region to be used when taking the FFT of the mode amplitude time-series.
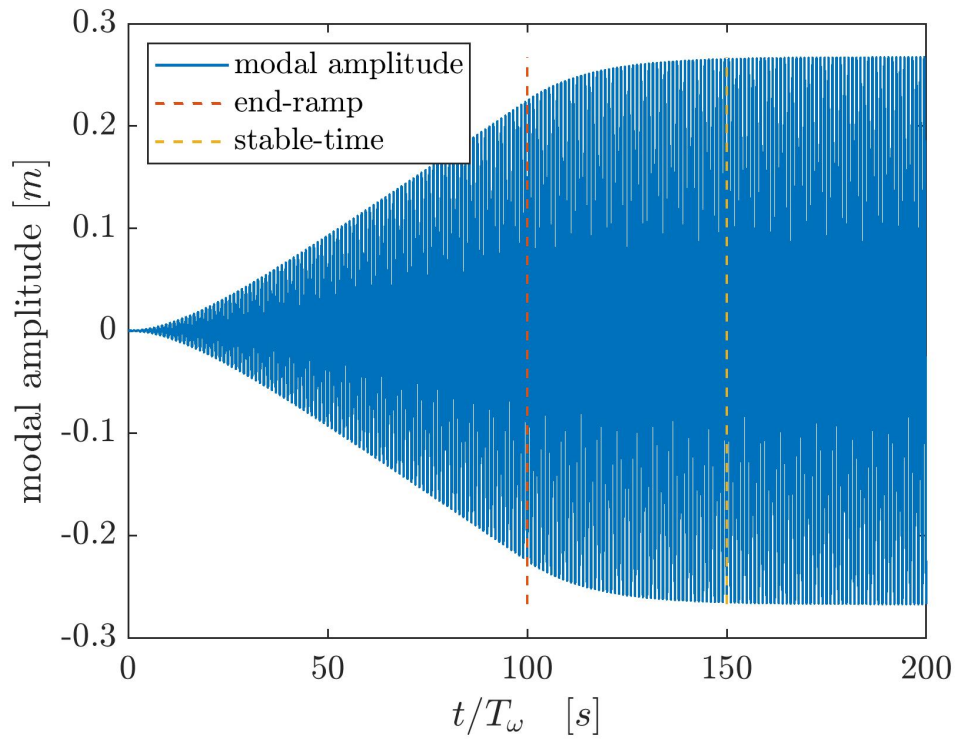
Figure C.3: Stable region illustration

Mode amplitude time-series in heave for a wave-condition at kR_n, corresponding to the floaters natural frequency in heave. *end-ramp* marks the end of ramping of the wave excitation force, while *stable-time* marks the time instant at which the stable region starts. The FFT of the signal is taken from the stable region, and from this the RAO value of the run is found.

C.3   Additional Vertical RAO Plots

(a) mode 7

(b) mode 8

(c) mode 9

(d) mode 10

(e) mode 11

(f) mode 12
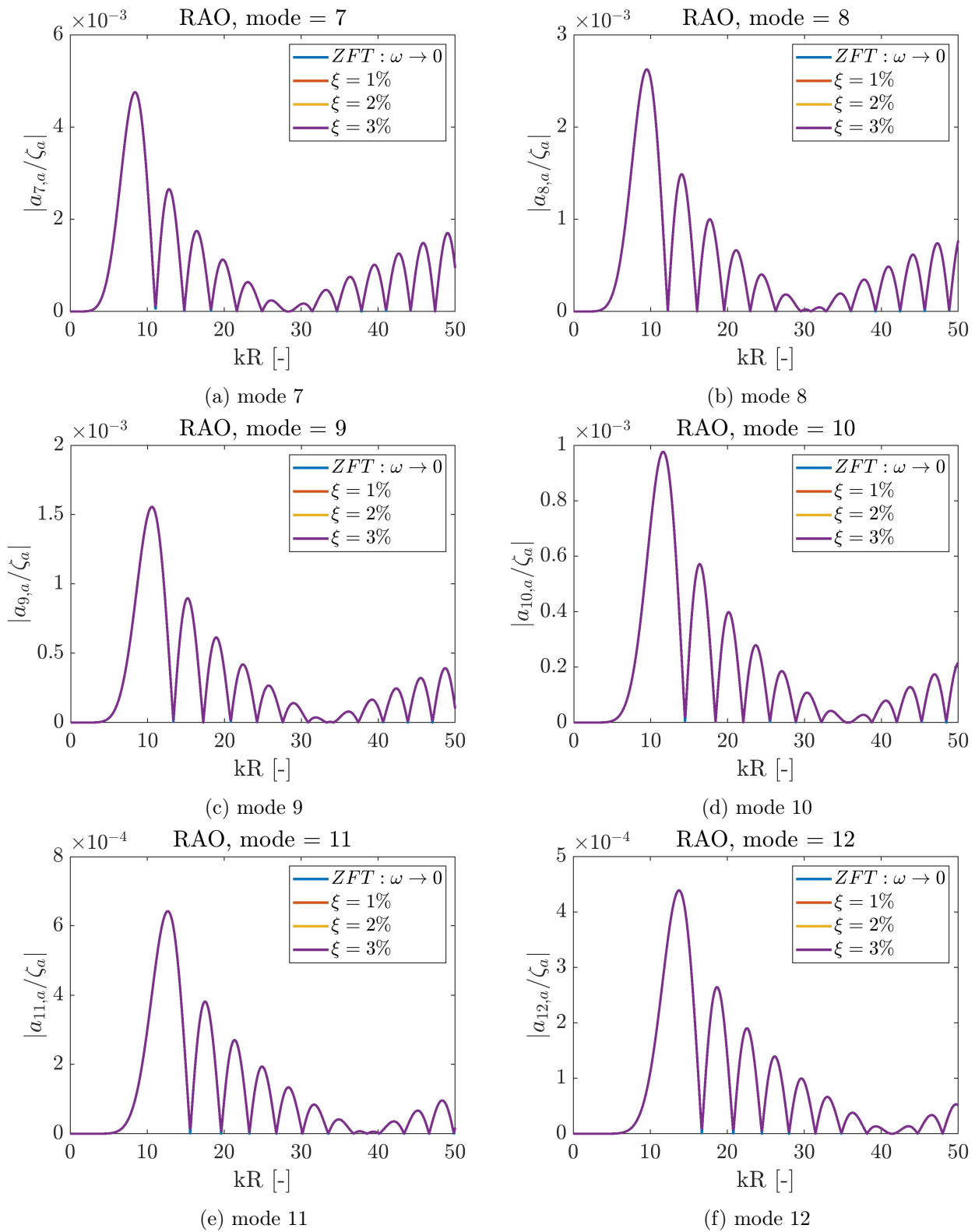
Figure C.4: RAO's for vertical modes 7-12

Numerical RAO for a single floater without trusses, plotted against the corresponding theoretical ZFT RAO, for vertical modes $7 - 12$. Rayleigh damping of $\xi = 1, 2$ and 3% are used in the numerical runs.
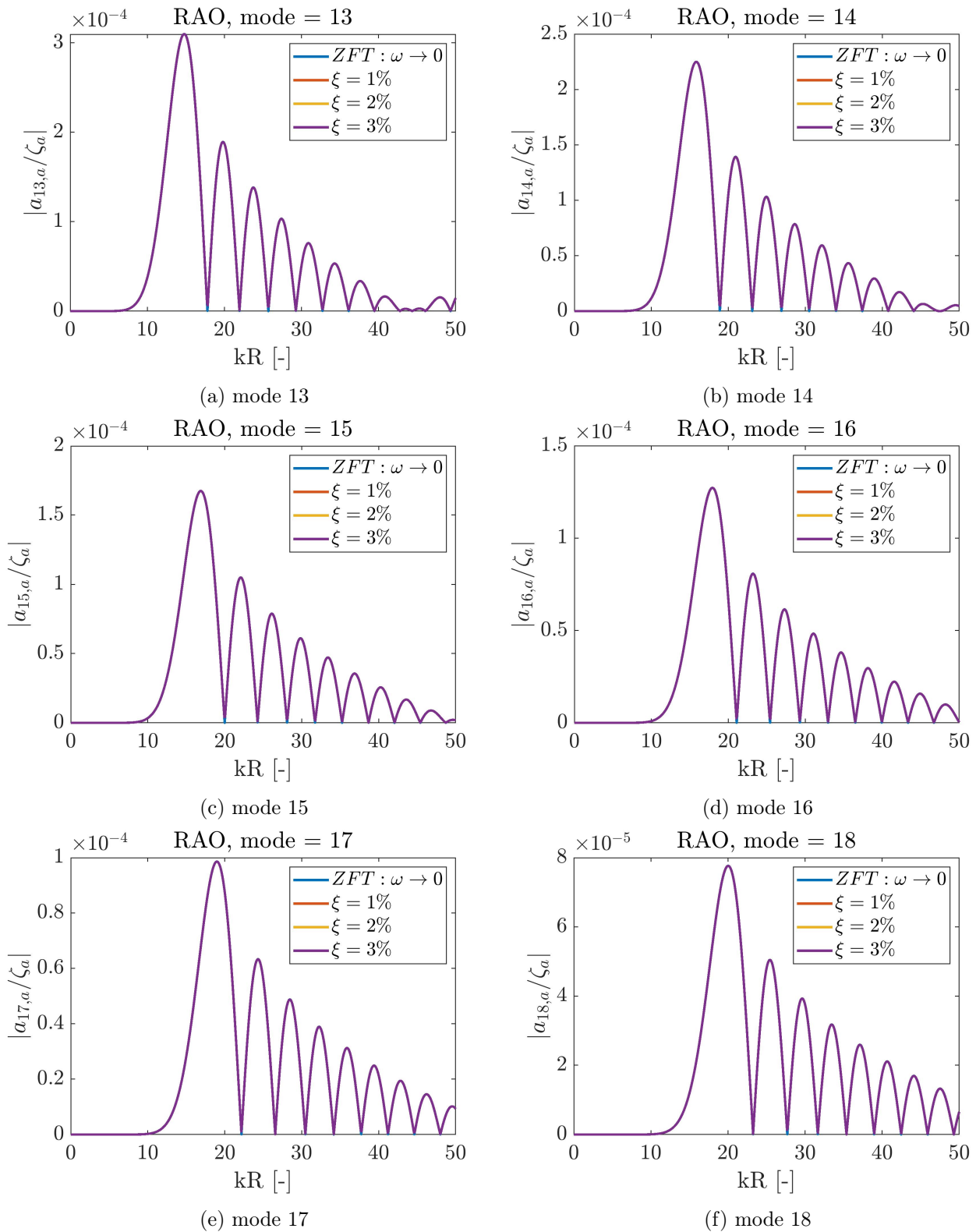
Figure C.5: RAO's for vertical modes 13-18

Numerical RAO for a single floater without trusses, plotted against the corresponding theoretical ZFT RAO, for vertical modes $13 - 18$. Rayleigh damping of $\xi = 1, 2$ and 3% are used in the numerical runs.

(a) mode 19

(b) mode 20
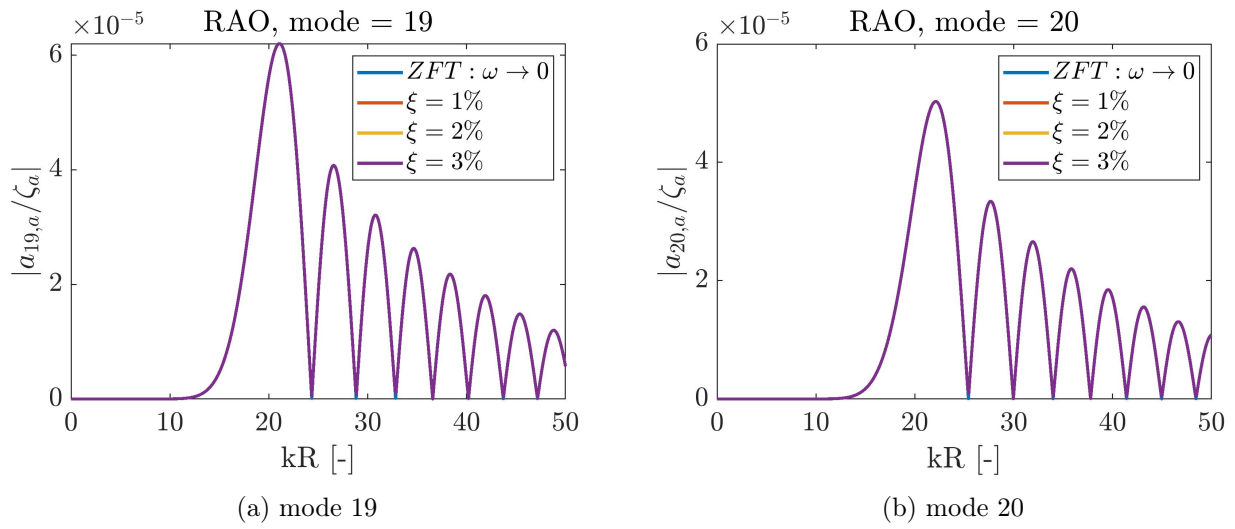
Figure C.6: RAO's for vertical modes 19-20
Numerical RAO for a single floater without trusses, plotted against the corresponding theoretical ZFT RAO, for vertical modes $19 - 20$. Rayleigh damping of $\xi = 1, 2$ and 3% are used in the numerical runs.

Appendix D

Supplement for Single Floater Lateral Motion Verification

D.1 Effect of mooring-line stiffness on theoretical RAO in Surge

Figure D.1 shows theoretical RAOs for a single floater, moored floater with 4 mooring-lines, at $\beta = 0, \pi/2, \pi$ and $3\pi/2$ rad, respectively. Two different values of mooring-line stiffness, k_m, are tested. It is seen that the RAO peak shifts to the left as the mooring-line stiffness decreases, which is in accordance with the natural frequency expression for surge.
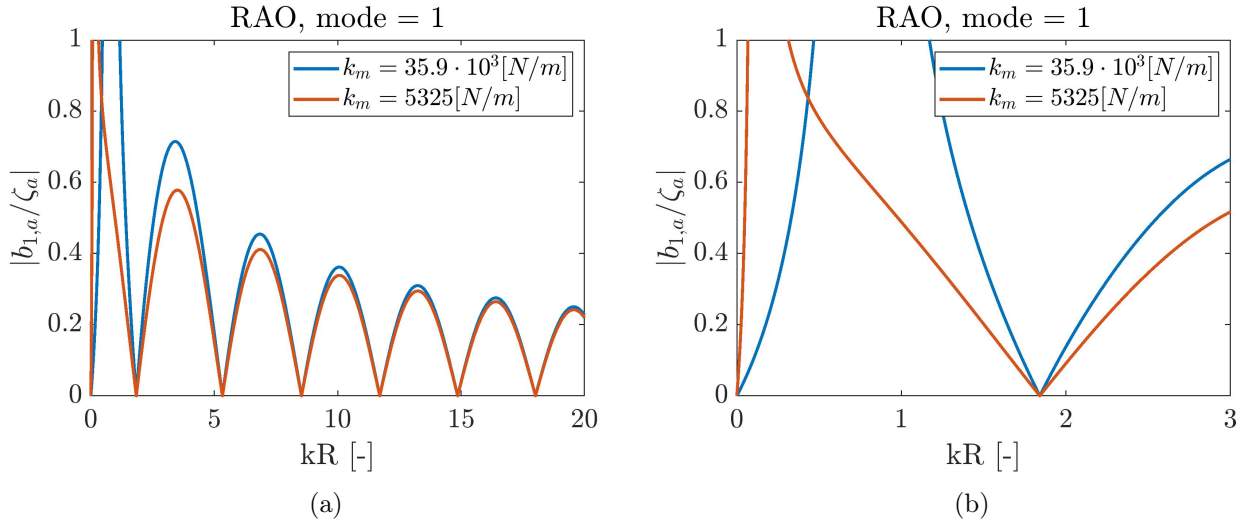
Figure D.1: Effect of mooring-line stiffness on ZFT surge RAO
Theoretical RAOs for a single floater with 4 mooring-lines, at $\beta = 0, \pi/2, \pi$ and $3\pi/2$ rad, respectively. Two different values of mooring-line stiffness, k_m, are tested. a) shows the full kR-range, while b) is zoomed in around the are of natural frequencies.

D.2 Time-step Study of radial Mode 20

This is a supplement to the verification study of radial mode 2 in Section 4.4.1. Figure D.2 shows the resulting RAOs for radial mode 20 using two different time-steps, $dt = 0.005$ and 0.0005 s, plotted against the corresponding theoretical RAO.
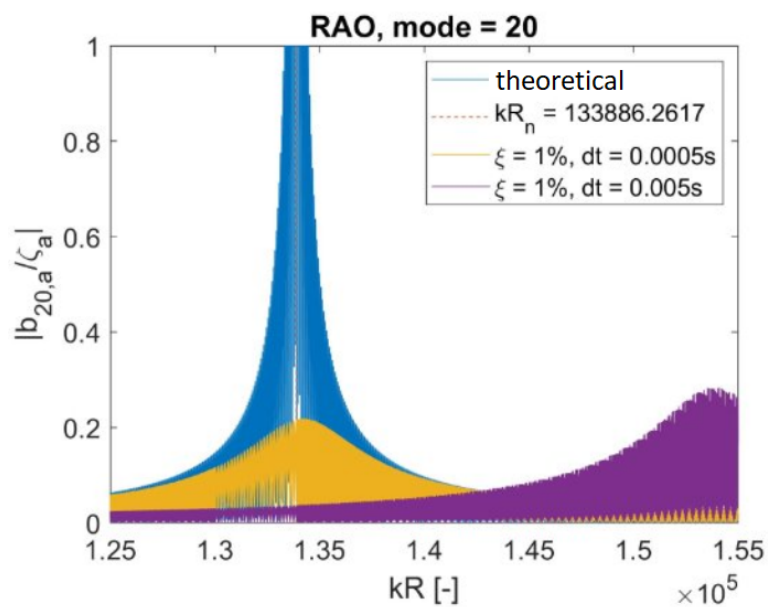
Figure D.2: Time-step study for radial mode 20
The kR range around the natural frequency of the mode is shown. Resulting RAOs from runs with $dt = 0.005$ and 0.0005 s are plotted against the corresponding theoretical RAO.

D.3 Damped RAOs for Radial Modes

(a) Mode 3

(b) Mode 3 zoomed in around kR_n

(c) Mode 4

(d) Mode 5

(e) Mode 6

(f) Mode 7
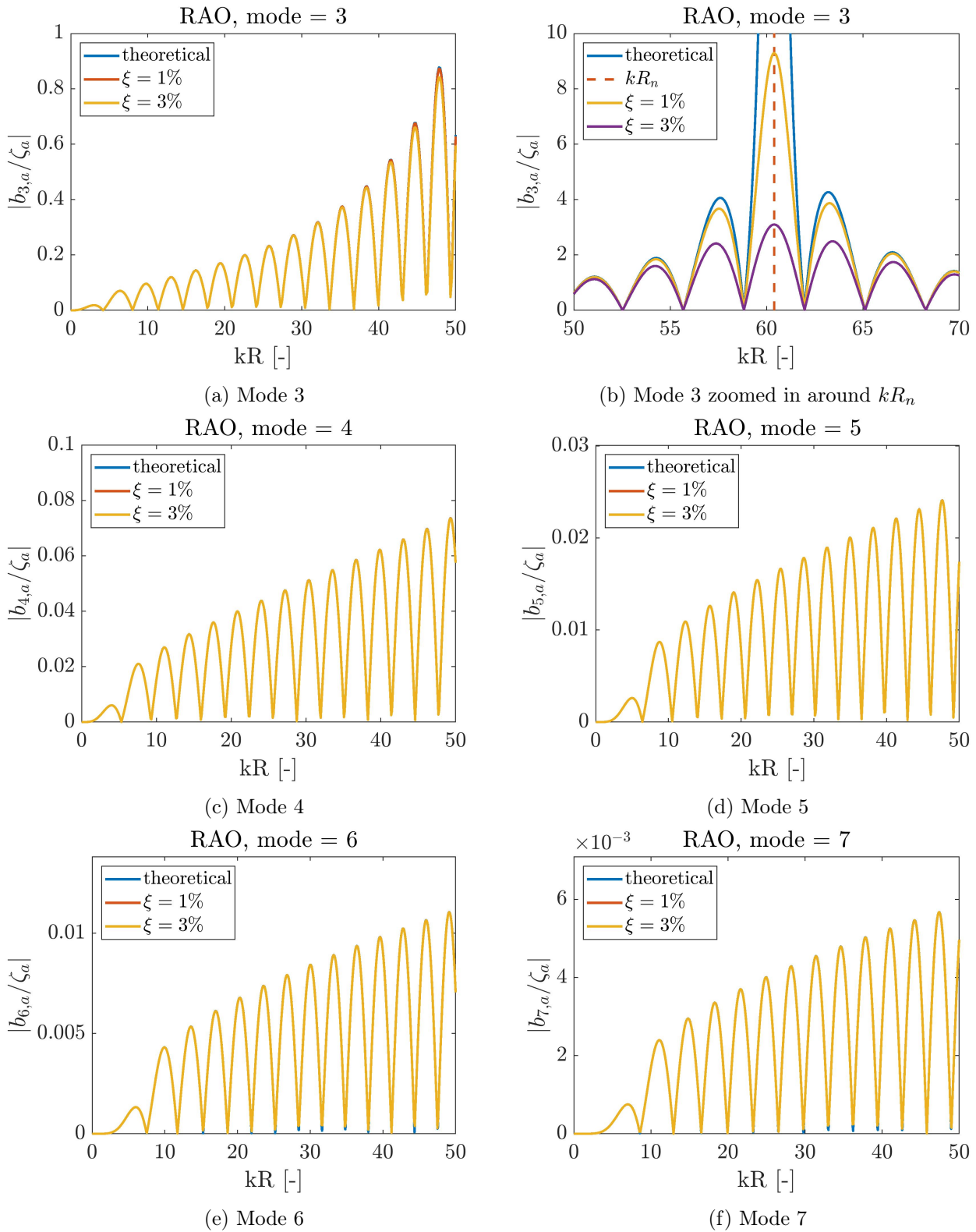
Figure D.3: Damped RAOs for radial modes 4-7

RAOs for a single floater without mooring-lines for Rayleigh damping values of 1 and 3%, plotted against the corresponding theoretical RAO. Figure b) is the same plot as in a), just zoomed in around kR_n.

(a) Mode 8

(b) Mode 9

(c) Mode 10
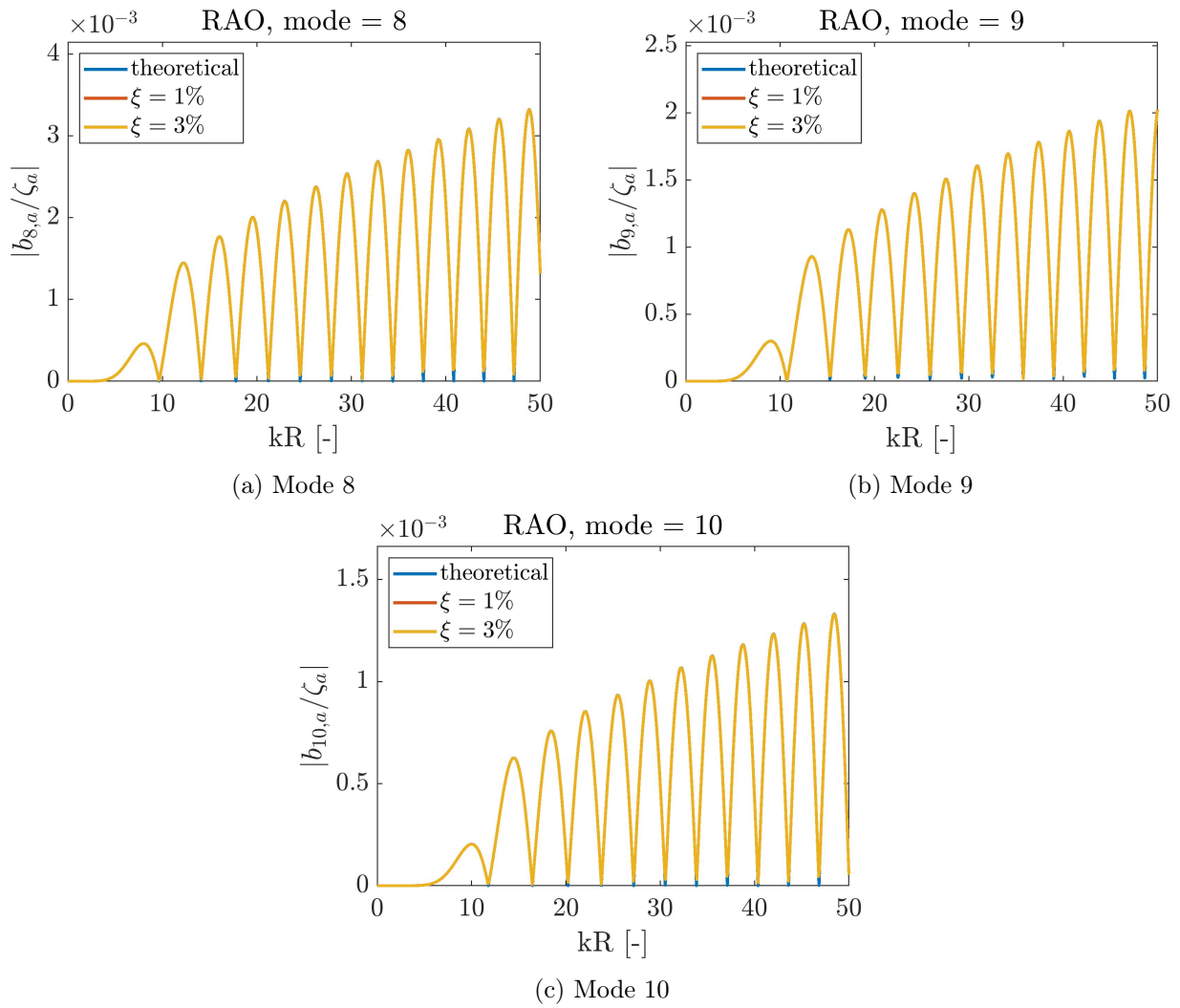
Figure D.4: Damped RAOs for radial modes 8-13

RAOs for a single floater without mooring-lines for Rayleigh damping values of 1 and 3%, plotted against the corresponding theoretical RAO.

D.4   RAOs for Radial Modes With vs Without Mooring-lines

(a) Mode 9

(b) Mode 10

(c) Mode 11

(d) Mode 12

(e) Mode 13

(f) Mode 14
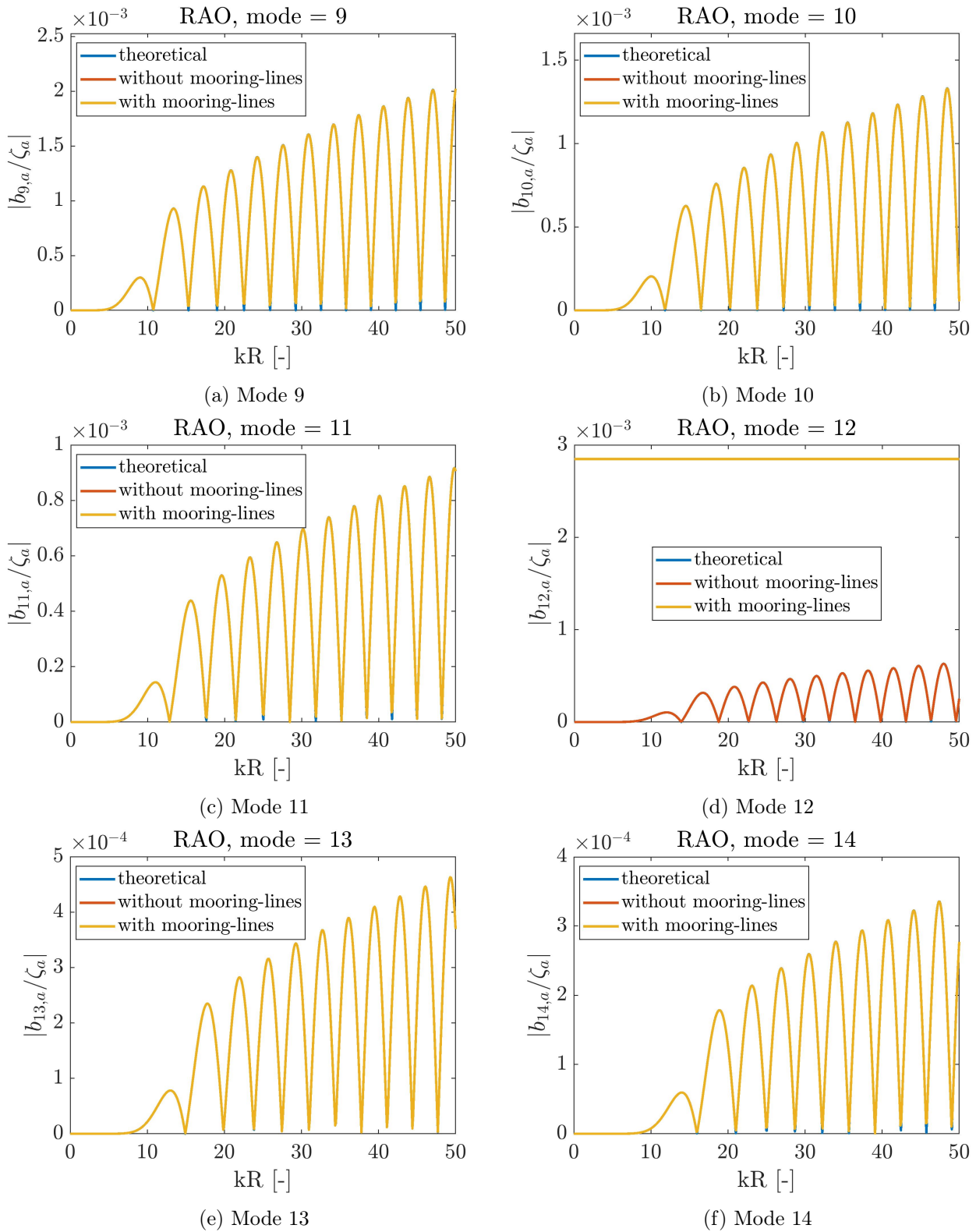
Figure D.5: Radial mode 9-14 RAOs - with vs without mooring-lines

Resulting numerical RAOs for a single floater, run both with and without mooring-lines. A Rayleigh damping value of 1% is used. The corresponding theoretical RAO is also plotted.

(a) Mode 15

(b) Mode 16

(c) Mode 17

(d) Mode 18

(e) Mode 19

(f) Mode 20
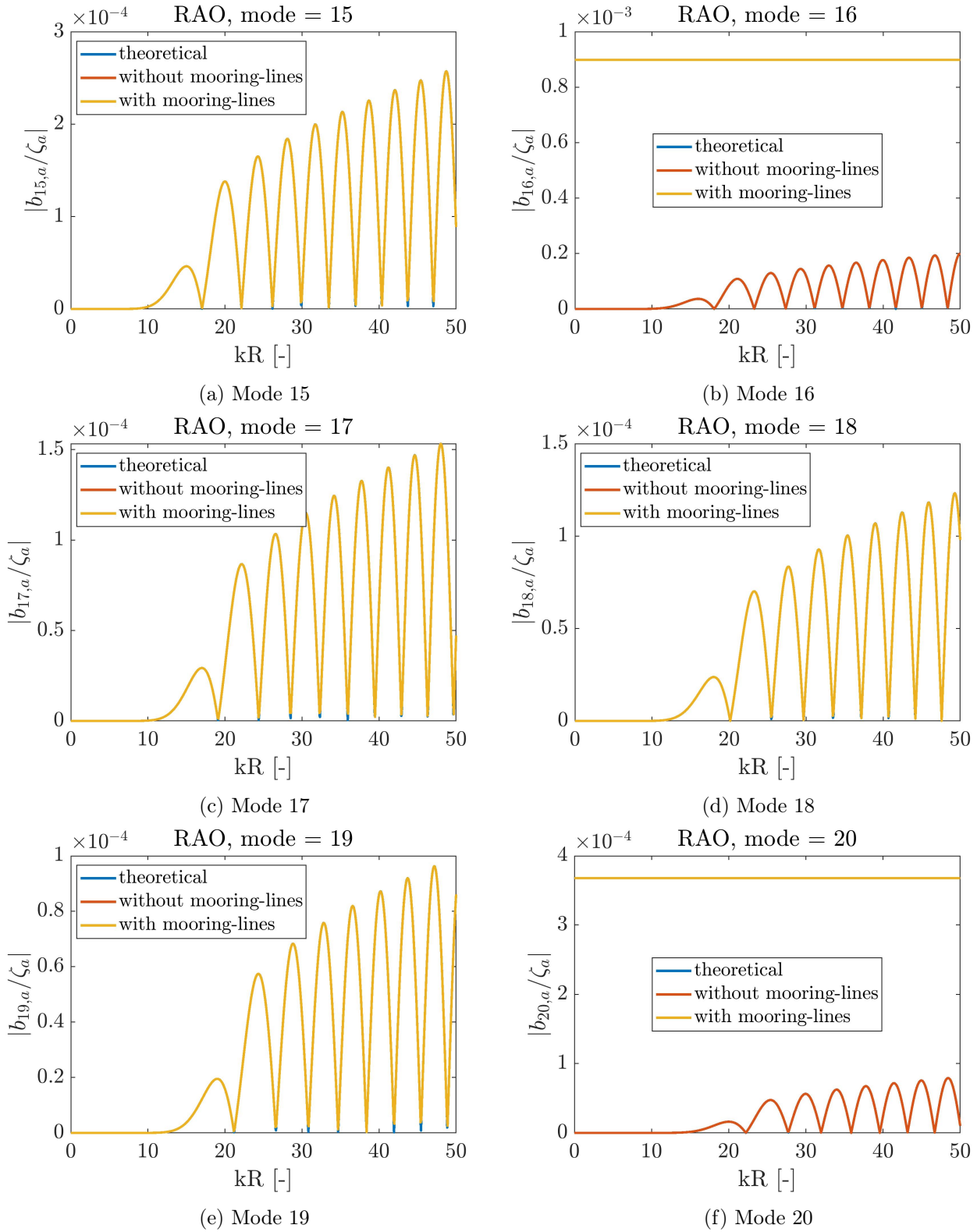
Figure D.6: Radial mode 15-20 RAOs - with vs without mooring-lines
Resulting numerical RAOs for a single floater, run both with and without mooring-lines. A Rayleigh damping value of 1% is used. The corresponding theoretical RAO is also plotted.

D.5   Problem With Modes Divisible by Four

The following plots are a supplement to the presentation in Section 4.4.3.
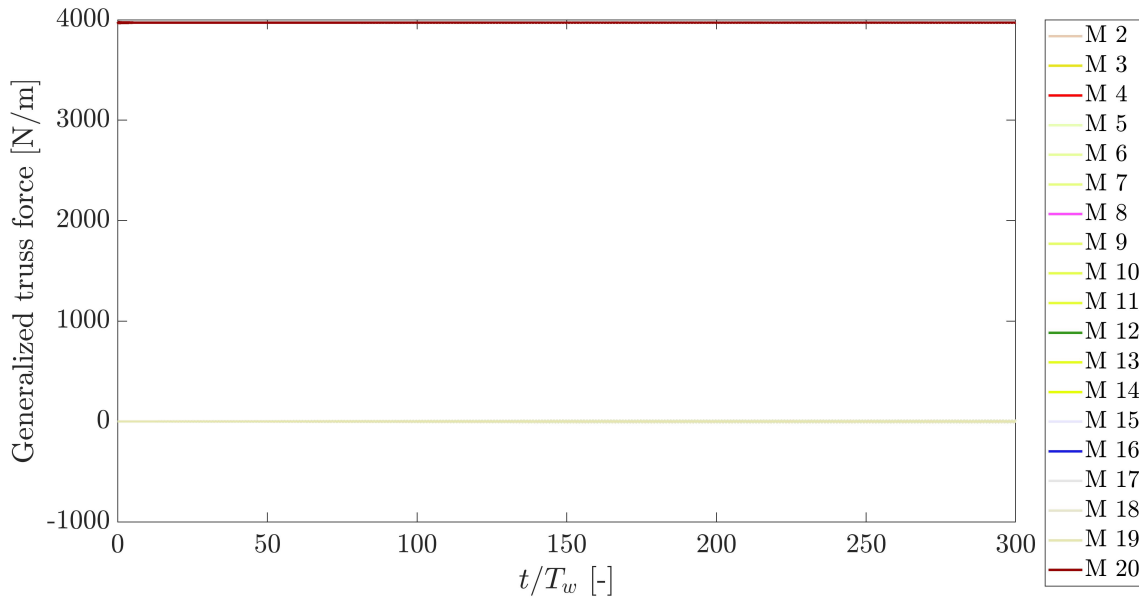
Figure D.7: Radial generalized truss-force problem
Generalized radial truss-force time-series are plotted for radial modes $M = 2 - 20$. A pre-tension of $Tp = 78125$ N is used.
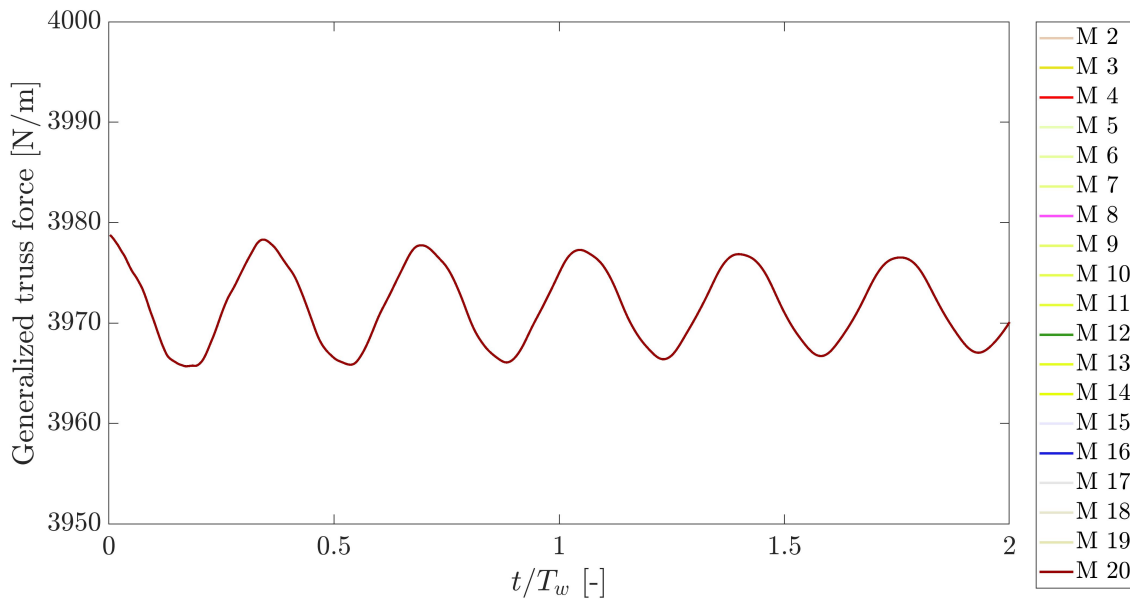
Figure D.8: Radial generalized truss-force problem - zoomed in version
Generalized truss-force time-series are plotted for radial modes $M = 2 - 20$. The plot is zoomed in on the initial part of the time-series. During plotting, it is observed that modes divisible by four are plotted over each other. A pre-tension of $Tp = 78125$ N is used.

(a)

(b)
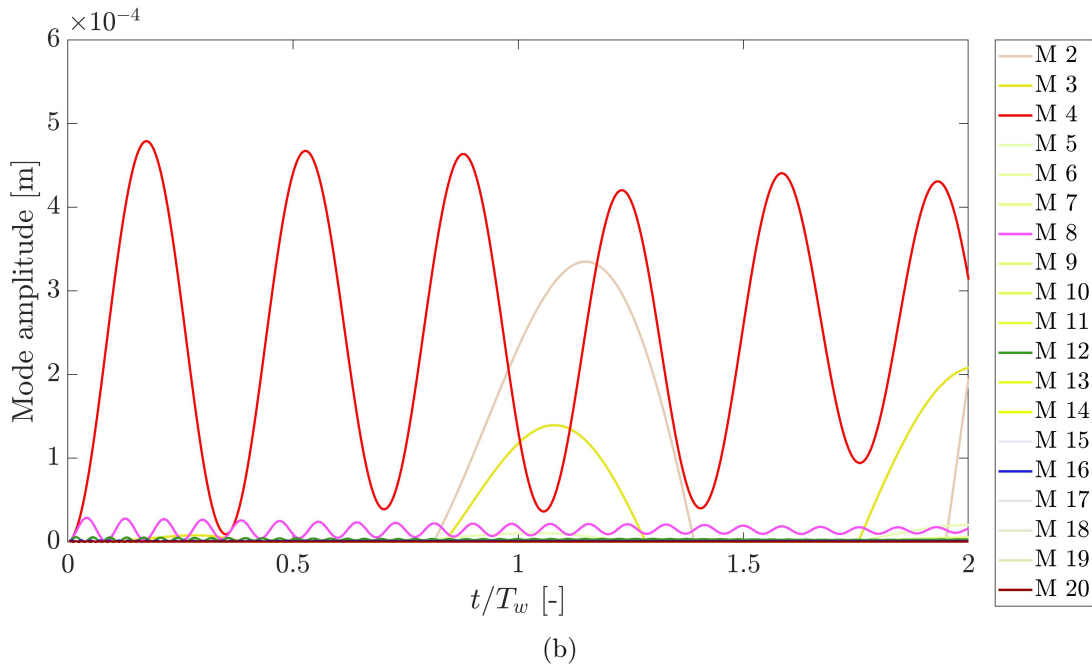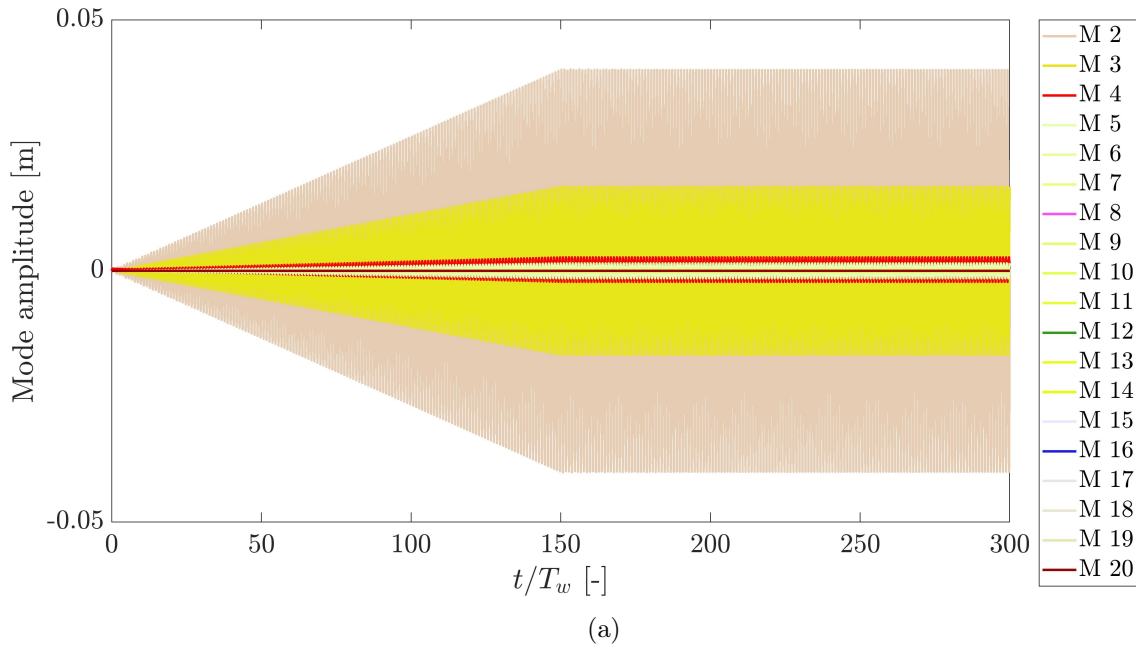
Figure D.9: Mode amplitude problem - lower pre-tension
Mode amplitude time-series are plotted for radial modes $M = 2 - 20$. Figure a) shows the full time-series, while b) is zoomed in version of the same plot. A pre-tension of $Tp = 781.25$ N is used.
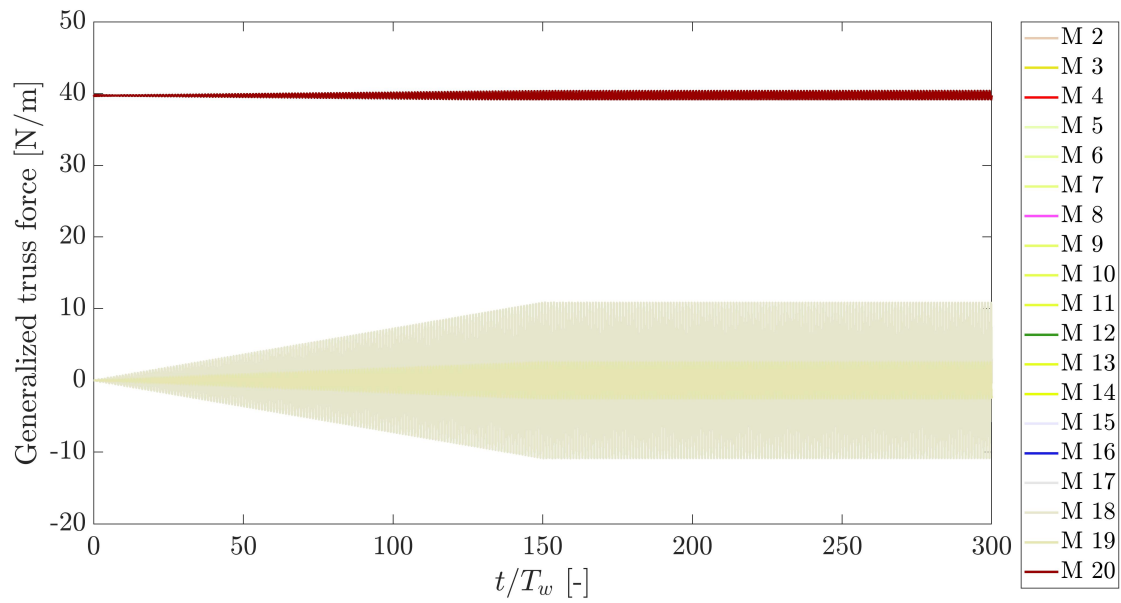
Figure D.10: Truss-force problem - lower pre-tension

Generalized truss-force time-series are plotted for radial modes $M = 2 - 20$. A pre-tension of $Tp = 781.25$ N is used.

Appendix E

Supplement for Single Floater Combined Motion Verification

Figure E.1 and Figure E.2 are a supplement to the combined mode verification case 1 in Section 4.5.1.

<div align="center">(a)</div>

<div align="center">(b)</div>
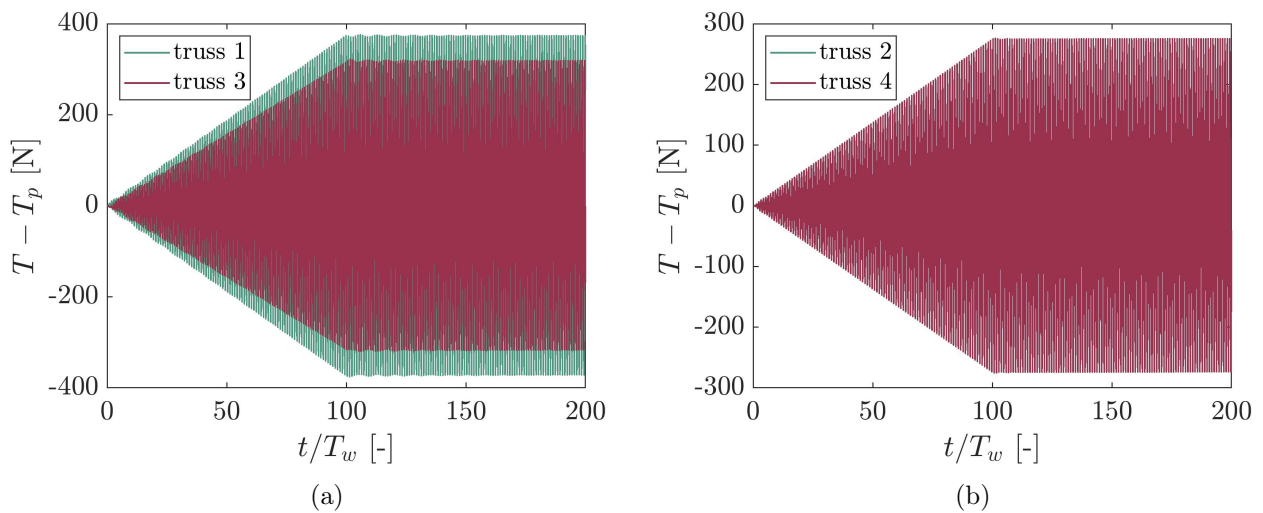
Figure E.1: Node motion for combined mode case 1

Figure a) shows the truss tension time-series for mooring-trusses 1 and 3. Figure b) shows the truss tension time-series for mooring-trusses 2 and 4. T is the instantaneous tension, while T_p is the initial pre-tension of the truss.
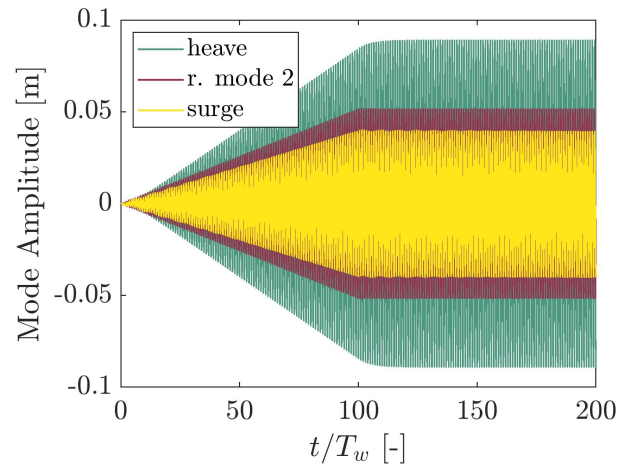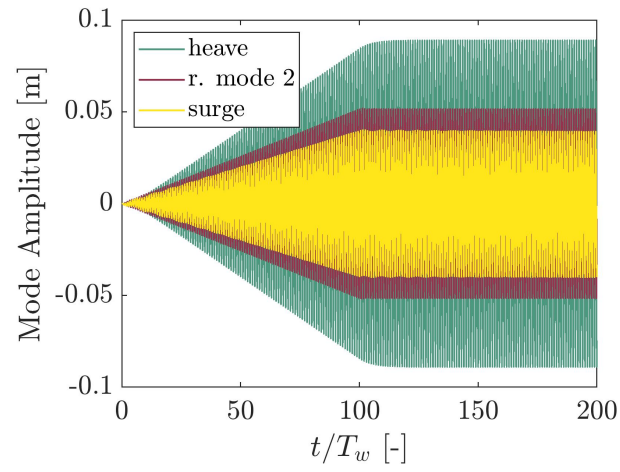
Figure E.2: Mode amplitudes for combined case 1
Mode-amplitude time-series for combined mode case 1. *r.mode 2* is radial mode 2, which is the first flexible lateral mode.

Figure E.3 and Figure E.4 are a supplement to the combined mode verification case 2 in Section 4.5.2.

(a)

(b)
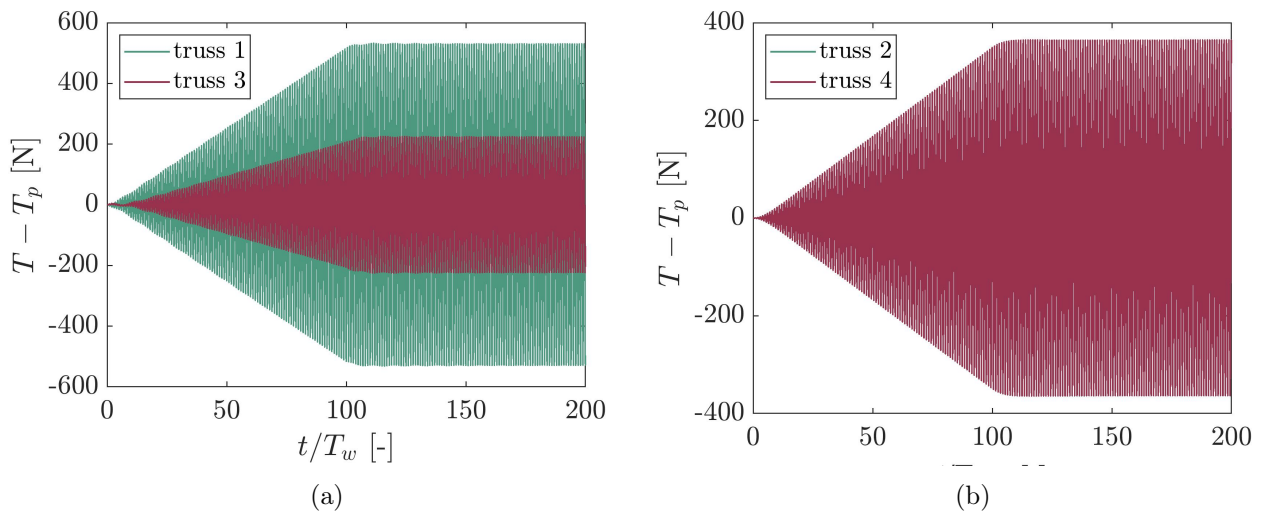
Figure E.3: Node motion for combined mode case 2
Figure a) shows the truss tension time-series for mooring-trusses 1 and 3. Figure b) shows the truss tension time-series for mooring-trusses 2 and 4. T is the instantaneous tension, while T_p is the initial pre-tension of the truss.
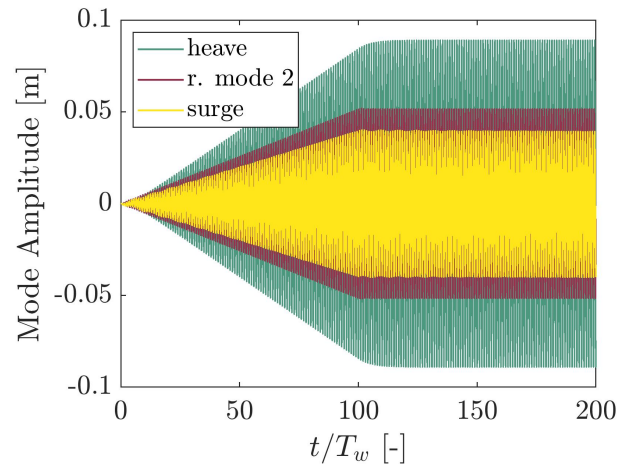
Figure E.4: Mode amplitudes for combined case 2
Mode-amplitude time-series for combined mode case 1. *r.mode 2* is radial mode 2, which is the first flexible lateral mode.

Figure E.5 and Figure E.6 are a supplement to the combined mode verification case 3 in Section 4.5.3.

(a)

(b)
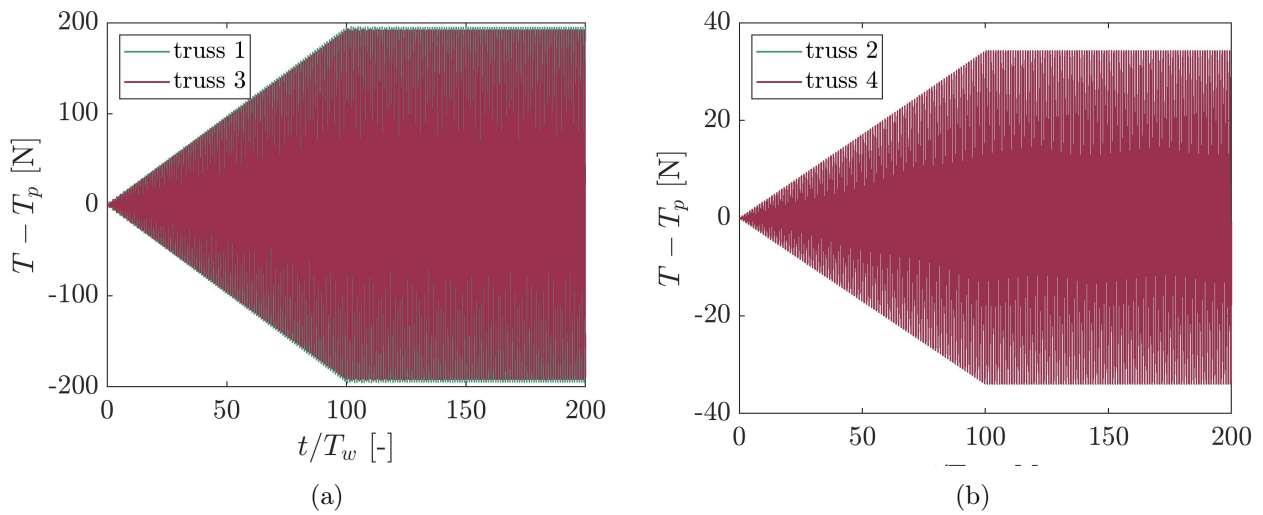
Figure E.5: Node motion for combined mode case 3
Figure a) shows the truss tension time-series for mooring-trusses 1 and 3. Figure b) shows the truss tension time-series for mooring-trusses 2 and 4. T is the instantaneous tension, while T_p is the initial pre-tension of the truss.

Figure E.6: Mode amplitudes for combined case 3
Mode-amplitude time-series for combined mode case 3 *r.mode 2* is radial mode 2, which is the first flexible
lateral mode.

Appendix F

Additional Information From Previous Model Tests

F.1 Regular Wave Test Matrix in Winsvold Model Tests

T [s]	$\lambda[m]$	$H/\lambda = 1/60$ H [m]	$H/\lambda = 1/40$ H [m]	$H/\lambda = 1/30$ H [m]	$H/\lambda = 1/20$ H [m]
2.0	6.2452	0.1041	0.1561	0.2082	0.3123
2.5	9.7582	0.1626	0.2440	0.3253	0.4879
3.0	14.0518	0.2342	0.3513	0.4684	0.7026
3.5	19.1260	0.3188	0.4782	0.6375	0.9563
4.0	24.9810	0.4163	0.6245	0.8327	1.2490
4.5	31.6165	0.5269	0.7904	1.0539	1.5808
5.0	39.0319	0.6505	0.9758	1.3011	1.9516
5.5	47.2222	0.7870	1.1806	1.5741	2.3611
6.0	56.1672	0.9361	1.4042	1.8722	2.8084
6.5	65.8153	1.0969	1.6454	2.1938	3.2908
7.0	76.0710	1.2679	1.9018	2.5357	3.8036
7.5	86.8002	1.4467	2.1700	2.8933	4.3400
8.0	97.8525	1.6309	2.4463	3.2618	4.8926
8.5	109.0881	1.8181	2.7272	3.6363	5.4544
9.0	120.3954	2.0066	3.0099	4.0132	6.0198
9.5	131.6953	2.1949	3.2924	4.3898	6.5848
10.0	142.9379	2.3823	3.5734	4.7646	7.1469
10.5	154.0946	2.5682	3.8524	5.1365	7.7047
11.0	165.1515	2.7525	4.1288	5.5050	8.2576
11.5	176.1040	2.9351	4.4026	5.8701	8.8052
12.0	186.9532	3.1159	4.6738	6.2318	9.3477
12.5	197.7033	3.2951	4.9426	6.5901	9.8852
13.0	208.3599	3.4727	5.2090	6.9453	10.4180
13.5	218.9295	3.6488	5.4732	7.2976	10.9465
14.0	229.4186	3.8236	5.7355	7.6473	11.4709

Figure F.1: Regular Wave Test Matrix in Winsvold Model Tests
Full scale test matrix for regular waves run in Winsvold model tests. Taken from Winsvold (2018).

F.1.1   Illustration of Experimental Mooring Set-Up by V. Sigstad
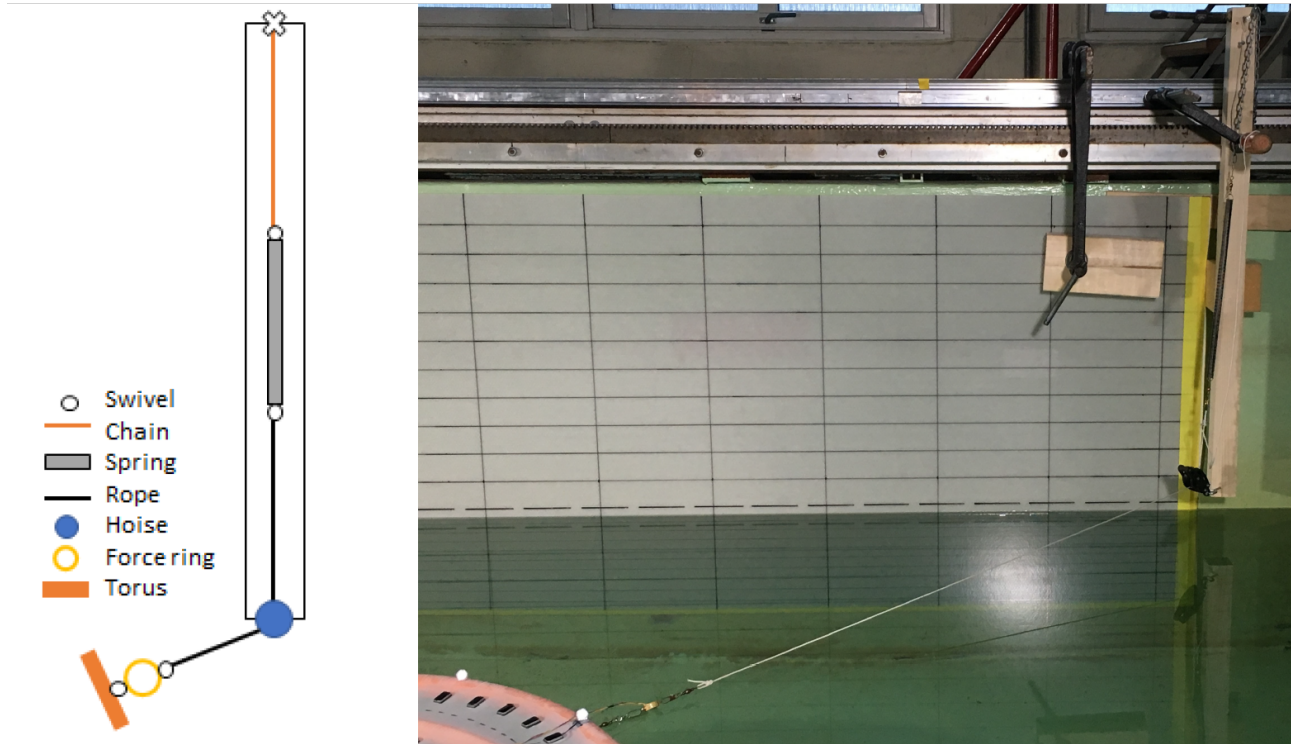
Figure F.2: Experimental Mooring-line set-up by V. Sigstad
To the left: Illustration of mooring-line set-up. To the right: photograph of the mooring-line set-up in the wave tank. Both are taken from Vassdokken Sigstad (2019)

F.1.2   Regular Wave Test Matrix in V. Sigstad Model Tests

Test	kD_{min} $[m^2]$	kD_{max} $[m^2]$	N_k [-]	$(H/\lambda)_{min}$ [-]	$(H/\lambda)_{max}$ [-]	$\Delta(H/\lambda)$ [-]	h [m]	N_T [-]	N_{ramp} [-]	t_{zero} [s]
1060	1.3764	12.5759	60	60	60	60	0.7	60	5	180
1050	1.3764	12.5759	60	50	50	50	0.7	60	5	180
1040	1.3764	12.5759	60	40	40	40	0.7	60	5	180
1030	1.3764	12.5759	60	30	30	30	0.7	60	5	180
3000	3.2146	5.5938	1	60	30	30	0.7	60	5	180

Figure F.3: Regular Wave Test Matrix in V. Sigstad Model Tests
Input to test matrix generation script for regular waves. k is the wave number, D the model diameter, N_k the number of wave numbers to be run, H/λ wave steepness, $\Delta(H/\lambda)$ change in steepness for each step, h the water level in the tank, N_T the number of wave periods, N_{ramp} the number of ramping wave periods at the start and end of a run, and finally t_{zero} the pause time between each series of waves. Taken from Vassdokken Sigstad (2019)

Appendix G

Additional Experimental Results

G.1   Full Experimental Heave RAO
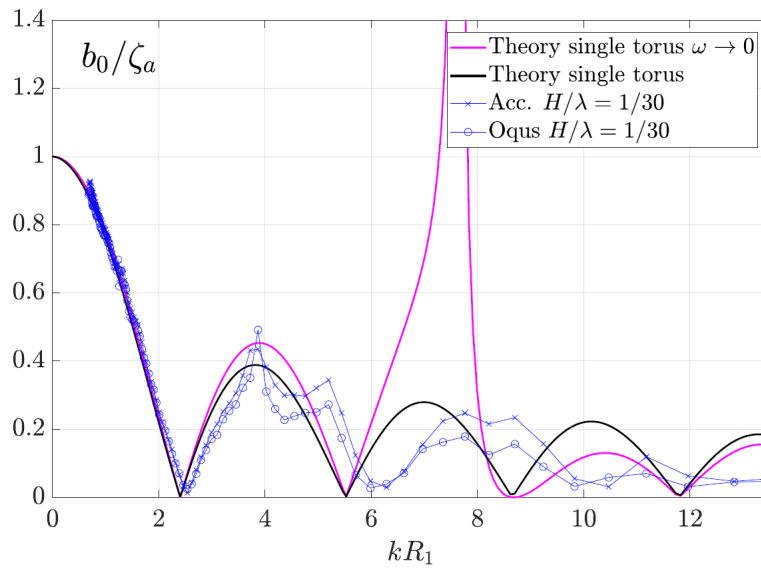
Figure G.1: Full experimental heave RAO by Winsvold

Full experimental heave RAOs for the outer torus, estimated from both accelerometers and the optical sensor system, plotted against the corresponding ZFT (pink) and low-frequency (black) RAOs. Taken from Kristiansen and Winsvold (2019).

G.2   Additional Experimental RAOs
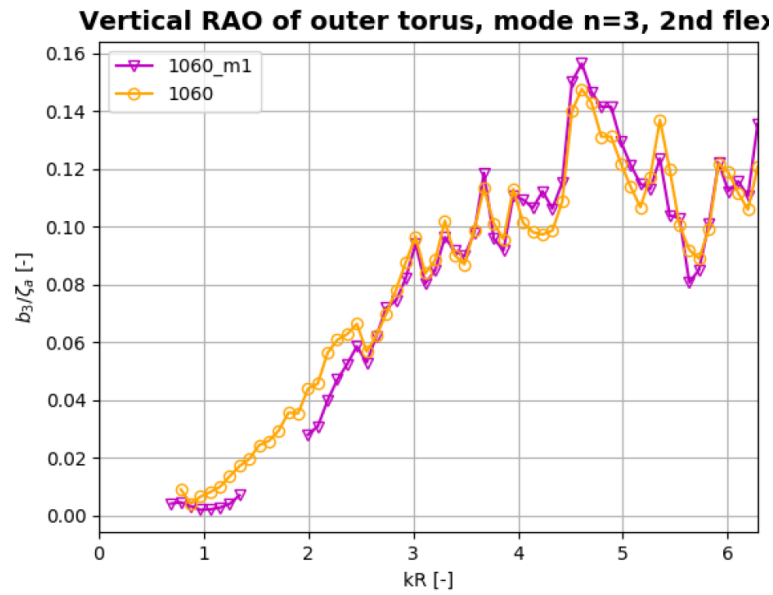
Figure G.2: Experimental RAO in second flexible vertical mode
Resulting experimental RAO in the second flexible vertical mode (b_3/ζ_a) for the outer torus, for the model
with membrane (1060_{m1}) and without (1060). The wave steepness is $H/\lambda = 1/60$. Taken from
Vassdokken Sigstad (2019).
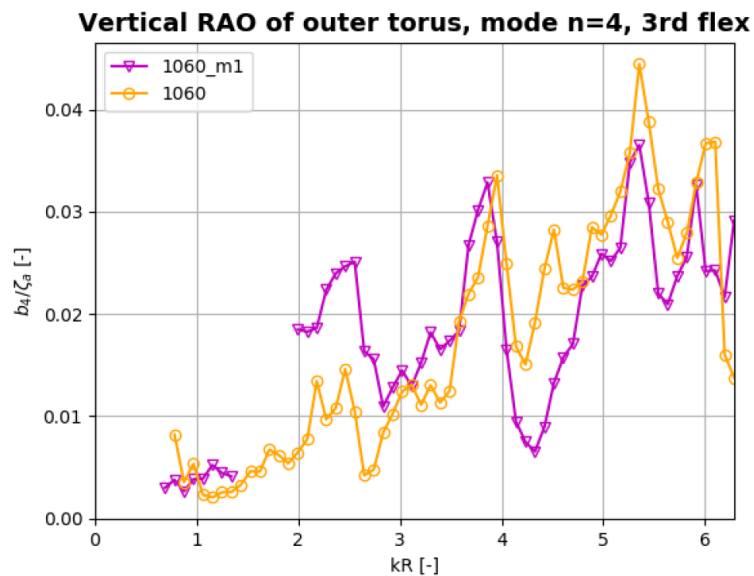
Figure G.3: Experimental RAO in third flexible vertical mode
Resulting experimental RAO in the third flexible vertical mode (b_4/ζ_a) for the outer torus, for the model with
membrane (1060_{m1}) and without (1060). The wave steepness is $H/\lambda = 1/60$. Taken from Vassdokken Sigstad
(2019).
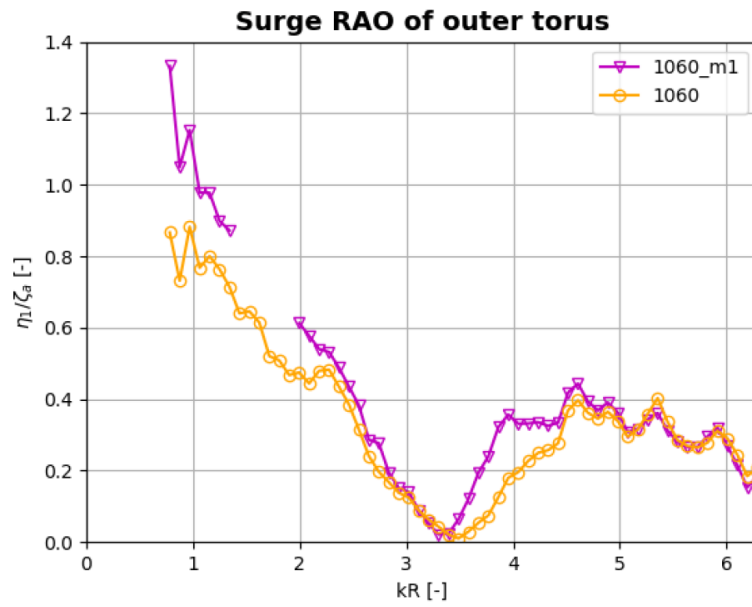
Figure G.4: Experimental RAO in surge
Resulting experimental RAO in surge (η_1/ζ_a) for the outer torus, for the model with membrane (1060_{m1}) and without (1060). The wave steepness is $H/\lambda = 1/60$. Taken from Vassdokken Sigstad (2019).
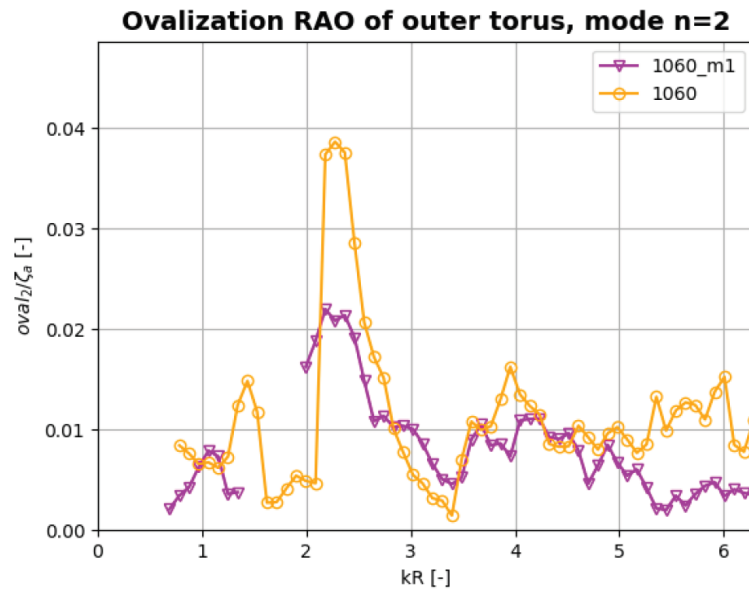
Figure G.5: Experimental RAO in the first flexible lateral mode
Resulting experimental RAO in first flexible lateral mode ($oval_2/\zeta_a$) for the outer torus, for the model with membrane (1060_{m1}) and without (1060). The wave steepness is $H/\lambda = 1/60$. Taken from Vassdokken Sigstad (2019).
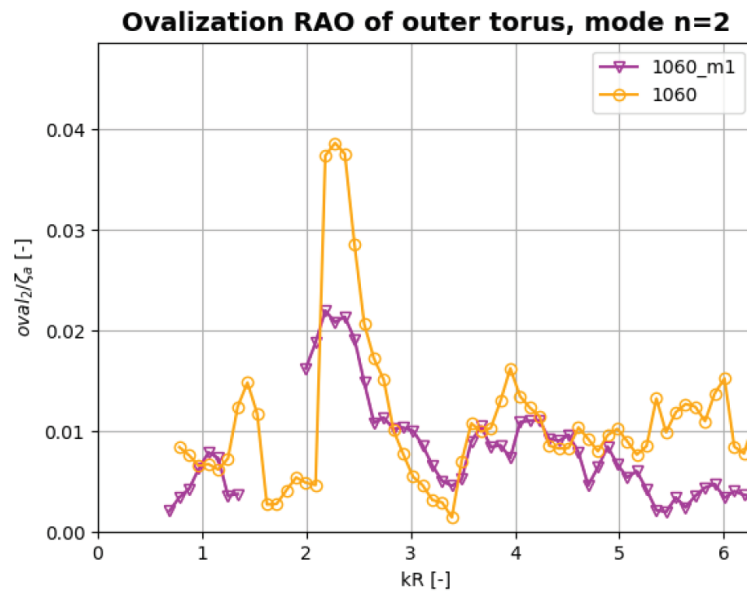
Figure G.6: Experimental RAO in the second flexible lateral mode
Resulting experimental RAO in second flexible lateral mode ($oval_3/\zeta_a$) for the outer torus, for the model with membrane (1060_{m1}) and without (1060). The wave steepness is $H/\lambda = 1/60$. Taken from Vassdokken Sigstad (2019).

Appendix H

Additional Numerical Solar Island Results

H.1   Flowchart

Figure H.1 shows a simplified flowchart for the numerical solar island that is implemented in MATLAB. The final code is complex, and in total about 1000 lines long.
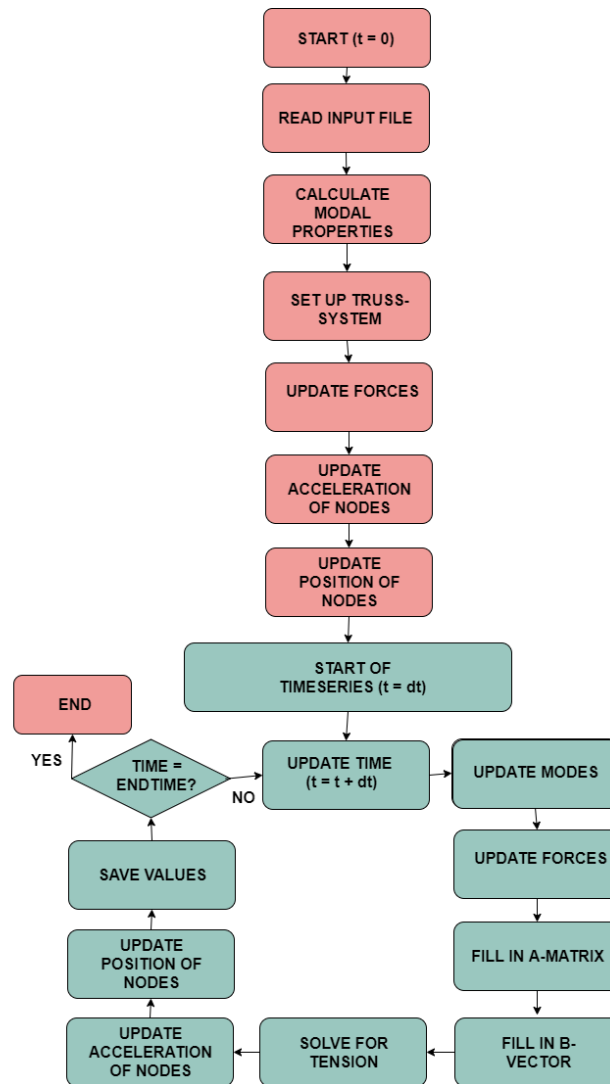
Figure H.1: Flowchart of numerical solar island code implementation
The chart illustrates the numerical solar island code as it is set up for a single time-series.

The updating of modes is done in the following manner:

$$\dot{u}^{n+1} = \dot{u}^n + dt\ddot{u}^n$$
$$u^{n+1} = u^n + dt\dot{u}^{n+1}$$

Here, u represents the mode-amplitude, and the method is the same for both vertical, radial and surge mode amplitudes. Keep in mind that each mode amplitude of each torus must be updated. n is a certain time instant, and $n+1$ the next, separated by dt.

H.2 2-Tori Model - low vs. initial pre-tension

(a) first flexible

(b) second flexible

(c) third flexible
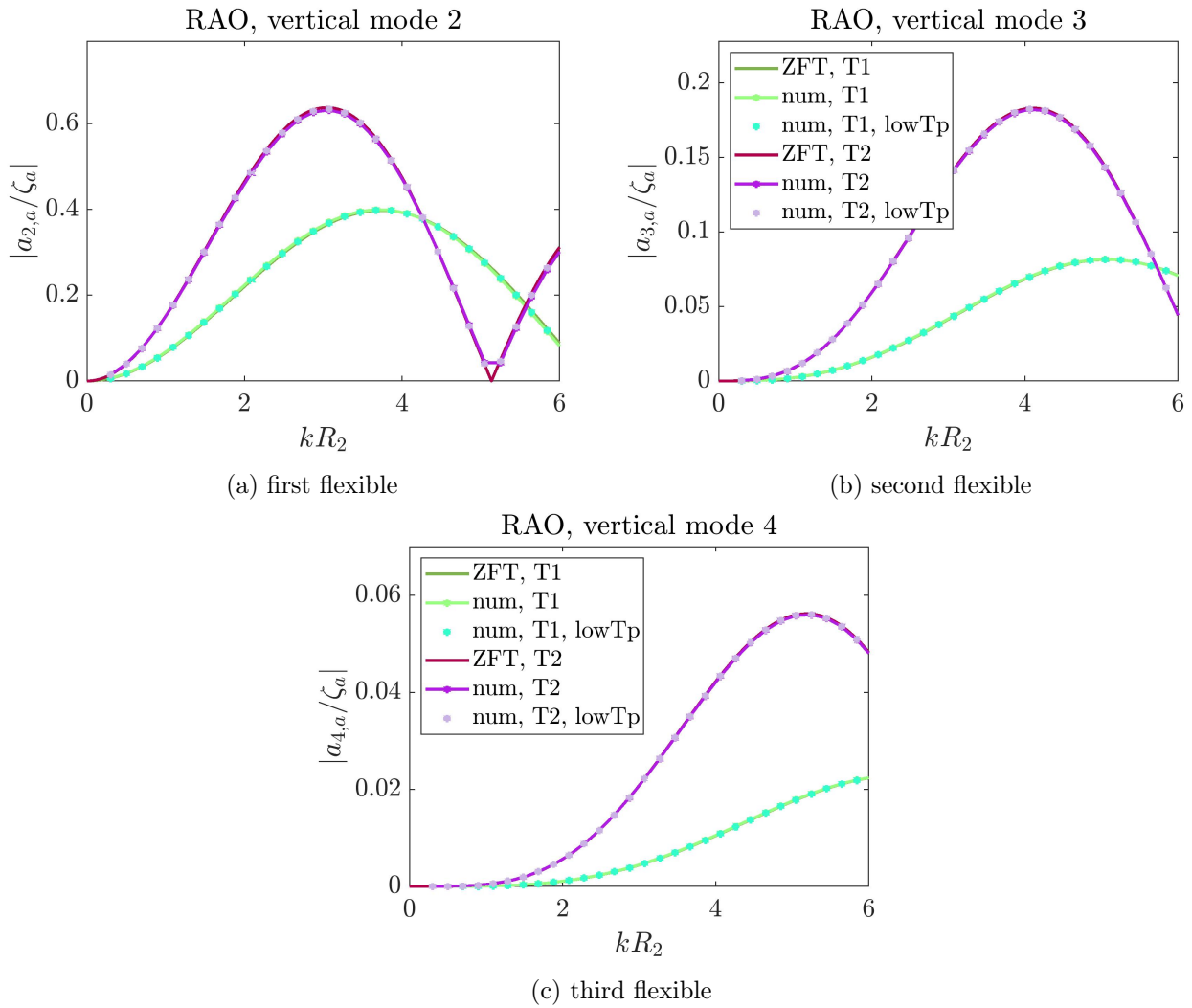
Figure H.2: Low vs. initial pre-tension - vertical mode RAOs
Resulting numerical RAOs for vertical modes plotted against ZFT, for each of the two tori in the 2-torus model. *num* denotes numerical results. Further, $T1$ denotes torus 1 and $T2$ torus 2, where the latter is the outer torus of the system. *lowTp* is from a run with $T_{pct} = 18550$, which is half of the pre-tension in the initial run.
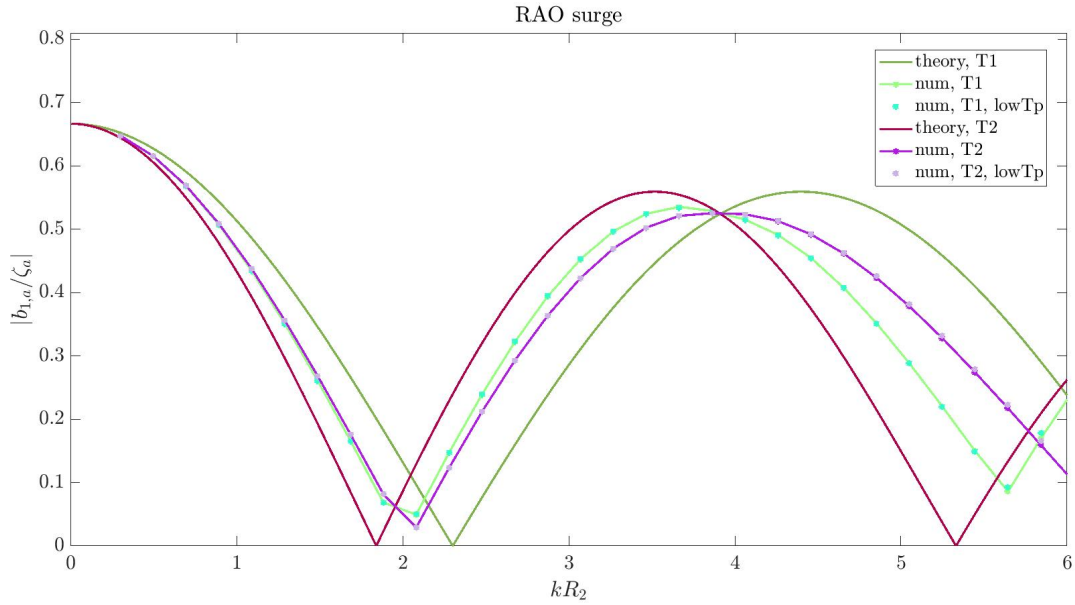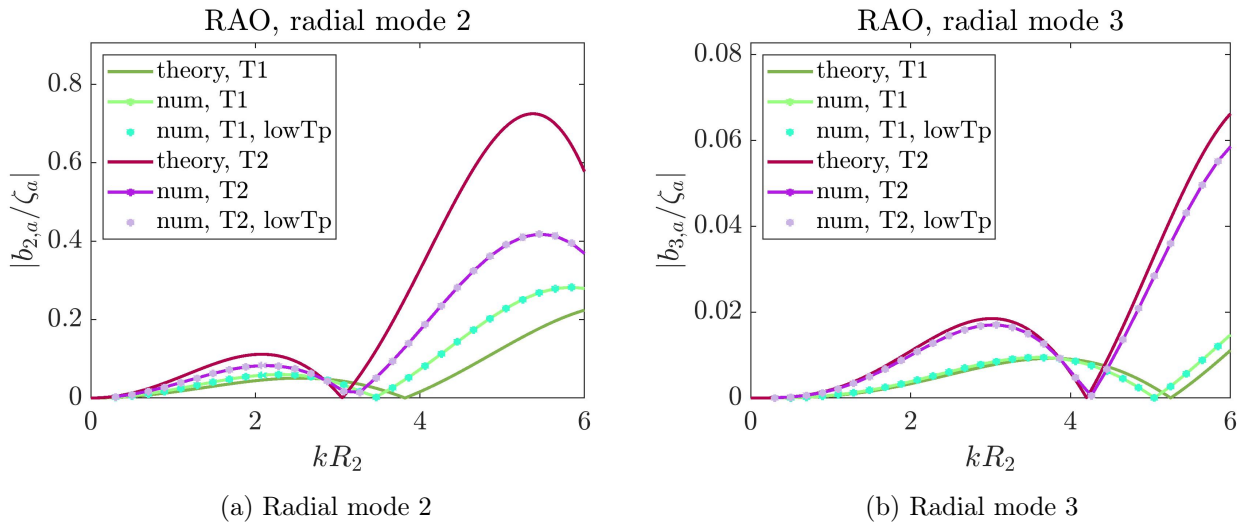
Figure H.3: Low vs. initial pre-tension - surge mode RAOs
Resulting numerical RAOs for surge mode plotted against ZFT, for each of the two tori in the 2-torus model. *num* denotes numerical results. Further, $T1$ denotes torus 1 and $T2$ torus 2, where the latter is the outer torus of the system. *lowTp* is from a run with $T_{pct} = 18550$, which is half of the pre-tension in the initial run.

(a) Radial mode 2

(b) Radial mode 3

Figure H.4: Low vs. initial pre-tension - radial mode RAOs
Resulting numerical RAOs for radial modes plotted against single floater theory, for each of the two tori in the 2-torus model. *num* denotes numerical results. Further, $T1$ denotes torus 1 and $T2$ torus 2, where the latter is the outer torus of the system. *lowTp* is from a run with $T_{pct} = 18550$, which is half of the pre-tension in the initial run.

H.3   5-Torus Model - Additional RAOs
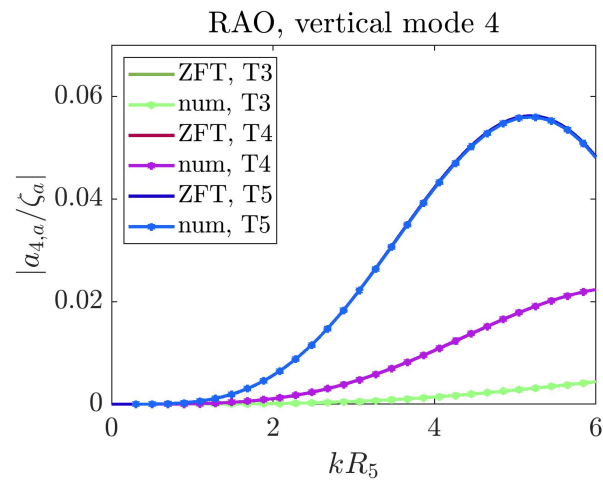
Figure H.5: Vertical mode 4 RAOs for 5-torus model
Resulting numerical RAOs in vertical mode 4 plotted against ZFT, for each of the three outer tori in the 5-torus model. *num* denotes numerical results. Further, $T3$ denotes torus 3, $T4$ torus 4 and $T5$ torus 5, where the latter is the outer torus of the system.
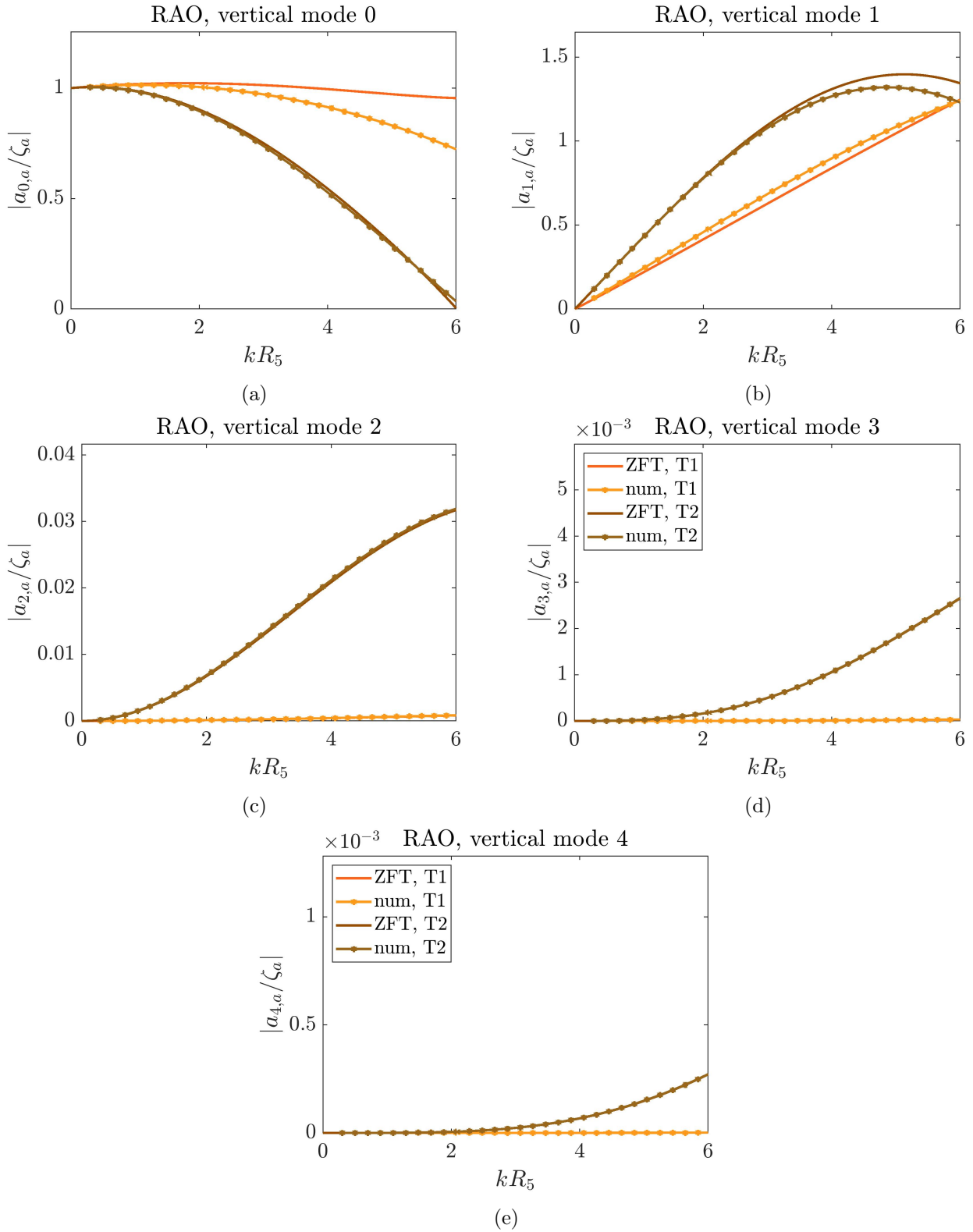
Figure H.6: Vertical mode RAOs for 5-torus model

Resulting numerical RAOs in the first four vertical modes plotted against single floater theory, for the two most inner tori in the 5-torus model. *num* denotes numerical results. Further, $T1$ denotes torus 1 and $T2$ torus 2, where the former is the inner torus of the system. The legend in d) is for all four plots.
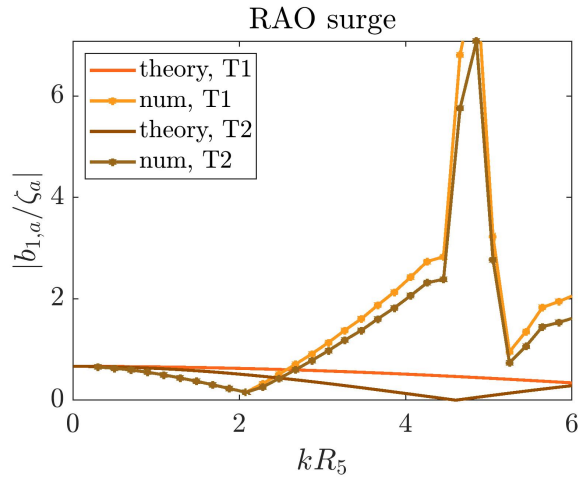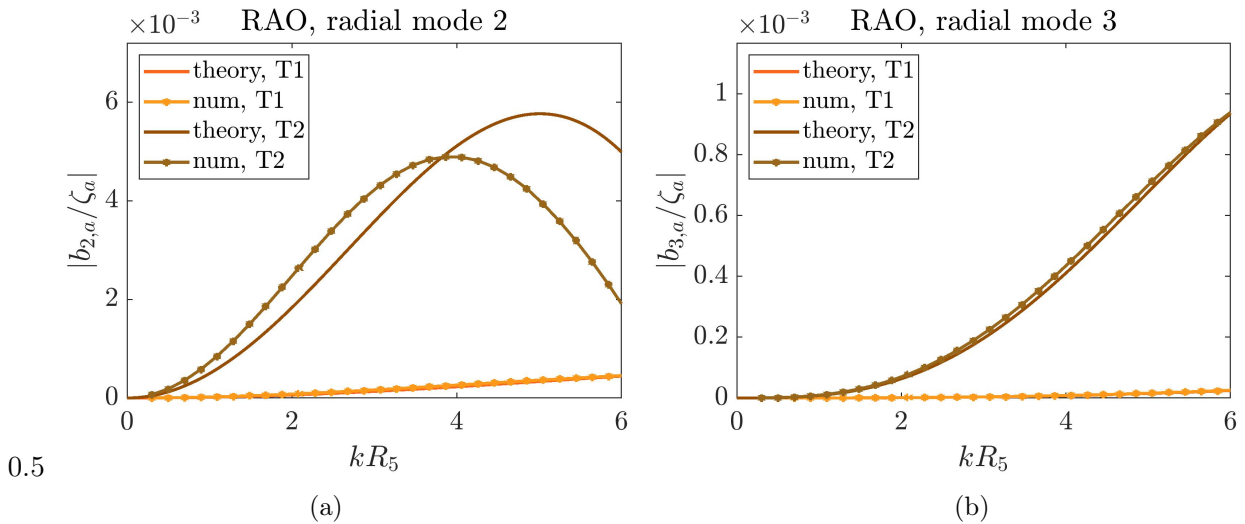
RAO surge

Figure H.7: Surge

Resulting numerical RAOs in surge plotted against theoretical RAOs for the two most inner tori in the 5-torus model. *num* denotes numerical results. Further, $T1$ denotes torus 1 and $T2$ torus 2, where the former is the inner torus of the system.

(a)

(b)

Figure H.8: Radial mode RAOs for 5-torus model

Resulting numerical RAOs in radial modes plotted against theoretical RAOs for the two most inner tori in the 5-torus model. *num* denotes numerical results. Further, $T1$ denotes torus 1 and $T2$ torus 2, where the former is the inner torus of the system.

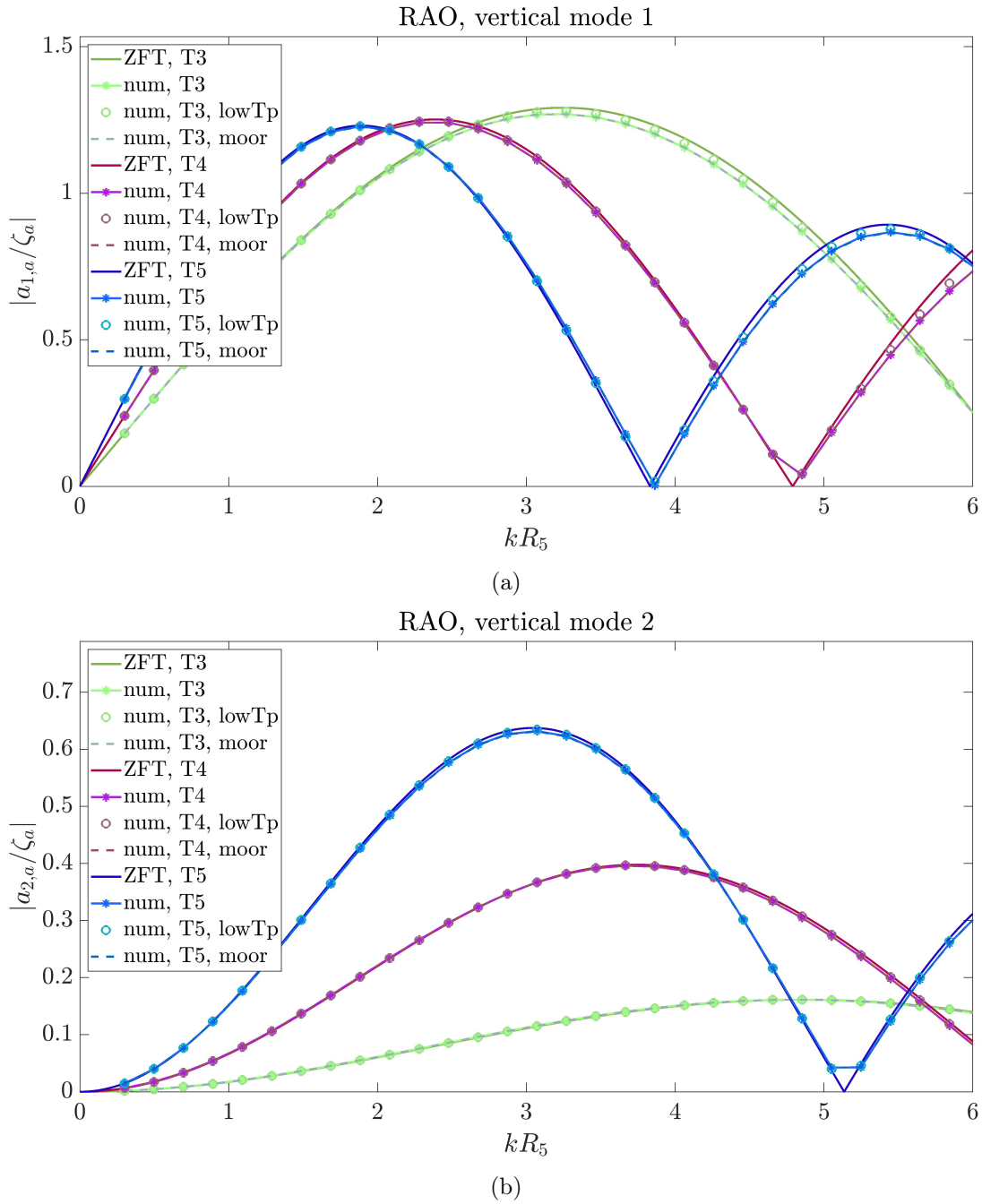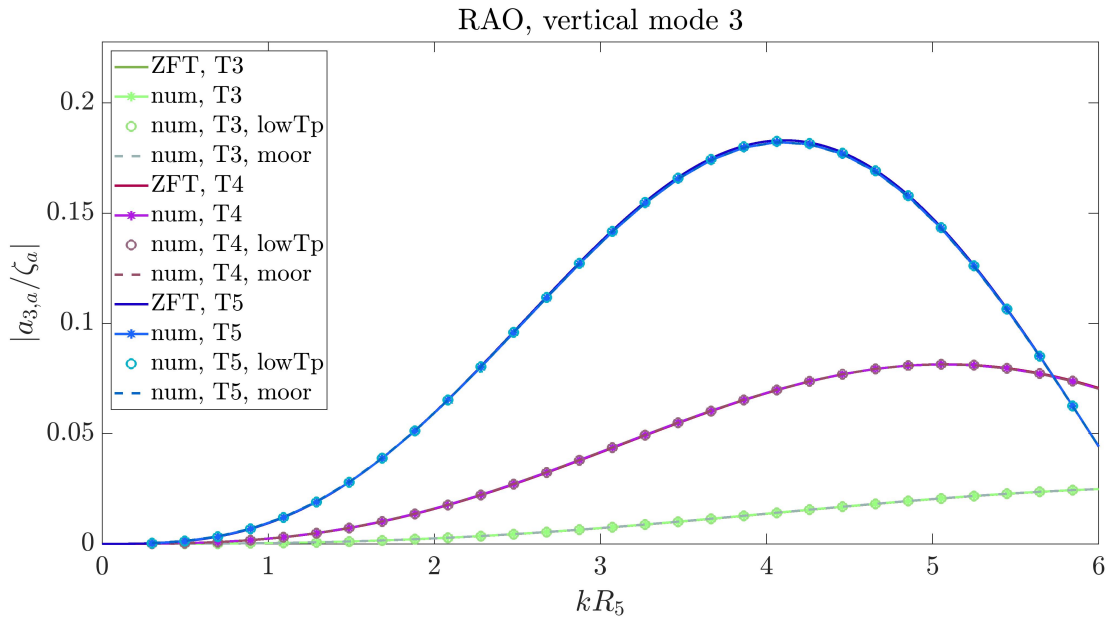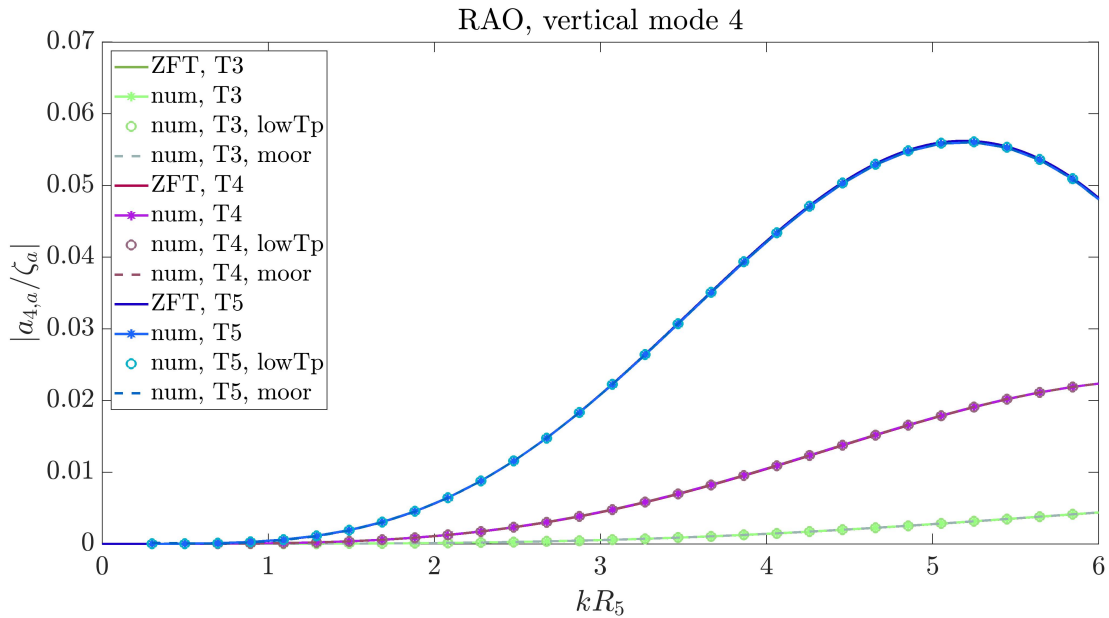## H.4   5-Torus Model - Additional Altered Version RAOs

(a)

(b)

Figure H.9: Vertical mode RAOs: 5-tours case vs. altered versions
Resulting numerical RAOs in vertical modes $1-2$ plotted against ZFT RAOs for the three outermost tori in the 5-torus model. *num* denotes numerical results. Further, $T3$ denotes torus 3, $T4$ torus 4 and $T5$ torus 5, where the latter is the outer torus of the system. *lowTp* is for a version with half the original pre-tension, $T_{pct} = 18550$ N, and *moor* is for a moored-version of the 5-torus case.
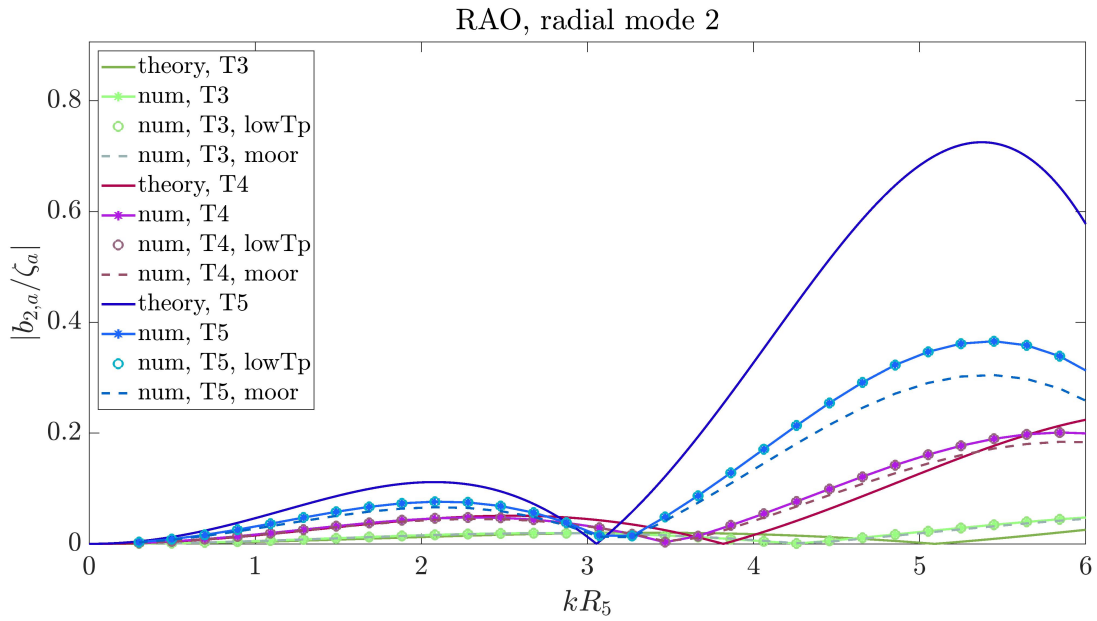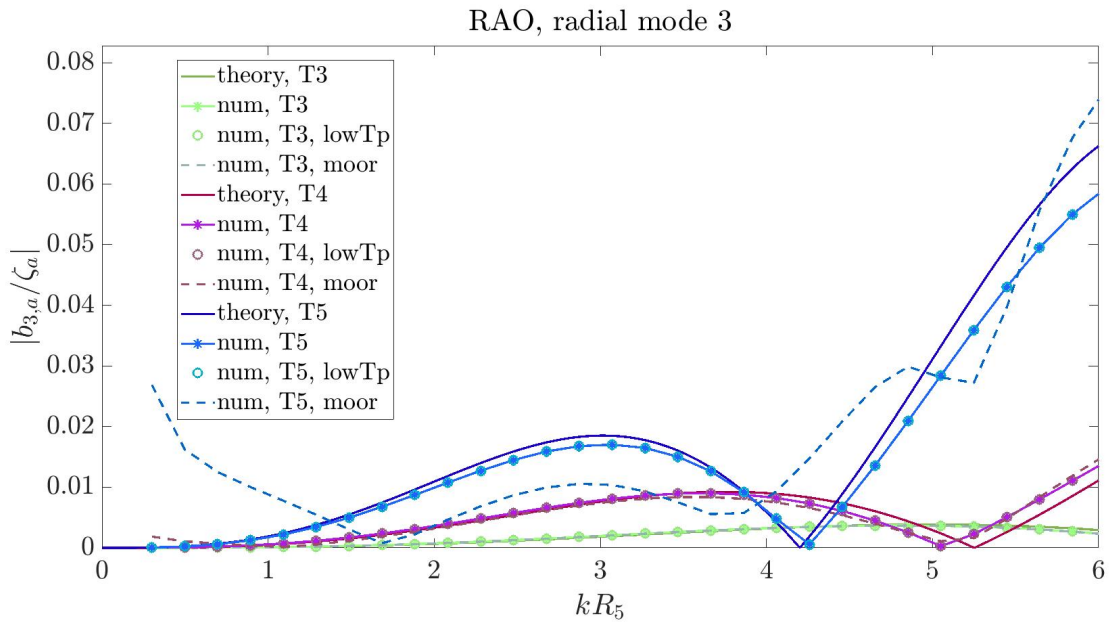
Figure H.10: Vertical mode RAOs, 5-tours case vs. altered versions

Resulting numerical RAOs in vertical modes $3-4$ plotted against theoretical RAOs for the three outermost tori in the 5-torus model. *num* denotes numerical results. Further, $T3$ denotes torus 3, $T4$ torus 4 and $T5$ torus 5, where the latter is the outer torus of the system. *lowTp* is for a version with half the original pre-tension, $T_{pct} = 18550$ N, and *moor* is for a moored-version of the 5-torus case.

(a)

(b)

Figure H.11: Radial mode RAOs, 5-tours case vs. altered versions

Resulting numerical RAOs in radial modes $2 - 3$ plotted against theoretical RAOs for the three outermost tori in the 5-torus model. *num* denotes numerical results. Further, $T3$ denotes torus 3, $T4$ torus 4 and $T5$ torus 5, where the latter is the outer torus of the system. *lowTp* is for a version with half the original pre-tension, $T_{pct} = 18550$ N, and *moor* is for a moored-version of the 5-torus case.

H.5   5-Torus Model: Additional Time-series

(a) 5-torus case

(b) 5-torus case, moored
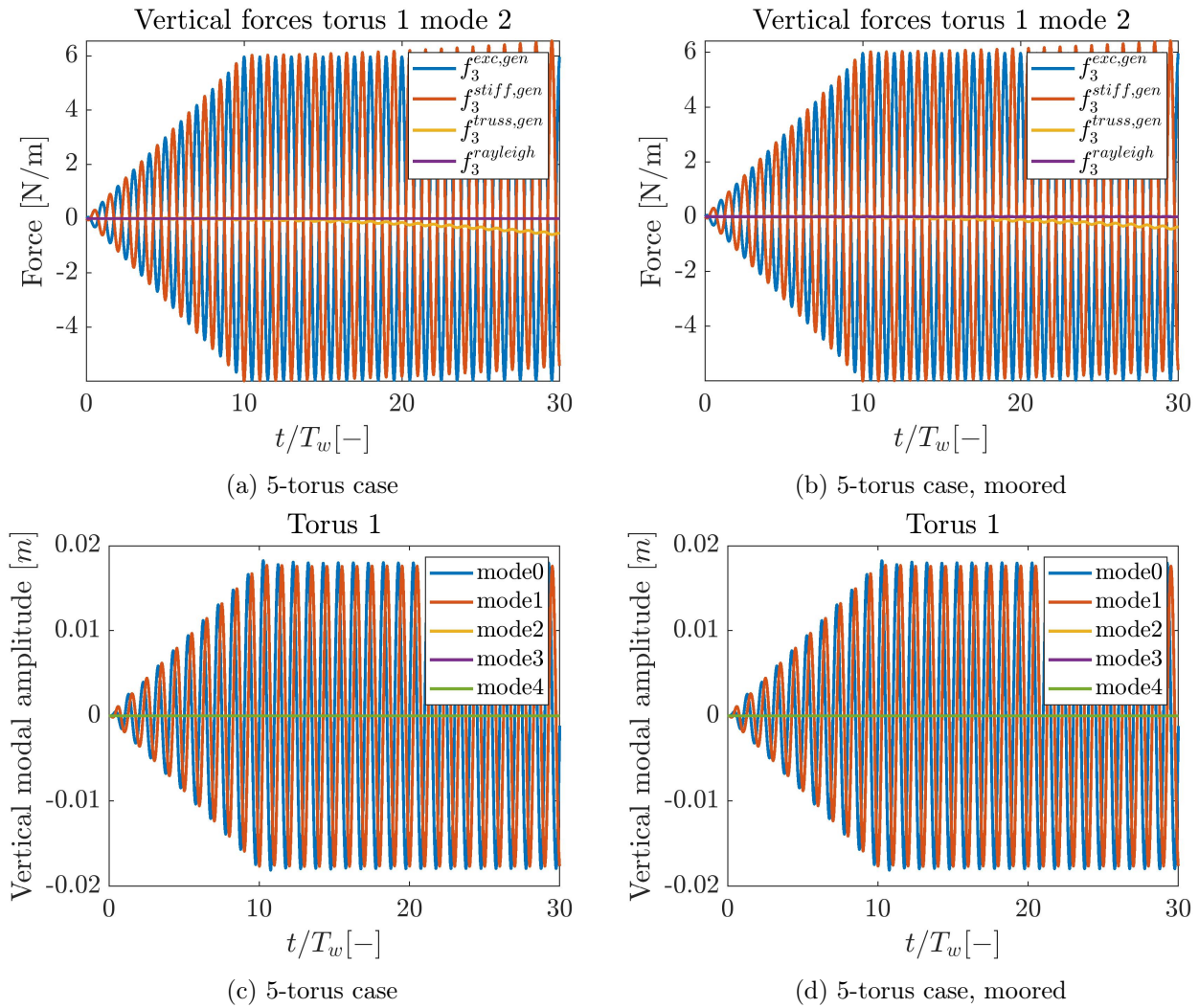
(c) 5-torus case

(d) 5-torus case, moored

Figure H.12: Vertical mode-amplitudes and forces in mode 2 on torus 1
a) shows the vertical generalized forces in vertical mode 2 on torus 1, for the 5-torus case. b) shows the same for the moored version of the 5-torus case. c) shows the vertical modal amplitudes for torus 1, for the 5-torus case. d) shows the same, only for the moored version of the 5-torus case.vertical mode amplitudes on the same torus. These plots are all for $kR_5 = 4$.

Svanhild Toppe Tolaas

A Numerical and Theoretical Study of a Multi-torus Floating Solar Island Concept

NTNU
Norwegian University of
Science and Technology